



HAL
open science

Modélisation multiéchelle du phénomène de fretting dans le contact aube-disque

Thomas Dick

► **To cite this version:**

Thomas Dick. Modélisation multiéchelle du phénomène de fretting dans le contact aube-disque. Mechanics [physics.med-ph]. École Nationale Supérieure des Mines de Paris, 2006. English. NNT : . tel-00136828

HAL Id: tel-00136828

<https://pastel.hal.science/tel-00136828>

Submitted on 15 Mar 2007

HAL is a multi-disciplinary open access archive for the deposit and dissemination of scientific research documents, whether they are published or not. The documents may come from teaching and research institutions in France or abroad, or from public or private research centers.

L'archive ouverte pluridisciplinaire **HAL**, est destinée au dépôt et à la diffusion de documents scientifiques de niveau recherche, publiés ou non, émanant des établissements d'enseignement et de recherche français ou étrangers, des laboratoires publics ou privés.



ECOLE DES MINES
DE PARIS

Collège doctoral

N° attribué par la bibliothèque

/-/-/-/-/-/-/-/-/-/-/-/-/-/-/-

THESE

pour obtenir le grade de
Docteur de l'Ecole Nationale Supérieure des Mines de Paris
Spécialité Sciences et Génie des Matériaux

par Thomas Dick

présentée et soutenue publiquement le 2 mai 2006

**Modélisation multiéchelle du phénomène de
fretting dans le contact aube–disque**

Directeur de thèse : Georges CAILLETAUD

Jury

| | | |
|--------------------------|------------|--|
| Prof. Patrick Chabrand | Président | Université de la Méditerranée, Aix-Marseille |
| Prof. Jean-Pierre Celis | Rapporteur | Katholieke Universiteit Leuven |
| Prof. Otmar Kolednik | Rapporteur | Erich Schmid Institut, Leoben |
| Prof. Georges Cailletaud | Examineur | Ecole des Mines de Paris |
| Dr. Siegfried Fouvry | Examineur | Ecole Centrale de Lyon |
| Prof. David McDowell | Examineur | Georgia Tech, Atlanta |
| Dr. Stéphane Deyber | Invité | Société SNECMA |
| Prof. Friedrich Franek | Invité | Technische Universität Wien |

**Centre des Matériaux P.M. FOURT de l'Ecole des Mines de Paris,
B.P. 87, 91003 EVRY Cedex**

Acknowledgements

This thesis was mainly prepared at the Centre des Matériaux, Ecole des Mines de Paris. I thank the managers Jean Pierre Trottier and Esteban Busso for accepting me at their laboratory.

I thank Patrick Chabrand for presiding the jury. I also want to thank Jean–Pierre Celis and Otmar Kolednik for having accepted to be referees, for reading the thesis carefully and for their critical and constructive remarks.

I want to thank SNECMA for funding my thesis and Christophe Jacq and Stéphane Deyber of SNECMA for having been supportive and open–minded industrial partners. I also thank Christophe Paulin and Siegfried Fouvry of LTDS, Ecole Centrale de Lyon, for being excellent scientific partners.

I thank Friedrich Franek for accepting me at the Austrian Center of Tribology, he always gave me the feeling of being welcome at his laboratory. I also want to thank Georg Vorlauffer for letting me be part of the simulation group and for our discussions that contributed to my general knowledge in the field of tribology.

The greatest thanks are reserved for Georges Cailletaud. I thank him for teaching me in admirable simplicity and clarity, for many good ideas, your open–mindedness, for providing me vast freedom and great support in scientific as well as in organisational concerns. In fact I cannot imagine a better supervisor than him.

I want to thank all colleagues of the groups Cocas and Val for their help. Special thanks to Gregory Sainte-Luce for his swift and friendly help whenever I had computer or network problems, to Stéphane Quilici for his competent advice in Zebulon development concerns and Laurent Jeanfaivre for supporting me at the start of the thesis. Thanks to Asmahana Zeghadi, Céline Gerard, Stéphanie Basseville, André Musienko and Nikolai Osipov for the good times we have had.

I thank Andrea for having lived this adventure together with me. Finally I thank my parents for the great support that I can always count on.

Abstract

Blade–disc fixings in the fan of aeroplane turbo–engines are highly loaded form–closed connections that allow micrometer size relative movement between blade and disc. This loading type is called fretting, the encountered damage mechanisms are wear and cracking. To reduce damage, palliative coatings are applied. To assure the reliability of the engine these coatings need to be reapplied during regular maintenance operations. The prediction of wear and fissuration in the fixings is a challenging task. Better tools for damage prediction will allow an optimisation of the maintenance intervals and the design of more damage resistant blade–disc fixings.

The goal of this work is the construction of a finite element (FE) model that is suitable for an accurate prediction of fretting damage in blade–disc fixations. With this goal in mind, methods are elaborated to take (i) the change of the friction coefficient, (ii) cyclic plastic material deformation, (iii) crack initiation, (iv) wear and related contact geometry change and (v) wear–fissuration interaction into account. Integrating some of the models into a finite element analysis of the blade–disc contact, an attempt to predict wear and fatigue in a blade–disc fixation is made.

To describe the change of the apparent friction coefficient during the wear of the coatings, analytical and FE models are made. In these the apparent friction coefficient is regarded to be the mean value of a micro–structurally heterogeneous contact. For the description of the cyclic plastic deformation of Ti6Al4V a multikinematic von Mises material model and a polycrystal plasticity material model is used. Both models are suitable for the description of ratchetting, additionally the polycrystal plasticity model takes micro–scale plastic deformation, crystallographic texture and mean stress relaxation into account. Crack initiation is computed using the Dang Van high cycle fatigue criterion. For the use with polycrystal plasticity models the criterion is reassessed. As a wear criterion the dissipated energy approach is used. Contact geometry change by wear is taken into account in FE computations by iteratively updating the mesh by the computed wear. An attempt to describe the interaction of wear and fatigue is made using polycrystal plasticity and the Dang Van criterion in FE fretting computations with a cylinder–plate contact pair. The computations are compared to corresponding fretting experiments provided by partners from LTDS – Ecole Centrale de Lyon. Finally geometry change by wear, cyclic plastic deformation and fissuration of the blade–disc assembly are calculated in 2D and 3D FE computations.

A main result is the circumstance that wear, fatigue and their interaction can be qualitatively described using a polycrystal plasticity material model and the Dang Van criterion without the use of a classical wear model. The fact that this is not possible with von Mises material models shows that replacing macro–scale phenomenological models by more physically based micro–scale models increases predictive power. In all FE computations with the blade–disc fixing including geometry change by wear and von Mises plasticity, wear increases fatigue life, cyclic plastic deformation can have the opposite effect. It is shown that a 2D simplification of the blade–disc model yields unrealistic results. This means that 3D modelling is indispensable.

A macro–scale model for the prediction of wear and cracking in the blade–disc fixing has been constructed in this thesis. An integration of the micro–scale models developed in this thesis into the blade–disc fretting model will further increase the predictive power.

Contents

| | |
|--|-------------|
| Introduction | xiii |
| I Industrial context | 1 |
| II Bibliography | 5 |
| II.1 Tribology | 5 |
| II.2 Fretting | 7 |
| II.2.1 A definition of fretting | 7 |
| II.2.2 Fretting tests | 8 |
| II.2.3 Fretting maps | 8 |
| II.2.4 Damage mechanisms in dry fretting contacts | 11 |
| II.2.5 The effect of palliative coatings on fretting damage | 11 |
| II.3 Fretting modelling | 12 |
| II.3.1 Frictional behaviour modelling | 12 |
| II.3.2 Material modelling of Ti6Al4V | 14 |
| II.3.3 Wear prediction models | 16 |
| II.3.4 Fretting fatigue prediction models | 18 |
| III The friction coefficient of composite contacts | 27 |
| III.1 Introduction | 27 |
| III.2 Analytic descriptions of a composite coefficient of friction | 30 |
| III.2.1 Definition | 30 |
| III.2.2 Estimation of the local coefficient of friction $\mu(x)$ | 31 |
| III.2.3 Discussion | 33 |
| III.3 Finite element computation setup | 35 |
| III.3.1 FE mesh | 35 |
| III.3.2 Contact formulation | 36 |
| III.3.3 Material behaviour | 37 |
| III.3.4 Boundary conditions | 37 |
| III.3.5 Determination of the coefficient of friction | 38 |
| III.4 Results and discussion | 38 |
| III.4.1 FE computations corresponding to the analytic estimation of a coefficient of friction | 38 |
| III.4.2 Different CSL geometries | 39 |
| III.4.3 Influence of the number of ESDs in the contact | 42 |
| III.4.4 Influence of plastic deformations | 42 |
| III.5 Conclusion | 46 |

| | | |
|------------|--|-----------|
| IV | Ti6Al4V material modelling | 49 |
| IV.1 | Introduction | 49 |
| IV.2 | Von Mises material model | 50 |
| IV.3 | Polycrystal plasticity model | 52 |
| IV.3.1 | FE model of the Ti6Al4V microstructure | 52 |
| IV.3.2 | Constitutive equations for single crystal plasticity | 52 |
| IV.3.3 | Computational methods for parameter identification in polycrystal plasticity | 53 |
| IV.3.4 | Dependence of the computation result on the RVE model size | 54 |
| IV.3.5 | Identification of the relative CRSS of slip families | 54 |
| IV.3.6 | Crystallographic texture and identification of the absolute CRSS | 56 |
| IV.3.7 | Identification of the cyclic material parameters | 58 |
| IV.4 | Discussion | 59 |
| IV.5 | Conclusion | 62 |
| V | Fretting wear modelling | 65 |
| V.1 | The wear activation period in a fretting wear test | 65 |
| V.1.1 | Introduction | 65 |
| V.1.2 | Experimental procedure | 65 |
| V.1.3 | FE mesh and boundary conditions | 66 |
| V.1.4 | Results and discussion | 67 |
| V.1.5 | Conclusion | 70 |
| V.2 | Contact geometry change by wear | 71 |
| V.2.1 | Introduction | 71 |
| V.2.2 | Mesh geometry updating strategy | 72 |
| V.2.3 | Computation setup | 73 |
| V.2.4 | Results and discussion | 74 |
| V.2.5 | Conclusion | 79 |
| VI | Fretting fatigue prediction | 81 |
| VI.1 | Introduction | 81 |
| VI.2 | Fatigue prediction with J_2 material models | 82 |
| VI.2.1 | FE mesh and boundary conditions for fretting modelling | 82 |
| VI.2.2 | Results and discussion | 82 |
| VI.3 | Fatigue prediction with polycrystal plasticity | 85 |
| VI.3.1 | FE mesh and boundary conditions for fretting modelling | 85 |
| VI.3.2 | Fretting modelling results and discussion | 86 |
| VI.4 | Discussion of J_2 and polycrystal plasticity approach | 94 |
| VI.5 | Conclusion | 96 |
| VII | Interaction of wear and fatigue in fretting contacts | 99 |
| VII.1 | Comparing experiments with crystal plasticity computations | 99 |
| VII.1.1 | Introduction | 99 |
| VII.1.2 | Computation setup | 100 |
| VII.1.3 | Results and discussion | 101 |
| VII.1.4 | Conclusions | 104 |
| VII.2 | FE models of wear and fatigue in the blade–disc contact | 105 |
| VII.2.1 | Introduction | 105 |
| VII.2.2 | Computations with a 2D mesh of blade and disc | 106 |
| VII.2.3 | Computations with a 3D mesh of blade and disc | 109 |

| | |
|---|------------|
| VII.2.4 Discussion | 117 |
| VII.2.5 Conclusion | 117 |
| VIII General conclusions and outlook | 119 |
| References | 123 |

List of Figures

| | | |
|-------|---|-----|
| .1 | Schema of the organisation of this thesis. Friction modelling, material modelling, wear modelling and fatigue modelling are treated in separate chapters. Then some of the models are applied to integrated computations of wear and fretting fatigue. | xiv |
| I.1 | Schema of the CFM56 aeroplane turbo-engine (www.airpictorial.com) | 2 |
| I.2 | The blade-disc fixing in a fan of a CFM56 aeroplane engine | 2 |
| I.3 | Cross section of the blade's contact surface: shot peened Ti6Al4V surface, CuNiIn layer and Molydag solid lubricant (Fridrici, 2002) | 3 |
| I.4 | Crack initiation and propagation in the specimen representing the disc. Three stages can be observed: (i) initiation (crack angle 45°, crack length 50µm), (ii) propagation in the contact stress field (crack angle 75°, crack length 1.6 mm), (iii) propagation in the bulk stress field (crack angle 90°, until fracture) (Fridrici, 2002) | 4 |
| II.1 | Adhesive wear damage of a copper bicrystal during sliding contact with a polycrystalline copper rider (Czichos, 1978). | 6 |
| II.2 | Definition of fretting and alternating sliding. | 7 |
| II.3 | Types of fretting tests. | 9 |
| II.4 | Fretting maps (Fouvry et al., 1999a). | 10 |
| II.5 | Fretting log in fretting wear test and model with a cylinder/plate contact and the tribological system Ti6Al4V / (Ti6Al4V + plasma sprayed CuNiIn + Molydag) in the total slip condition. | 13 |
| II.6 | Microstructure of Ti6Al4V (Guerrier, 2000). | 15 |
| II.7 | Wear mechanism map for a steel on steel sliding pair using a pin-on-disc configuration (Lim and Ashby, 1987). | 17 |
| II.8 | Analogy between contact mechanics and fracture mechanics (Gianakopoulos et al., 1998). | 21 |
| II.9 | Modes of cyclic plastic strain behaviour: (a) elastic shakedown, (b) reversed cyclic plasticity, and (c) plastic ratchetting (Goh et al., 2003b). | 22 |
| II.10 | (a) Schema of the FE contact model of a rigid cylinder and a elastic/plastic half space. (b) Plastic strain map of the half space (elastic perfectly-plastic material model) (Ambrico and Begley, 2000). x and y are normalised with the contact half length a_h | 23 |
| II.11 | Plastic strain behaviour fretting map of a elastic/perfectly plastic material model under a fretting contact (Ambrico and Begley, 2000). | 24 |
| II.12 | Plastic strain map of the subsurface region of the plate after the 3rd fretting cycle. 2D model of a cylinder/plate contact. x and y are normalised with the contact half length a . (a) based on J_2 plasticity and (b) on crystal plasticity (Goh et al., 2003b). | 24 |

| | | |
|--------|--|----|
| II.13 | Plastic strain behaviour fretting maps based on (a) J_2 plasticity and (b) crystal plasticity (Goh et al., 2003a). | 25 |
| II.14 | (a) Schema of the fretting contact in a fretting fatigue test. The zone where cracks form is on the left border of contact (marked with a box). (b) A contour plot of the cumulative effective plastic strain at the left border of contact, obtained from a finite element computation including crystal plasticity, is shown (Goh et al., 2001). | 26 |
| III.1 | Change of the COF with the number of cycles. Fretting wear test of a Ti6Al4V surface in contact with a rough CuNiIn layer covered with a solid lubricant (Fridrici et al., 2003). | 28 |
| III.2 | Fretting wear test of a Ti6Al4V surface in contact with a rough CuNiIn layer covered with a solid lubricant. Work by Christophe Paulin, LTDS/ECL. | 29 |
| III.3 | Formation of a CSL from a rough surface, covered with a soft layer . . . | 29 |
| III.4 | Boundary conditions on the RSE | 32 |
| III.5 | Upper and lower analytic estimation of the coefficient of friction of a composite contact. | 33 |
| III.6 | Deformation of the CSL if the contact pressure is assumed to be constant ($p(x) = \text{const.}$). | 34 |
| III.7 | A simple model, allowing the deformation of counter body and substrate by shear. | 34 |
| III.8 | Finite element mesh of a cylinder/plate contact | 36 |
| III.9 | Elementary surface domains: different surface shares of component 2 . . | 37 |
| III.10 | Application of the boundary conditions | 38 |
| III.11 | Determination of Q/P in a FE computation | 39 |
| III.12 | ESDs for FE computations corresponding to the analytic estimation. . . | 40 |
| III.13 | Comparison of analytic estimations and corresponding FE computations of the COF. | 40 |
| III.14 | Comparison of the contact pressures of the analytic estimations and in one ESD of the corresponding FE computations, sliding contact, 50% component 2. | 41 |
| III.15 | FE computations with different ESD shapes. | 43 |
| III.16 | COF in FE computations with different ESD shapes. | 44 |
| III.17 | Contact pressure in one ESD in FE computations with different ESDs, sliding contact, 50% component 2. | 44 |
| III.18 | Contact pressure in one ESD in FE computations with different ESDs, only normal contact, 50% component 2. | 45 |
| III.19 | ESDs of different size. | 45 |
| III.20 | Influence of the ESD size on the resulting COF in FE computations. . . | 46 |
| III.21 | COF in FE computations with and without plastic yielding of the CSL. . | 47 |
| III.22 | FE computation of the contact pressure in a sliding contact with and without plastic yielding in the CSL. One ESD is shown, 50% component 2 surface share. | 47 |
| III.23 | Equivalent accumulated strain in the CSL of type R40 with different surface shares of component 2. | 48 |
| IV.1 | FE meshes (regular, quadratic elements) of aggregates of grains. | 53 |
| IV.2 | Average strain–stress response of a RVE using the Kröner, Taylor and finite element method. | 55 |

| | | |
|------|---|----|
| IV.3 | Relative slip in the pyramidal $\langle a+c \rangle$ slip family using the Kröner, Taylor and finite element method. | 56 |
| IV.4 | Relative slip in the prismatic, basal and pyramidal $\langle a+c \rangle$ slip systems in FE computations with three different realisations of the grain orientations. 15x15x15 element mesh. | 57 |
| IV.5 | Direct stereographic projections of the c -direction of the hexagonal lattice of 40 grains, three realisations of a basal texture. | 58 |
| IV.6 | Experimental tensile test and FE computations with the coarse mesh, 3 realisations of grain orientations with a basal texture. | 59 |
| IV.7 | Cyclic test in the $R_\epsilon = -1$ condition: experiment and material models, first and 50th cycle. | 60 |
| IV.8 | Cyclic test in the $R_\epsilon = 0$ condition: experiment and material models, first and 200th cycle. | 61 |
| IV.9 | Mean stress in the polycrystal plasticity model and in experiments, first and 200th cycle, in $R_\epsilon = 0$ tests. | 63 |
| V.1 | Schema of the fretting experiment and the measured data (LTDS/ECL). A normal load is applied to the contact, then a tangential displacement is applied. Tangential force Q and displacement δ are measured and visualised in fretting logs (Fig. II.3(c)). | 66 |
| V.2 | FE model: mesh and boundary conditions. The spots in the mesh where the boundary conditions are applied are marked with thick lines. A zoom of the left half of the contact zone is given. | 67 |
| V.3 | Evolution of the fretting log during 1000 fretting cycles in a fretting wear test. Normal force 133 N/mm, displacement amplitude 75 μm . Work by Christophe Paulin, LTDS/ECL. | 68 |
| V.4 | SE micrographs of cylinder and plate contact surfaces at the same contact spot after 100 fretting cycles. One micrograph is horizontally mirror-inverted. Work by Christophe Paulin, LTDS/ECL. | 69 |
| V.5 | Contact surface of the plate after a 100 cycle fretting test stopped by reducing the displacement amplitude to zero during some additional cycles. An asperity (contour marked with black line) is pasted from the SE micrograph of the cylinder surface to the corresponding contact spot on the micrograph of the plate surface. Work by Christophe Paulin, LTDS/ECL. | 69 |
| V.6 | FE mesh of the cylinder/plate contact after 100 fretting cycles. The SE micrograph shown in Fig. V.5 was used for the mesh construction. | 70 |
| V.7 | von Mises stress (σ_{mises}) in total sliding, at $\delta = 0$, after 100 cycles. (a): smooth contact, $\mu = 0.8$, conventional material model. (b): smooth contact, $\mu = 0.8$, multikinematic material model. (c): FE computation using a mesh of a fretting scar after 100 cycles, $\mu = 0.5$, conventional material model | 71 |
| V.8 | Fretting log, computed in finite elements with a schematic mesh of the contact geometry of a specimen after 100 fretting cycles | 72 |
| V.9 | Schema of a cyclic fretting computation including wear and related geometry change. | 74 |
| V.10 | FE mesh of a cylinder/plate contact model and boundary conditions | 75 |
| V.11 | Surface geometry change of the plate's contact surface due to wear in a 2D and 3D computation. For the 3D computation a profile at $z = -50\mu m$ is shown. | 76 |

| | | |
|-------|--|----|
| V.12 | Decreasing normal force in a 100 cycle wear computation where the normal loading is imposed by displacements. The shown values have been obtained at the end of each fretting cycle when $u_1 = 0\mu m$ | 76 |
| V.13 | Control of the correctness of the wear computation. | 77 |
| V.14 | Build up of the wear scar during 4000 computed wear cycles. For unilateral wear the geometry of the non-deformed plate is given. For bilateral wear for each point in the 1-direction the sum of geometry change on plate and cylinder is plotted in the non-deformed mesh. | 78 |
| V.15 | Fretting log in the 400th and 4000th cycle. In one computation wear and related geometry change were computed on the plate, in the other wear and geometry change were computed on both surfaces. | 79 |
| V.16 | Contact pressure in the first, 2000th and 4000th cycle. Computed once with unilateral and once with bilateral wear and contact geometry change. | 80 |
| VI.1 | Accumulated plastic strain at the contact after 100 cycles, multikinematic identification method. The left half of the contact is shown. In the vertical direction the first 20 μm from the contact surface into the material are shown. | 83 |
| VI.2 | Contact pressure evolution in a fretting computations using the multikinematic von Mises material model | 84 |
| VI.3 | Strain-stress response at integration points marked in Fig. VI.1. | 85 |
| VI.4 | DangVan high cycle fatigue criterion. Top: Contour plots for the 1st and 100th fretting cycle, on the left half of the cylinder/plate contact. Zones where the HCF limit is violated are white. Bottom: Dang Van plots at two integration points on cylinder and plate where the Dang Van criterion of the first fretting cycle is maximum. | 86 |
| VI.5 | 3D FE mesh for crystal plasticity computations | 87 |
| VI.6 | Equivalent inelastic strain maps after the 10th fretting cycle in three realisations of grain shape and orientation using the model including crystal plasticity. | 88 |
| VI.7 | Contact pressure in the fretting model including polycrystal plasticity and the analytic Hertz solution. | 90 |
| VI.8 | Equivalent inelastic deformation at three integration points marked in Fig. VI.6 in realisation 1. | 91 |
| VI.9 | $\sigma_{11}^{dev} - \sigma_{22}^{dev}$ trajectory (designated with lines), mean stress (designated with points) and the radius of the smallest sphere in 6 dimensional stress space which can be circumscribed to the stress trajectory of the loading cycle (designated by a circle). Shown for point 1 marked in Fig. VI.6 in realisation 1 for cycle two and 40. | 92 |
| VI.10 | Von Mises norm of the mean stress tensor in the second and 40th cycle on the left half of the plate where the polycrystal plasticity model is used. | 93 |
| VI.11 | Dang Van curve at point 1 marked in Fig. VI.6 in realisation 1. Stress range R and alternatively the von Mises stress J_2 are plotted over the hydrostatic tension. The straight line represents the HCF limit found with equ. VI.1. | 94 |
| VI.12 | Contour maps of the HCF limit using the Dang Van parameter, once using the stress range R and once using the von Mises stress J_2 , 40th fretting cycle, left half of the plate where the polycrystal plasticity model is used. | 95 |

| | | |
|--------|--|-----|
| VII.1 | Material response fretting map as found by (Fridrici, 2002). The loading conditions of computations shown in this section are marked. | 100 |
| VII.2 | Dang Van HCF criterion computed for the first fretting cycle under various loading conditions. | 102 |
| VII.3 | Sum of all accumulated crystallographic slip after the first fretting cycle under various loading conditions. | 103 |
| VII.4 | Fretting computation using the classical von Mises material model (section IV.2). Normal load and displacement amplitude are 333 N/mm and $\delta^*=50\mu\text{m}$ | 105 |
| VII.5 | FE mesh and loading schema of the 2D blade/disc contact model. | 106 |
| VII.6 | Comparison of wear computations with imposed displacement and imposed force. Elastic material model. | 108 |
| VII.7 | Contour plots of the blade/disc contact after 100 numerical wear cycles and consecutively 100 computational cycles with the multikinematic von Mises material model. | 110 |
| VII.8 | Contour plots of the blade/disc contact after 100 numerical wear cycles and consecutively 100 computational cycles with the multikinematic von Mises material model. | 111 |
| VII.9 | FE mesh, dimensions and boundary conditions | 111 |
| VII.10 | Wear per cycle in the contact on the disc. The units are mm/cycle. | 112 |
| VII.11 | Total wear in the contact on the disc during 29 numerical wear cycles. The wear height is given in the units mm. | 113 |
| VII.12 | Contour plot of the Dang Van HCF parameter. The computations have been made with the FE mesh after 20 computational wear cycles. The multikinematic J_2 material model has been used and the Dang Van parameter has been computed on the 5th computational cycle. Regions where high cycle fatigue is predicted are black. | 115 |
| VII.13 | Cyclic plastic deformation and development of the Dang Van HCF parameter at 2 integration points marked in Fig. VII.12(c). The computations have been made with the FE mesh after 20 computational wear cycles. The multikinematic J_2 material model has been used and the Dang Van parameter has been computed on the 5th computational cycle. | 116 |

List of Tables

| | | |
|-------|---|-----|
| III.1 | Properties of two CSLs | 33 |
| III.2 | Material properties | 37 |
| III.3 | Relation between the number of ESDs in contact and the ESD size (contact length $2a$, surface length of a ESD l_{ESD} , number of ESD in contact nb_{ESD}). | 42 |
| IV.1 | Set of constitutive equations for cyclic viscoplasticity | 51 |
| IV.2 | List of material constants for both sets of constitutive equations of Ti6Al4V | 51 |
| IV.3 | Dependence of the computation result at $\langle \varepsilon_{22}^{\text{total}} \rangle = 0.05$ on the RVE model size. | 54 |
| IV.4 | Relative CRSS of the α -phase of Ti6Al4V found in the literature. | 55 |
| IV.5 | Relative activity (in %) of each slip family in the α -phase of Ti6Al4V (Fundenberger et al., 1997). | 57 |
| IV.6 | Parameters of the crystal plasticity material model. | 62 |
| VII.1 | 2D blade–disc model, maximum values of von Mises stress and Dang Van HCF parameter on blade and disc. Using meshes with no, 20 and 100 cycles of computational wear. With these meshes once an elastic and once a multikinematic J_2 plasticity model was used. In the elastic computation the values were taken from the 2nd, in the J_2 computations from the 100th cycle. All values have the unit MPa. | 109 |
| VII.2 | 3D blade–disc computation, maximum values of von Mises stress and Dang Van HCF parameter on blade and disk. Using meshes with no, 10 and 20 cycles of computational wear. With these meshes once an elastic and once a multikinematic J_2 plasticity model was used. In the elastic computation the values were taken from the 2nd, in the J_2 computations from the 5th cycle. All values have the unit MPa. | 113 |

Introduction

The industrial problem treated in this thesis is situated in turbo engines used for the propulsion of passenger jets. The air enters the engine through the fan which passes a part of the air flux to the low pressure compressor, the greater share of the flux is immediately released generating two thirds of the engine's thrust. The rotating fan structure is severely loaded by centrifugal forces that change periodically in takeoff-flight-landing cycles. Because of its high strength to weight ratio and good mechanical properties the titanium alloy Ti6Al4V is commonly used for the fan parts. The fan is made of blades mounted on a disc by a form-closed connection. This allows a micrometer scale relative movement (fretting) of blade and disc in their connection during cyclic loading. Unfortunately, titanium alloys in moving contact show adhesion, a high friction coefficient and are susceptible to wear and crack initiation. This is why the blades' contacting surfaces are protected by palliative coatings of plasma-sprayed CuNiIn and the solid lubricant Molydag.

During service wear removes at first the solid lubricant which is accompanied by a rise of the friction coefficient in the blade-disc contact. Then the CuNiIn coating comes into contact and wear continues. Finally all palliative layers are exhausted and the titanium surfaces of blade and disc come into contact. Wear continues whereby titanium alloy is consumed, additionally fretting fatigue cracks can initiate in the blade-disc contact.

During maintenance the coatings can be reapplied. If titanium is lost by wear the fan blades or even the disc need to be replaced which increases the already high costs of maintenance activities. As a consequence industry is interested in improved methods for wear prediction because this allows them an optimisation of the maintenance intervals. A second problem is cracking. The initiation and growth of a fretting fatigue crack in the blade-disc contact can lead to catastrophic failure. Industry awaits that new methods of fatigue modelling will allow a better understanding of fretting fatigue crack initiation which will help improving the engine design.

The goal of this work is the construction of a finite element computation for the prediction of wear, fatigue cracking and wear-cracking interaction in the blade-disc contact. For this ultimately frictional behaviour models of the coating-titanium and titanium-titanium contact need to be developed and identified. Additionally the material behaviour in cyclic deformation needs to be represented for the coating materials as well as the titanium bulk material. Damage needs to be predicted using a wear criterion and a criterion for crack initiation. Cyclic plastic material deformation changes the strain-stress state in the structure and can accelerate or retard crack initiation. Wear can remove a coating, then another material comes into contact and the friction coefficient changes. Wear can remove material where cracks would initiate and thus retard or inhibit cracking. All these examples show the necessity to couple the material, friction, wear and fatigue models.

The blade-disc structure has a size of hundreds of millimetres, the blade-disc contact

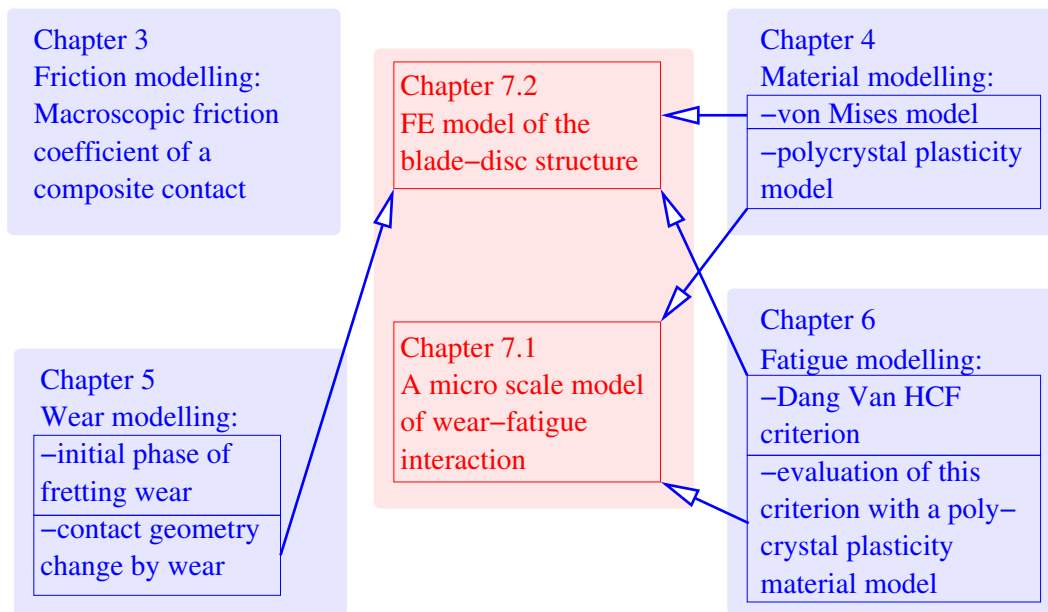


Figure .1 : Schema of the organisation of this thesis. Friction modelling, material modelling, wear modelling and fatigue modelling are treated in separate chapters. Then some of the models are applied to integrated computations of wear and fretting fatigue.

zone is confined to only some millimetres and regions in the contact zones that experience high cyclic stresses have a size that fits on a micrometer scale. Fretting fatigue cracks initiate in these micrometer small regions. On this length scale the heterogeneous micro structure of the implicated materials cannot be neglected. And for a realistic representation of friction and wear, surface asperities cannot be neglected. Then fatigue criteria that are suitable for the application with micro scale material models need to be developed and applied. For computations with the whole blade-disc structure micro scale models would necessitate enormous computational resources. A more reasonable approach is the computation of the whole blade-disc structure with macro scale models and to treat critical parts of the structure in submodels resolving the smaller scales. The final product of our efforts is envisaged to be an integrated multi scale model of fretting damage.

This work is organised in seven chapters. In the first chapter the blade-disc contact and the encountered damage is explained. In the bibliographic chapter the work of other authors in tribology, especially the fretting condition and fretting modelling, is summarised. In the consecutive chapters the components of the fretting model that is developed in this thesis are presented. A schema of the organisation of the work is shown in Fig. .1.

At first a model of a friction coefficient of a composite contact is developed. The purpose of the model is the description of the friction coefficient during the period when one coating is progressively worn off and the material beneath comes into contact. During this transition both the coating and its substrate are in contact and the model shows how the macroscopic friction coefficient depends on the morphology, mechanical material properties and friction properties of the involved materials.

The fourth chapter is about material modelling. A macro scale von Mises material model of cyclic plasticity of the titanium alloy Ti6Al4V that is also suitable for the description of ratchetting is described. Then a micro structural scale polycrystal plasticity model of Ti6Al4V is identified. It incorporates 3D slip in a hexagonal crystal, crystallographic texture, the cyclic model parameters are identified from fatigue tests. The model is able to reproduce the mean stress relaxation observed in experiments.

In the fifth chapter fretting wear of dry titanium–titanium contacts is treated. In the first part the initial phase of fretting wear is regarded. This work is done in close collaboration with the LTDS (Ecole Centrale de Lyon) whereby fretting wear experiments are performed by the LTDS and corresponding fretting computations are made by us. The common work highlights the rapid change of the contact surface morphology during the 1000 initial fretting cycles. And the change of the fretting log in this phase of a fretting wear experiment can be explained by interaction of asperities on opposite contacting surfaces. In the second part of this chapter the dissipated energy approach, developed and identified for a Ti6Al4V–Ti6Al4V cylinder–plate contact by the LTDS is applied as a wear criterion in FE modelling. An iterative method for taking contact geometry change by wear into account is implemented. This technique is used to compute fretting wear of a cylinder–plate contact pair. By this the huge impact of wear on the contact pressure and contact size is shown.

Next comes a chapter about fretting fatigue prediction. Using a cylinder–plate FE model and once the macro scale von Mises material model and once the polycrystal plasticity model 100 and 40 fretting cycles, respectively, are computed. Then a close look at the impact of cyclic plastic deformation on the stress-strain state in the fretting contact in both computations is taken. With the computation with von Mises plasticity the Dang Van criterion is used for fatigue prediction. Using the fretting computation with polycrystal plasticity the Dang Van criterion that implies a micro scale plasticity hypothesis and a scale transition is reassessed and a slight modification is proposed.

Some of the models developed in these four chapters serve as components of integrated wear–fatigue computations shown in chapter seven. In the first part of this chapter a series of fretting experiments with Ti6Al4V–Ti6Al4V contact and the cylinder–plate contact pair, that has been performed at LTDS, is modelled using the polycrystal plasticity material model. Then the damage in the experiment and the computed damage measures in the model are compared. This way a qualitative match of the observed damage (only wear, only cracking, wear and cracking) in experiments and computations is obtained when the Dang Van HCF criterion is applied. It is shown that this result is only obtained when the micro–scale polycrystal plasticity model is used, the macro scale material model does not yield these results.

In the second part of this chapter computations with 2D and 3D meshes of the blade–disc structure are shown. In these computations again dry Ti6Al4V–Ti6Al4V contact is modelled, no coatings are taken into account. The macro scale von Mises material model is used and wear and contact geometry change by wear are taken into account. The Dang Van HCF criterion is applied to predict the nucleation of fatigue cracks. These computations allow an investigation into the impact of cyclic plastic deformation and wear on crack nucleation in the cyclically loaded blade–disc structure. A comparison of 2D and 3D model shows that a 2D simplification yields unrealistic results.

Chapter -I-

Industrial context

The problem addressed in this thesis is encountered in an aeroplane turbo-engine, hence a short description of this system is given at first. In Fig. I.1 a schema of the engine is shown. Air enters by the fan which acts as a ventilator. The greatest share of the air flow exits the engine immediately behind the fan and this is how two thirds of the thrust of the engine are generated. The rest of the air enters at first the low pressure compressor and then the high pressure compressor. In the combustion section fuel is injected into the compressed air and the mixture is burned whereby the temperature rises to 1500°C . The combusted air powers the high pressure turbine and the low pressure turbine and then exits the engine. The high pressure turbine drives the high pressure compressor, the low pressure turbine drives the low pressure compressor and the fan.

The fan is composed of fan blades suspended on the disc (see Fig. I.2(a)). Blade as well as disc are made of the titanium alloy Ti6Al4V. The disc is manufactured in the following successive steps: it is forged, then hardened and tempered, machined, checked by an ultrasonic control, machined. Then a final control of the structure and micro structure is performed. The blades are manufactured in the following successive steps: they are forged and tempered, then the blade roots are machined and the blade wings are forged. At last the blades and their micro structures are controlled. The elastic material properties of blade and disc are $E = 119\text{GPa}$, $\nu = 0.29$ and the elastic limit is 850MPa .

In use the fan is mainly loaded by centrifugal forces generated by the rotation of the fan around the engine axis. The cyclic loading consists of takeoff-landing cycles and cycles with smaller amplitude and higher frequency during flight. The cyclic loading of the blade is passed to the disc through a closed shape connection schematically shown in Fig. I.2. At the blade-disc contact high local stress fields are induced and the contacting surfaces experience relative motion with micrometer scale amplitudes. This contact situation is called fretting. It causes the two damage mechanisms cracking and wear. To improve the damage resistance of the contact zones some surface treatments are performed. The contact zones of blade and disc are shot peened to introduce compressive residual stresses that prevent crack nucleation and inhibit crack growth. This treatment induces a compressive residual stress field with about 650MPa from the surface to a depth of $50\mu\text{m}$. Additionally protecting layers are applied to the contacting surfaces of the blade. A CuNiIn layer with a thickness of 150 to $200\mu\text{m}$ is plasma sprayed onto the shot peened titanium surface. The function of the coating is to allow a better accommodation in the blade/disc contact by plastic deformation of the soft CuNiIn layer. Additionally the very high roughness of the surface ($R_{t\text{ max}} = 50\mu\text{m}$) traps the solid lubricant in the contact and holds down the friction coefficient for an increased number of

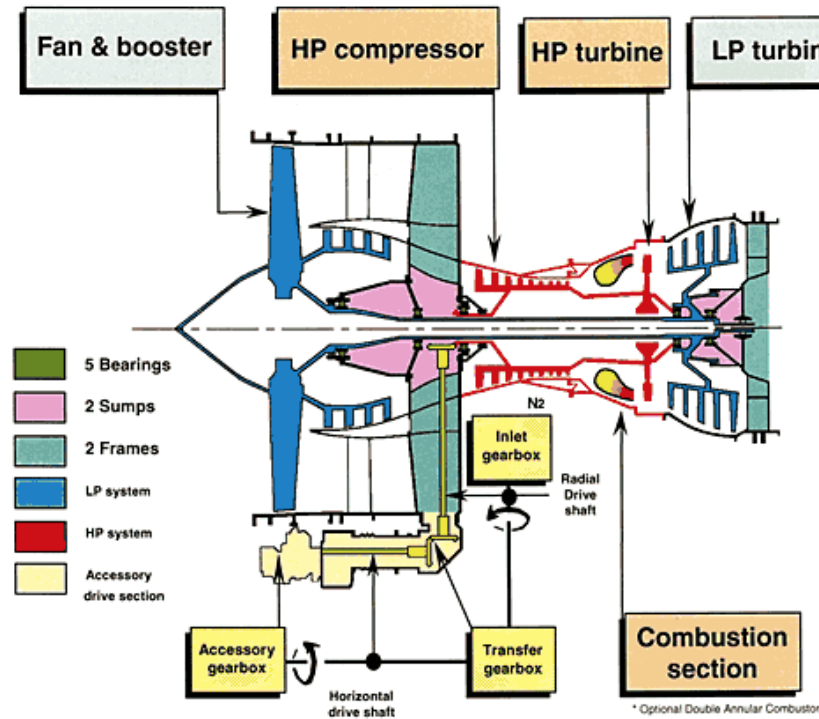
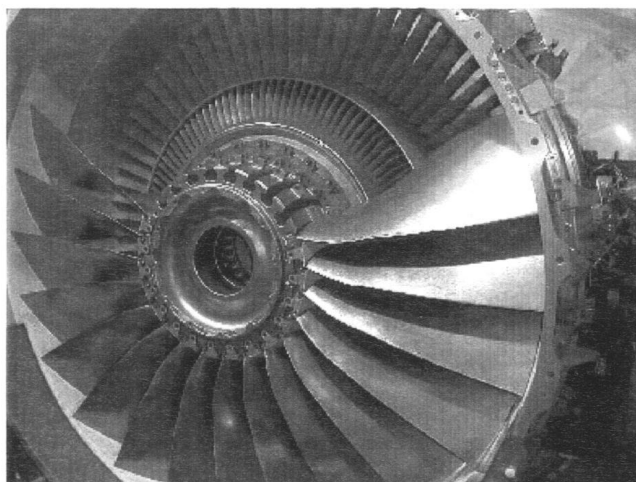
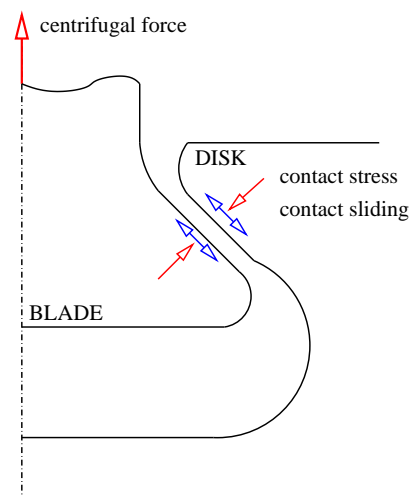


Figure I.1 : Schema of the CFM56 aeroplane turbo-engine (www.airpictorial.com)



(a) Blade/disc assembly in the fan of a CFM56 engine (photo provided by SNECMA, (Fridrici, 2002))



(b) Schema of the blade/disc contact

Figure I.2 : The blade-disc fixing in a fan of a CFM56 aeroplane engine

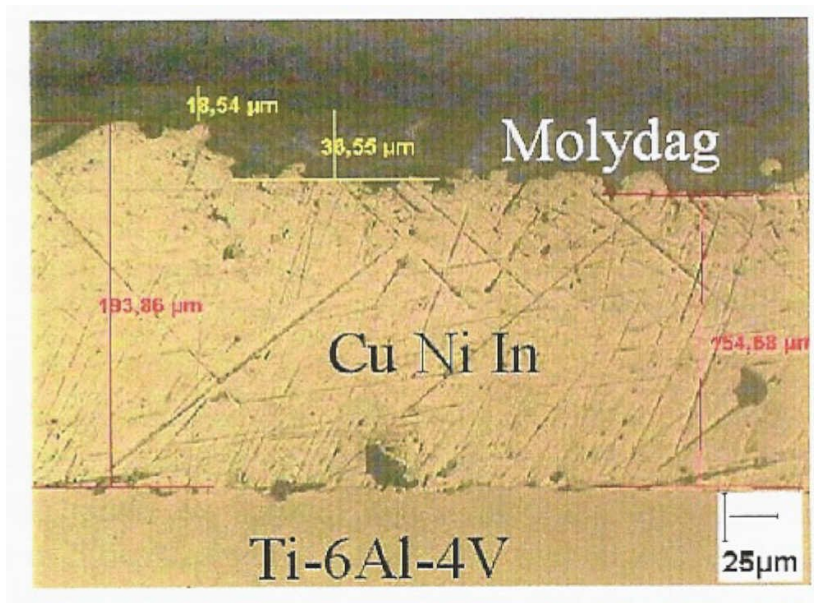


Figure I.3 : Cross section of the blade's contact surface: shot peened Ti6Al4V surface, CuNiIn layer and Molydag solid lubricant (Fridrici, 2002)

fretting cycles. The solid lubricant Molydag 254 is used. It consists of MoS_2 powder, carbon and other solid lubricants in a thermosetting phenolic resin. It is applied to the CuNiIn coating surface using a brush, dried on air and then heat treated for polymerisation. The layer thickness is 15–25 μm. In Fig. I.3 a cross section of the coating is shown.

In the blade–disc connection the most critical area where cracking can appear is on the side of the disc. The initiation site is the contact surface near to the inner border of contact as can be seen in Fig. I.4. An analysis of a cross section of the crack shows that cracks initiate at an angle of about 45° to the contact surface. At a length of 50 μm the crack direction changes to an angle of 75° . It is suspected that after reorientation of the crack growth direction to 75° the contact stress fields have the dominating influence on crack growth. At a length of about 1.6 mm the crack angle changes to 90° to the contact surface and it is assumed that the crack grows in mode I governed by the structural bulk stress and not any more by the contact stresses. Wear proceeds at the same time. On the disc wear depths of up to 200 μm can be observed which is more than the depth affected by shot peening. So wear may promote cracking by eliminating the compressive stress field induced by shot peening. About the damage of the blades less information has been assessed since these are not critical to the fan lifetime and failure and more often repaired and replaced.

SNECMA developed a technological testing procedure to simulate the cyclic loading of specimens representative of the blade–disc fixings. They performed tests with specimens with different surface treatments and concluded:

- that crack initiation always happens at the inner border of contact on the disc.
- if no coatings are applied to any contact surface cracks always initiate. Shot peening has only small influence on crack initiation.
- if a CuNiIn coating is applied to one contact surface crack initiation is retarded but not inhibited.

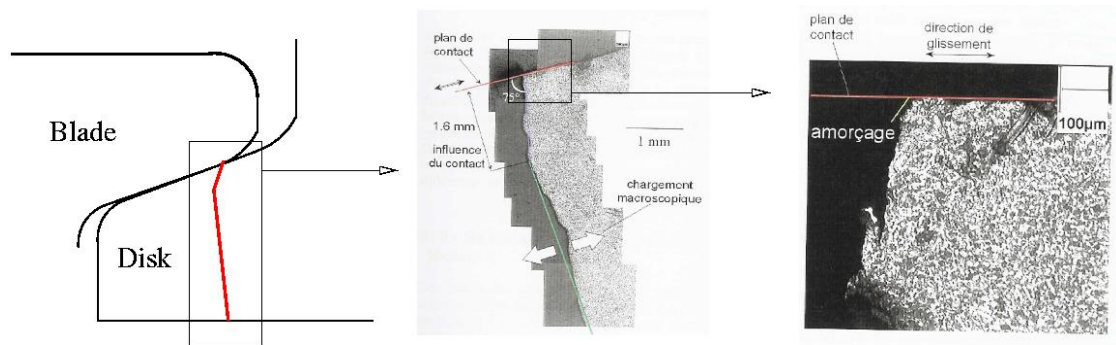


Figure I.4 : Crack initiation and propagation in the specimen representing the disc. Three stages can be observed: (i) initiation (crack angle 45° , crack length $50\mu\text{m}$), (ii) propagation in the contact stress field (crack angle 75° , crack length 1.6 mm), (iii) propagation in the bulk stress field (crack angle 90° , until fracture) (Fridrici, 2002)

- if a CuNiIn coating and the solid lubricant Molydag are applied no cracking is observed in a 10^5 cycle test.

Chapter -II-

Bibliography

II.1 Tribology

The complexity of the interaction of sliding surfaces where several physical mechanisms act simultaneously is a main limitation in modelling wear and fatigue in fretting surfaces. In the Oxford English Dictionary the term Tribology was defined as: "The science and technology of interacting surfaces in relative motion and of related subjects and practices." A general overview over the phenomena encountered in contact situations will help understanding and criticising the work performed in the more special fretting situation. This is why a short summary of the first chapters of a recognised book on tribology (Czichos, 1978) is presented here.

Scales of observation. When two perfectly smooth bodies are in elastic contact the contact stress and size can be computed using analytical contact mechanics (Johnson, 1987) or the finite element method. If the surfaces are not smooth but rough on a smaller scale the before mentioned calculations deliver "nominal" values and a different result for the contact area and contact stresses is found at the smaller scale where "asperity contact" is regarded.

Peculiarities of surfaces. Mechanical properties of materials are usually assessed for the bulk material. Near the surface these properties are not necessarily valid. A several nanometre thick layer on the surface is exposed to the environment and physical adsorption, chemisorption and oxidation take place. A several micrometer thick work-hardened surface layer is typically generated during manufacturing.

Adhesion. When two real bodies are brought together under a normal load, contact will usually be limited to asperities. The asperities will experience plastic deformation which results in interfacial bonding and the generation of adhesive junctions. For example, when two pieces of clean gold are placed in contact metallic bonds will form over the region of atomic contact and the interface will have the strength of bulk gold. Adhesion can be caused by van der Waals, electrostatic, metallic or covalent bonding. Experimentally adhesion is studied by loading a contact with a normal force F_N and measuring the force F_A that is necessary for the separation of the surfaces. The coefficient of adhesion is defined with $a = F_A/F_N$. Performing experiments with many metals a dependence on metal hardness and

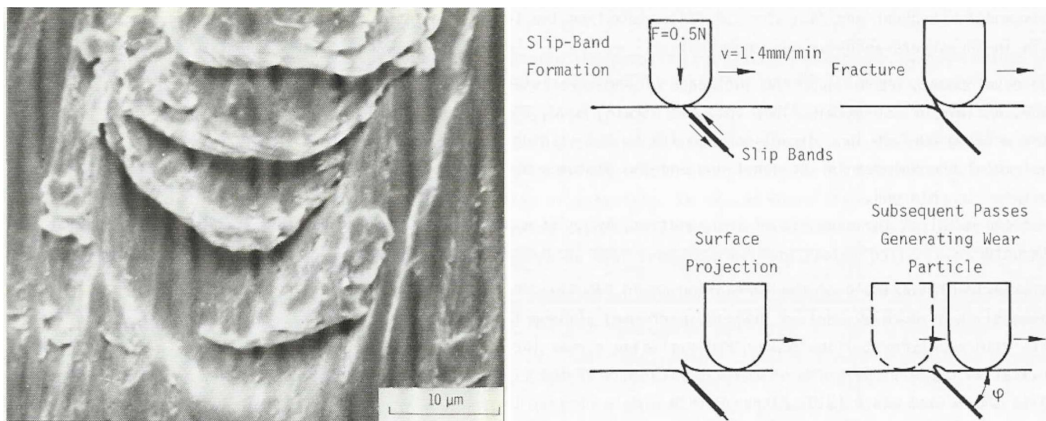


Figure II.1 : Adhesive wear damage of a copper bicrystal during sliding contact with a polycrystalline copper rider (Czichos, 1978).

crystallographic structure has been found. Harder metals have a smaller adhesion coefficient, face centred cubic metals have a higher adhesion coefficient than body centred cubic and hexagonal close packed metals.

Sliding friction may occur through asperity interaction through varying combinations of elastic and plastic asperity deformation, adhesion bonding and separation of micro contacts.

Wear can be defined as "the progressive loss of substance from the operating surface of a body occurring as a result of relative motion at the surface". So wear may be classified by the type of relative motion (rolling, sliding, oscillating ...). Another possibility is the separation of wear mechanisms into four groups: surface fatigue, abrasion, adhesion and tribo-chemical wear. The first two mechanisms may be possibly described using intrinsic material properties, for the last two mechanisms physical and chemical surface properties need to be considered. It is well established that all four wear mechanisms are active in oscillating (fretting) contacts of metals.

Surface fatigue wear is usually associated with repeated stress cycling in rolling or sliding contacts. Cracks form near the contacting surfaces and combine until pieces of material become loose.

Abrasive wear is caused by the ploughing and removing of a softer material by the asperities of the harder material surface.

Adhesive wear occurs usually more rapidly than other mechanisms, leading to severe forms of failure in the form of scuffing or seizure and material transfer from one surface to the other. An instructive experimental example of adhesion is shown in Fig. II.1. In the experiment a polycrystalline copper rider slides across a surface of bicrystal copper. In a single sliding path cracks developed. A closer examination of the cracks showed that they had formed in crystallographic slip planes by adhesion. In a second sliding path a wear particle was generated.

Tribo-chemical wear means that at least one contacting partner reacts with the environment. by the rubbing of the two surfaces the reaction product is continuously removed and new reaction products form.

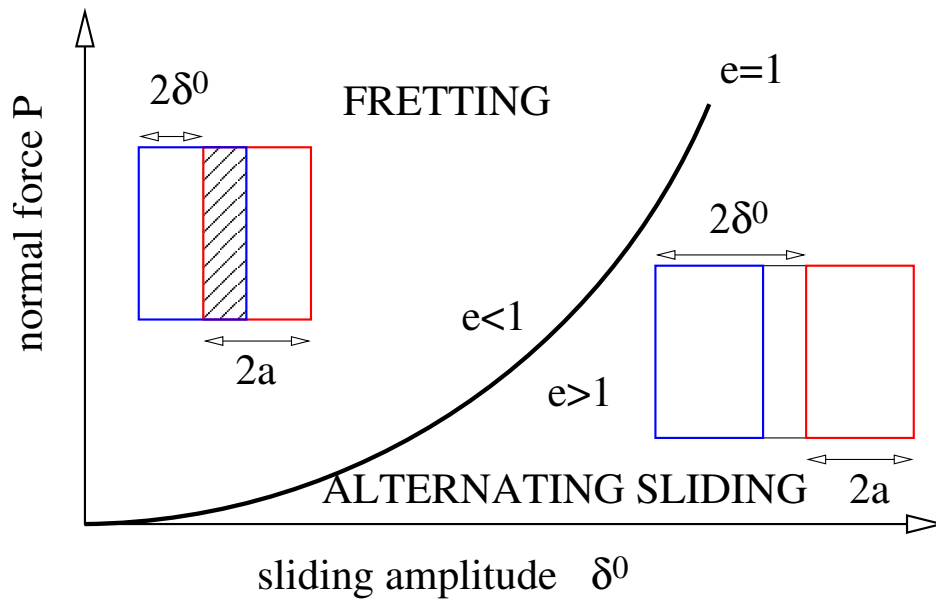


Figure II.2 : Definition of fretting and alternating sliding.

II.2 Fretting

II.2.1 A definition of fretting

At first the fretting condition can be defined by its distinction from the alternating sliding condition (Fridrici, 2002). So if a cylinder performs an oscillatory sliding movement on a plate, the contact size in the sliding direction ($2a$) and twice the sliding amplitude ($2\delta_0$) can be compared using the ratio $e = \delta_0/a$ (see Fig. II.2). Then fretting is the term used when $e < 1$. In this regime a zone in the centre of the plate is always in contact, other zones of the plate surface experience periodical change between contact and non-contact. If $e > 1$ the whole surface of the plate is out of contact during a part of a sliding cycle and the regime is called "alternating sliding".

In fretting two sliding conditions can be distinguished.

- In the *partial sliding condition* slip occurs in fractions of the contact surface, a part of the contact always remains sticking. When the relative displacement between the contacting bodies is increased the sliding region grows in detriment of the sticking region. Logging tangential force and relative displacement between the contacting bodies in a cyclic fretting experiment a curve with a closed shape and a small hysteresis is obtained. For pairs of simple elastic bodies (cylinder/plate, sphere/plate) the sliding and sticking fractions and contact stresses can be computed using the Mindlin solution (Johnson, 1987).
- When the relative displacement between the bodies is further increased the sticking fraction in the contact will be reduced to zero and the whole contact will slide. In this *total sliding condition*, the tangential force does not further increase when the displacement is increased and a coefficient of friction can be computed as the ratio between applied normal force and maximum tangential force $\text{COF} = Q/P$. The log of relative displacement (between the contacting bodies) and tangential force during a fretting cycle has then an open shape with a huge hysteresis.

II.2.2 Fretting tests

Two types of fretting tests should be distinguished.

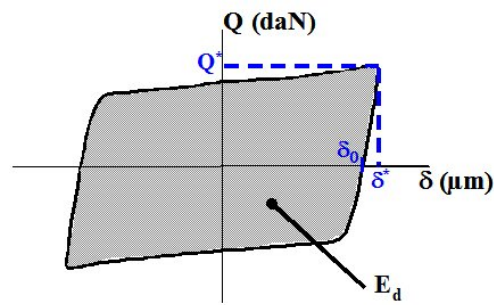
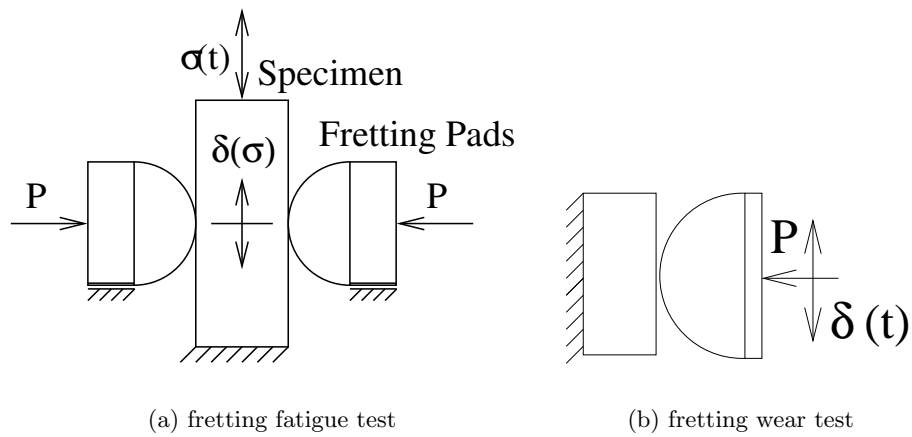
- The fretting fatigue test is a derivation of the classical fatigue test. In many testing setups a flat fatigue specimen is cyclically loaded, additionally fretting pads are mounted on the test rig and clamped to the specimen (see Fig. II.3(a)). So the specimen experiences a cyclic bulk load and a contact load at the same time. Crack initiation happens first at the contact site. As the cracks grow into the specimen the bulk load in the specimen becomes the driving force of further crack growth. Comparing classical fatigue tests to fretting fatigue tests with the same bulk loading a shorter lifetime is obtained in fretting fatigue because crack initiation is facilitated by the contact. This kind of testing is performed by Farris in the USA, Hills and Nowell in Great Britain, Mutoh in Japan and Fouvry at the LTDS/ECL in France and others.
- The fretting wear test is characterised by the application of a contact load only. This is usually done by the application of constant normal force (P) and a cyclic relative tangential displacement of the contacting bodies (δ), see Fig. II.3(b). Measuring the imposed relative displacement (δ) and the tangential force (Q), fretting logs can be recorded (see Fig. II.3(c)). In this figure maximum tangential force (Q^*) and displacement amplitude (δ^*) of a fretting cycle is indicated. δ_0 signifies the residual displacement when $Q=0$ during the inversion of the displacement direction. In the total sliding regime δ_0 corresponds to the *sliding amplitude* in the contact while δ^* gives the *displacement amplitude* between the moving and the static part of the test rig. The dissipated friction energy (E_d) of the fretting cycle is given by the area circumscribed by the fretting log. With this test setup, not only wear but also crack initiation and crack growth in the contact zone are studied. This test is used by the groups of Celis in Belgium, Klaffke in Germany, Vingsbo in Sweden and Fouvry in Lyon among others.

II.2.3 Fretting maps

The concept of fretting mapping was introduced by Vingsbo (Vingsbo and Soderberg, 1988) for the case of a sphere/plate contact for tracing the transition between the sliding conditions in partial slip and total slip. Later a possible change of the sliding condition during fretting tests was integrated to the mapping approach by the group of Leo Vincent (LTDS) (Fouvry et al., 1999a). A change of the sliding condition can be caused by a modification of the interface between the contacting bodies during testing. They found three sliding conditions:

- the partial slip regime (PSR) corresponds to partial slip during the whole test.
- the gross slip regime (GSR) or total slip regime corresponds to total slip during the whole test.
- the mixed slip regime (MFR) is encountered when total slip and partial slip are present at different times during one test.

In Fig. II.4, the first map shows the three conditions depending on normal force and displacement amplitude. The second fretting map shows the kind of material damage encountered in the contact. Cracking has been observed to dominate in the partial slip regime, wear dominates in the total slip regime and a competition between wear and cracking has been reported in the mixed slip regime. The size and shape of the domains in this map depend on the number of fretting cycles. The border between no degradation and cracking for example shifts to lower normal forces and displacement amplitudes when more fretting cycles are taken into account.



(c) Fretting log of one fretting wear cycle

Figure II.3 : Types of fretting tests.

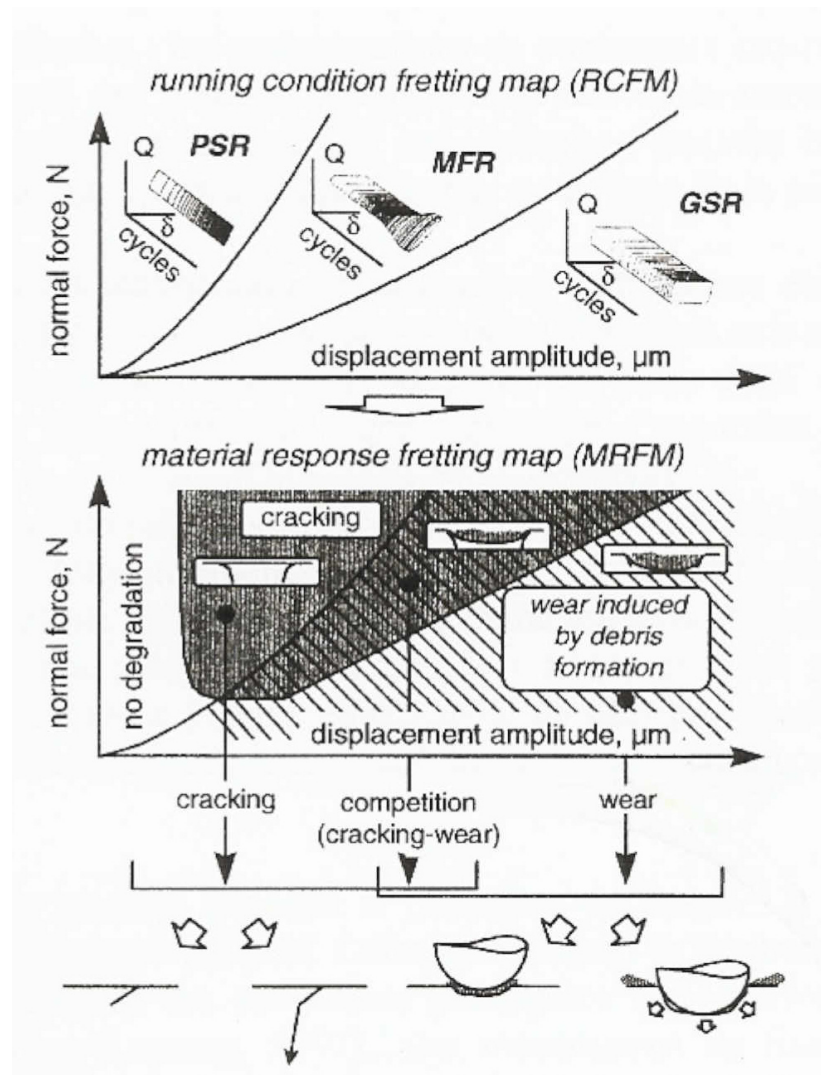


Figure II.4 : Fretting maps (Fouvry et al., 1999a).

II.2.4 Damage mechanisms in dry fretting contacts

Much experimental work on fretting damage of metals has been published and a general consensus about the involved processes has been reached. In the initial stage of fretting the oxide layers protecting the surfaces are destroyed. Then adhesion between the sliding surfaces takes place which leads to severe plastic deformation and possibly micro-cracking. The tribology research group of the LTDS/ECL has shown that a material transformation is caused by the plastic straining, the resulting nano structured material has been baptised "Tribologically Transformed Structure" (TTS) (Sauger et al., 2000). It is reported that the TTS is established within the first 1000 fretting cycles. In this material layer a higher hardness than in the initial material has been measured and micro-cracks have been observed. Observations suggest that TTS fractures and debris detaches from this layer. The debris in contact is called "third body" because it separates the two initial contacting bodies (Berthier et al., 1989). The third body is reported to break and oxidise during continued fretting so the particle size becomes smaller and the extent of oxidation higher.

Oxidation plays a prominent role in fretting (Shima et al., 1997). Measuring the friction coefficient of non-lubricated and high/low viscosity oil-lubricated contacts it has been observed that low viscosity oil reduces the friction coefficient while high viscosity oil increases the friction coefficient because it does not penetrate the contact. It only surrounds the contact, blocking oxygen and water access to the contact surfaces. As oxidation is inhibited more severe metal-metal contact is sustained.

Micro-cracks form from the start of a fretting test. They can contribute to wear when two micro-cracks meet near the surface detaching a wear particle (Szolwinski and Farris, 1996). A fretting fatigue crack is formed when a micro-crack manages to escape from the proximity of the surface, grows through the material concerned by the contact stresses and propagates into the bulk material.

II.2.5 The effect of palliative coatings on fretting damage

CuNiIn coating: A similar plasma sprayed coating of CuNi on a Ti6Al4V specimen has been tested in fretting fatigue by (Hutson et al., 2002). Tests were performed with coated and bare specimens in the same loading conditions. In tests with CuNi coated specimens an improvement of the fretting fatigue resistance but also more scatter was observed. They suspected that the improvement was due to the high surface roughness of the CuNi layer and less due to the material itself. (Wu et al., 2000) performed wear experiments with plasma sprayed CuNiIn coatings and other palliative coatings and concluded that CuNiIn coated surfaces had the same friction coefficient as bare Ti6Al4V and led to an increased material loss by wear. They observed that the CuNiIn layers had a poor adhesion strength on the substrate and showed delamination during wear tests. (Fridrici, 2002) worked with the same Ti6Al4V substrate and CuNiIn coating as used in the SNECMA aeroplane engine blade-disc contact. Fridrici observed that at low displacement amplitudes the coating reduces wear because its roughness and its low Young's modulus allow increased elastic accommodation of relative displacement which reduces contact sliding. At big displacement amplitudes he observed CuNiIn to be detrimental, promoting material loss by wear, which is consistent with the work of Wu et al.. Measuring the length of surface cracks that had formed he found that the presence of a CuNiIn coating reduced the apparent crack length. This again is consistent with the observation of Hutson et al. who showed that plasma sprayed CuNi coatings have a beneficial effect on fretting fatigue resistance.

MoS₂ coating: The fretting wear behaviour of coatings consisting of MoS₂ in epoxy resin applied to steel substrates has been described by (Zhu and Zhou, 2001; Xu et al.,

2003b). At the start of fretting tests a friction coefficient of approximately 0.1 was measured. Damage started by the formation of an MoS₂ plastic flow layer. Using X-ray photo-electron spectroscopy it was found that oxidation of MoS₂ in the plastic flow film took place and it was suspected that this led to an embrittlement. Micro cracking started, crack networks formed and ultimately delamination caused the destruction of the coating.

SNECMA blade–disc contact: In the blade/disc contact treated in this work a very rough 200 μ m thick plasma sprayed CuNiIn coating and on top of it a 20 μ m thick solid lubricant coating of Molydag (consisting mainly of MoS₂ in a phenolic resin) are used. From his work (Fridrici, 2002) drew the conclusion that the CuNiIn coating has two main functions. It serves for the accommodation of relative displacement by elastic deformation. And its high roughness serves as reservoir for the solid lubricant Molydag retarding the destruction of the solid lubricant layer. Molydag has the function of inhibiting adhesion and lowering the friction coefficient.

II.3 Fretting modelling

II.3.1 Frictional behaviour modelling

a) History and general remarks

One of the first scientists who studied friction systematically was Leonardo da Vinci (1452–1519). He stated two basic laws of friction: (i) The area in contact has no effect on friction. (ii) If the load of an object doubles, the friction doubles too. Guillaume Amontons (1663–1705) rediscovered the work of Da Vinci and added the theory that friction was predominantly a result of the work done to lift one surface over the roughness of the other surface or from the deforming or wearing of the surfaces (Amontons, 1699), but these beliefs would not hold. After the introduction of the concept of a force by Isaac Newton (1643–1737) Charles Auguste Coulomb (1736–1806) added to Da Vincis 2nd law of friction that "strength due to friction is proportional to compressive force" (Coulomb, 1821). The second law of friction is now known as the "Amontons–Coulomb law". These laws have been found in experiments where two bodies perform a linear relative movement. Already Coulomb stated that "for large bodies friction does not follow exactly this law". By the time many concepts have been added to friction modelling, examples are the introduction of a static and dynamic friction coefficient, the dependence of friction on the sliding velocity, normal pressure, roughness and other factors. The friction coefficient is not an intrinsic material property and the second law of friction should be seen as a rough working hypothesis.

In fretting contacts special friction conditions exist. From the viewpoint of contact mechanics two fretting sliding regimes may be depicted. In the total sliding regime the two bodies are in sliding contact during a part of the cyclic movement. In the partial sliding regime only a part of the contact surface slides while some regions rest in the sticking condition during the whole fretting cycle. Only when the whole contact slides a Amontons-Coulomb friction coefficient can be obtained during a fretting test by measuring the tangential and normal load during total sliding, and even then the friction coefficient can be highly variable. In a fretting test in the partial sliding condition the friction coefficient cannot be measured since the tangential force never reaches the critical value for total sliding. As the friction coefficient is a decisive parameter in fretting modelling some effort has been made to find a realistic model.

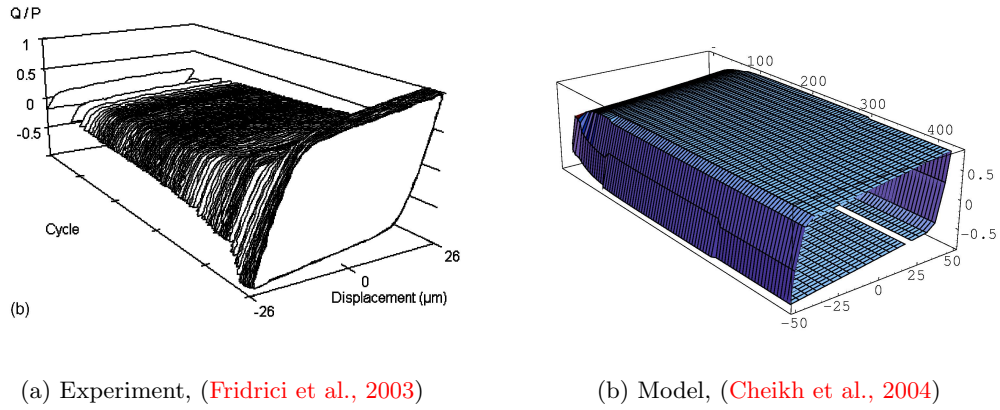


Figure II.5 : Fretting log in fretting wear test and model with a cylinder/plate contact and the tribological system Ti6Al4V / (Ti6Al4V + plasma sprayed CuNiIn + Molydag) in the total slip condition.

b) A model of a variable friction coefficient in fretting

In industrial applications fretting contacts are frequently protected by the application of coatings. In the fan blade–disc contact in SNECMA engines the titanium alloy parts are protected by coatings of CuNiIn and Molydag, applied to the blade surface. Fridrici et al. have performed fretting wear tests with this coated contact and a cylinder–plate contact pair (Fridrici et al., 2003). In Fig. II.5(a) a fretting log of a typical test can be seen. In this log the measured tangential force Q , divided by the imposed normal force P is drawn over the measured displacement between cylinder and plate. The shown test results are obtained in the total sliding condition and Q/P is a measurement of the global coefficient of friction during the fretting movement. During a test the global friction coefficient changes from 0.1 (at the start of the test when Molydag covers the whole contact) to 1 (when Molydag is eliminated and only CuNiIn and titanium alloy are in contact).

To describe this frictional behaviour a FE contact friction model has been developed by Mohammed Cheikh et al. (Cheikh et al., 2004). In this model a local coefficient of friction is defined at the nodes of one contact surface and changes as a function of nodal sliding (Cheikh et al., 2004). In analogy to material models for cyclic plasticity, the evolution is decomposed into an initial part μ_0 , an isotropic evolution μ_{iso} and a kinematic evolution μ_{kin} (see equation II.1). The isotropic part describes the cycle-by-cycle change of the friction coefficient and depends on the accumulated nodal slide \bar{s} (equation II.2). The kinematic part describes the change of the friction coefficient during a cycle. It depends on the maximum slide s^* , the actual slide s and the accumulated slide \bar{s} (see equation II.3). The fretting log obtained from the computation of some hundreds of fretting cycles can be seen in Fig. II.5(b).

$$\mu = \mu_0 + \mu_{isotropic} + \mu_{kinematic} \quad (\text{II.1})$$

$$\mu_{isotropic} = \mu_{iso} \cdot (1 - e^{(-b_{iso}\bar{s})^{\beta_{iso}}}) \quad (\text{II.2})$$

$$\mu_{kinematic} = \mu_{kin} \cdot (1 - e^{(-b_{kin}\bar{s})^{\beta_{kin}}}) \cdot \frac{s}{s^*} \quad (\text{II.3})$$

c) The friction coefficient in fretting in the partial slip regime

In the partial slip regime a sliding friction coefficient cannot be measured during a test but a method for an estimation has been developed (Hills and Nowell, 1994; Dini and Nowell, 2003). The authors propose to perform a fretting test, stop it after a defined number of cycles and then to increase the tangential force until total sliding of the contact is assured while keeping the normal load constant. By this a mean friction coefficient can be measured. With a known contact geometry and a mechanical contact model the friction coefficient of the sliding zone can be estimated. The slip zone friction coefficient is believed to be higher than the average value and it is assumed that the friction coefficient is a function of the number of fretting cycles for every contact spot that experiences sliding. Two contact geometries – the Hertz contact and a flat contact with rounded edges are presented, the approach is extendable to other geometries.

(Swalla and Neu, 2003) stated that the friction coefficient has a large impact to fretting damage prediction. They performed fretting fatigue experiments and elastic/plastic finite element analysis. With a model of their fretting fatigue test rig, a material behaviour model of stainless steel and multiaxial fatigue parameters they correlated experiments and computations changing the friction coefficient between 0.75 and 1.5. For them a value of 1.5 for the slip zone friction coefficient, which is 2.5 times higher than the measured mean value gave the best results in fatigue prediction.

(Naboulsi and Nicholas, 2003) gave a summary on the very different values of the friction coefficient (ranging from 0.3 to 1.5) that had been used in Ti6Al4V fretting fatigue modelling. For a more detailed investigation they developed a model of a variable friction coefficient for the application in finite element analysis. In this model the friction coefficient was allowed to change between a higher static μ_s and a lower dynamic μ_d limit. An exponential slip magnitude dependence was used whereby friction decreased with higher slip magnitudes. A pressure dependence was introduced with a power law whereby pressure increased the friction coefficient. They performed a parameter study and compared the results to fretting fatigue experiments with three contact geometries. They found good correspondence with $\mu_s = 2$ and $\mu_d = 1$, which is much higher than the mean value of 0.6 which is consistent with the work of (Swalla and Neu, 2003).

II.3.2 Material modelling of Ti6Al4V

a) General properties

The microstructure of the alloy is visualised by etching polished micro sections with the reagent of Kroll. The composition is 50% lamellar packs of hcp α -phase and bcc β -phase and 50% α grains with a grain size of 30 μm . On the whole the β -phase does not constitute more than a few percent in this alloy. A picture of the microstructure is shown in Fig. IV.6. It has been shown that crystallographic texture is present on two scales in this titanium alloy. The material exhibits a macro texture. This means that a preferential orientation of all grains in a macro scale volume of this material is present. Additionally micro texture has been shown to exist. This means that domains of neighbouring grains have a very similar orientation constituting super grains (Ari-Gur and Semiatin, 1998). Some qualitative information about the macro texture of the material of the SNECMA fan discs can be found in (Guerrier, 2000). The main texture is caused by a preferential orientation of the c-axis of the hexagonal lattice in the normal direction (ND) of the specimen whereby uniaxial tests with an imposed deformation in the "rolling direction" (RD) were made. The material has the elastic constants 119 GPa, $\nu = 0.29$ and an elastic limit of $R_p^{0.2} = 850$ MPa and a tensile strength of $R_m \approx 1000$ MPa.

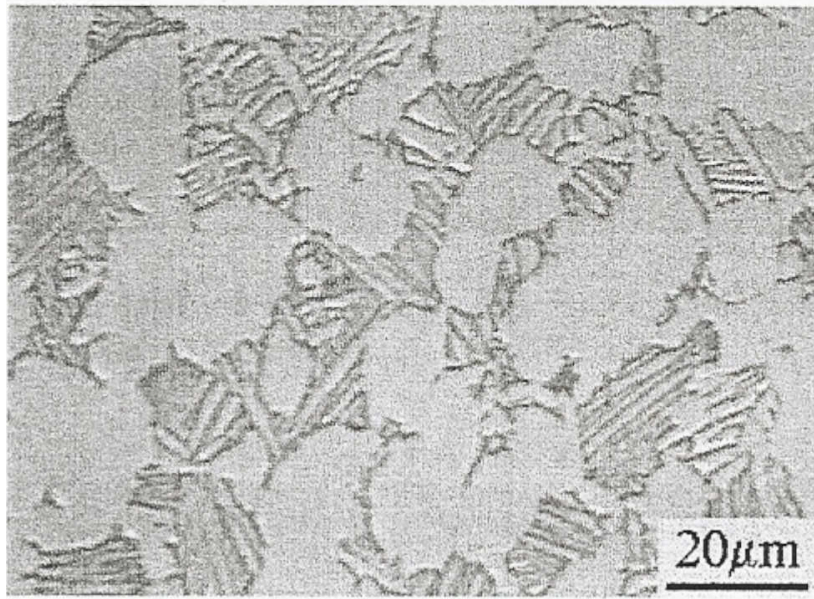


Figure II.6 : Microstructure of Ti6Al4V (Guerrier, 2000).

b) Macroscopic mechanical material modelling

In the PhD thesis of (Guerrier, 2000) the cyclic mechanical properties of Ti6Al4V were determined. Material specimens from a fan disc of a CFM56 plane engine of SNECMA were used. For cyclic material modelling a phenomenological "von Mises" approach (Chaboche and Lemaitre, 2001) was applied with two different identification methods. The first variant consisted of an elastic/plastic framework with a model for isotropic material softening and nonlinear kinematic hardening. The second identification strategy used a viscoplastic framework with isotropic softening and multikinematic hardening. With the second approach time dependency of material behaviour as loading frequency and creep could be taken into account, but it was found that time dependency was of subordinate importance. All material parameters were identified using cyclic fatigue tests under deformation control at $R_\epsilon = \epsilon_{\min}/\epsilon_{\max} = -1$.

c) Microstructural mechanical material modelling

(Morrissey et al., 1999) performed fatigue tests with Ti6Al4V specimens. These were carried out under load control with different stress ratios $0.1 < R_\sigma = \sigma_{\min}/\sigma_{\max} < 0.8$ and testing frequencies between 70 Hz and 1800 Hz. A main finding was a transition from crack initiation and crack growth at low stress ratios to void nucleation and growth at high stress ratios $R_\sigma > 0.75$. While the first fatigue mechanism was related to cyclic plastic deformation the second was related to ratchetting. Creep was found to be of subordinate importance. The authors claimed that the observed material behaviour depending on the stress ratio can be modelled using von Mises models presented in (McDowell, 1995). (Morrissey et al., 2001) developed a polycrystal plasticity model of Ti6Al4V with the main goal of capturing the transition from cyclic plasticity to ratchetting. Ti6Al4V has a duplex microstructure whereby grains of hcp α -grains and lamellar packs of hcp α - and bcc β -phase exist. In 2D finite element meshes they modelled 451 grains whereby each grain consisted of 96 elements. By a random process they assigned each grain to be either an α -grain or a lamellar region and a crystallographic orientation was assigned. For the α -grains triple slip was used as a simplified

model of the hcp crystal (3 slip systems at 0° , 120° and 240° respectively). In the lamellar regions only 1 slip system parallel to the lamellae was implemented. On each slip system plastic deformation was governed by a Norton type flow rule whereby the resolved shear stress and nonlinear kinematic hardening but no yield criterion were used.

With this model the transition between cyclic plasticity and ratchetting could effectively be reproduced. An important field of improvement of their approach is the transition to a 3D crystal plasticity model. This is so because the 2D triple slip model assumes a perfect texture in the 3D hexagonal crystal where the basal planes lie within the considered 2D plane. Secondly the transition from cyclic plasticity to ratchetting but not the ratchetting rate is reproduced by the model so an improvement of the description of cyclic material behaviour would be beneficial to the approach.

II.3.3 Wear prediction models

a) Development of wear prediction for metals

(Ludema and Meng, 1995) made a review of wear prediction between 1957 and 1992 and divided the development into three periods.

- Up to 1970 empirical equations were developed.
- Mainly between 1970 and 1980 contact mechanics based equations dominated. The most important one was developed well in advance by (Archard, 1953):

$$V_{Wear} = K_{Archard}PS \quad (II.4)$$

where V_{Wear} is the wear volume, S the sliding distance, P the applied load and $K_{Archard}$ the Archard wear coefficient. Though published after the paper of Ludema and Meng the dissipated energy approach (Fouvry et al., 1996; Fouvry et al., 1997; Fouvry et al., 2003) developed for fretting contacts falls into the same category:

$$V_{Wear} = K_{Energy}E_{dc} \quad (II.5)$$

where V_{Wear} is the wear volume, E_{dc} the in all fretting cycles cumulated dissipated friction energy (E_d , see Fig. II.3(c)) and K_{Energy} the energy wear coefficient.

- More recently equations based on material failure have dominated. These are based on dislocation mechanics, fatigue properties, shear failure and other mechanisms and methods.

Interestingly the number of variables in the equations is reported to have increased through time. While before 1970 the average number of variables per equation was 4.8 it was 5.8 1970–1980 and 8.9 1980–1992. Nevertheless, up to now no equation can predict metal wear only by material data and contact information. As a consequence an alternative to "scientifically guided empiricism" (Hsu et al., 1997) is not in sight. This means that wear equations need to be constructed and adapted to each individual contact situation and the limited range of their validity should be respected. For such an approach the wear mechanism maps developed by (Lim and Ashby, 1987) are valuable. An example for a steel on steel sliding pair using a pin-on-disc configuration is shown in Fig. II.7. In the map zones with different dominant wear mechanisms over a big range of pressure (normalised by hardness) and sliding velocity are delimited. In each zone one wear equation is valid, the resulting wear rate is given by contours in the map.

For the use in finite element analysis wear equations have been adapted. Usually wear equations are defined in a global manner using parameters such as wear volume, contact load,

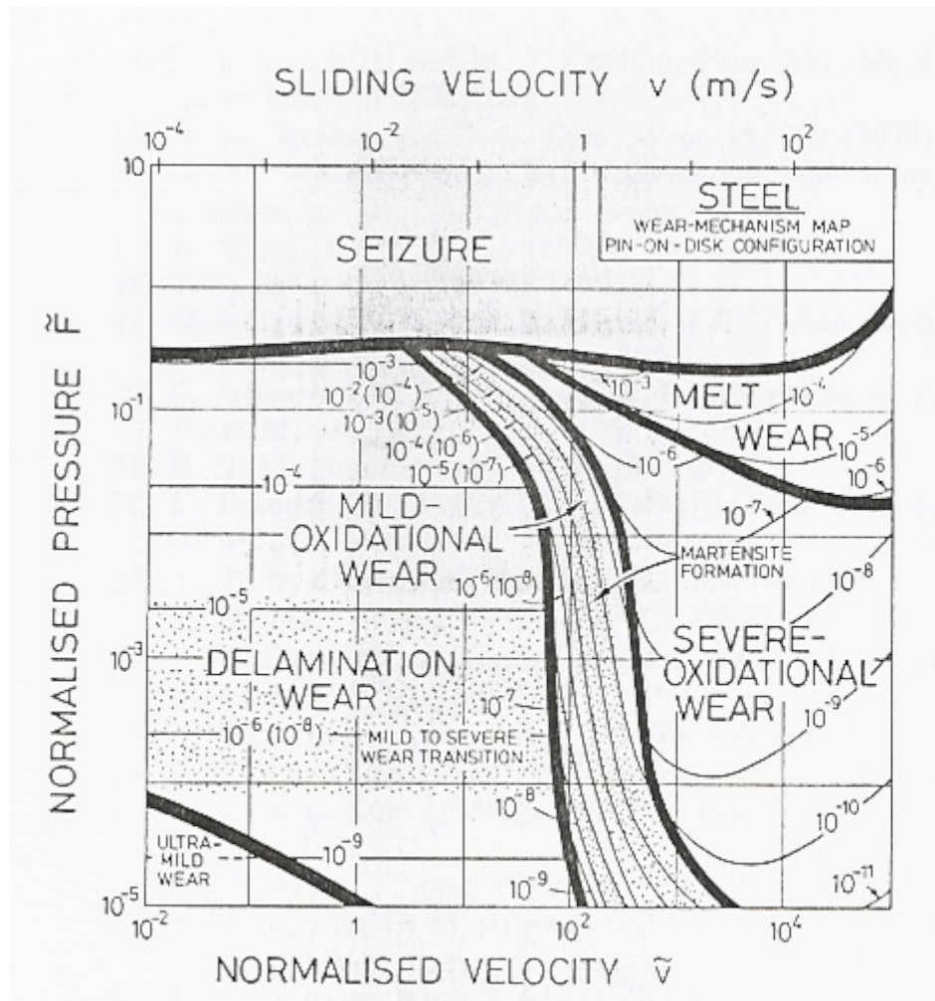


Figure II.7 : Wear mechanism map for a steel on steel sliding pair using a pin-on-disc configuration (Lim and Ashby, 1987).

global sliding distance et cetera. In finite element analysis, wear needs to be computed at each contact node. So the wear equation needs to be applied locally by replacing the wear volume by a wear height and by using the contact pressure and sliding distance computed at the contact nodes. (Maxian et al., 1996), who computed the wear in a total hip replacement, applied the following formulation of the Archard equation at each contact node:

$$h_{Wear} = K_{Archard}ps \quad (II.6)$$

where h_{Wear} is the wear depth, $K_{Archard}$ an Archard wear coefficient, p is the local contact pressure and s the local sliding distance. In this work the contact pressure and slide at each contact node during one loading cycle were computed and used with the local wear equation. By this the wear of a single loading cycle was obtained and by the multiplication with the number of loading cycles during service life total wear was assessed. (Stupkiewicz and Mroz, 1999) did similar computations with a "dissipated energy approach".

Some authors (Oqvist, 2001; Ratsimba et al., 2004) have computed wear using finite element analysis and took the contact geometry change by wear into account. This was done by an iterative process where (i) the contact stress and sliding during a loading cycle were computed, (ii) a wear equation was applied and (iii) the contact geometry was adapted by the calculated wear before the same steps were repeated for the next loading cycle. Advantages of this method are the assessment of more realistic contact stresses and the possibility to predict the geometry of the forming wear scar. A major shortcoming of this approach is its simplistic description of wear as it is assumed that material "disappears" as a function of slide and pressure. A more realistic method would need to take the process of wear particle formation (third body formation) and particle ejection from the contact into account (Godet, 1984). Recent work has had the goal to formalise a third body approach to wear modelling (Dragon-Louiset, 2001). This was done by the introduction of a wear criterion based on the principles of thermodynamics. It has been designed for the application in finite element analysis but with the experimental techniques we dispose of today the determination of the model parameters is difficult, maybe even impossible (Fridrici, 2002).

II.3.4 Fretting fatigue prediction models

a) History and general remarks

A survey over the literature on fretting fatigue modelling can be found in (Szolwinski and Farris, 1996). An early approach, that has been successfully applied to the prediction of the fracture site was found by Ruiz (Ruiz et al., 1984). It was formulated for the use on the dovetail joint of blade and disc in gas turbines.

$$k_{Ruiz} = (\sigma_T)_{max}(\tau\delta)_{max} \quad (II.7)$$

In this equation $(\sigma_T)_{max}$ is the maximum tangential stress (stress parallel to the surface) and $(\tau\delta)_{max}$ is the maximum frictional work, calculated as the product of the shear stress and slip amplitude at the surface. A fretting fatigue crack is predicted to initiate at the location with the highest value of k_{Ruiz} . But this model could not propose a method for lifetime prediction. In (Hills et al., 1988) a fracture mechanics-based approach was proposed, but since they needed to introduce an assumed finite crack still no lifetime prediction could be made as they stated: "there is no means of predicting the number of cycles to initiate a crack". Two approaches have helped to overcome the problem of crack initiation. (i) (Szolwinski and Farris, 1996) took in multiaxial fatigue parameters for an estimation of crack initiation. (ii) An alternative solution was conceived by (Giannakopoulos et al., 1998) who showed the equivalence of a fretting contact with a notched fatigue specimen. From this point of view a

fretting contact does not need to initiate a crack since it exists from the beginning. In the following sections recent works on multiaxial fatigue parameters and fracture mechanics in fretting contacts is presented. At last some work of other authors on the role of material modelling in fretting fatigue prediction is presented.

b) Multiaxial fatigue parameters

A frequently cited early work on multiaxial fatigue parameters is (Szolwinski and Farris, 1996). In this work a fretting fatigue test was modelled. Cylindrical fretting pads were used, on them cyclic normal and tangent loads were applied. At the fatigue specimen an independent cyclic bulk load was applied. Szolwinski et al. analysed the stress and strain state during cyclic loading using an analytic method with an elastic material model. They applied the Smith-Watson-Topper parameter (Smith et al., 1970; Socie, 1987) on the whole analysed structure.

$$SWT = \sigma_{max} \left(\frac{\Delta\varepsilon}{2} \right) \quad (\text{II.8})$$

The parameter is composed of the maximum value of the stress component σ_{max} perpendicular to a plane at any instant of an analysed fretting cycle and $\Delta\varepsilon$ is the difference between the maximum and minimum strain perpendicular to a plane, experienced during the cycle. The critical plane is one that experiences the largest value of $\sigma_{max}\Delta\varepsilon$. Through the evaluation of the whole structure the location with the highest SWT parameter can be determined. This point determines the number of cycles until crack initiation, additionally the crack orientation is given by the critical plane. So they could make a quantitative model of a series of fretting tests published by (Nowell and Hills, 1990) and they found that the crack propagation time (about 10^4 cycles) was negligible compared to the time necessary to initiate a 1 mm crack (about 10^5 cycles). What they could not describe was the scale effect seen in the experiments.

This scale effect was captured in the experiments by varying the contact size while keeping the peak Hertzian contact pressure constant in all experiments of a series. For purely elastic contact, this condition translates into the same stresses and strains in all experiments in a series. The fatigue model always gave the same lifetime estimation, which was good for big but very conservative for small contact sizes. An equivalent scale effect had been found earlier for notched fatigue specimens. For small notch radii high stresses at the notch tip were computed and the lifetime of the specimen was underestimated when a multiaxial fatigue parameter was directly used. (Flavenot and Skalli, 1989) were successful in integrating this scale effect into fatigue prediction by averaging the stresses at the notch tip over a critical depth and then applying a multiaxial fatigue parameter. (Fouvry et al., 1999b) used such a type of stress averaging for the prediction of crack initiation in a fretting wear test. Only instead of a critical length a critical volume was used for the averaging procedure. Then (Araujo and Nowell, 2002) published a similar work predicting crack initiation in a fretting fatigue test. They tried out two averaging procedures. Once they averaged over a critical length along a predicted critical plane. And once they averaged over a critical volume. With both methods they obtained the same results. On the size and physical meaning of the averaging volume no general agreement has been reached. (Fouvry et al., 1999b) and (Araujo and Nowell, 2002) found averaging volumes with approximately the same size as the grains. In a similar work of (Naboulsi and Mall, 2003) the averaging volume was three to four times bigger than the grain size. When it comes to a physical explanation Fouvry et al., who used experimental data from one material with one multiaxial fatigue parameter, imagined a relation to easy slip and crack nucleation in unfavourably oriented grains. Another proposed explanation was crack arrest at grain boundaries. Araujo et al. used experimental data from tests with two materials and two multiaxial fatigue parameters. They could not find one single averaging volume for one material and concluded that the averaging volume is not a true material constant.

Some different multiaxial fatigue parameters have been applied to fretting fatigue prediction and a short overview is given here. Fouvry et al. (Fouvry et al., 1996) used the Dang Van parameter (Dang Van et al., 1984; Dang Van, 1993) which can be described by the following formula.

$$\Delta\tau + \alpha p < \beta \quad (\text{II.9})$$

Where $\Delta\tau$ is the shear stress range in the most unfavourably oriented plane, p is the hydrostatic pressure and α and β are material constants. When the inequality is fulfilled during the whole fretting cycle, then no fatigue, else fatigue is predicted.

(Goh et al., 2001) and (Araujo and Nowell, 2002) used the SWT-parameter (see equ. II.8) to correlate normal stress/strain-dominated fatigue crack formation and early growth and the Fatemi-Socie-parameter FS (Fatemi and Socie, 1988) to correlate shear-dominated crack formation and early growth. The FS parameter has the form

$$FS = \frac{\Delta\gamma_{max}}{2} \left(1 + K \frac{\sigma_n^{max}}{\sigma_y}\right) \quad (\text{II.10})$$

where $(\Delta\gamma_{max})/2$ is the maximum shear strain amplitude, σ_n^{max} is the maximum normal stress on the plane of the maximum shear strain amplitude, (σ_y) the yield strength and K is a constant which is close to unity for HCF and lower for LCF. Naboulsi and Mall have applied other fatigue parameters to fretting (Naboulsi and Mall, 2003).

c) Fatigue damage approach

Another approach is the computation of damage as proposed by ONERA (Chaboche and Lemaitre, 2001). Here damage (D) is a scalar value that is a function of the stress state in an elementary material volume. It is equal to zero in the initial condition and one when a crack forms. During a fixed cyclic loading the stress state in a given material volume is usually transient which is due to cyclic plastic material response as softening, hardening or strain ratchetting. So a priori the accumulation of damage needs to be computed taking the whole loading history into account. But if the cyclic stress response converges, the resulting stabilised cyclic stresses can be directly used for the computation of life until failure (when $D=1$).

In the case of unidirectional loading the fatigue model uses the maximum stress σ_M and mean stress $\bar{\sigma}$ as critical values.

$$\frac{dD_f}{dN} = [1 - (1 - D)^{\beta+1}]^{\alpha(\sigma_M, \bar{\sigma})} \left[\frac{\sigma_M - \bar{\sigma}}{M(\bar{\sigma})(1 - D)} \right]^\beta \quad (\text{II.11})$$

$$\alpha(\sigma_M, \bar{\sigma}) = 1 - \gamma \left\langle \frac{\sigma_M - \sigma_l(\bar{\sigma})}{\sigma_u - \sigma_M} \right\rangle \quad (\text{II.12})$$

$$\sigma'_l = \sigma_{l0}(1 - b_1\bar{\sigma}) ; \sigma_l = \sigma'_l + \bar{\sigma} \quad (\text{II.13})$$

$$M(\bar{\sigma}) = M_0(1 - b_2\bar{\sigma}) \quad (\text{II.14})$$

Where σ_u is the ultimate stress and σ_{l0} the fatigue limit in $R_\sigma = -1$ fatigue tests. Then the number of cycles to failure N_f , computed with the stabilised stress response is given by:

$$N_f = \frac{1}{(\beta + 1)\gamma} \left\langle \frac{\sigma_u - \sigma_M}{\sigma_a - \sigma'_l} \right\rangle \left(\frac{\sigma_a}{M} \right)^{-\beta} \quad (\text{II.15})$$

In multiaxial loading conditions the stress amplitude $\sigma_a = \sigma_M - \bar{\sigma}$ is replaced by $\Delta J(\boldsymbol{\sigma})$, designating the von Mises norm of the greatest distance between the deviatoric mean stress the

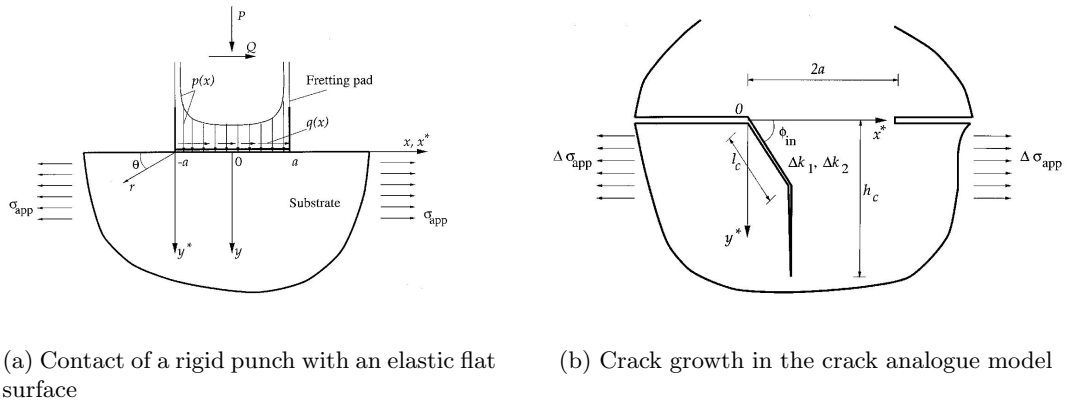


Figure II.8 : Analogy between contact mechanics and fracture mechanics (Giannakopoulos et al., 1998).

actual stress $\underline{\sigma}$. The maximum stress σ_M is replaced by the greatest von Mises stress $J_{max} = \max(J(\underline{\sigma}))$ and the mean stress $\bar{\sigma}$ by the mean hydrostatic stress $\bar{\sigma}_H = \frac{1}{6}(\max(\text{tr}(\underline{\sigma})) + \min(\text{tr}(\underline{\sigma})))$. Then it is obtained

$$N_F = \frac{1}{(\beta + 1)\gamma} \left\langle \frac{J_{max} - \sigma_u}{\Delta J/2 - \sigma_l'} \right\rangle \left(\frac{\Delta J/2}{M} \right)^{-\beta} \quad (\text{II.16})$$

where $\gamma, \beta, \sigma_l, M$ are material coefficients.

d) Fracture mechanics approach

(Giannakopoulos et al., 1998) showed an equivalence between fracture mechanics and contact mechanics. They developed it for the case of a rigid punch on a flat elastic surface, whereby the punch experienced a normal and tangential load and the flat surface a bulk stress. By this a fretting fatigue test was modelled (see Fig. II.8(a)). Since the stress fields had a singularity at the contact edges, crack initiation was instantaneous. Then small crack growth could be computed. In stage I, when the crack was very short the contact stress field dominated the crack growth. In stage II, when the crack had reached a certain length (l_c , see Fig. II.8(b)) the bulk stress under the flat surface dominated further growth because the contact stresses diminished rapidly. Depending on the relation between stress intensity at the crack tip and stress intensity threshold, the crack could arrest in stage I or re-orient and grow in stage II to a critical length (h_c) at which failure occurred as the fracture toughness of the material was reached. The same authors extended this approach to the geometry of a rigid punch with rounded edges in contact with a flat elastic surface (Giannakopoulos et al., 2000).

If fatigue tests with notched specimens and equivalent fretting fatigue tests are performed the theory of Giannakopoulos et al. predicts the same fatigue life. (Nowell and Dini, 2003) mentioned that a notch/contact edge comparison would give insight into the role of the stress gradients at contact (which can be reproduced by equivalently notched specimens) and of the friction properties (which play their role only in the fretting fatigue tests). They showed that notched specimens that are equivalent to standard fretting fatigue specimens can be made by standard machining techniques.

(Chan et al., 2001) analysed a fretting fatigue test with a punch with rounded edges on a flat surface. They computed the stress fields using an analytical linear elastic solution. Then

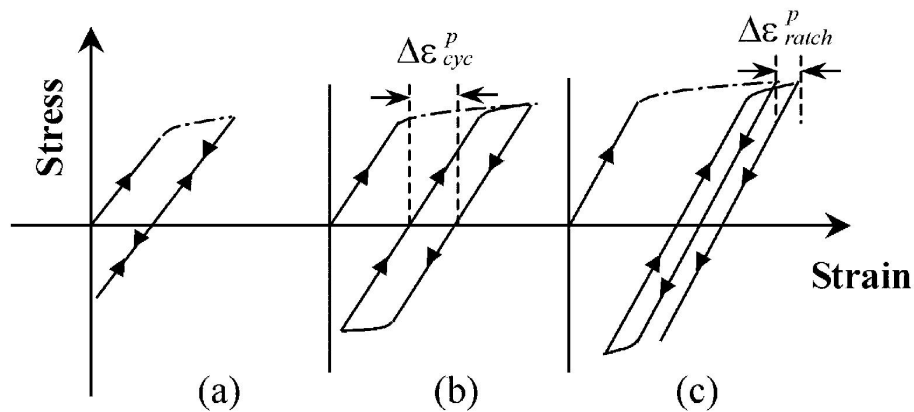


Figure II.9 : Modes of cyclic plastic strain behaviour: (a) elastic shakedown, (b) reversed cyclic plasticity, and (c) plastic ratchetting (Goh et al., 2003b).

they fixed the border of contact to be the crack initiation site. Using a continuum dislocation approach they computed a mixed mode (I+II) stress intensity factor and compared it to a small crack threshold. This way they could describe (i) fretting crack initiation, (ii) fretting crack arrest and (iii) propagation to failure. (Nicholas et al., 2003) used the same approach with finite element analysis for the stress field computation and the weight function method for the computation of the stress intensity factor.

e) Material modelling

In the before mentioned approaches to fretting fatigue prediction elastic material behaviour was assumed. (Ambrico and Begley, 2000) investigated the role of plasticity in fretting using von Mises material models with three different types of hardening (elastic perfectly-plastic, isotropic hardening and kinematic hardening). One advantage of a material model including plasticity is the possibility to distinct different modes of cyclic plastic deformation that can lead to different types of fatigue (see Fig. II.9). Elastic shakedown is characterised by plastic deformation in the initial cycles and only elastic deformation afterwards. This mode can be linked to "eternal" fatigue life or HCF. Cyclic plasticity is used to refer to regions that experience continued reversed plastic straining, which will lead to HCF or LCF. Ratchetting is used to describe regions where plastic strains continue to accrue with each loading cycle, which is commonly linked to ductile material failure comparable to that in a tensile test (Kapoor, 1994; Morrissey et al., 1999).

(Ambrico and Begley, 2000) used a 2D finite element model of a rigid cylinder in contact with an elastic-plastic semi-infinite half space. The cylinder was loaded with a constant normal force and a cyclic tangential load (see Fig. II.10(a)). They computed some fretting cycles to find a stabilised strain state and then produced plastic strain maps of the subcontact region of the half space (see Fig. II.10(b)). In the shown computation result the whole subsurface region experienced plastic deformation, whereby elastic shakedown happened in the biggest part, cyclic plasticity was confined to regions closer to the contact surface and ratchetting dominated at the contact borders.

They performed computations with different loading conditions to explore loading situations with similar material behaviour (see Fig. II.11). In this diagram the tangential load amplitude Q and the normal load P are normalised with the smallest normal force P_Y that causes plastic deformation in the half space. In the shakedown domain initial plastic

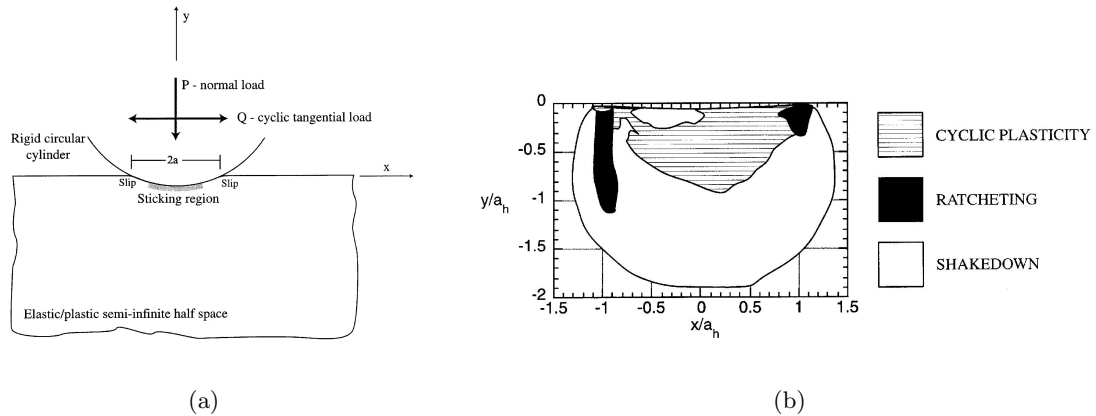


Figure II.10 : (a) Schema of the FE contact model of a rigid cylinder and an elastic/plastic half space. (b) Plastic strain map of the half space (elastic perfectly-plastic material model) (Ambrico and Begley, 2000). x and y are normalised with the contact half length a_h

deformation is present in the first cycles but shakes down everywhere in the structure. For loading conditions where active plastic zones are present, the cases are delineated as surface or subsurface plasticity, depending on which dimension is largest (maximum dimension across each region). The total slip boundary, predicted by the Coulomb law is given by $1/\mu$. But severe material yielding near the contact can start at lower tangential loads than necessary for total slip. This is the domain called "plastic shearing" as shear yielding is the dominant material response all over the contact vicinity. (Ambrico and Begley, 2001) compared their elastic perfectly plastic computations to elastic ones and showed that elastic models are expected to underestimate lifetime in fretting in the partial slip regime if the slip zone is small and overestimate it if the slip zone is large.

(Goh et al., 2003b) used the same FE model as Ambrico et al. with a macroscopic and a microstructural material model of Ti6Al4V. The macroscopic model had a von Mises yield criterion and linear kinematic hardening and behaved nearly elastic perfectly-plastic. For the microstructural scale, model groups of elements were assigned as grains, each grain had one common crystallographic orientation. A 2D crystal plasticity model with three slip systems was used. On each slip system kinematic hardening and no yield criterion was used in a viscoplastic framework. Macroscopic and microstructural model gave the same macroscopic strain-stress response. With both models they performed fretting computations and compared the results. An example is shown in Fig. II.12. The main difference is a more extended plastically deformed zone and extended fields of ratchetting in the polycrystal plasticity model.

In (Goh et al., 2003a) they extended the comparative study to a whole set of computations with different loading conditions and compiled them in plastic strain behaviour maps (see Fig. II.13). The behaviour map of the von Mises material model is very similar to that of Ambrico et al.. The map of the polycrystal plasticity model shows an extended subsurface plasticity zone and reduced shakedown and surface plasticity zones. This result can be explained by the fact that the absence of a yield criterion in the crystal plasticity model admits progressive cycle by cycle viscous strain in the presence of mean stress which is provided by sufficient normal loads $P/P_Y > 1$.

In (Goh et al., 2001) they applied this microstructural material model to a FE fretting fatigue computation and compared the result to an equivalent fretting test (see the schema

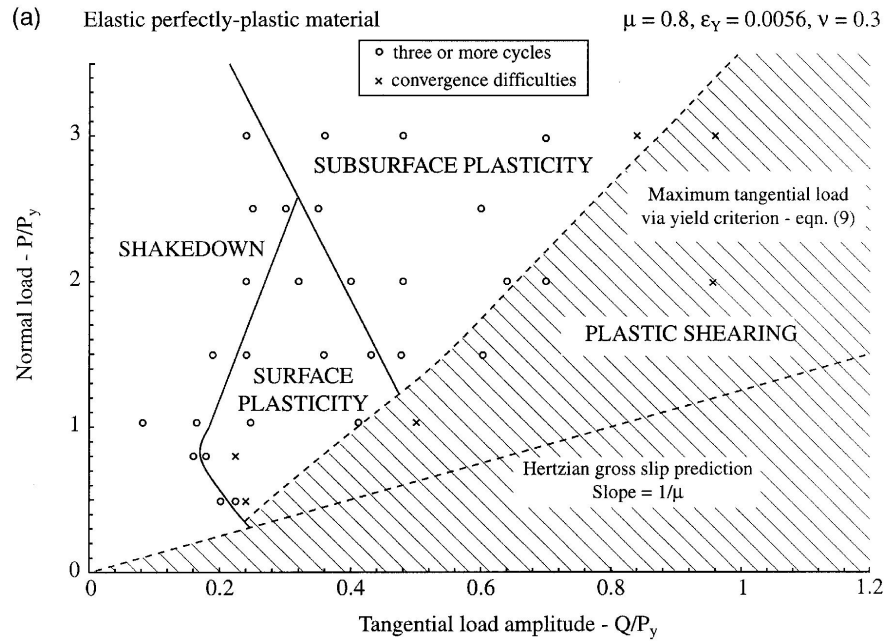


Figure II.11 : Plastic strain behaviour fretting map of an elastic/perfectly plastic material model under a fretting contact (Ambrico and Begley, 2000).

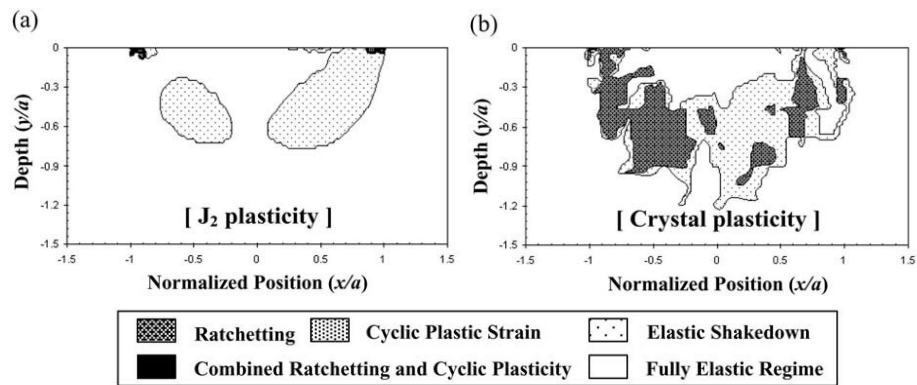


Figure II.12 : Plastic strain map of the subsurface region of the plate after the 3rd fretting cycle. 2D model of a cylinder/plate contact. x and y are normalised with the contact half length a . (a) based on J_2 plasticity and (b) on crystal plasticity (Goh et al., 2003b).

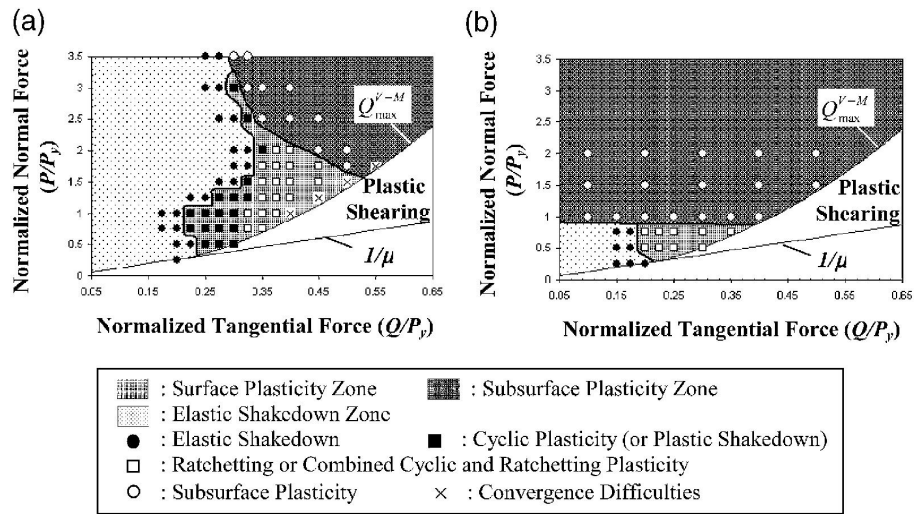


Figure II.13 : Plastic strain behaviour fretting maps based on (a) J_2 plasticity and (b) crystal plasticity (Goh et al., 2003a).

in Fig. II.14(a)). In the experiment at the left border of contact between fatigue specimen and cylindrical fretting pad cracks were observed. At the same location in the FE mesh (Fig. II.14(b)) plastic deformation was obtained. They observed plastic deformation and multiaxial fatigue parameters based on plastic strain to be more consistent with experimental results than total strain based parameters, obtained with classical elastic computations.

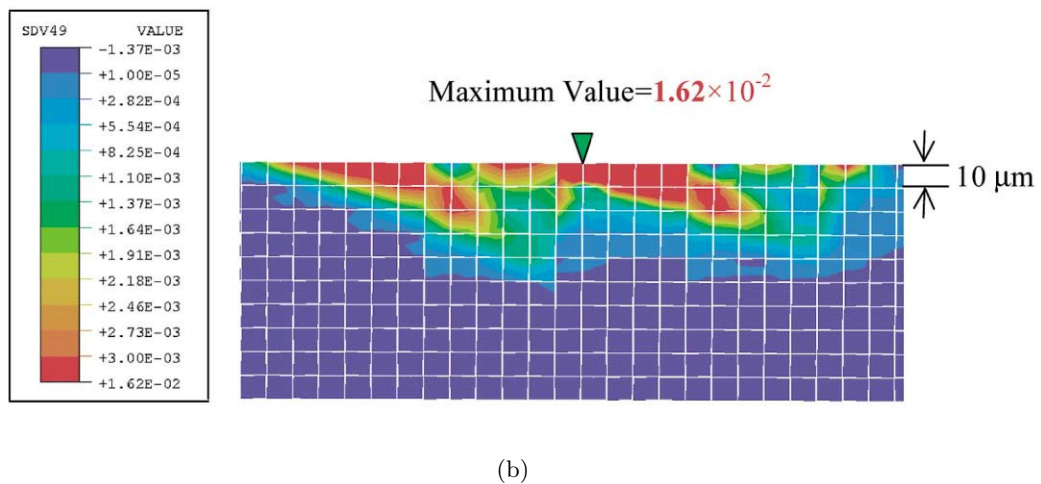
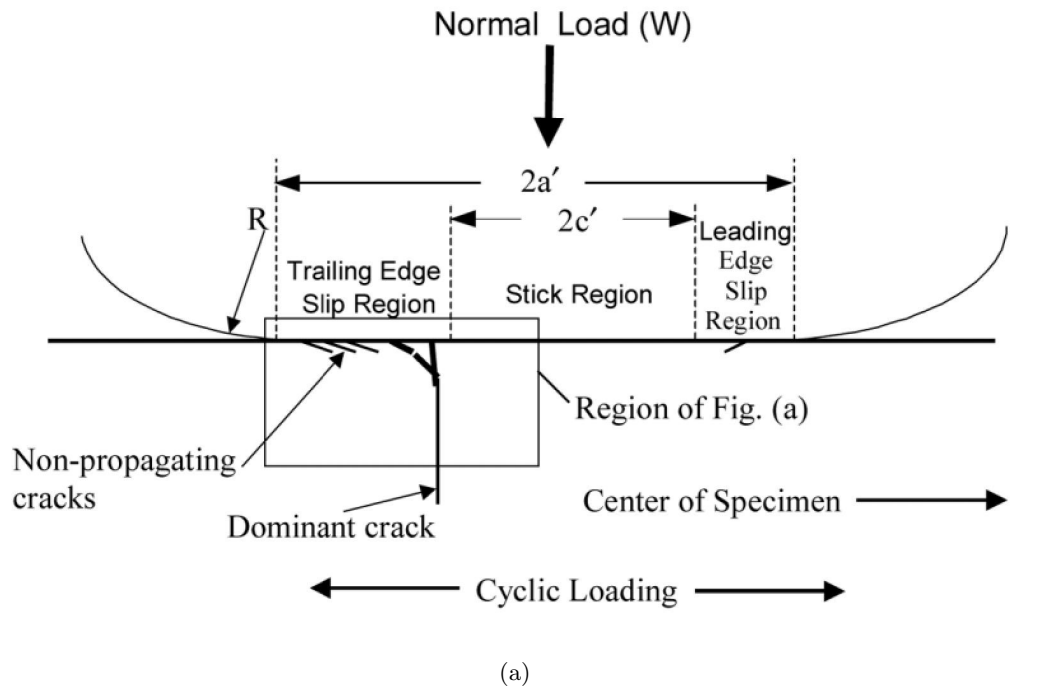


Figure II.14 : (a) Schema of the fretting contact in a fretting fatigue test. The zone where cracks form is on the left border of contact (marked with a box). (b) A contour plot of the cumulative effective plastic strain at the left border of contact, obtained from a finite element computation including crystal plasticity, is shown (Goh et al., 2001).

Chapter -III-

The friction coefficient of composite contacts

III.1 Introduction

Guillaume Amontons and later Charles Auguste Coulomb stated that the strength due to friction is proportional to the compressive force and introduced the coefficient of friction (COF) as ratio between friction force and compressive force of a contact (Amontons, 1699; Coulomb, 1821). In mechanical modelling the Coulomb friction law with a constant COF can be applied if the contact properties are the same all over the contacting area. If the contacting area is heterogeneous, the COF introduced by Coulomb has to be regarded as the homogenised global contact property of a heterogeneous contacting area. In this case a local heterogeneous friction formulation should be used in mechanical modelling and the ratio of frictional and compressive force resulting from this mechanical model should be identical to the global COF obtained from a friction test.

A similar problem can be met in the field of wear modelling. Archard's law (Archard, 1953), the dissipated energy approach (Fouvry et al., 1996) and other wear laws were developed to give a measure of wear on the whole contact. In these laws wear is defined to be the material volume that has been removed from the contacting surfaces. Various authors have used the Archard law in finite element models to predict the amount of wear and the shape of the wear scar (Ratsimba et al., 2004; Oqvist, 2001; Ireman et al., 2002; Maxian et al., 1996; Goryacheva, 1998). In these FE models again the wear law needs to be rewritten in terms of a local wear depth and local contact parameters. A major problem in local contact modelling is the difficulty to access local contact information in friction tests and to have a realistic description of the local geometry.

Some authors have worked on modelling local contact properties. For a stick/slip fretting test Dini and Nowell (Dini and Nowell, 2003) calculated a slip zone COF from measured values of normal and tangential contact forces. Naboulsi and Nicholas (Naboulsi and Nicholas, 2003) introduced a model of a local COF depending on contact pressure and slip rate. Heterogeneous materials have been treated by various authors. Goh et al (Goh et al., 2003b) modelled a fretting contact of two bodies made of a titanium alloy introducing the heterogeneous metallic microstructure. In these cylinder/plate fretting computations the stick/slip boundary was not smooth as in the analytic Mindlin solution but depended on the crystallographic orientation of individual grains. Carman et al. (Carman et al., 1993)

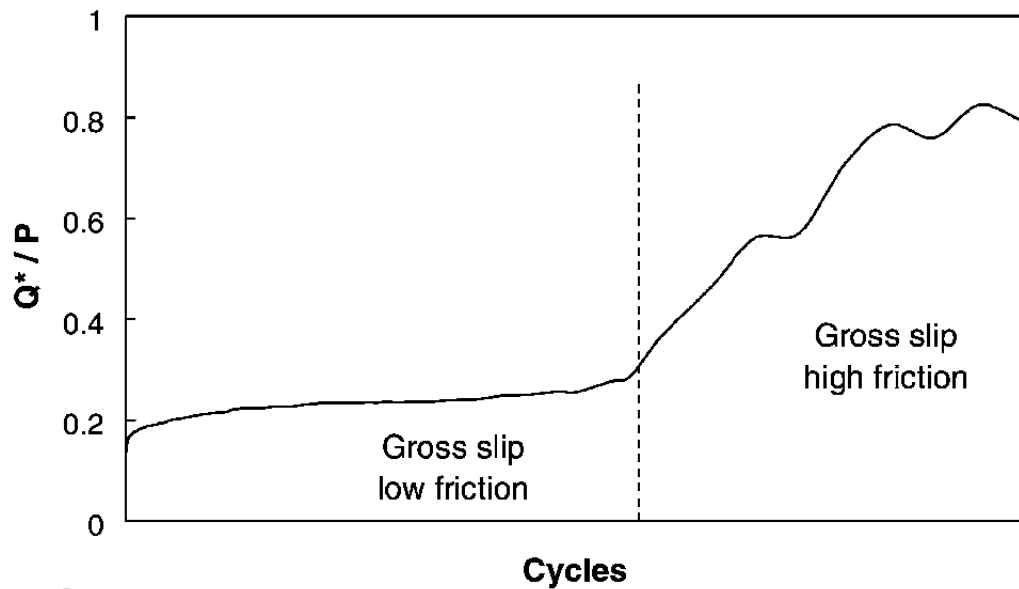


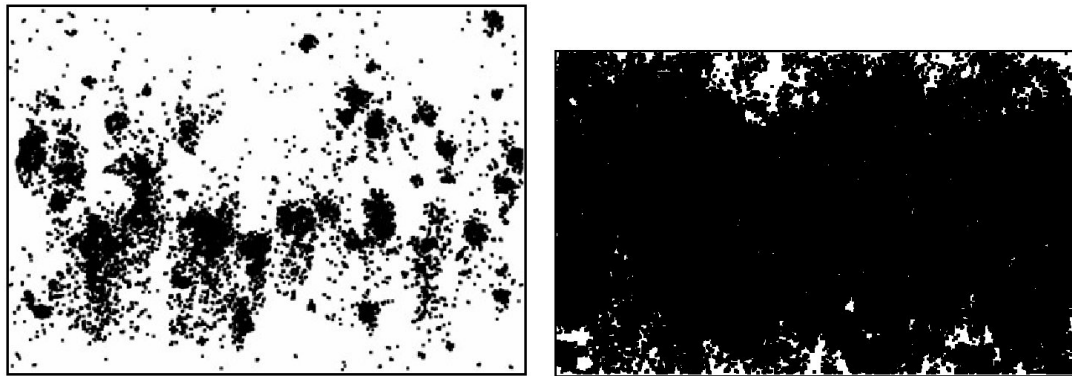
Figure III.1 : Change of the COF with the number of cycles. Fretting wear test of a Ti6Al4V surface in contact with a rough CuNiIn layer covered with a solid lubricant (Fridrici et al., 2003).

computed the local stresses in matrix and fibres of a composite plate in contact with a hardened steel ball by a micro mechanical model. The effect of asperities on local contact stress fields has been treated by R. Holm (Holm, 1946), K.L. Johnson (Johnson, 1987), D.A. Hills and D. Nowell (Hills and Nowell, 1994) and others.

Recently the fretting wear of surfaces, lubricated with a solid layer of polymer bound MoS₂ has been subject to different studies (Xu et al., 2003a; Xu et al., 2003b; Fridrici et al., 2003). In the work of Fridrici et al. the lubricating layer is deposited on a very rough plasma sprayed CuNiIn surface. In these fretting wear tests the COF is found to change rapidly (see Fig. III.1). It is believed that not only one mechanism contributes to the shape of this curve. Among the mechanisms are the change of the surface roughness, oxidation and the formation of a heterogeneous contact. Using Energy-Dispersive X-Ray (EDX) analysis Christophe Paulin (LTDS/ECL) has measured the composition of the contact surfaces after fretting tests with different cycle numbers. Before the first fretting cycle the surface consisted only of polymer bound MoS₂ (Molydag). With increasing cycle numbers the amount of CuNiIn on the surface increased (see Fig. III.2(a), Fig. III.2(b)). He showed that the increase of the CuNiIn concentration in the heterogeneous contact is accompanied by an increase of the COF (see III.2(c)).

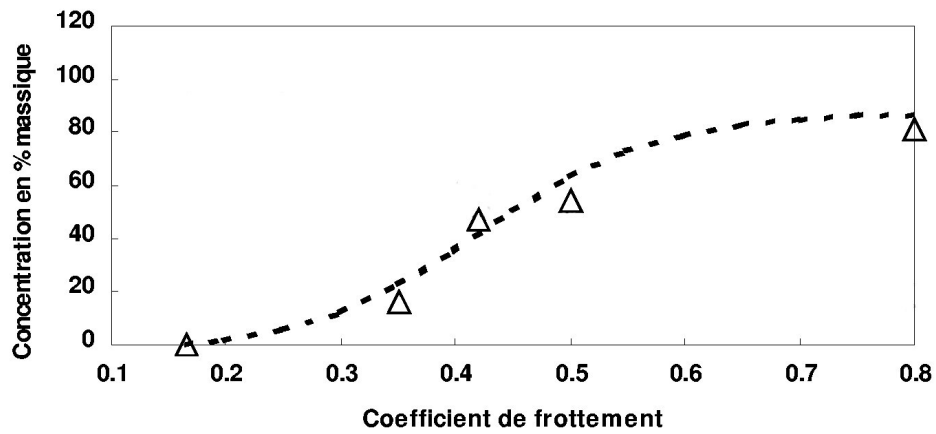
The formation of the heterogeneous contact might happen as follows (see Fig. III.3). Because of the low resistance of the polymer bound MoS₂ layer we assume that the lubricant fills the holes between the asperities of the metal surface. The excess lubricant is then removed during the early stage of fretting wear. As wear proceeds the tops of the metal asperities reach the contact surface. The contact is then divided into a share where MoS₂ is in contact with the counter body and the other share where CuNiIn is in contact with the counter body. This is what we will call a composite surface. The asperities of the rough metal surface and the solid lubricant filling the space between them build a composite surface layer (CSL).

We think that a model linking the global COF, which is easy to measure, to small scale contact properties, which can be tested before and after tests, can help with the assessment of



(a) Composition of the coated contacting surface when $COF=0.2$. White and black color designate Molydag and CuNiIn, respectively.

(b) Composition of the coated contacting surface when $COF=0.8$. White and black color designate Molydag and CuNiIn, respectively.



(c) Change of the COF as a function of the concentration of CuNiIn in the contacting surface.

Figure III.2 : Fretting wear test of a Ti6Al4V surface in contact with a rough CuNiIn layer covered with a solid lubricant. Work by Christophe Paulin, LTDS/ECL.

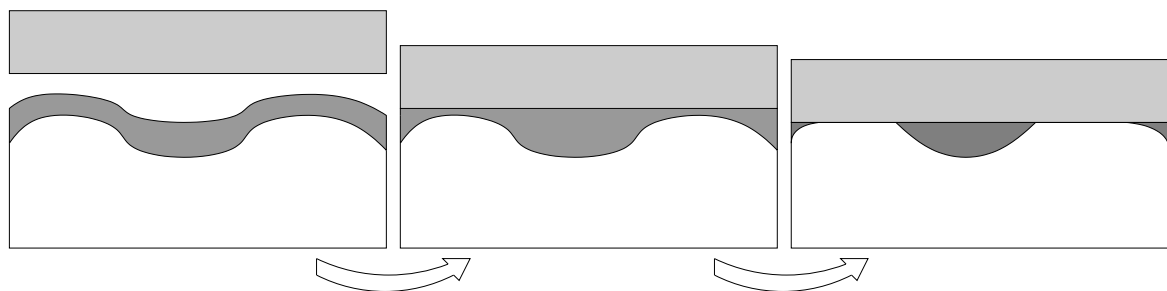


Figure III.3 : Formation of a CSL from a rough surface, covered with a soft layer

small scale information during classical tribological tests. In this work we consider contacts with heterogeneous material behaviour, related local COFs and subsurface geometry. We develop an analytical model to estimate the upper and lower bound of a global COF from small scale material and surface properties. Doing this we recognise the theory of homogenisation (Bornert et al., 2001; Besson et al., 2001), the bounds of Voigt and Reuss are the paradigms for our analytic model. We discuss the analytic model and compare it to FE computations. As an additional aspect plastic material behaviour is introduced in FE computations.

III.2 Analytic descriptions of a composite coefficient of friction

III.2.1 Definition

If two bodies are pressed into contact and undergo a relative motion the Coulomb friction law can be applied. It assumes a constant ratio between the contact normal force (P) and the contact tangential force under full slip (Q_{slip}). This coefficient is called coefficient of friction (COF).

$$\text{COF} = \frac{Q_{\text{slip}}}{P} \quad (\text{III.1})$$

In the contact at a point x the contact reactions are expressed in terms of contact pressure $p(x)$ and contact traction $q(x)$. Their integrals on the whole contact surface S give normal and tangential contact forces (P , Q_{slip}) and we can express the global COF in terms of stress.

$$\text{COF} = \frac{\int q(x)dS}{\int p(x)dS} \quad (\text{III.2})$$

We assume the Coulomb law to be valid in every point of the contact. Then the ratio between traction and contact pressure is called the local coefficient of friction $\mu(x)$ of every point of the contact surface.

$$\mu(x) = \frac{q(x)}{p(x)} \quad (\text{III.3})$$

Now the global COF can be expressed by the local coefficient of friction and the contact pressure.

$$\text{COF} = \frac{\int \mu(x)p(x)dS}{\int p(x)dS} \quad (\text{III.4})$$

Then the COF is the contact pressure weighted average of the local coefficient of friction $\mu(x)$. Within this context fretting contacts in the partial slip regime have been studied by Dini et al. (Dini and Nowell, 2003). They found a higher local coefficient of friction $\mu(x)$ in the slip zone than in the stick zone of the contact by comparing their analytic contact model with experiments.

Our intention is now to descend to an even smaller scale. For this it is useful to introduce a clean separation of scales. We introduce contact heterogeneities with a characteristic size d , that are much smaller than a "representative surface element" (RSE). The RSE is the smallest piece of a heterogeneous contact, on which a representative local coefficient of friction $\mu(x)$ can be found. In the RSE a capital X indicates the location, the bigger scale location in the contact of two macroscopic bodies is indicated with a small x . The RSE needs to be big enough to contain a representative population of heterogeneities. The size l of the RSE in its

turn is assumed to be much smaller than the contact size L . Additionally the stress gradients of the macroscopic stress fields with the characteristic length L_z need to be negligible on the scale of the RSE.

$$d \ll 1 \ll L, L_z \quad (\text{III.5})$$

$p(x)$ can then be considered to be constant in the RSE. We assume the Coulomb law to be still valid in the RSE.

$$\mu(X) = \frac{q(X)}{p(X)} \quad (\text{III.6})$$

This is the scale of asperities (Hills and Nowell, 1994; Johnson, 1987) and even possibly of grains in polycrystal metals (Goh et al., 2003a). In this work we want to derive the local coefficient of friction $\mu(x)$ by a homogenisation operation in a RSE of a heterogeneous contact:

$$\mu(x) = \frac{\int \mu(X)p(X)dS}{\int p(X)dS} \quad (\text{III.7})$$

The interest of this approach is the following. In a FE computation each contact node can have a local coefficient of friction $\mu(x)$. The information collected on the contact node can be used on the smaller scale RSE to reevaluate node parameters, for example $\mu(x)$ or a local wear constant. These node parameters are then updated on the contact nodes for the next computation step.

III.2.2 Estimation of the local coefficient of friction $\mu(x)$

The purpose of this section is to give realistic estimates of a local coefficient of friction $\mu(x)$, according to different geometries, material properties and surface properties. No analytical solution like the Hertz model is available for this composite surface, so that the stress profile is not known. As an alternative, seeking an analogy with the Voigt and Reuss approach, we estimate upper and lower limits of $\mu(x)$. We do not provide a proof that the found upper and lower limits are strict bounds so we prefer to use the term "estimations".

The RSE of the contact consists of two bodies. One is homogeneous with a homogeneous surface and will be called counter body. The bulk of the second body is again homogeneous and only its surface layer carries the heterogeneities. We will call it composite surface layer (CSL) because all heterogeneities are aligned on the surface. Both surfaces are assumed to be flat and smooth. That means that no geometric asperities are taken into account. The subsurface geometry of the CSL is unknown. Material and contact properties are introduced. Each component of the CSL has a constant coefficient of friction μ_i and the contact surface share f_i with the counter body. The composite surface component materials, the substrate and the counter body are compressible and linear elastic. We assume a uniform stress in the vicinity of the surface. Lateral strains are supposed to be zero ($\varepsilon_x = \varepsilon_z = 0$), so that an analytical relation between pressure and ε_y can easily be found. If we neglect the shear components, strain and stress in the direction normal to the contact (y-direction) follow this relation.

$$p_i = C_i \varepsilon_{yi}, \quad C_i = \frac{E_i}{(1 - \nu_i^2)} \frac{(1 - \nu_i)^2}{(1 - 2\nu_i)} \quad (\text{III.8})$$

Then the local coefficient of friction can be written like

$$\mu(x) = \frac{\sum \mu_i p_i f_i}{\sum p_i f_i} \quad (\text{III.9})$$

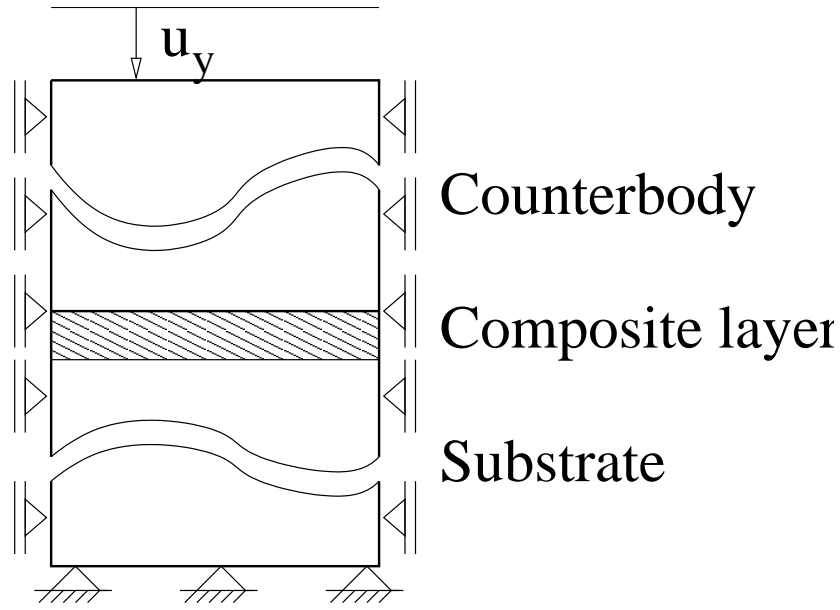


Figure III.4 : Boundary conditions on the RSE

It was mentioned before that we consider the contact pressure $p(x)$ to be constant on the RSE. This load is applied to the RSE by a homogeneous constant normal displacement imposed at a large distance from the CSL between the counter body and the substrate (see Fig. III.4).

Under these circumstances the contact pressure is still unknown. But contact pressure and contact normal strain are linked by the material constant C_i (eq. III.8). This relation can be used to find two estimates of the local coefficient of friction assuming either that the normal strain ε_y is constant in the RSE or once that the contact pressure p_i is constant. So with $p_1 = p_2 = p_i$ we find

$$\mu(x) = \frac{\sum \mu_i f_i}{\sum f_i} \quad (\text{III.10})$$

and with $\varepsilon_{y1} = \varepsilon_{y2} = \varepsilon_{yi}$ we find

$$\mu(x) = \frac{\sum \mu_i C_i f_i}{\sum C_i f_i} \quad (\text{III.11})$$

Material properties (C_i) and surface properties (μ_i) enter the formulas. We will show the behaviour of the upper and lower estimation with a simple example. A CSL consists of two material components, each of them having individual material and surface properties (see Tab III.1). In contact A the component 1 is the more compliant material ($C_1 < C_2$) and has the lower coefficient of friction. In this case the lower estimation is found with eq. III.10, the upper estimation is found with eq. III.11 (see Fig. III.5(a)). In contact B the component 1 is the stiffer material ($C_1 > C_2$) but has still the smaller coefficient of friction. Then eq. III.10 gives the upper estimation, eq. III.11 the lower estimation (see Fig. III.5(b)). So the upper and lower estimation can be interpreted as follows. Eq. III.10 describes the case where only the surface parameters (μ_i, f_i) determine the homogenised coefficient of friction $\mu(x)$. Eq. III.11 gives the maximum influence of the material properties. The μ_i of the stiffer material has a stronger influence on the homogenised coefficient of friction than the μ_i of the more

| Cont. A | ν | E (GPa) | C (GPa) | μ | Cont. B | ν | E (GPa) | C (GPa) | μ |
|---------|-------|---------|---------|-------|---------|-------|---------|---------|-------|
| Comp. 1 | 0.32 | 8 | 11.45 | 0.1 | Comp. 1 | 0.15 | 55 | 58.08 | 0.1 |
| Comp. 2 | 0.15 | 55 | 58.08 | 0.5 | Comp. 2 | 0.32 | 08 | 11.45 | 0.5 |

Table III.1 : Properties of two CSLs

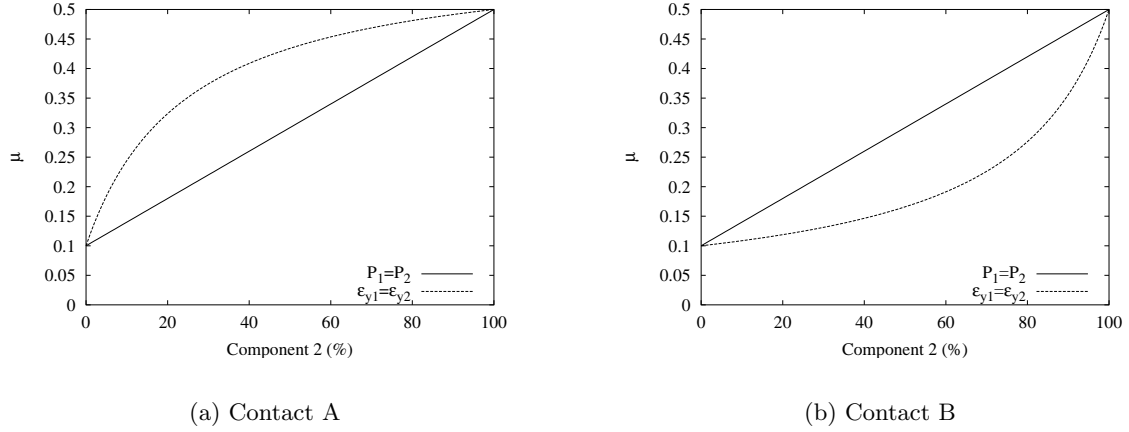


Figure III.5 : Upper and lower analytic estimation of the coefficient of friction of a composite contact.

compliant material. This has to be related to the fact that the stiffer material will carry more load.

III.2.3 Discussion

In order to better understand, under which conditions which estimation is approached a small qualitative model, taking the shear stresses in the counter body and the substrate into account is made. A CSL in two dimensions consists of two different material components as shown in Fig. III.6(a). The material domains have a rectangular regular shape. As in eq. III.10 we assume the contact pressure to be constant ($p_1 = p_2$). Then the surface layer is unevenly deformed as shown in Fig.III.6(b). Using eq. III.8 the difference in the deformation of Component 1 and Component 2 is found to be:

$$\Delta u = ph\left(\frac{1}{C_1} - \frac{1}{C_2}\right) \tag{III.12}$$

where h is the initial thickness of the CSL. Δu is separated into one part on the side of the counter body and one part on the side of the substrate.

$$\Delta u = \Delta u_{CB} + \Delta u_S \tag{III.13}$$

To follow the deformation of the CSL, the counter body and the substrate are allowed to undergo a shear deformation as shown in Fig. III.7. This is taken into account by the assumption of a constant shear stress τ and the shear modulus of counter body G_{CB} and substrate G_S .

The shear stress is given by the equation:

$$\tau = G\left(\frac{\delta u_n}{\delta X} + \frac{\delta u_t}{\delta Y}\right) \tag{III.14}$$

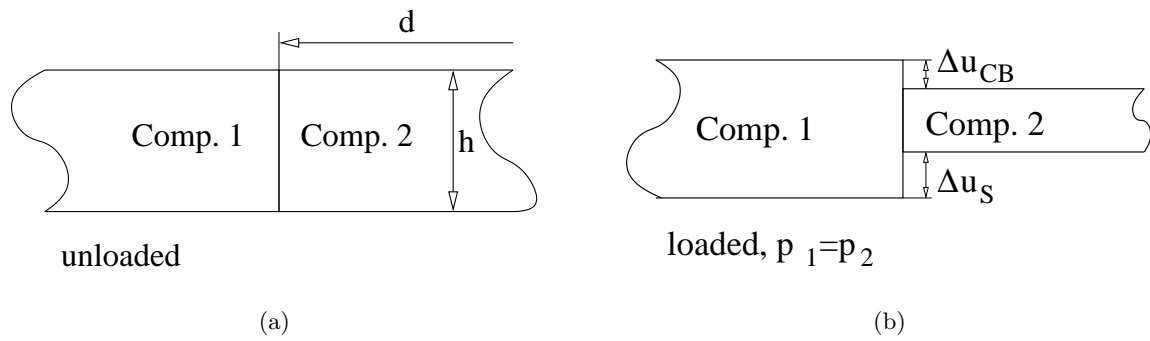


Figure III.6 : Deformation of the CSL if the contact pressure is assumed to be constant ($p(x) = \text{const.}$).

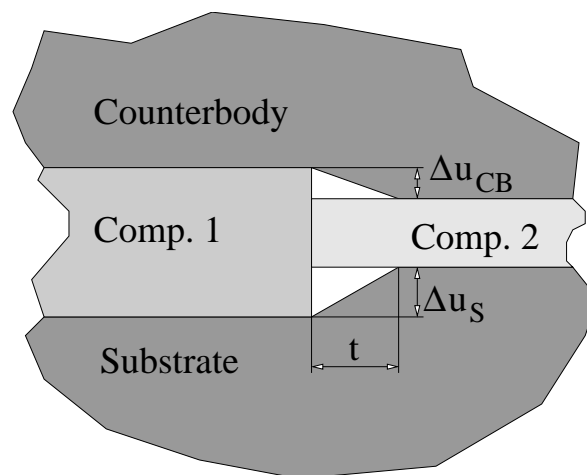


Figure III.7 : A simple model, allowing the deformation of counter body and substrate by shear.

where u_n and u_t are the normal and tangential displacements, respectively. In this model $\delta u_t/\delta Y$ is much smaller than $\delta u_n/\delta X$ so only the bigger component is considered and the other one is assumed to be zero. Then on the side of the counter body and the substrate it is obtained:

$$\frac{\delta u_n^{CB}}{\delta X} = \frac{\Delta u_{CB}}{t}, \quad \frac{\delta u_n^S}{\delta X} = \frac{\Delta u_S}{t} \quad (\text{III.15})$$

where t is the length over which the constant shear stress needs to act to follow the imposed deformation of the composite layer. With eq. III.13 it is found:

$$\Delta u = \tau t \left(\frac{1}{G_S} + \frac{1}{G_{CB}} \right) \quad (\text{III.16})$$

Comparing the deformations of the CSL (eq. III.12) and counter body and substrate (eq. III.16) we find:

$$\frac{\tau t}{p h} = \frac{\left(\frac{1}{C_1} - \frac{1}{C_2} \right)}{\left(\frac{1}{G_S} + \frac{1}{G_{CB}} \right)} \quad (\text{III.17})$$

We suppose $\tau/p = k$ to be constant. If t is much bigger than the characteristic size (d) of a component domain of the CSL, counter body and substrate cannot follow the assumed deformation of the CSL at all and the local coefficient of friction will approach the value given by eq. III.11. If t is much smaller than d , counter body and substrate follow the deformation of the CSL and the assumption that the contact pressure is constant is approximated. Then the local coefficient of friction will approach the value given by eq. III.10.

$$k \frac{d}{h} \gg \frac{\left(\frac{1}{C_1} - \frac{1}{C_2} \right)}{\left(\frac{1}{G_S} + \frac{1}{G_{CB}} \right)} \implies \mu(x) = \frac{\mu_1 f_1 + \mu_2 f_2}{f_1 + f_2} \quad (\text{III.18})$$

$$k \frac{d}{h} \ll \frac{\left(\frac{1}{C_1} - \frac{1}{C_2} \right)}{\left(\frac{1}{G_S} + \frac{1}{G_{CB}} \right)} \implies \mu(x) = \frac{\mu_1 C_1 f_1 + \mu_2 C_2 f_2}{C_1 f_1 + C_2 f_2} \quad (\text{III.19})$$

From these equations it can be read what influences the homogenised local coefficient of friction at a given surface share of the components. There is an influence of the layer geometry represented by d/h , an influence of the difference of the material properties of the components ($1/C_1 - 1/C_2$) and the influence of the rigidity of substrate and counter body together ($1/G_S + 1/G_{CB}$). The linear mixture rule (eq. III.10) for example is promoted by a shallow layer with big component domains, when the components have similar mechanical properties and when the substrate or the counter body are compliant.

III.3 Finite element computation setup

The previous section allows us to qualitatively characterise the behaviour of the system. Finite elements are now used to provide quantitative data for specific systems. The FE code used is Zebulon (Besson and Foerch, 1998; Besson et al., 1998).

III.3.1 FE mesh

A cylinder/plate system is modelled by a 2D mesh as shown in Fig. III.8(a). The cylinder has a radius of 10 mm. The plate has a side length of 10 mm and 6 mm in the horizontal and vertical direction, respectively. At the top surface of the plate a composite surface layer

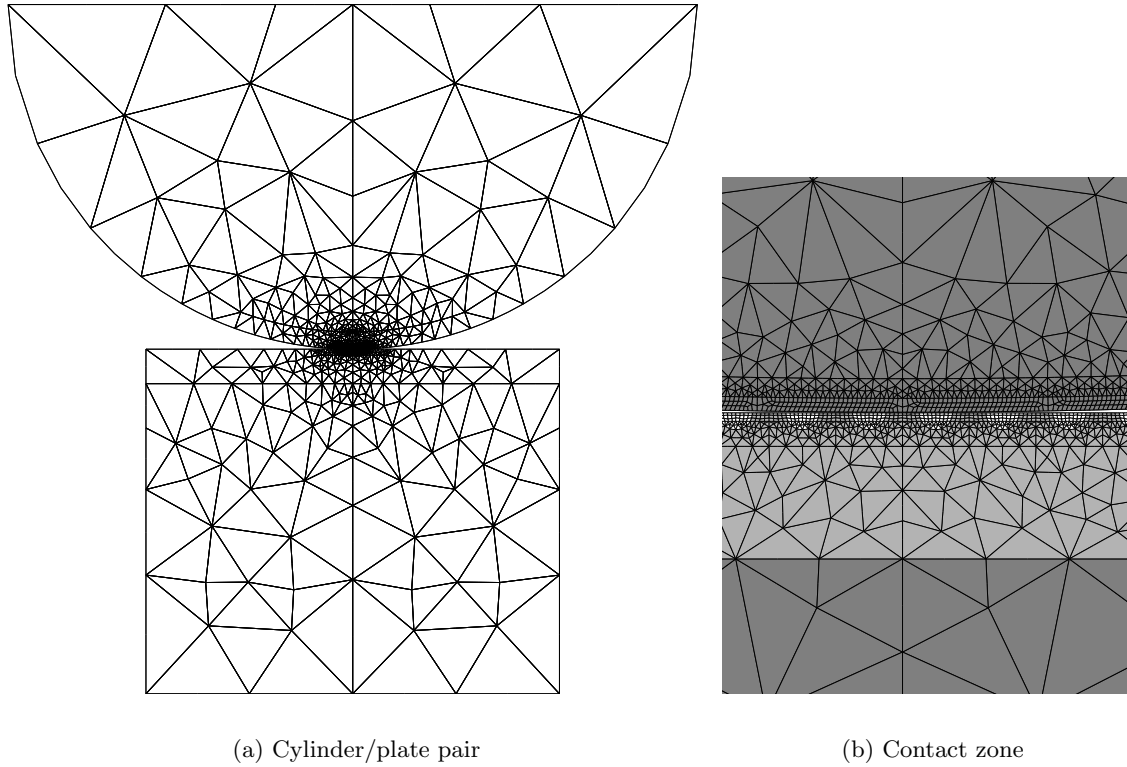


Figure III.8 : Finite element mesh of a cylinder/plate contact

(CSL), consisting of two components, is built by the repetition of an elementary surface domain (ESD) which carries all CSL characteristics. Fig. III.9 shows examples of ESDs. The surface share of the components is set by broadening the ESD while keeping the size and shape of the central domain (component 1) constant. For all meshes, quadratic, full integration, plane strain elements are used. Because the composition of CSL and plate differs among the computations shown in the results section a more precise description is given there.

It has to be mentioned that 2D meshes are used even though the problem is intrinsically three dimensional. The use of 3D meshes would make the FE models too costly for a first comparison. The 3D CSLs feature inclusions with a closed shape and a matrix material in which the inclusions are embedded. Our 2D meshes would be good models of 3D CSLs that featured very elongated inclusions (out of plane in the 2D meshes). Real 3D and modelled 2D CSLs with the same surface composition do not have the same overall interface length between inclusion and matrix. It should be kept in mind that the overall interface length in the 2D meshes is smaller than that in the real 3D surfaces.

The clean separation of scales introduced in the analytic part of this paper is not respected in FE modelling. Respecting the separation of scales would have made the CSL very fine and again the FE meshes would have become too big. Because in the FE mesh the CSL is a periodic repetition of ESDs it seems sufficient to ensure that the gradient of the Hertzian contact pressure is small in an ESD. Then we can compare the coefficient of friction of the FE model (Q/P) to the analytic estimation of the coefficient of friction of a RSE ($\mu(x)$).

III.3.2 Contact formulation

The contact is introduced by a direct method using the influence matrix (Jean and Touzot, 1988). In this method the contact conditions are not explicitly added to the variational

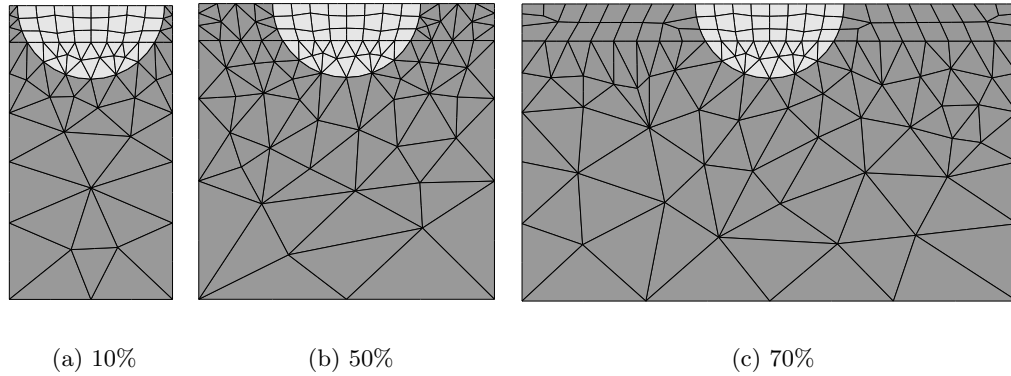


Figure III.9 : Elementary surface domains: different surface shares of component 2

| | Bulk material | Component 1 | Component 2 |
|----------------------|---------------|-------------|-------------|
| E (GPa) | 119 | 8 | 55 |
| ν | 0.29 | 0.32 | 0.15 |
| R ₀ (MPa) | - | 200 | 500 |

Table III.2 : Material properties

problem but the contact reactions are at first computed in a local contact algorithm and then added to the global problem. The contact is modelled with an impactor/target technique. The relevant surface nodes of the cylinder are assigned to the target, the surface nodes of the plate are defined as impactor. The frictional contact force is introduced by the Coulomb law with a constant isotropic coefficient of friction. The component 1 has a coefficient of friction of 0.1, the component 2 a coefficient of friction of 0.5 with the cylinder.

III.3.3 Material behaviour

In most computations all materials are linear elastic. In computations taking plastic deformations into account the CSL components are elastic/plastic with a constant limit of elasticity R₀, the bulk material of cylinder and plate is always elastic. The material parameters are listed in Tab. III.2. Component 1 is the central domain of the ESD, the rest of the material on the surface is component 2. If a different material behaviour is used it is explicitly indicated.

III.3.4 Boundary conditions

The loading is applied under displacement control. So the boundary conditions in the FE model are defined in terms of prescribed displacements. The loading is done in two steps (see Fig. III.10). At first a vertical displacement (u₂) of 7 μm is imposed at the top of the half cylinder while the plate is fixed by locking its bottom and side nodes. The displacement (u₂) causes a vertical force (P) which is obtained as the sum of the vertical node reactions at the top surface of the cylinder. Then the cyclic loading is started. The cylinder is fixed by locking the top nodes. The plate performs one cycle of an oscillating horizontal displacement (u₁) with a triangular time-displacement curve. This displacement is imposed on the bottom

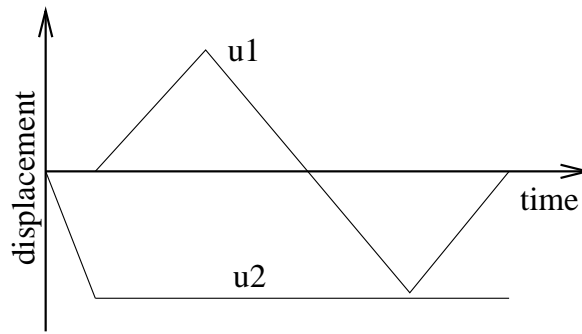


Figure III.10 : Application of the boundary conditions

and side nodes of the plate with an amplitude of $\delta_{\max} = 50 \mu\text{m}$. The horizontal reaction force (Q) is obtained as the sum of horizontal reactions of the same nodes.

III.3.5 Determination of the coefficient of friction

The resulting COF (Q/P) of the cylinder/plate system shows some dispersion. In Fig. III.11, Q/P in the first fretting cycle is shown. In computations with elastic materials, Q/P shows some variation, but the mean value stays unchanged. The variation comes from the discretisation of the contact problem. Finer meshes and a finer resolution of time would diminish the variation but increase the computational costs. In computations with plastic materials, Q/P shows less variation since the plastic modulus characterising the stress variation for a given strain increment is much smaller than the Young's modulus. On the other hand the mean value decreases because the contact stresses redistribute among the contact materials as plastic deformation proceeds. Because of these peculiarities, the COF, shown in the results section, is averaged over the gross slip period indicated in Fig. III.11.

III.4 Results and discussion

In this section at first computations with assemblies that correspond to the analytical model are made. Then other, more complex compositions are tried out to see if their results lie within the analytical upper and lower estimations. Then the influence of the number of ESDs in the contact on the obtained COF is studied. Finally the influence of plastic deformation in the CSL on the resulting COF is treated.

III.4.1 FE computations corresponding to the analytic estimation of a coefficient of friction

At first we want to know whether we can obtain results from FE computations that reach the upper and lower bound estimations made with the analytical model in section III.2.2. So we choose the two elementary surface domains (ESD) shown in Fig. III.12. In these meshes the CSL is made of component 1 and component 2, the cylinder serves as counter body and the plate under the CSL as substrate. So this assembly corresponds to that in the analytical model, here cylinder (counter body) and plate (substrate) are taken to have the same material properties. CSLs made with the ESD P1-10 are thin compared to that made with the ESD P2-10. The "10" in the ESD-name stands for the surface length ($10 \mu\text{m}$) of the component 1 domain in the centre of the ESD. The properties of the CSL components are given in Tab.

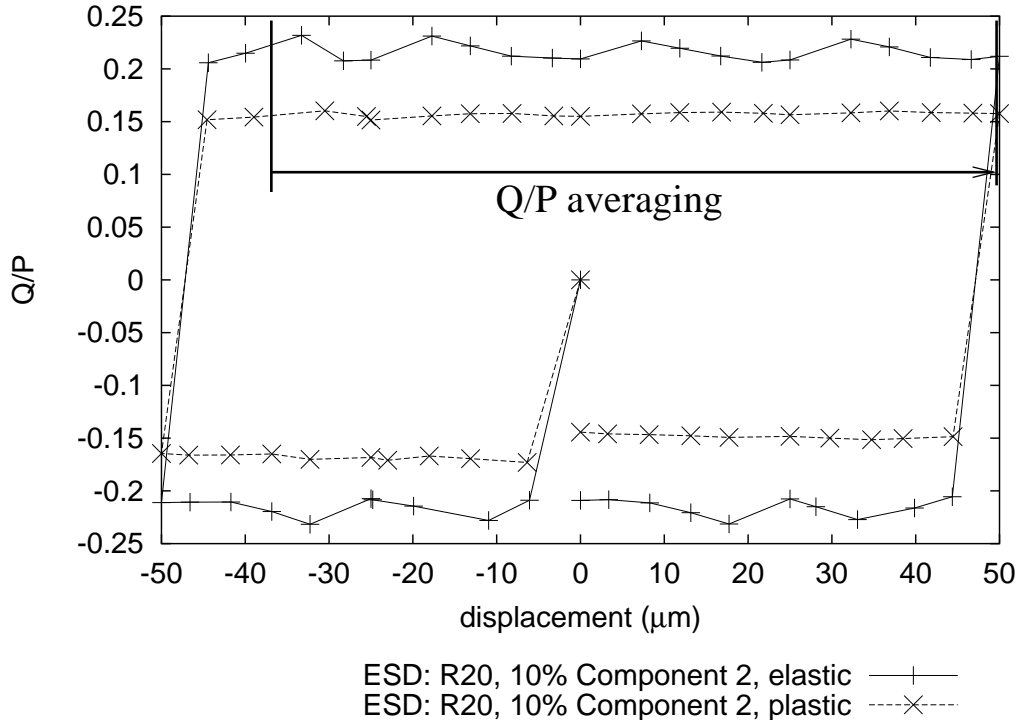


Figure III.11 : Determination of Q/P in a FE computation

III.2. The bulk material of plate and cylinder (white domain in the ESD) are chosen to promote extreme cases as given by eq. III.18 and eq III.19. For computations with P1-10 we take a low modulus $E = 1190$ MPa; for P2-10 the high modulus $E = 119000$ GPa is taken, the Poisson ratio is $\nu = 0.29$ in both cases. With the ESDs we make meshes varying the surface shares of the CSL components, we compute one fretting cycle and we plot the obtained COF over the surface share of component 2 (Fig. III.13). With the P1-10 computations we get a very good agreement with the analytic estimation, the P2-10 computations have the same shape as the upper analytic estimation but the values are somewhat lower. Since the obtained COF depends on the contact pressure distribution in the CSL, it is shown in Fig. III.14 for a CSL with 50% surface share of component 2. The contact pressures are normalised so that the pressure in the component 1 domains ($p_{\text{Comp.1}}$), which are located at the left and right sides, is equal to 1. Then $p_{\text{Comp.2}}$ (centre) in the P1-10 computations is equally about 1, in the P2-10 computations it is more than 5 times bigger. The maximum pressure difference estimated with the analytic model is given by the difference between $C_{\text{Comp.1}}$ and $C_{\text{Comp.2}}$ (eq. III.8). In Fig. III.13 these two material parameters are normalised so that $C_{\text{Comp.1}}$ is equal to 1. Then $C_{\text{Comp.2}}$ agrees well with $p_{\text{Comp.2}}$ in the P2-10 computations. There is some deviation from the analytic estimation at the left and right sides of the component 2 domain, which is due to the deformation of the CSL caused by the tangential loading of the sliding contact. This deformation is smaller in thinner CSLs, so the upper analytic limit can be best approached by FE computations with a rigid bulk material and CSLs with thin elongated domains.

III.4.2 Different CSL geometries

We make computations with different types of CSLs (Fig. III.15). The ESDs S20, R20 and L20 have component 1 domains in the shape of inclusions in a matrix of component 2. The

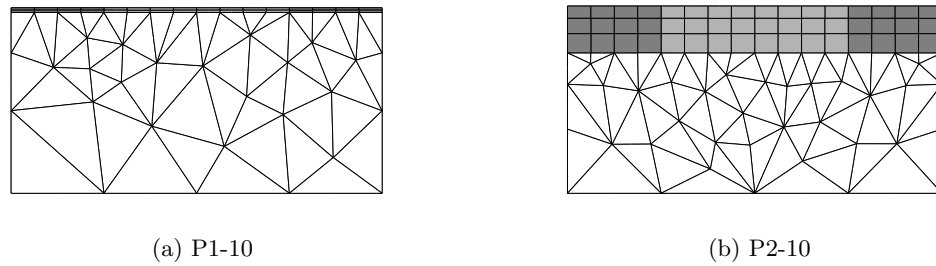


Figure III.12 : ESDs for FE computations corresponding to the analytic estimation.

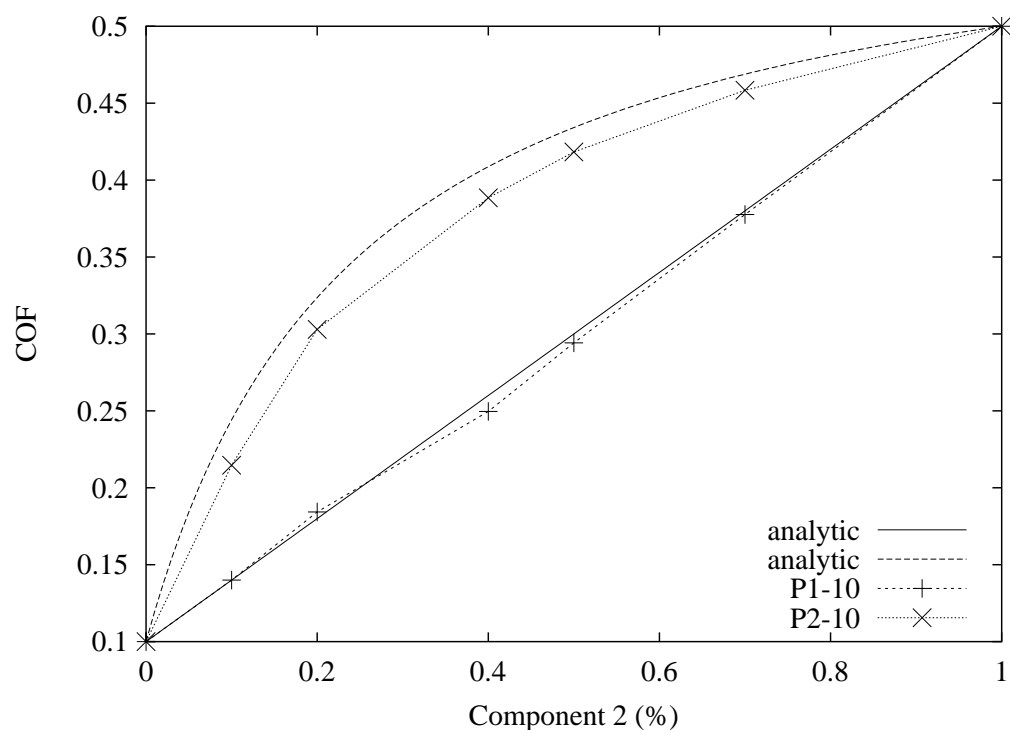


Figure III.13 : Comparison of analytic estimations and corresponding FE computations of the COF.

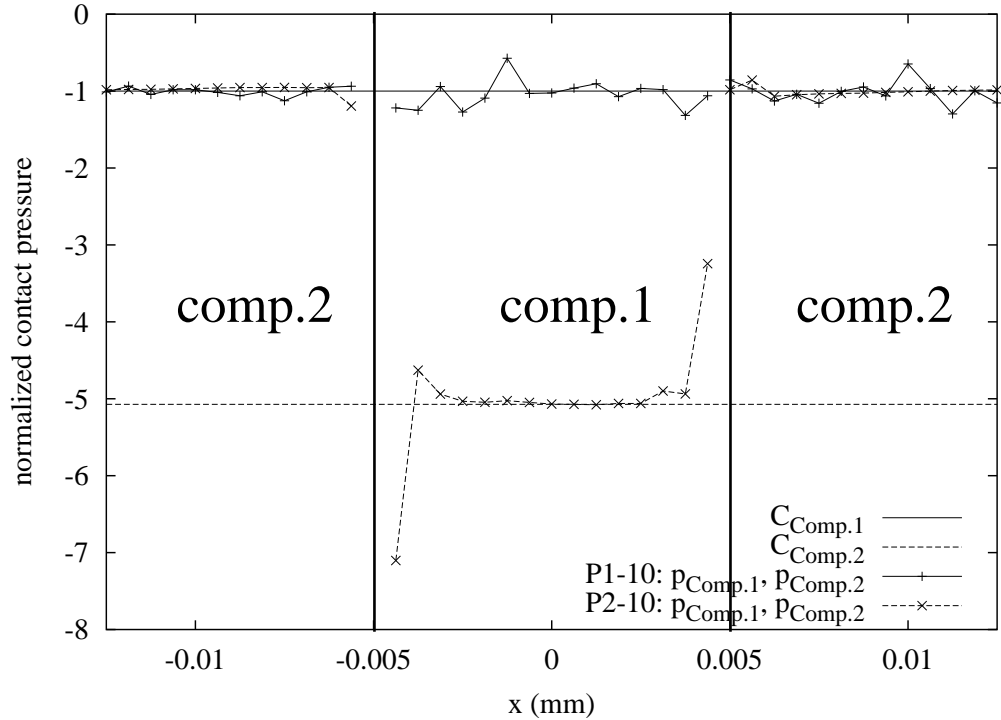


Figure III.14 : Comparison of the contact pressures of the analytic estimations and in one ESD of the corresponding FE computations, sliding contact, 50% component 2.

”20” in the ESD-name stands for the surface length ($20 \mu\text{m}$) of the component 1 domain. Comp.2 builds a layer on the plate with a thickness of $175 \mu\text{m}$. The ESDs differ in their shape and the depth of the inclusions. In L20 meshes the inclusion is deep, in S20 meshes it is shallow. The ESD Lxx is of the same type as L20, but the inclusion reaches to the bottom of the plate. Using these ESDs, meshes of the cylinder/plate contact are constructed varying the surface share of component 2. One fretting cycle is computed, the resulting COFs are shown in Fig. III.16. The used material properties are listed in Tab. III.2.

The COF in S20 computations is near the analytic lower bound estimation. The contact pressure (during sliding) in component 2 is uniform and not much larger than that in component 1 (see Fig. III.17). With R20 ESDs the expected happens, the COF is higher, the contact pressure difference between the components is larger and the pressure distribution in component 2 is regular. Using the L20 ESDs the resulting COF is not very different from that of the R20 computations. A look at the contact pressure in the sliding contact reveals that the pressure in component 2 is no more constant but shows a slope (Fig. III.17). On the right side the pressure is smaller, on the left it is bigger than in R20 computations, so the average is about the same as in R20, which explains the similar COF. If only a normal load is applied the difference in the contact pressure of the CSL components is bigger in L20 than in R20 computations (see Fig. III.18). We conclude that the non-constant contact pressure in a sliding contact comes from the deformation of the CSL by the tangential loading of the sliding contact. In the Lxx computations the same effect is more pronounced and even leads to a decrease of the COF. In Fig. III.18 the curves are almost symmetric because of the symmetry of the ESD in combination with the normal loading. The asymmetric part comes from the fact, that the centre of the ESD does not coincide with the centre of the cylinder/plate contact. In this figure it is particularly well visible that no convergence is

| ESD type | 2a (μm) | 10% comp.2 | | 70% comp.2 | |
|----------|----------------------|------------------------------------|--------|------------------------------------|--------|
| | | l_{ESD} (μm) | nb.ESD | l_{ESD} (μm) | nb.ESD |
| R10 | 360 | 11.1 | 32.4 | 33.3 | 10.8 |
| R20 | 360 | 22.2 | 16.2 | 66.6 | 5.4 |
| R40 | 360 | 44.4 | 8.1 | 133.3 | 2.7 |

Table III.3 : Relation between the number of ESDs in contact and the ESD size (contact length 2a, surface length of a ESD l_{ESD} , number of ESD in contact nb.ESD).

attained at the border between the elastic domains of component 1 and component 2. For sure, the singularity cannot be reached by such a FE technique, nevertheless we think that the approach is relevant to capture the average value of the load on the CSL, which is the only value needed for this approach.

III.4.3 Influence of the number of ESDs in the contact

The number of ESDs in contact is varied by increasing or decreasing the size of the ESDs while keeping the size of the cylinder/plate assembly constant. We use ESDs of the type "R" with the three component 1 surface lengths $10\mu\text{m}$, $20\mu\text{m}$ and $40\mu\text{m}$ (see Fig. III.19) and ESDs of the type "S" with the component 1 surface lengths $20\mu\text{m}$ and $40\mu\text{m}$. The same meshes and computations as described in the last section are made with these ESDs.

The relation between the cylinder/plate contact width and ESD size is given for the "R" type computations in Tab. III.3. In this table l_{ESD} means the surface length of a ESD and nb.ESD the number of ESDs in contact. The contact width (2a) is equal to $360\mu\text{m}$ in all computations. Since the surface composition of a CSL is changed by adjusting the surface length of component 2 while keeping component 1 constant, all ESDs have different sizes. All computation results are given in Fig. III.20. The smallest ESD is R10–10%–comp.2. In this FE computation 32.4 ESDs are in the contact. The biggest ESD is R40–70%–comp.2. In this computation only 2.7 ESDs are in the contact. Still we find the same COF in this computation as in that with R10–70%–comp.2 where 10.8 ESDs are in the contact. This insensitivity of the COF on the ESD size can be attributed to the fact that the result is not only homogenised by a sufficient number of ESDs in contact but also by the averaging of the COF over a sliding stroke of $131\mu\text{m}$. No computations with less than 2.7 ESDs in the contact are made in this work.

III.4.4 Influence of plastic deformations

Plastic deformation of the CSL is studied using "R40" and "S40" type computations. Every set of computations is made once with an elastic CSL and once with an elastic/plastic CSL. The material parameters can be found in Tab. III.2. The COF obtained for CSL of the type "S40" does not show sensitivity to the material behaviour even though some plastic deformation occurs in the computation (see Fig. III.21). For type "R40" the COF with an elastic/plastic material description is lower for component 1 surface shares inferior to 70%. With lower component 2 surface shares higher amounts of plastic deformation are obtained and a bigger share of the component 2 surface is concerned (see Fig. III.23). In this figure the equivalent accumulated plastic strain in the CSL is shown. In computations with lower component 2 surface shares the difference between the COFs of elastic and elastic/plastic material computations is bigger. The difference of the contact pressure in elastic and elastic/plastic computations can be seen in Fig. III.22. In the "R40" type computations stress redistribution

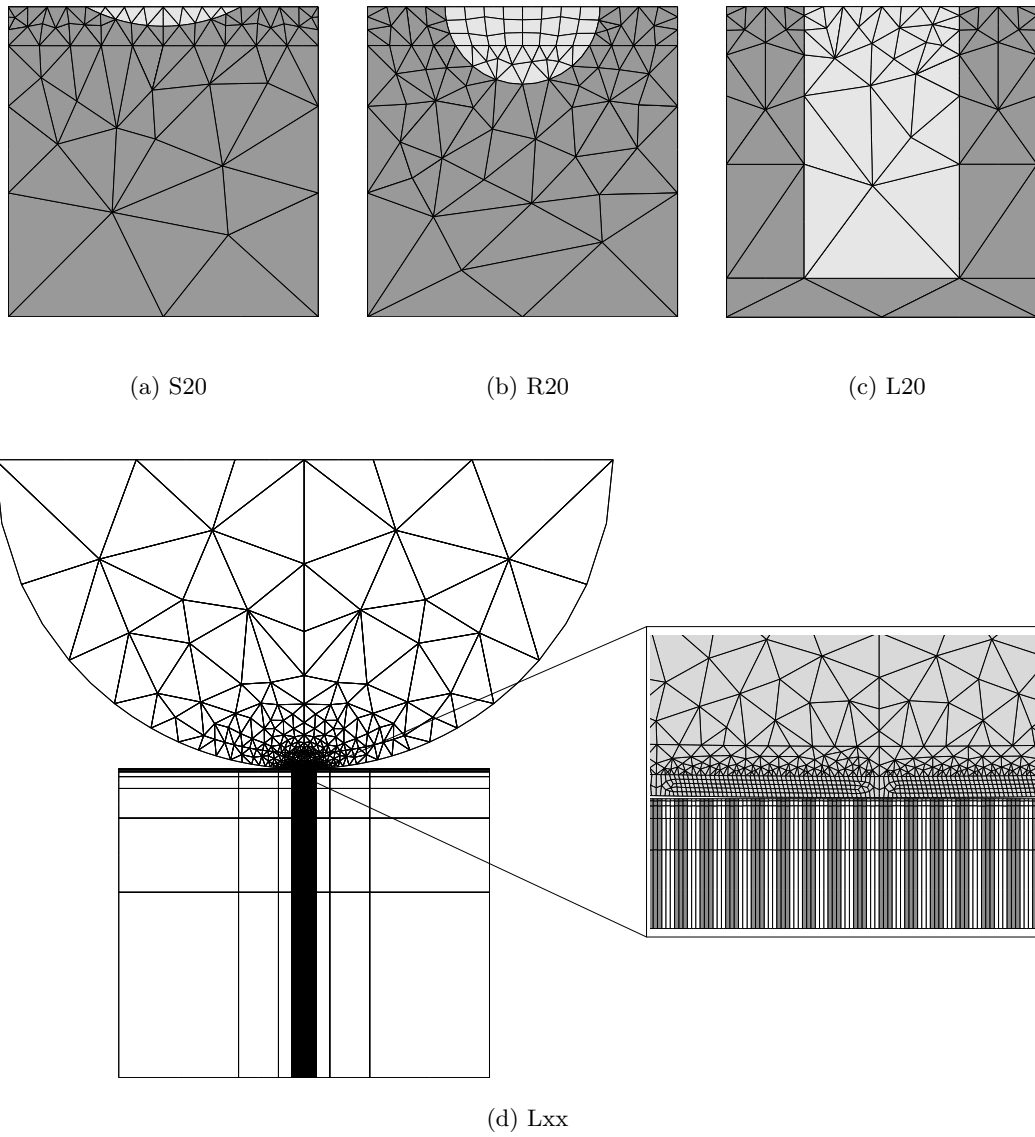


Figure III.15 : FE computations with different ESD shapes.

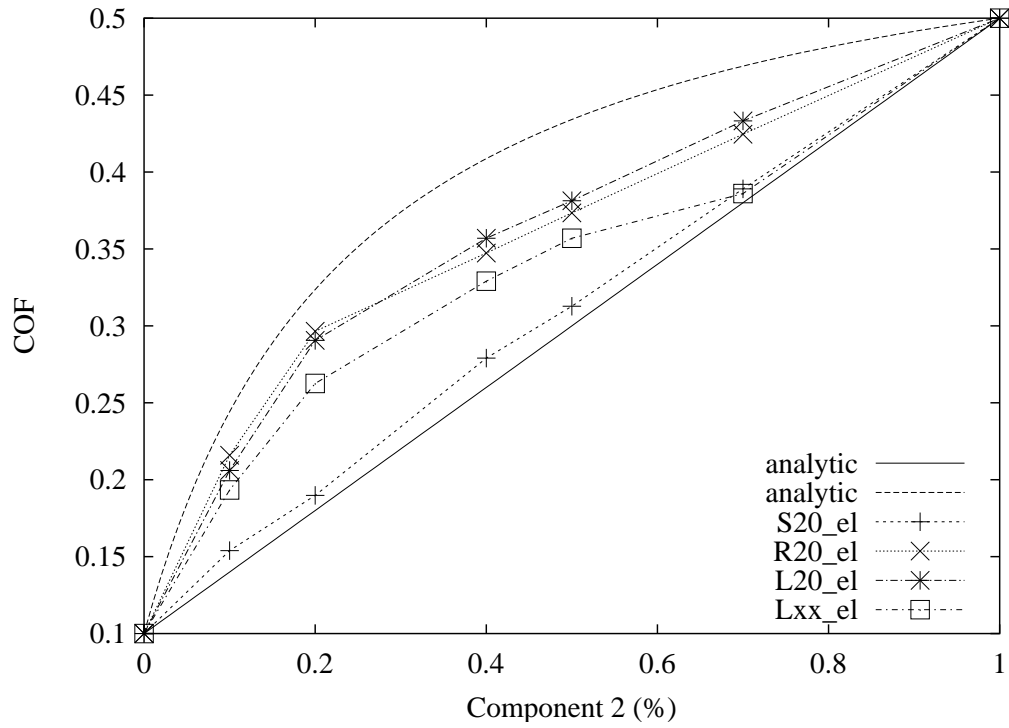


Figure III.16 : COF in FE computations with different ESD shapes.

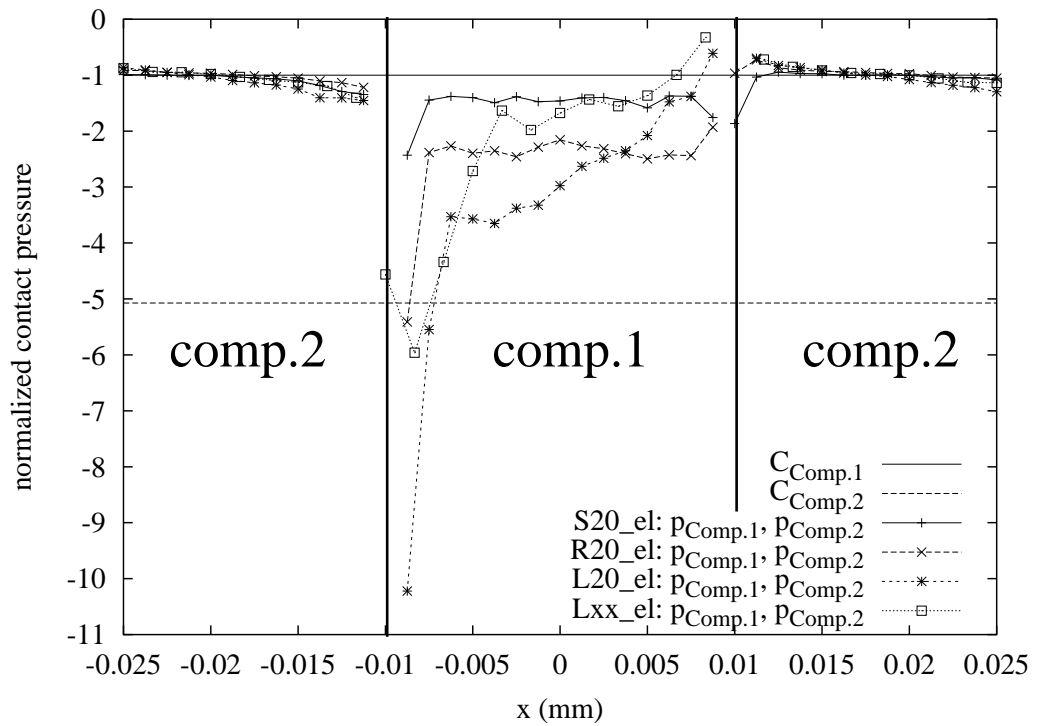


Figure III.17 : Contact pressure in one ESD in FE computations with different ESDs, sliding contact, 50% component 2.

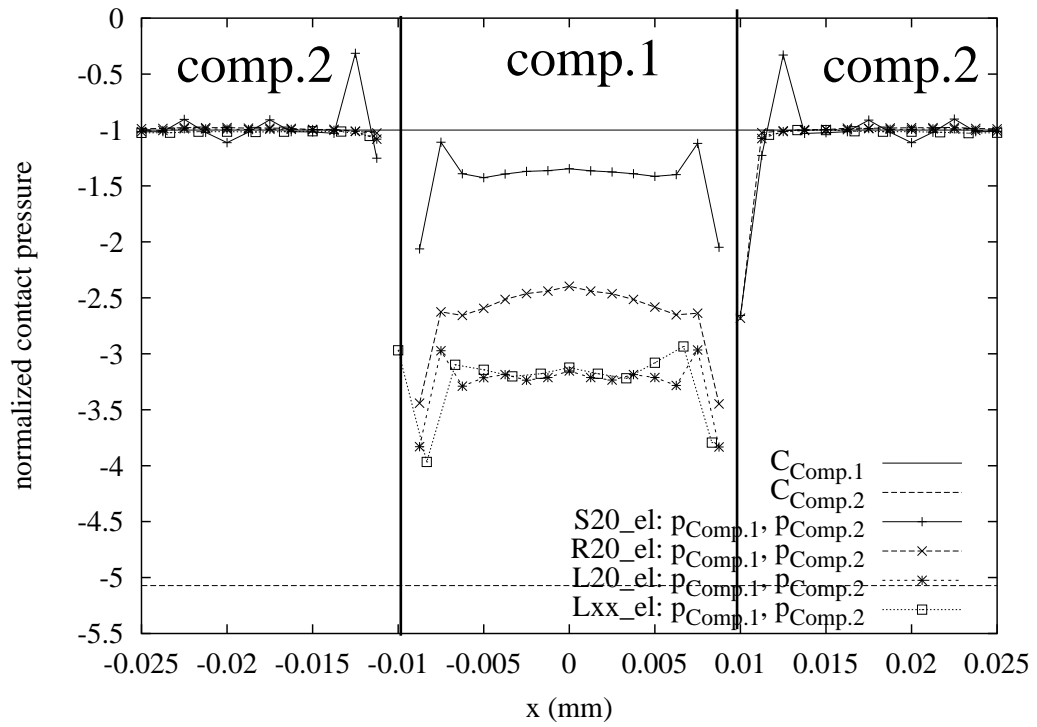


Figure III.18 : Contact pressure in one ESD in FE computations with different ESDs, only normal contact, 50% component 2.

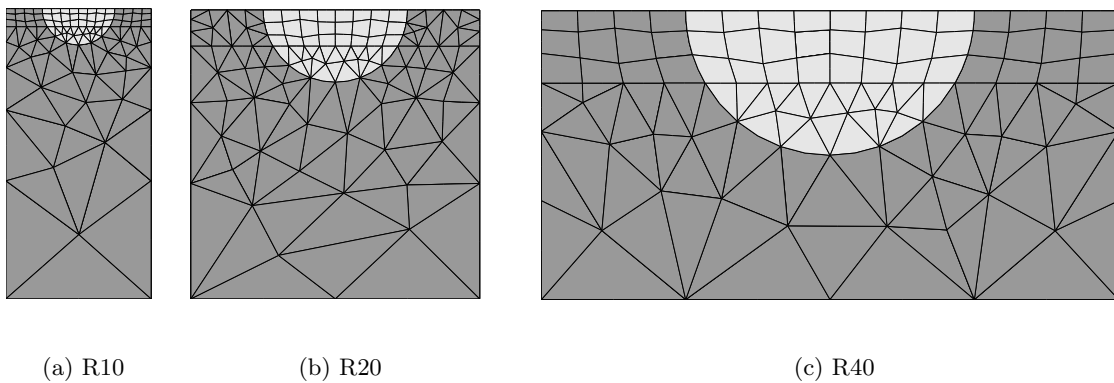


Figure III.19 : ESDs of different size.

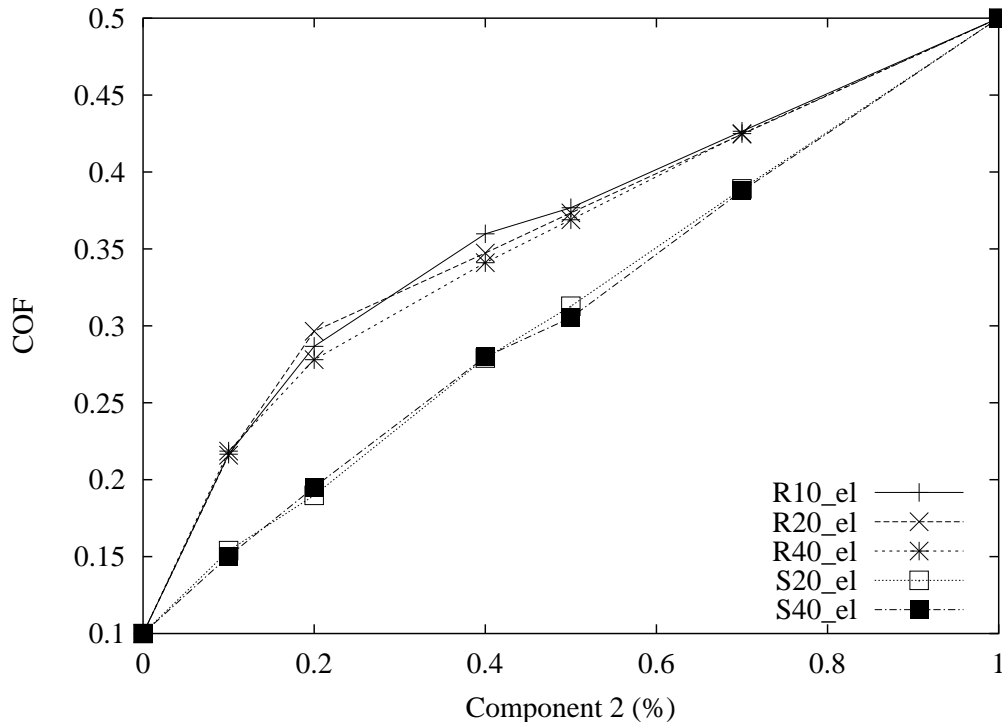


Figure III.20 : Influence of the ESD size on the resulting COF in FE computations.

from component 2 domains to component 1 domains continues during the whole computation. This can be seen in Fig. III.22 comparing the contact pressures of elastic and elastic/plastic computations. The stress redistribution leads to a change of the global COF that does not stop until the end of the computation (see fig. III.11). Due to plasticity, the system evolves from a "prescribed strain" status towards a "prescribed stress" one. This is accompanied by the alignment of the contact pressures in the CSL components and the consecutive abatement of the COF. In "S" type computations the difference of the contact pressure in the CSL components is very small from the beginning, so plastic deformation has no effect on the COF.

III.5 Conclusion

In this work the coefficient of friction of a composite surface layer (CSL) on a homogeneous substrate in contact with a homogeneous counter body has been investigated. With an analytic model an estimation of the upper and lower bound of the resulting friction coefficient was made whereas the material and surface properties of the CSL components were known and no information about their geometrical arrangement was at hand. Like the Voigt and Reuss bounds the estimations made here gave two values for a given CSL surface composition, within which the resulting friction coefficient was expected to lie. Discussing the analytic estimation it was found that the friction coefficient of a CSL for a given surface composition was influenced by the CSL geometry, the dissimilarity of the CSL component materials and the compliance of substrate and counter body.

The friction coefficient of a CSL in contact with a heterogeneous counter body was then computed using the FE method. Computations with conditions for that the analytic

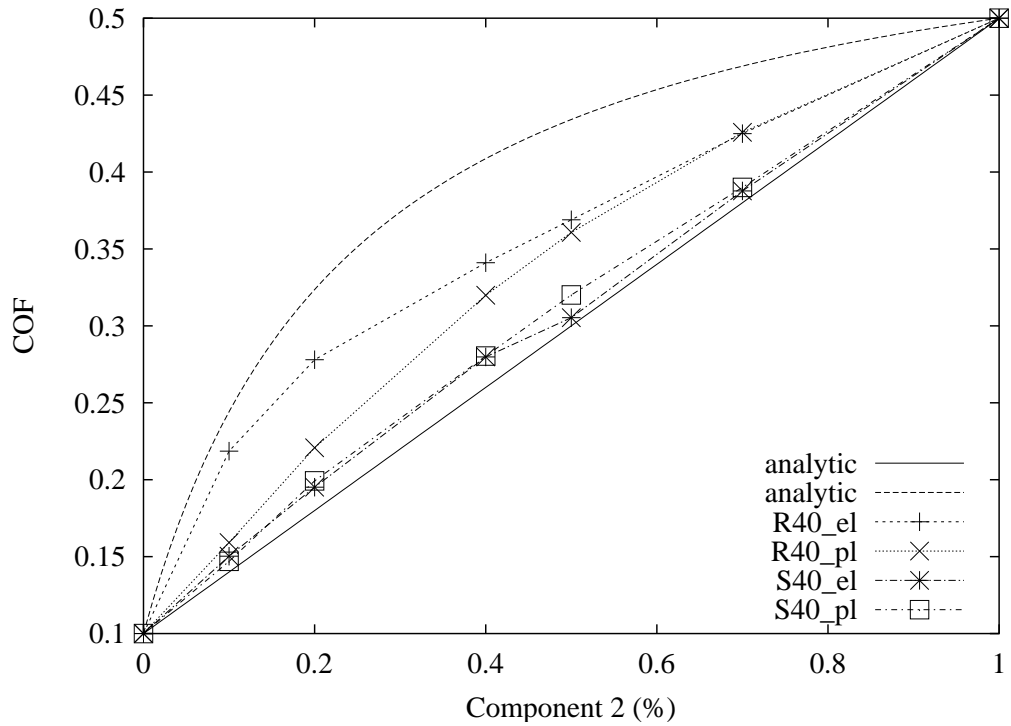


Figure III.21 : COF in FE computations with and without plastic yielding of the CSL.

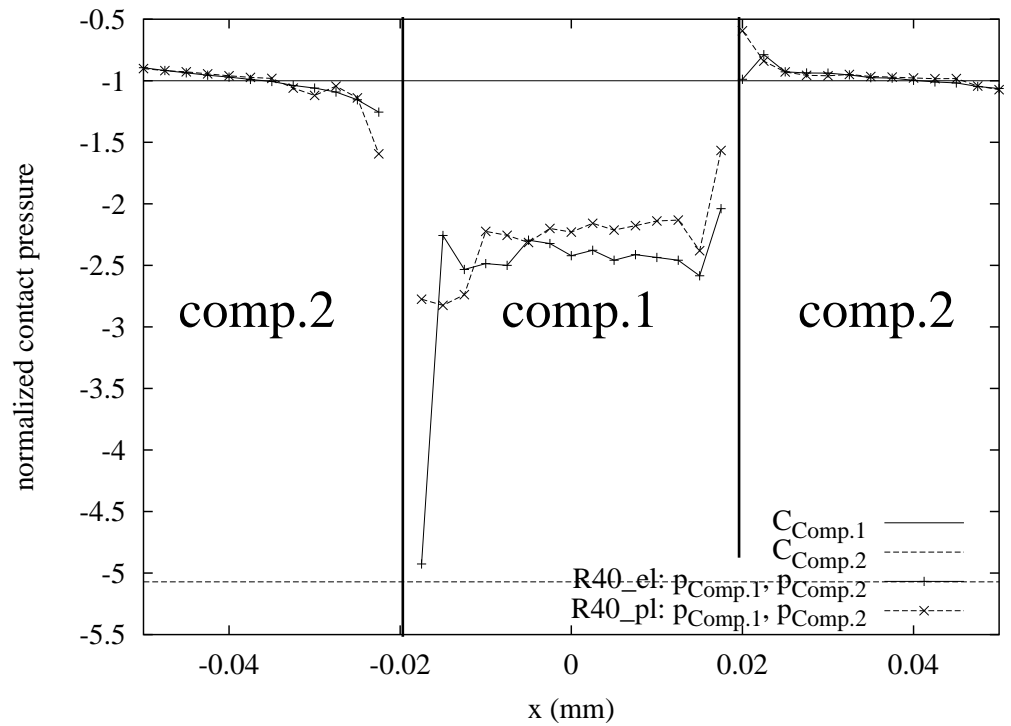


Figure III.22 : FE computation of the contact pressure in a sliding contact with and without plastic yielding in the CSL. One ESD is shown, 50% component 2 surface share.

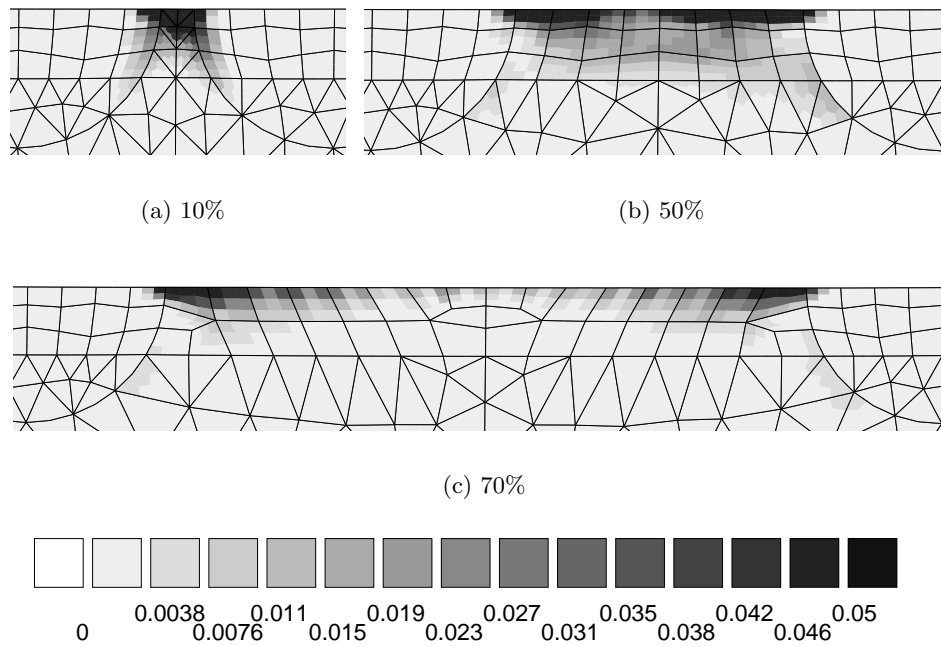


Figure III.23 : Equivalent accumulated strain in the CSL of type R40 with different surface shares of component 2.

estimation falls near the upper and lower bounds were made. In these computations, the linear analytic estimation was reached. The nonlinear estimation was approached but not reached in FE computations, the difference was attributed to the tangential loading of the sliding contact that was not taken into account in the analytic model. Different CSL geometries were meshed and the friction coefficient was computed. The results showed that thin CSLs had a friction coefficient as expected from the analytic model, thick CSLs had a lower friction coefficient than estimated. This was so because in thick CSLs the surface deformation due to the tangential loading of the sliding contact changed the CSL contact pressure distribution considerably. In thin CSLs the same deformation and related contact pressure change was small. CSLs with identical geometry and identical material model that had different sizes in relation to the cylinder/plate contact were made. The computations were found not to be sensitive to the CSL size. By computations on the same FE model, using once elastic and once elastic/plastic material models for the CSL components, the influence of plastic deformation on the global friction coefficient was studied. It was found that plastic deformation led to the rapprochement of the linear analytic estimation.

This rather simple small scale model can be useful in wear modelling. Small scale information as roughness, shape of asperities and properties of components of heterogeneous contacts can be collected before and after wear tests and used in the model presented here. If finite element wear computations are made, this model can then be applied at every contact node. The data obtained on every node in the FE computations (contact pressure, slide, ..) can then interact with the small scale model. As a result for every node individual wear rates and coefficients of friction can be computed which may lead to a more realistic and robust wear prediction.

Chapter -IV-

Ti6Al4V material modelling

IV.1 Introduction

Other authors have shown that reversed cyclic plastic deformation and ratchetting are possible modes of cyclic plastic deformation under fretting contacts. Cyclic plastic deformation can be accounted for with von Mises material models with kinematic and isotropic hardening. But it has been found that ratchetting is difficult to take into account in initially isotropic J_2 constitutive equations. Work done by J.L. Chaboche and D. Nouailhas and D. McDowell (Chaboche and Nouailhas, 1989a; Chaboche and Nouailhas, 1989b; McDowell, 1995) has shown that kinematic hardening over-predicts the accumulated plastic strain in ratchetting but that the results can be improved by superposing several kinematic hardening components with fast strain response while lowering the initial yield radius. The authors showed that this approach which needs many coefficients can be seen as the exponential series expansion of a simple power law given by an endochronic approach (Valanis, 1980). This facilitates the identification of the parameters which can be achieved in two consecutive steps. At first the parameters of the endochronic power law are identified from experimental data. Then an initial yield radius and the parameters of the kinematic hardening components are obtained by a fit of this power law. By this method refined constitutive models of stainless steel and nickel base alloys have been made and it can be assumed that it applies to other metallic alloys as well. In this work we compare the plastic response of two von Mises material model identification methods. The first "traditional" identification method uses a high initial yield radius. The second "multikinematic" method uses a low initial yield radius compensated by kinematic hardening as proposed by J.L. Chaboche and should be more appropriate for the description of ratchetting.

If fatigue tests under imposed strain are performed, a related second order phenomenon – mean stress relaxation – can be observed. The titanium alloy Ti6Al4V shows mean stress relaxation where the mean stress converges to a non-zero value. This can not be taken into account by the J_2 material models we propose here as nonlinear kinematic hardening features a total mean stress relaxation while linear kinematic hardening features none. This could be represented by a special version of kinematic hardening using a threshold (Chaboche, 1991). An identification of such a type of model has now been made in the framework of a recent research project with SNECMA (Chaboche et al.,). Since the material parameters were not available at the time of this study, we did not try this type of modelling. We used a polycrystal plasticity model instead.

Morrissey et al. have developed a crystal plasticity material model of Ti6Al4V formulated in 2D with 3 slip systems in the α grains and 1 slip system for the lamellar α - β zones of the microstructure. The construction of a 3D crystal plasticity model would have some additional advantages. Crystallographic texture has a prominent effect on the mechanical behaviour of Ti6Al4V. On one hand, there is macroscopic texture which depends on the heat treatment and forming process (Ari-Gur and Semiatin, 1998). On the other hand it has been observed that microscopic textures exist, which means that colonies of several α -phase grains can have almost the same orientation and form "super-grains" (Guerrier, 2000). To take these effects into account a 3D model of the microstructure is needed and all relevant slip systems should be captured.

Some authors have worked on the identification of the active slip systems in Ti6Al4V and their relative critical resolved shear stress (CRSS) (Philippe et al., 1995; Fundenberger et al., 1997; Perilla and Sevillano, 1995). Only the α -phase of the two phase alloy is regarded in their modelling approaches. A consensus among the authors exists on the type of slip encountered during plastic deformation of Ti6Al4V. Disagreement is there about the relative CRSS among the slip families as very diverging values can be found in literature. This may be caused by differences in the alloy purity since interstitial oxygen changes the activity of the slip systems. Additionally heat treatment and forming history may play a role. But an important factor is certainly the mechanical model which is used for the CRSS identification. Most authors used a Taylor (uniform strain assumption) or a Sachs (uniform stress assumption) model. Today more advanced methods as FE computations using crystal plasticity material models are available.

In this work the aim is the construction of a 3D polycrystal plasticity model of Ti6Al4V. The slip systems reported in the literature will be used. The relative CRSS found in literature will be re-evaluated FE as a homogenisation model. The crystallographic macro texture of the material employed for fatigue testing will be introduced to the model. The model will be apt for the description of cyclic plasticity including ratchetting and mean stress relaxation. The necessary material model parameters will be identified from standard fatigue tests under imposed strain.

IV.2 Von Mises material model

The constitutive equations used in this work are built by the superposition of different hardening rules in a viscoplastic framework. The model includes a yield surface that is found by a von Mises criterion, the change of the yield surface is governed by the internal hardening variables. The constitutive equations are formulated in small deformations. The general thermodynamic framework is described in (Besson et al., 2001; Chaboche and Lemaitre, 2001). This initially isotropic material model allows the description of the cyclic behaviour of Ti6Al4V in a phenomenologic way by the identification of the model parameters from material testing data.

All equations can be found in Table IV.1. In the viscoplastic framework, the actual stress is allowed to surpass the yield surface. Then the viscoplastic potential (Ω) depends on the distance between the yield surface and the current stress (which means overstress). The overstress gives rise to a plastic strain whereby overstress and plastic strain rate ($\dot{\xi}^p$) are linked by a power law with the parameters K and n. The initial yield radius is given by the parameter R_0 . The kinematic hardening corresponds to the translation of the center of the yield surface in the deviatoric stress space. It describes the fast stress-strain evolution in an individual cycle. The parameters C^{kin} give the initial kinematic hardening modulus and D^{kin} determine the nonlinear behaviour. Several non-linear kinematic variables (X_k) can

| | |
|--------------------------------|--|
| Viscoplastic potential | $\Omega = \frac{K}{n+1} \left\langle \frac{J(\underline{\boldsymbol{\sigma}} - \underline{\boldsymbol{X}}) - R - R_0}{K} \right\rangle^{n+1}$ $J(\underline{\boldsymbol{\sigma}} - \underline{\boldsymbol{X}}) = \left[\frac{3}{2} (\sigma'_{ij} - X'_{ij})(\sigma'_{ij} - X'_{ij}) \right]^{1/2}$ |
| Viscoplastic flow rate | $\dot{\underline{\boldsymbol{\varepsilon}}}^p = \frac{3}{2} \left\langle \frac{J(\underline{\boldsymbol{\sigma}} - \underline{\boldsymbol{X}}) - R - R_0}{K} \right\rangle^n \frac{\underline{\boldsymbol{\sigma}}' - \underline{\boldsymbol{X}}'}{J(\underline{\boldsymbol{\sigma}} - \underline{\boldsymbol{X}})}$ |
| Non-linear kinematic hardening | $\underline{\boldsymbol{X}} = \sum_k \underline{\boldsymbol{X}}_k$ $\dot{\underline{\boldsymbol{X}}}_k = \frac{2}{3} C_k^{\text{kin}} \dot{\underline{\boldsymbol{\varepsilon}}}^p - D_i^{\text{kin}} \underline{\boldsymbol{X}}_i \dot{p}$ |
| Isotropic hardening | $\dot{R} = b(Q - R)\dot{p}; \quad \dot{p} = \left[\frac{2}{3} \dot{\underline{\boldsymbol{\varepsilon}}}^p_{ij} \dot{\underline{\boldsymbol{\varepsilon}}}^p_{ij} \right]^{1/2}$ |

Table IV.1 : Set of constitutive equations for cyclic viscoplasticity

| model | Q | b | K | n | R ₀ | C ₁ ^{kin} | D ₁ ^{kin} | C ₂ ^{kin} | D ₂ ^{kin} | C ₃ ^{kin} | D ₃ ^{kin} |
|----------------|------|---|-----|------|----------------|-------------------------------|-------------------------------|-------------------------------|-------------------------------|-------------------------------|-------------------------------|
| conventional | -240 | 9 | 251 | 7.41 | 800 | 105000 | 300 | - | - | - | - |
| multikinematic | -240 | 9 | 251 | 7.41 | 300 | 105000 | 300 | 250000 | 1000 | 750000 | 3000 |

Table IV.2 : List of material constants for both sets of constitutive equations of Ti6Al4V

be used in one material model. The isotropic hardening describes the slow evolution of the yield surface from one cycle to another. Its evolution changes the yield radius. The isotropic hardening variable starts with zero and tends to Q with the accumulation of plastic strain (p) in a nonlinear way governed by the parameter b .

The constitutive equations are applied in two variations. The material constants are given in Table IV.2. The first set of material parameters has been identified with cyclic tests under deformation control in the conditions $R_\varepsilon = 0$ and $R_\varepsilon = -1$. We call it the "conventional" identification method because its initial yield radius R_0 is as high as can be expected from cyclic and tensile tests that we dispose of. While the "conventional" identification method is suitable for the modelling of cyclic plasticity it has been found that it is poor in the description of ratchetting. Earlier work (Chaboche and Nouailhas, 1989a) has shown that ratchetting effects can be covered by abating the initial yield radius and fitting the elastic-plastic transition with kinematic hardening components. For this identification method the material tests of which we dispose can be used. Additionally ratchetting tests, which were not available for this computational study, are required. So we decided to follow the identification method in a qualitative manner, abated the initial yield radius by 500 MPa and compensated the difference by two components of kinematic hardening. The purpose of this set of material parameters is to show the ratchetting influence in fretting contacts. It is called "multikinematic" in this work. The material model exhibits the same behaviour under common monotonic and cyclic loading conditions with both sets of parameters. In ratchetting tests only the multikinematic version gives a realistic description of the material response (Chaboche and Nouailhas, 1989b). The elastic constants of Ti6Al4V are $E = 119\text{GPa}$ and $\nu = 0.29$.

IV.3 Polycrystal plasticity model

IV.3.1 FE model of the Ti6Al4V microstructure

The Ti6Al4V titanium alloy consists of a hexagonal α -phase and a cubic-centered β -phase. It has a duplex microstructure with equiaxed α -phase nodules with a size of $30 \mu\text{m}$ and stacks of α/β lamella. The β -phase does not exceed 8% volume fraction in this alloy (Combres and Champin, 1991). In the microstructural model the β -phase is neglected and only equiaxed α -phase grains are present. Volumes containing many grains are represented in a finite elements model. This is done by constructing 3D meshes using quadratic full integration elements. Grains are defined as groups on integration points. The grain shape is found using a Voronoi polyhedra model which provides planar boundaries separating grains and by which the process of isotropic growth of grains from random seeds is reproduced (Decker and Jeulin, 2000; Barbe et al., 2001). The crystallographic orientation of each grain is defined by three Euler angles. Non-textured grain orientations can be found by an algorithm using a fully random process. Heterogeneous textures can be generated by adding preferential grain orientations (by means of a vector) to the algorithm. Each vector is equipped with an angle of tolerance (20 degrees) and an intensity in "multiple random units" (MRU). A preferential orientation with MRU=10 means that the probability of a grain to have an orientation within 20 degrees of the preferential orientation is 10 times higher than if just a fully random process were used. To each grain a crystal plasticity material model respecting the hexagonal lattice and the crystallographic orientation is applied.

IV.3.2 Constitutive equations for single crystal plasticity

In the finite element code ZeBuLon a crystal plasticity model is available (Méric and Cailletaud, 1991). Since twinning is almost inexistent in Ti6Al4V (Philippe et al., 1995) it is assumed that slip is the only deformation mechanism. The resolved shear stress which is found with the Schmid law is used as criterion for inelastic material flow. In order to avoid problems related with the determination of the active slip systems a viscoplastic framework is chosen. A threshold is introduced both in positive and negative direction on each slip system. The hexagonal α -phase is modelled with three prismatic ($\{10\bar{1}0\}$, $\langle 11\bar{2}0 \rangle$) slip systems, three basal ($\{0001\}$, $\langle 11\bar{2}0 \rangle$) slip systems and 12 pyramidal $\langle a+c \rangle$ ($\{10\bar{1}1\}$, $\langle 11\bar{2}3 \rangle$) slip systems. Two hardening variables are defined for each slip system. The isotropic hardening r^s describes an expansion, the kinematic hardening x^s the translation of the elastic domain. A system will be active when its resolved shear stress τ^s is greater than $x^s + r^s$ or less than $x^s - r^s$. The state variables used to describe the evolution of r^s and x^s are the accumulated slip γ_{cum}^s for isotropic hardening and α^s for kinematic hardening. Knowing the stress tensor $\underline{\sigma}^g$ applied to the grain g, the resolved shear stress can be classically written according to (IV.1), \vec{n}^s and \vec{m}^s being respectively the normal to the slip plane and the slip direction of the slip system. The hardening variables can then be expressed as a function of γ_{cum}^s and α^s following (IV.2) and their actual values allow to compute the viscoplastic slip rate $\dot{\gamma}^s$, the viscoplastic strain rate tensor $\underline{\dot{\epsilon}}^g$ (IV.3) and the hardening rules (IV.4,IV.5). The present formulation gives a saturation of the hardening in both monotonic and cyclic loading and takes into account the interaction between slip systems through the matrix h_{rs} as described in (Kocks and Brown, 1966). Nine material-dependent coefficients are involved in the model (E, ν , K, n, c, d, R_0 , Q, b). Due to the saturation of the hardening and the presence of kinematic hardening, the present model is valid for the simulation of cyclic loadings.

$$\tau^s = \underline{\sigma}^g : \underline{\mathfrak{m}}^s = \frac{1}{2} \underline{\sigma}^g : (\vec{n}^s \otimes \vec{m}^s + \vec{m}^s \otimes \vec{n}^s) \quad (\text{IV.1})$$

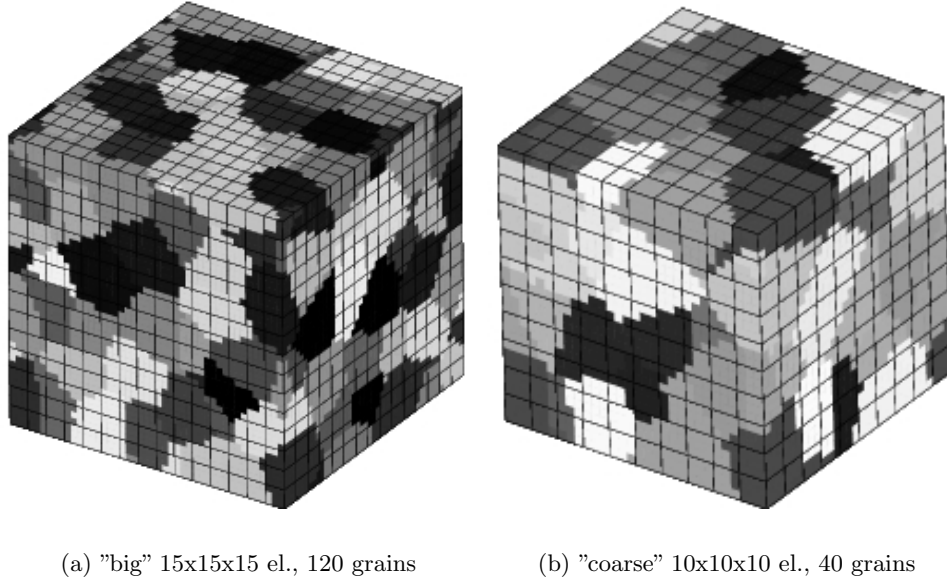


Figure IV.1 : FE meshes (regular, quadratic elements) of aggregates of grains.

$$x^s = c\alpha^s; r^s = R_0 + Q \sum_r h_{rs} \{1 - e^{-b\gamma_{cum}^r}\} \quad (\text{IV.2})$$

$$\dot{\gamma}^s = \dot{\gamma}_{cum}^s \text{sign}(\tau^s - x^s); \dot{\xi}^g = \sum_s \mathbf{m}^s \dot{\gamma}^s \quad (\text{IV.3})$$

$$\dot{\gamma}_{cum}^s = \left\langle \frac{|\tau^s - x^s| - r^s}{K} \right\rangle^n; \text{ with } \langle x \rangle = \text{Max}(x, 0) \text{ and } \gamma_{cum}^s(t=0) = 0 \quad (\text{IV.4})$$

$$\dot{\alpha}^s = \dot{\gamma}^s - d\alpha^s \dot{\gamma}_{cum}^s \text{ with } \alpha^s(t=0) = 0 \quad (\text{IV.5})$$

IV.3.3 Computational methods for parameter identification in polycrystal plasticity

The material parameters of the model are identified using macroscopic material tests, microstructural observations and a polycrystal plasticity model. If a FE model of the polycrystal is used, the mesh needs to contain a sufficient number of grains and integration points per grain to serve as a model of a macroscopic test specimen while it should be as small as possible to minimize the computational costs. It can be called "Elementary Representative Volume" (RVE) when it is the smallest material volume that has the same average properties as the macroscopic material. The RVE is modelled using cubes of quadratic full integration 20 node elements. Periodic Voronoi grain shapes are generated and periodic boundary conditions are applied. FE models with two different sizes are used (see Fig. IV.1). The coarse one contains 10x10x10 elements and 40 grains (675 integration points per grain), the bigger one 15x15x15 elements and 120 grains (759 integration points per grain).

Alternatively the computationally less demanding self-consistent scheme can be applied. The application in plasticity has been developed by Hill (Hill, 1965) after work done by Kröner (Kroener, 1961) who applied the Eshelby solution for the problem of an ellipsoidal inclusion in an infinite medium (Eshelby, 1957). In this work the Kröner model is used. It

| elements | $\langle \sigma_{22} \rangle$ (MPa) | prismatic (%) | basal (%) | pyramidal <a+c> (%) |
|----------|-------------------------------------|---------------|--------------|---------------------|
| 10x10x10 | 1120 ± 17 | 44 ± 3.0 | 41 ± 0.3 | 14 ± 3.0 |
| 15x15x15 | 1131 ± 5 | 44 ± 0.4 | 37 ± 1.8 | 18 ± 1.5 |

Table IV.3 : Dependence of the computation result at $\langle \varepsilon_{22}^{total} \rangle = 0.05$ on the RVE model size.

is valid for the case of a plastically deforming inclusion in an elastic infinite medium and is consequently a good approximation of the initial plastic deformation of polycrystals.

$$\underline{\sigma}^g = \underline{\sigma} + \alpha\mu(\underline{E}^p - \underline{\varepsilon}^{pg}) \quad (\text{IV.6})$$

The relation (IV.6) shows the model where $\underline{\sigma}$ and \underline{E}^p are the average stress and plastic strain tensors and $\underline{\sigma}^g$ and $\underline{\varepsilon}^{pg}$ are the stress and plastic strain tensor of a grain. From a physical point of view this means that grains with higher than average plastic deformation have a lower than average stress. μ is the shear modulus and α is equal to 1. Using this equation the older and less realistic Taylor model (uniform plastic strain) (Taylor, 1938) is approached as α reaches infinity. In this work $\alpha = 100$ is used for approximating the Taylor model.

IV.3.4 Dependence of the computation result on the RVE model size

Computations employing both FE meshes shown in Fig. IV.1 have been performed. The material parameters were $K=20 \text{ MPa} \cdot \text{s}^{1/n}$, $n=7.41$, $c=0 \text{ MPa}$, $d=0$, $Q=0 \text{ MPa}$, $b=0$ for all slip families. The elastic properties were isotropic with $E=119000 \text{ MPa}$, $\nu=0.29$ and an isotropic texture was used. A unidirectional average deformation of 10 % was applied in 10 seconds. The critical resolved shear stress (CRSS) of prismatic, basal and pyramidal <a+c> systems were 380, 400 and 640 MPa respectively. The results at $\langle \varepsilon_{22}^{total} \rangle = 0.05$ are listed in Table IV.3. Among the results on the relative amount of slip some systematic difference exists whereby the pyramidal <a+c> slip is underestimated when the coarse mesh is used. For $\langle \sigma_{22} \rangle$ the difference between the mean values is very small. The standard deviation is two to three times bigger among the computations using the coarse mesh. For computations where the relative amount of slip is searched for the bigger mesh should be used. For the computation of the average stress (for example $\langle \sigma_{22} \rangle$) a small standard deviation of only 1.5% is obtained even when the coarse mesh is employed, so this model will be used for the computation of the average stress. An important advantage of a smaller but still accurate model is that an increased number of loading cycles can be computed at lower computational costs for the identification of cyclic material properties.

IV.3.5 Identification of the relative CRSS of slip families

Critical resolved shear stresses (CRSS) for the active slip families in the α -phase of Ti6Al4V have been proposed by Fundenberger et al. (Fundenberger et al., 1997) and Perilla et al. (Perilla and Sevillano, 1995) (see Table IV.4). The estimations are based on experimental observations and a polycrystal plasticity model. Fundenberger et al. found the values using a Taylor model (uniform plastic strain), Perilla et al. used a Sachs model (uniform stress) and the scatter between their proposed values is high. Confused about this result we saw the necessity to perform computations using the same RVE, material parameters and loading conditions and changing only the polycrystal plasticity model using once the Kröner, the approximated Taylor and the FE model (small mesh). The same material parameters and

| | Prismatic | Basal | Pyramidal <a> | Pyramidal <a+c> |
|-------------------------------|-----------|-------------|---------------|-----------------|
| (Fundenberger et al., 1997) | 1 | 3–6 | 3–6 | 4–10 |
| (Perilla and Sevillano, 1995) | 1 | ≈ 1 | ≈ 1 | ≈ 1.4 |

Table IV.4 : Relative CRSS of the α -phase of Ti6Al4V found in the literature.

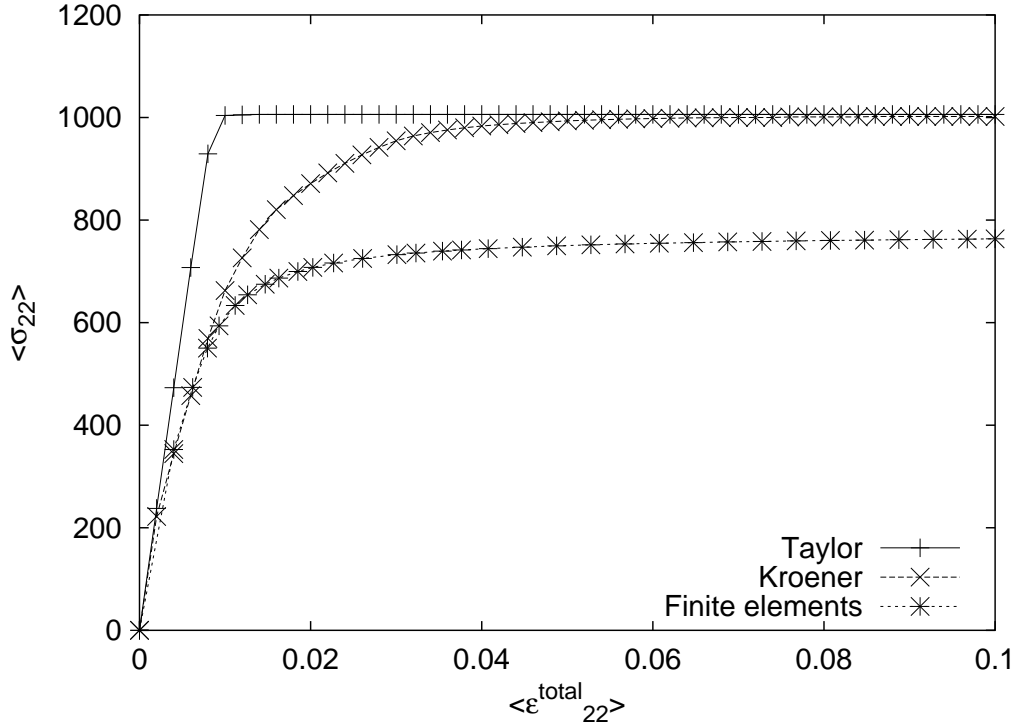


Figure IV.2 : Average strain–stress response of a RVE using the Kröner, Taylor and finite element method.

loading conditions as in section IV.3.4 were used. The CRSS of prismatic, basal and pyramidal <a+c> were $R_0 = 80, 400$ and 640 respectively as proposed by Fundenberger et al.. The resulting average $\langle \sigma_{22} \rangle - \langle \varepsilon_{22}^{total} \rangle$ curves are shown in Fig. IV.2. While a large elastic domain exists in the Taylor result, yielding starts from low stresses in the other models and the FE model predicts less hardening than the Kröner model. In Fig. IV.3 the relative amount of slip in the pyramidal <a+c> family is drawn over the average total deformation. The Kröner result indicates less pyramidal <a+c> slip than Taylor and the FE result predicts even less, the relative amount of slip changes during deformation in all but the Taylor model. The results show that different polycrystal plasticity models deliver very different results which is one reason for the big scatter between the CRSS reported in the literature. The FE model is most complete because it disposes of an explicit description of the 3D crystal morphology. In the Kröner model the crystal morphology is replaced by a linear concentration law which is valid when plastic deformations are small. The uniform plastic strain assumption makes the Taylor model the least realistic description. Finally, we recover the well known result: both models are too stiff since they demand too much deformation from the harder deformation mechanisms like the pyramidal systems.

As a consequence we decided to use the microstructural observations found in the

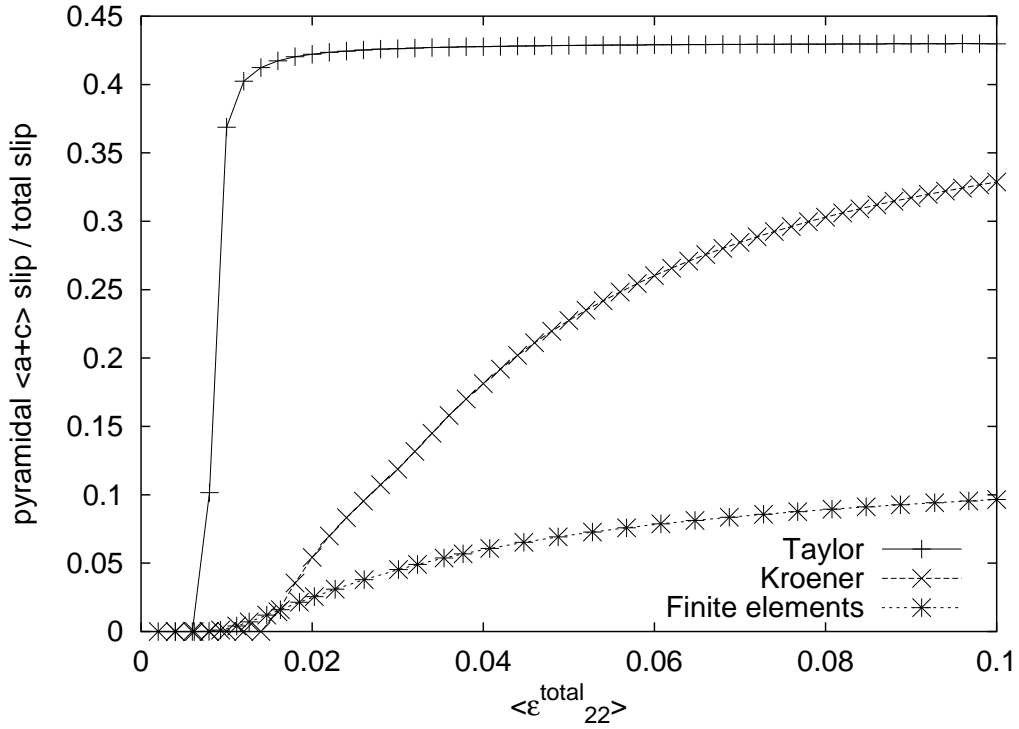


Figure IV.3 : Relative slip in the pyramidal $\langle a+c \rangle$ slip family using the Kröner, Taylor and finite element method.

literature together with a FE polycrystal model to re-identify the CRSS. Fundenberger et al. (Fundenberger et al., 1997) give data obtained from microstructural observations by Philipp et al. (Philippe et al., 1988) and Zaeferrer (Zaeferrer, 1996) who have assessed the relative activity of the slip systems in the α -phase of Ti6Al4V during deformation. The results are shown in Table IV.5, the relative activity of a slip system was obtained by summing up the activation of each system in all grains in which the system could be observed. Grains with all possible orientations were included to eliminate the effect of crystallographic texture. FE computations with 3 realisations of the non-textured grain orientations were made using the big mesh. With the same material parameters and loading conditions as mentioned before the relative CRSS were searched for whereby the activity of the slip families and a plausible shape of the $\langle \sigma_{22} \rangle - \langle \epsilon_{22}^{total} \rangle$ curve were respected. A good result was found with 1 : 1.05 : 1.68 for the relative CRSS of the prismatic, basal and pyramidal $\langle a+c \rangle$ slip families. The relative amount of slip in the 3 slip families is shown in Fig. IV.4. At $\langle \epsilon_{22}^{total} \rangle = 0.05$, 44% of the slip happens in the prismatic, 37% in the basal and 18% in the pyramidal $\langle a+c \rangle$ systems. At this instant of the computation, the pyramidal $\langle a+c \rangle$ slip in observation and model correspond closely, the prismatic slip is by 6% smaller than observed, the basal slip contributes 17% more in the model than in the observations because the basal slip is the only $\langle a \rangle$ slip family other than prismatic slip in the model. It should be compared to 30% non-prismatic $\langle a \rangle$ slip in the observations. Some incertitude comes from the fact that the slip distribution in the FE model changes during deformation while no corresponding information is provided with the observations. More prismatic slip and less basal slip would have been found with a higher CRSS for the basal systems, but then more hardening and a smaller linear elastic domain would have been obtained which is not consistent with experimental results.

| | Prismatic $\langle a \rangle$ | Basal $\langle a \rangle$ | Total $\langle a \rangle$ | Pyramidal $\langle a+c \rangle$ |
|--------------|-------------------------------|---------------------------|---------------------------|---------------------------------|
| Activity (%) | 50 | 20 | 80 | 20 |

Table IV.5 : Relative activity (in %) of each slip family in the α -phase of Ti6Al4V (Fundenberger et al., 1997).

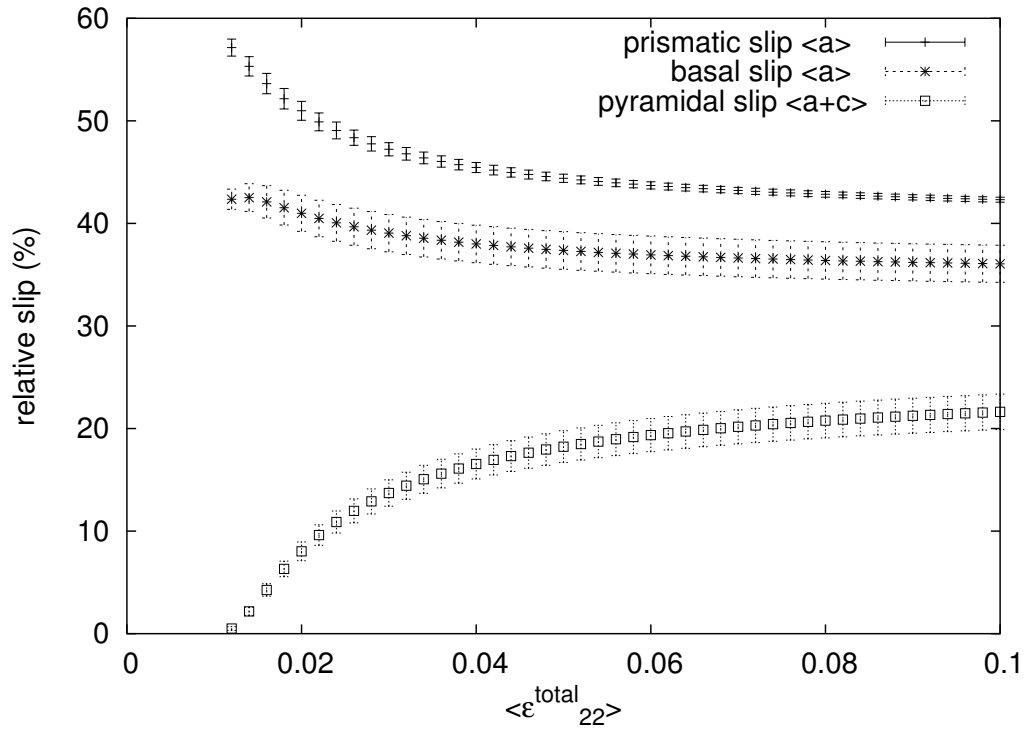


Figure IV.4 : Relative slip in the prismatic, basal and pyramidal $\langle a+c \rangle$ slip systems in FE computations with three different realisations of the grain orientations. $15 \times 15 \times 15$ element mesh.

IV.3.6 Crystallographic texture and identification of the absolute CRSS

Before the absolute CRSS can be found the crystallographic texture needs to be introduced to the model. It has been shown that texture is present on two scales in this titanium alloy (Ari-Gur and Semiatin, 1998; Guerrier, 2000). In addition to the macrotexture a microtexture, formed by the similar orientation of α -grains in big domains, exists. In this work only the macrotexture is treated. Some qualitative information about the macrotexture of the material modelled in this study has been found in (Guerrier, 2000). The main texture is made by a preferential orientation of the c -axis of the hexagonal lattice in the normal direction (ND) of the specimen whereby uniaxial tests with an imposed deformation in the "rolling direction" (RD) were made. This basal texture was reproduced in the model as described in section IV.3.1 with an intensity of MRU=10. In Fig. IV.5 the 3 texture realisations used for computations can be seen. In these direct stereographic projections the c -direction of 40 hexagonal grains is shown. The smaller FE model with these textures and the same material parameters and loading conditions as in the last section were used for computations. The identification was performed using tensile test results. The resulting CRSS are 380 : 400 : 640 MPa for the prismatic, basal and pyramidal $\langle a+c \rangle$ systems. In Fig. IV.6 the experimental

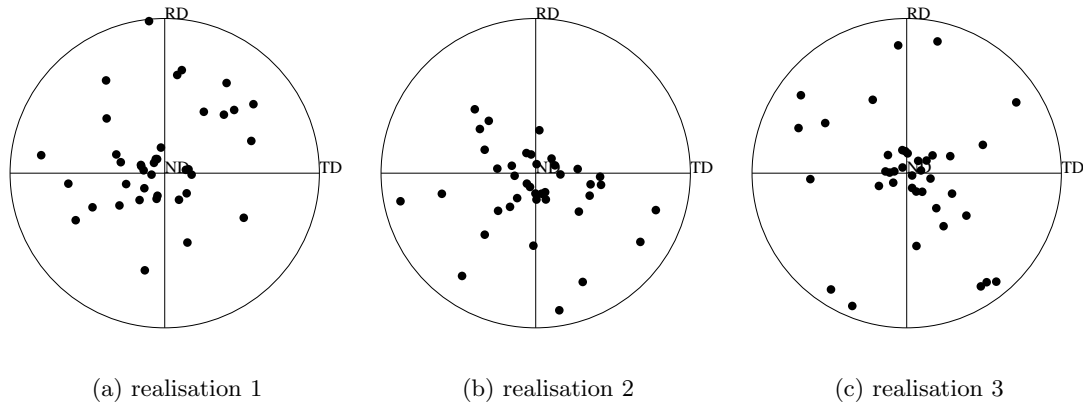


Figure IV.5 : Direct stereographic projections of the c -direction of the hexagonal lattice of 40 grains, three realisations of a basal texture.

curves and the result of computations with 3 texture realisations can be seen. The scatter among the computations is smaller than between the experiments which may be attributed to the presence of microtexture in the material that is not introduced in the model. Almost no hardening takes place in experiments while it is present in the model although the hardening parameters on the slip systems are set to zero. The hardening in the model is caused by internal stresses which are on their part due to the strong anisotropy of the hexagonal crystal behavior. Comparing this to an equivalent computation with no texture it can be seen that the basal texture reduces the hardening effect. If a perfect basal texture ($MRU=\infty$) is used, no hardening (elastic/perfectly plastic behavior) is obtained.

IV.3.7 Identification of the cyclic material parameters

The identification of the cyclic material parameters was performed with macroscopic fatigue tests with various deformation amplitudes under deformation control and the FE model with the coarse mesh, textured grain orientations and the elastic properties $E=119000$ MPa, $\nu=0.29$. In order to limit the computational costs of the identification procedure, the computations were stopped after 200 cycles. All parameters that were identified are given in Table IV.6. The viscous parameters K and n were chosen in a way that a very small strain rate dependence was obtained. For the identification of the parameters for nonlinear isotropic hardening the $R_\epsilon = -1$ tests were used. For b one value was chosen for all slip families, for Q the relative CRSS of the slip families were respected. Since Ti6Al4V exhibits cyclic softening, the values are negative. The interaction matrix h_{rs} was set to one in the diagonal and zero elsewhere, so only selfhardening and no crosshardening is present. The parameters of nonlinear kinematic hardening were found using $R_\epsilon = 0$ tests. In these tests the material shows mean stress relaxation but in contrast to many other materials the mean stress tends to a non-zero threshold. In the FE polycrystal plasticity model, kinematic hardening is obtained in the average material response even when no hardening is present in the constitutive equations of the slip systems. This "microstructural" hardening alone allowed a good description of cyclic plasticity but no mean stress relaxation was obtained in a 200 cycle computation. So the parameters of nonlinear kinematic hardening (c , d) were identified on the mean stress relaxation in the experiments. The value of d was set to make the strain hardening response of the slip systems much faster than the "microstructural" hardening. The parameters c and d were used together to fit the experimental mean stress relaxation

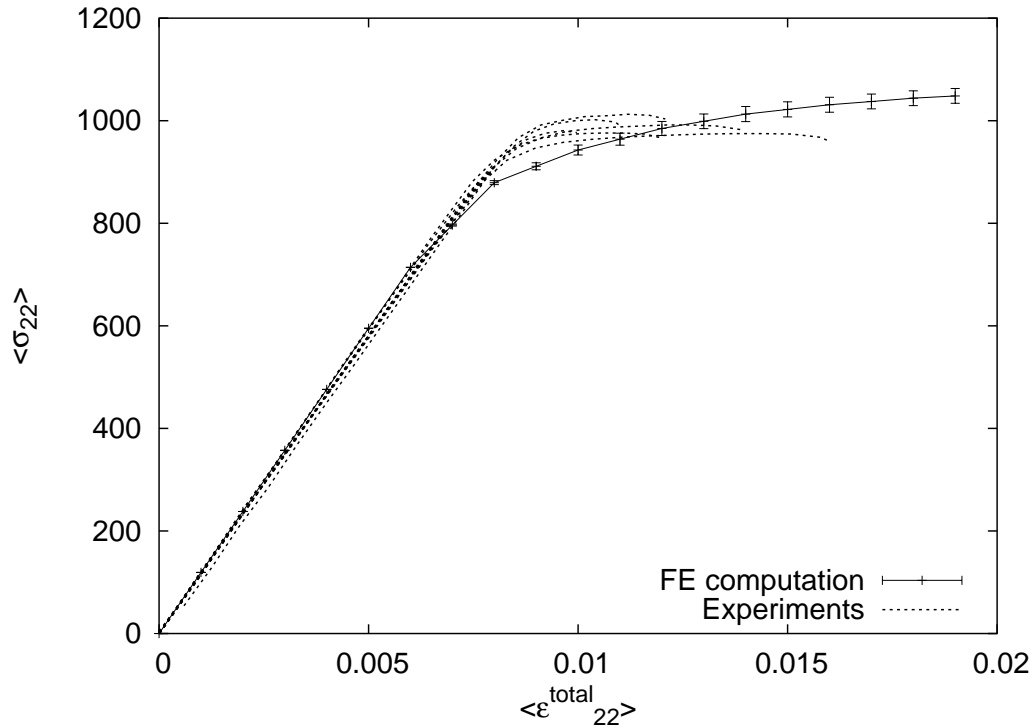


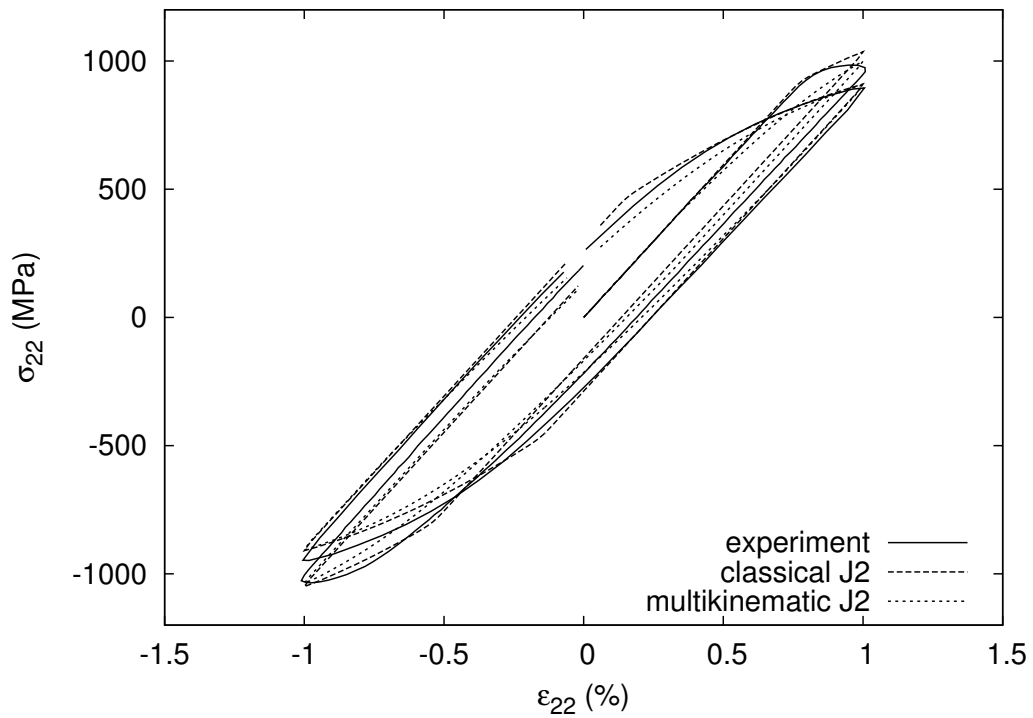
Figure IV.6 : Experimental tensile test and FE computations with the coarse mesh, 3 realisations of grain orientations with a basal texture.

after 200 cycles. One set of parameters was chosen for all slip families. The elastic limit of the cyclic model was found with $R_0^{\text{sys}} = \text{CRSS}^{\text{sys}} - c/d$, whereby c/d gives the saturation of kinematic hardening.

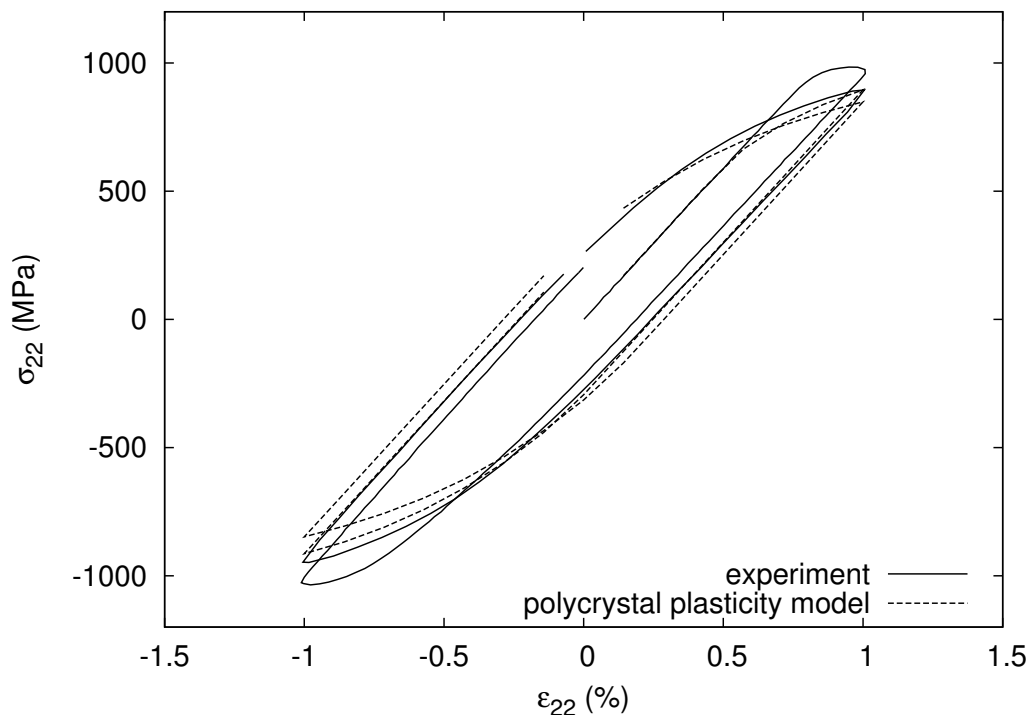
IV.4 Discussion

In Fig. IV.7 a comparison of the material models with a corresponding experiment in the $R_\varepsilon = -1$ condition with $\pm 1\%$ deformation amplitude is shown. For models and experiment the first and 50th loading cycle are displayed. Examining the first cycle, it can be seen that the classical J_2 model fits the initial elastic limit best, the multikinematic J_2 model shows significant yielding at lower stresses than observed in the experiment. The polycrystal plasticity model shows yield at lower stress too and underestimates the stress by an even bigger amount. In the 50th experimental cycle the stress amplitude has diminished. The material softening observed in the first 50 cycles of the experiment is reproduced by all models. Both von Mises models fit the experimental curve well, the polycrystal plasticity too approaches but it generally shows a softer behaviour than the other two models. In all the deviation between models and experiment is highest in the first cycle and lessens until cycle 50. The material shows an asymmetry between tension and compression yield stress that is not incorporated in any modelling approach applied in this work.

In Fig. IV.8 a comparison in the testing condition $R_\varepsilon = 0$ with 0% and 1.4% minimum and maximum strain respectively is shown. In the first cycle of this test the maximum total deformation is higher than in the test discussed before and it can be seen that the von Mises models overstate hardening at high plastic deformation amplitudes. The polycrystal plasticity

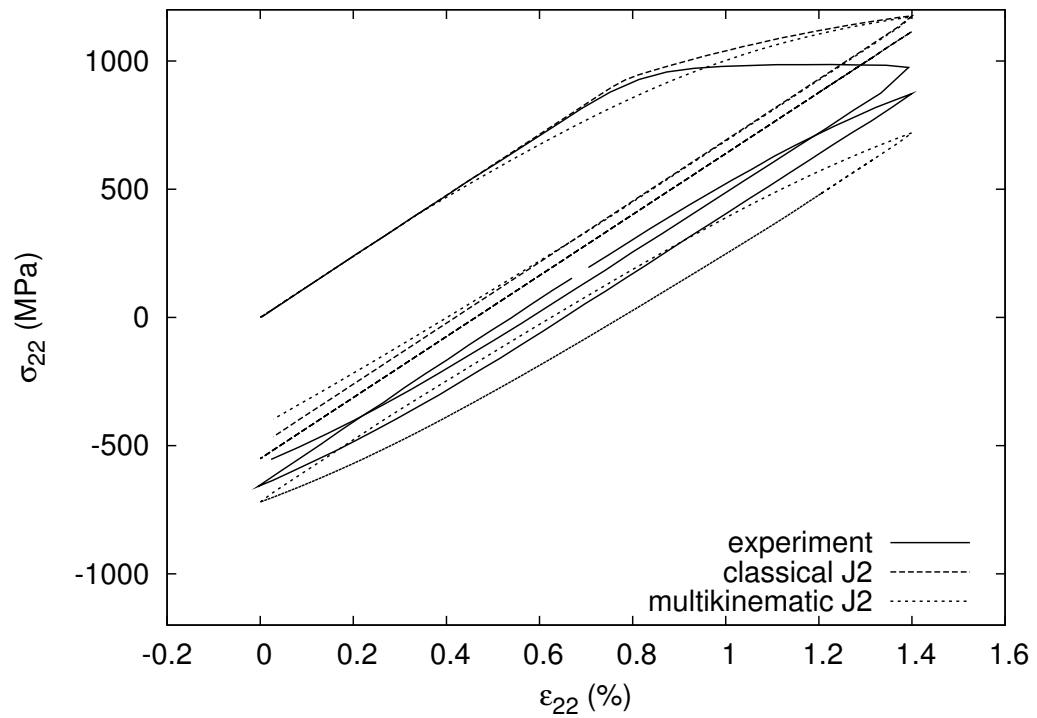


(a) Von Mises material models

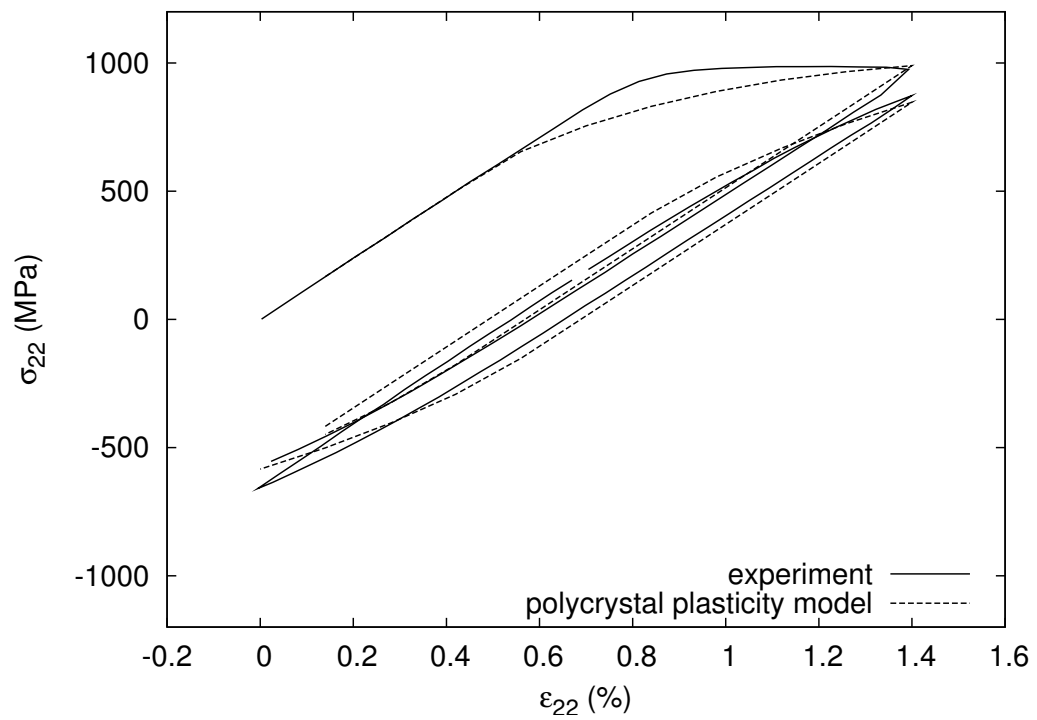


(b) Polycrystal plasticity material model

Figure IV.7 : Cyclic test in the $R_\epsilon = -1$ condition: experiment and material models, first and 50th cycle.



(a) Von Mises material models



(b) Polycrystal plasticity material model

Figure IV.8 : Cyclic test in the $R_\epsilon = 0$ condition: experiment and material models, first and 200th cycle.

| parameter | prismatic | basal | pyramidal <a+c> |
|----------------|---------------------------|---------|-----------------|
| K | 20 MPa · s ^{1/n} | | |
| n | 7.41 | | |
| R ₀ | 280 MPa | 300 MPa | 540 MPa |
| Q | -49 MPa | -52 MPa | -83 MPa |
| b | 2 | | |
| c | 30000 MPa | | |
| d | 300 | | |

Table IV.6 : Parameters of the crystal plasticity material model.

model features a lower elastic limit than observed in the experiment. It underestimates the material resistance until $\varepsilon_{22}^{total} = 1.4\%$. At higher total strains the material resistance in the first cycle would be overestimated. In the 200th cycle the experiment shows a decreased mean stress which is found with $\sigma_{mean} = (\sigma_{max}^{22} + \sigma_{min}^{22})/2$. It is a special property of the Ti6Al4V titanium alloy that mean stress relaxation takes place at the beginning of such tests but does not continue until the mean stress becomes zero. It stops at a significant non-zero value. Using the von Mises material models, this means that stress relaxation cannot be correctly described. In the classical J_2 material model, mean stress relaxation is lower than in the experiment because plastic deformation after the first cycle is very tiny. But as only nonlinear kinematic hardening is used the mean stress falls to zero if a sufficiently high number of cycles is computed. In the multikinematic material model the decrease of the mean stress is overstated. This is so because the low initial yield surface allows the accumulation of more plastic deformation which causes softening through the isotropic hardening equation. In this test the polycrystal plasticity model allows a more faithful description of the experimental result. The maximum and minimum stress in the polycrystal plasticity model and experiment correspond closely; only the amount of cyclic plasticity is somewhat overstated in the model. A closer look at the mean stress relaxation in polycrystal plasticity computations is now taken. In Fig. IV.9 the mean stress in the first and 200th cycle is plotted over the maximum deformation in some $R_\varepsilon = 0$ tests. In this graph, the points at $\varepsilon_{22}^{max} = 1.4\%$ belong to the particular test shown before. Comparing polycrystal plasticity model and experiment in the first cycle the biggest difference is observed at small strain amplitudes where plastic deformation is overstated in the model. At higher strain amplitudes the mean stress corresponds more closely. In the 200th cycle the deviation between experiment and model is reduced.

IV.5 Conclusion

The character of all models, their advantages and inconveniences may be sketched as follows.

- The classical von Mises material model is most frequently applied in industry. It describes well first order effects in cyclic plastic deformation as strain hardening and cyclic material softening. Its limits lie in the description of second order effects as strain ratchetting in force control fatigue tests or mean stress relaxation under displacement control.
- The multikinematic von Mises material model attempts to add ratchetting to the before mentioned description capabilities. The parameters of the additional kinematic

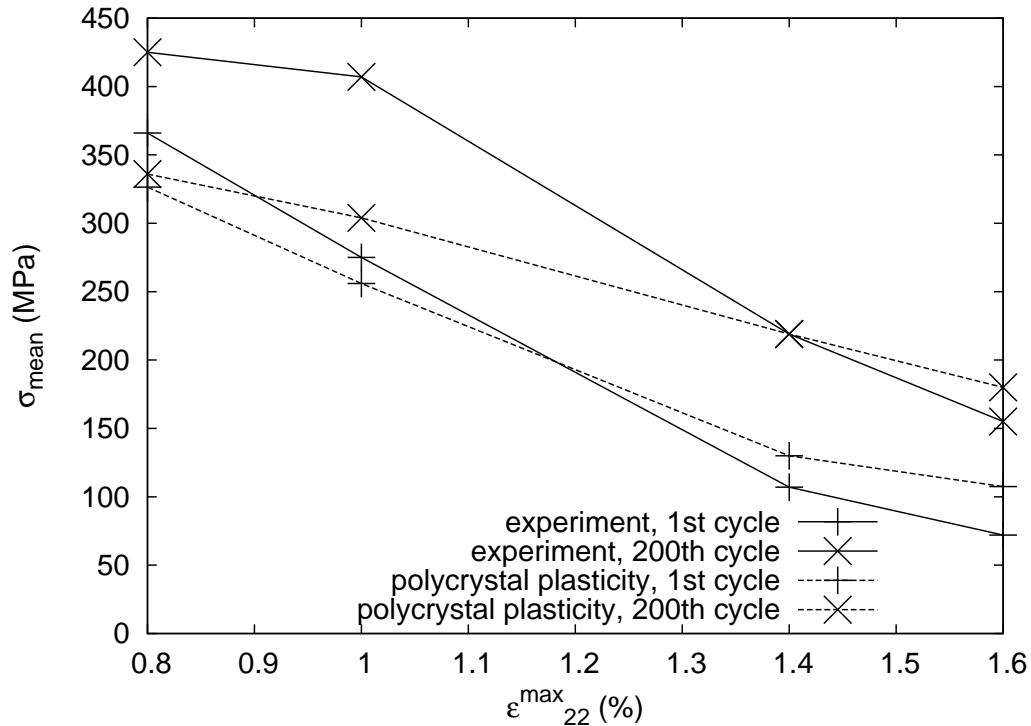


Figure IV.9 : Mean stress in the polycrystal plasticity model and in experiments, first and 200th cycle, in $R_\epsilon = 0$ tests.

hardening equations need to be identified from ratchetting tests. This has not been done in this work, so the multikinematic material model presented here is of qualitative nature. It will be applied in following chapters to show the possible effect of strain ratchetting in fretting contacts.

- The polycrystal plasticity material model allows a good description of the microstructural and the cyclic macroscopic behaviour at the same time. First order effects (cyclic softening and strain hardening) and second order effects as ratchetting and mean stress relaxation of Ti6Al4V can be modelled at once. The main difference between experiments and the model is caused by the initial plastic strain. In the experiments almost no hardening is observed in the first quarter cycle. In the model hardening is inevitable because it is mainly caused by internal stresses which are on their part due to the strong anisotropy of the hexagonal crystal behaviour. On one hand this hardening may be reduced by changing the CRSS of the slip families. But this would contradict the microstructural identification process which was performed using experimental data on the relative activity of the slip systems. On the other hand a very strong basal texture would cause the same effect, but this too compromises the model relevance to the micro scale behaviour of Ti6Al4V. A second issue is the fact that a comparatively small number of 200 loading cycles was used for cyclic material parameter identification. This is due to the high computational cost of the necessary FE computations. The computation of 200 cycles using the coarse mesh takes about one week on a Pentium PC (2GHz) and many computations are necessary for the parameter identification. Other homogenisation methods as that of Kröner would be computationally less demanding, but they deteriorate the correctness of the result as

has been shown in section [IV.3.5](#).

Chapter -V-

Fretting wear modelling

V.1 The wear activation period in a fretting wear test

V.1.1 Introduction

Previous experimental studies have shown that wear in fretting tests can be predicted by an energy approach (Fouvry et al., 2003). Sauger et al. showed that this approach is only valid after an initial wear activation period (Sauger et al., 2000). In fretting wear tests with 1000 fretting cycles he observed that the activation of the wear mechanisms is closely linked to the development of a layer called Tribologically Transformed Structure (TTS). He remarked that the TTS grows during the activation of the wear mechanisms and has a constant thickness when wear is established.

In this study we point out the mechanisms that act during the first hundreds of cycles before the activation of wear. Fretting experiments with up to 2000 cycles are performed by Christophe Paulin at LTDS/ECL. The tests are performed with the titanium alloy Ti6Al4V. In a cooperative work we try to relate the damage and geometry change in the specimen contact to the results of FE computations. Particular material aspects as adhesion phenomena, commonly encountered with such materials, or strong deformation caused by sliding wear are taken into account.

V.1.2 Experimental procedure

Fretting wear tests were carried out at the LTDS/ECL using a tension compression MTS hydraulic machine. The tests were performed with Ti6Al4V cylinders and plates with the elastic properties mentioned in section IV.2. A schema of the experimental setup is shown in Fig. V.1.2. The setup has been developed at the LTDS in a way that the normal force P remains constant while a tangential displacement is imposed during the test. The setup allows the measurement of the tangential displacement δ and the tangential force Q during testing, so fretting logs as shown in Fig. II.3(c) can be recorded. The shown fretting log with a nearly rectangular shape is typical for fretting tests in the total sliding condition. The hysteresis of the fretting log corresponds to the dissipated energy E_d whereas the residual opening (i.e. the residual displacement when $Q = 0$) is related to the full sliding amplitude δ_0 .

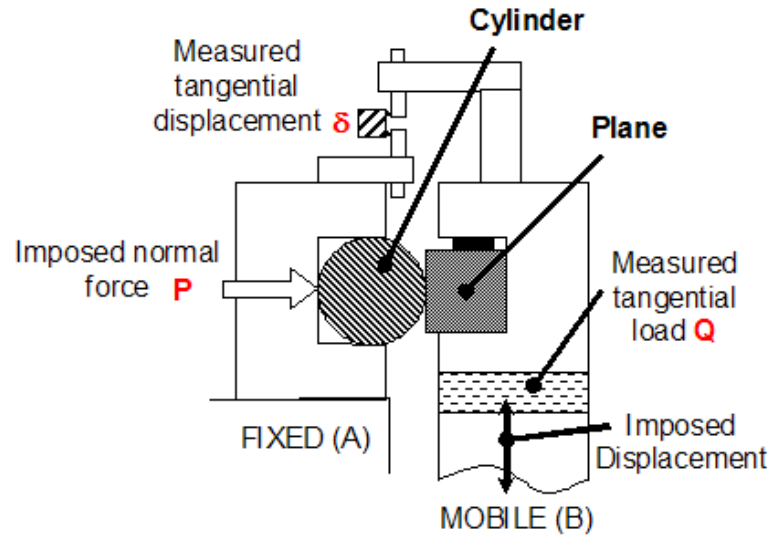


Figure V.1 : Schema of the fretting experiment and the measured data (LTDS/ECL). A normal load is applied to the contact, then a tangential displacement is applied. Tangential force Q and displacement δ are measured and visualised in fretting logs (Fig. II.3(c)).

The fretting tests were performed with a cylinder on plate contact pair. The cylinder had a radius of 10 mm, the length of the cylinder/plate contact line was 4 mm. A normal load of 133 N/mm and a tangential displacement with a frequency of 5 Hz and an amplitude of 75 μm were applied. With the imposed normal load a Hertzian maximum contact pressure and contact half length of 524 MPa and 161 μm respectively are obtained. The tests were performed at room temperature and a relative humidity of 40% to 50%. The specimen roughness was $R_a = 0.1 \mu\text{m}$. Prior to testing all specimens were cleaned with acetone and ethanol. 100 to 2000 fretting cycles were performed. The tests were stopped in two different ways. Once the displacement was stopped abruptly after the last fretting cycle and once the displacement amplitude was reduced to zero during several cycles. After testing the specimens were analysed by SEM and 2D profilometry.

V.1.3 FE mesh and boundary conditions

A fretting wear test is represented in a FE computation using the code ZeBuLon. It has been proved sufficient to take the half cylinder and the plate into account (Fig.V.2). These contacting bodies, both made of Ti6Al4V, are represented by one set of constitutive equations. Computations with J_2 viscoplasticity with both the conventional and multikinematic identification method (see section IV.2) are made. Linear plane strain elements are used. Remote from the contact zone free domain meshes with 3-node triangular elements are used. In order to combine a high precision with reasonable computation times, the mesh is gradually refined towards the contact. The proximity of the contact zone is meshed with regular domains of rectangular 4-node elements with a size of 2 μm by 1.8 μm . The contact is modelled with an impactor/target technique, the frictional contact force is introduced by the Coulomb law with a constant isotropic coefficient of friction of 0.8.

In the fretting wear test the loading is applied under displacement control. So the boundary conditions in the FE model are defined in terms of imposed displacements. The loading is done in two steps. The locations where the boundary conditions are applied are marked with thick lines in the mesh. At first a vertical displacement (u_2) is imposed at the

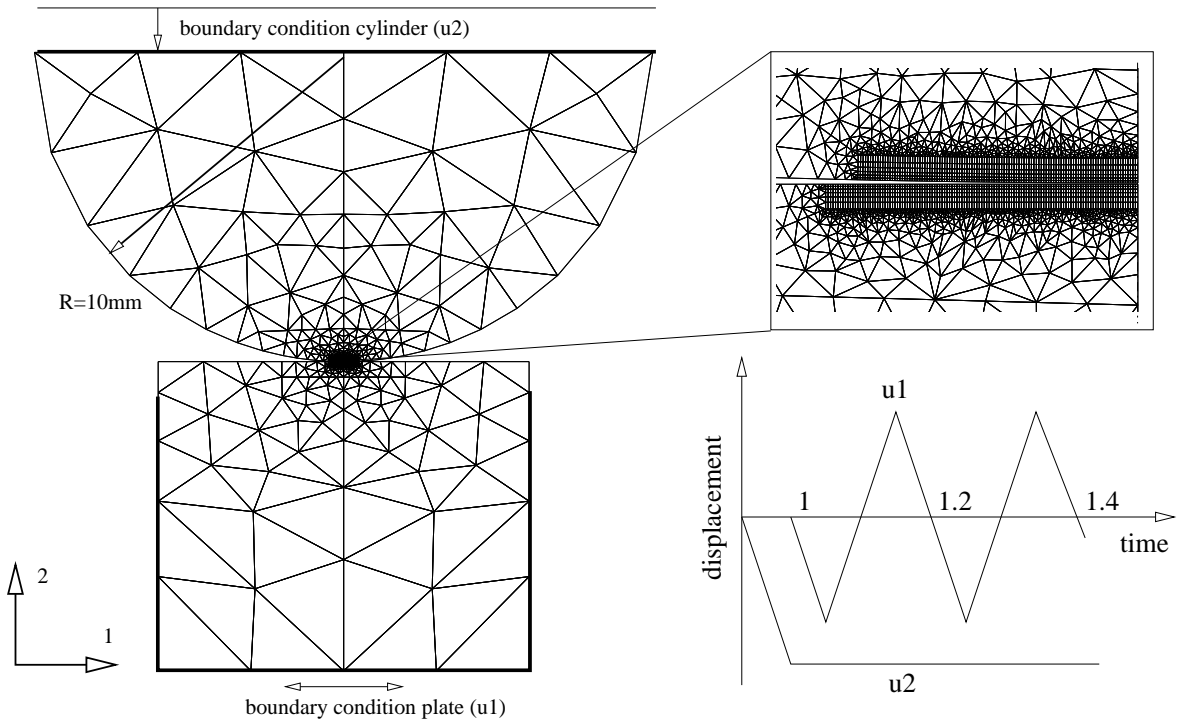


Figure V.2 : FE model: mesh and boundary conditions. The spots in the mesh where the boundary conditions are applied are marked with thick lines. A zoom of the left half of the contact zone is given.

top of the half cylinder while the plate is fixed by locking its bottom and side nodes. The displacement (u_2) causes a vertical force (P) of 147 N/mm. The force (P) is obtained as the sum of the vertical node reactions of the cylinder top. Then the cyclic loading is started. The cylinder is fixed by locking the top nodes. The plate performs an oscillating horizontal movement (u_1) with a triangular time-displacement curve. This movement is imposed on the bottom and side nodes of the plate with an amplitude of $\delta^* = 75 \mu\text{m}$ and a frequency of 5 Hz, the horizontal reaction force (Q) is obtained as the sum of the horizontal reactions of the same nodes. These loading conditions cause fretting in the total sliding regime.

This model was validated by a comparison with the analytic Hertz solution which gives a maximum contact pressure of 551 MPa and a contact half length of 170 μm . The contact pressure in the FE model is 564 MPa, the contact half length is 168 μm . For our purposes the deviation between analytic and FE result, which decreases with increasing mesh refinement seems to be a good tradeoff between a lower computation time and a higher accuracy.

V.1.4 Results and discussion

The fretting log which changes during the experiment, can be seen in Fig. V.3. In the first fretting cycle an almost perfect rectangular loop is obtained and the tangential force is constant during total sliding. After 100 cycles the loop has changed in a way that a sharp peak of the tangential force can be observed at the displacement amplitude. After subsequent inversion of the displacement direction the tangential force is again constant until the next amplitude is reached. During the 1000th cycle a linear increase of the tangential force during sliding from one displacement amplitude to the other can be observed.

By SEM the topography of the fretting surfaces was analysed. At the beginning of the fretting experiment the contacting surfaces were smooth with no notable features. After 100

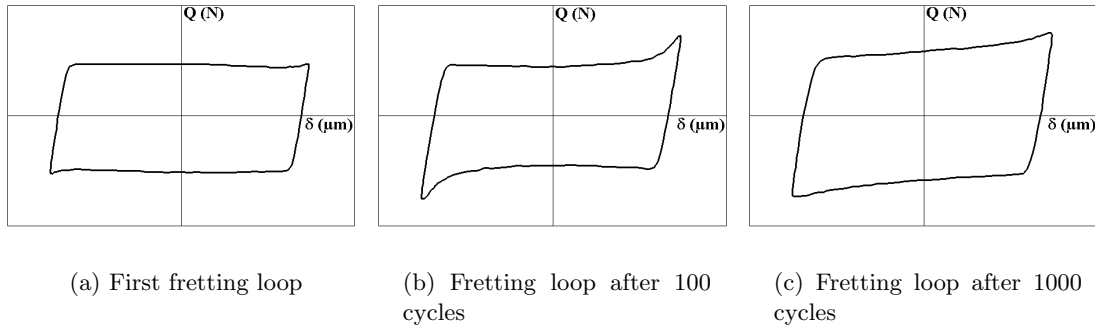
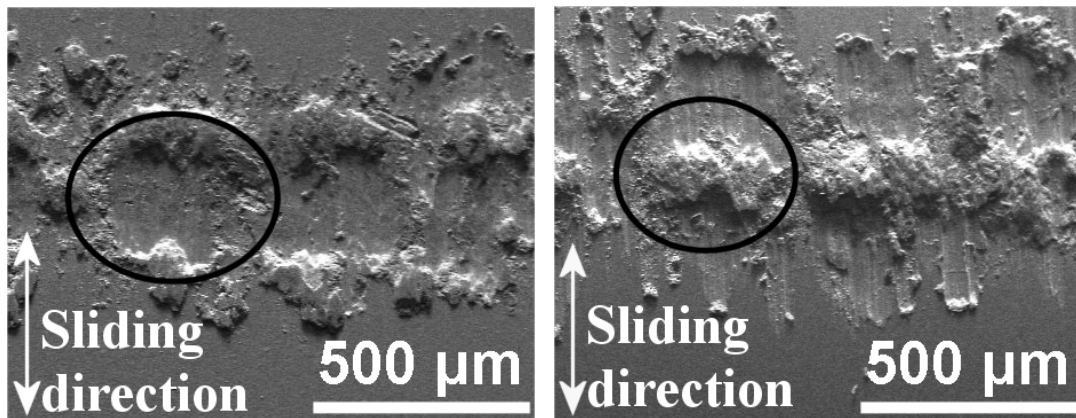


Figure V.3 : Evolution of the fretting log during 1000 fretting cycles in a fretting wear test. Normal force 133 N/mm, displacement amplitude 75 μm . Work by Christophe Paulin, LTDS/ECL.

cycles geometric features had developed. In Fig. V.4 the surfaces of plate and cylinder at the same contact spot are shown, whereby one SE-image is horizontally mirror-inverted so that the contact can be reproduced by laying one picture over the other. This experiment was stopped abruptly after 100 cycles. It can be observed that if the plate features an asperity at a contact spot, a hole will be found at the same spot of the cylinder. By 2D profilometry it was measured that the asperities had a height of 5 μm to 10 μm . Figure V.5 shows the contact surface of the plate after 100 fretting cycles whereby the experiment was stopped by reducing the displacement amplitude to zero during some additional cycles. From the SE micrograph of the same contact spot on the cylinder one asperity was cut out and its contour pasted in dark colour to the corresponding location in the shown picture. In the sliding direction the hole on the plate surface is by about 140 μm larger than the asperity on the cylinder. In the fields between asperities on cylinder and plate parallel lines perpendicular to the sliding direction can be seen. These mark the decreasing amplitude of the relative movement of the asperity on the cylinder surface and the hole in the plate surface. While the displacement amplitude is decreasing fretting logs with no peaks of the tangential force were measured. The SE micrographs of all samples with more than 500 fretting cycles showed rough fretting scars and debris formation, no clear correlation of geometric features on cylinder and plate surfaces could be made.

In the FE model the initial geometry of the samples was well respected. A difference comes from the ideal smoothness of the surfaces in the model while some roughness exists in the real surfaces. The applied loading in experiment and model differed by a small amount which we judge negligible. The applied material models allowed an accurate description of cyclic material tests performed with Ti6Al4V. Computations using the conventional material model indicated no plastic deformation at all, so the contact geometry remained unchanged. Using the multikinematic material model strain ratchetting and cyclic plasticity were obtained which caused geometry change, stress redistribution and the formation of residual stress fields. In section VI.2 these results are shown in detail. But the maximum equivalent deformation did not exceed one percent in 100 fretting cycles. The fretting logs obtained from computations showed a constant ratio of tangential and normal force in total sliding, which was equal to the imposed friction coefficient of 0.8, irrespective of the applied material model.

Comparing computations to experiments it needs to be stated that the model is unable to describe the rapid change of the surface morphology and debris formation and the associated change of the fretting log. We suppose that it is the contact description that limits our approach. On one hand our model contained a constant friction coefficient which is a



(a) SE micrograph of the plate contact surface

(b) SE micrograph of the cylinder contact surface

Figure V.4 : SE micrographs of cylinder and plate contact surfaces at the same contact spot after 100 fretting cycles. One micrograph is horizontally mirror-inverted. Work by Christophe Paulin, LTDS/ECL.

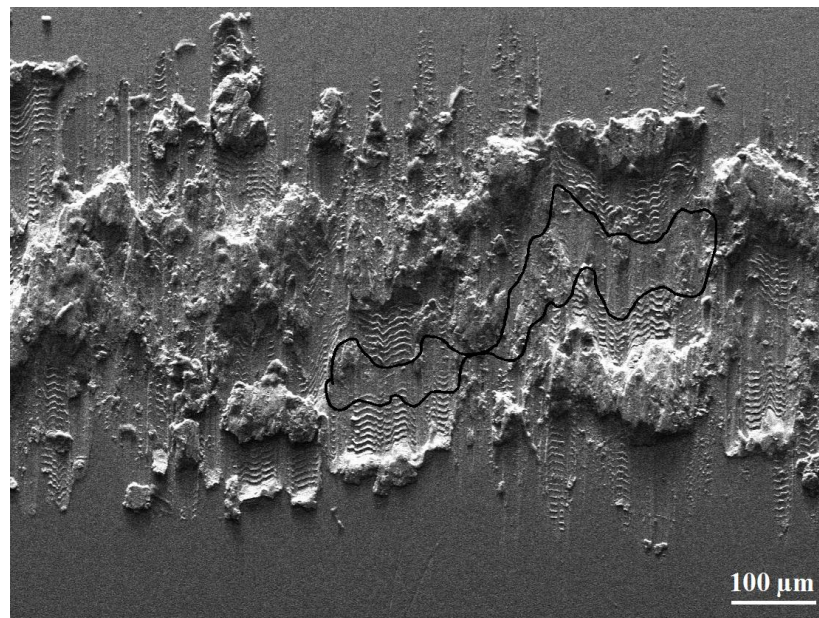


Figure V.5 : Contact surface of the plate after a 100 cycle fretting test stopped by reducing the displacement amplitude to zero during some additional cycles. An asperity (contour marked with black line) is pasted from the SE micrograph of the cylinder surface to the corresponding contact spot on the micrograph of the plate surface. Work by Christophe Paulin, LTDS/ECL.

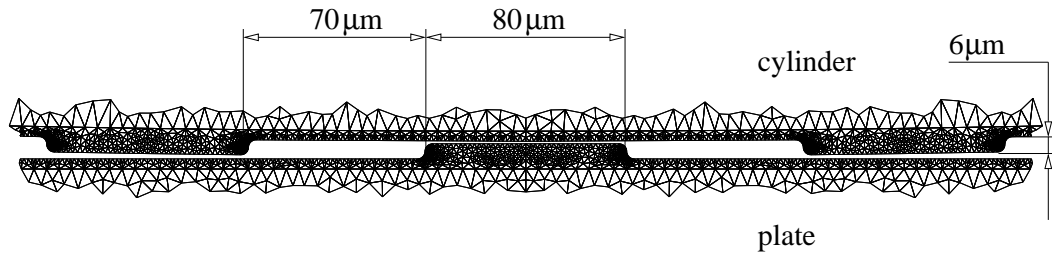


Figure V.6 : FE mesh of the cylinder/plate contact after 100 fretting cycles. The SE micrograph shown in Fig. V.5 was used for the mesh construction.

very global description of diverse contact phenomena as adhesion, asperity interaction and third body flow. On the other hand micro scale properties as the initial roughness or the microstructure of the specimens are not regarded.

We decided to modify the contact geometry of the FE mesh to take into account the asperities that formed in a 100 cycle fretting test. The contact region of this FE mesh, which is otherwise identical to that presented in section V.1.3, is shown in Fig. V.6. It represents in a schematic way the contact situation shown in Fig. V.5. Using the "conventional" material model and a coefficient of friction of 0.5 one fretting cycle was computed. The boundary conditions presented in section V.1.3 were used. Then three models of the 100th fretting cycle can be compared. In Fig. V.7 contour plots of the von Mises stress during total sliding in the position $\delta = 0$ while the plate is moving from left to right can be seen. The plot on the left shows the result of a 100 cycle computation with a smooth contact and the "conventional" material model. The material response is purely elastic and the maximum von Mises stress is 789 MPa. In the plot at the centre the result of a 100 cycle computation with an initially smooth contact and the "multikinematic" material model is shown. The stress field has evolved and the maximum von Mises stress has increased to 803 MPa. On the right a 1 cycle computation with the rough contact built from experimental results (see Fig. V.6) is shown. Very high local von Mises stresses with a maximum of 1342 MPa were obtained with this discontinuous contact model even despite the use of a lower friction coefficient of 0.5. The fretting log of the last computation is shown in Fig. V.8. It has the same shape as that of the corresponding fretting experiment. The peaks at maximum displacement are caused by interlocking of asperities on cylinder and plate. The interlocking is accompanied by severe plastic deformation. The high stresses and severe deformation together may explain the instability of the asperities and the formation of a debris field in the contact when a fretting test is continued.

We conclude that in the cross slip regime a more realistic contact description is necessary while more refined material modelling is of subordinate importance. In the partial slip regime though slip is confined to the border of contact, slip amplitudes are very small and contact surface evolution is small. Then a local contact description might be of subordinate importance and a constant coefficient of friction could be sufficient.

V.1.5 Conclusion

Fretting tests with up to 2000 fretting cycles have been made and a corresponding FE model has been constructed. A cylinder/plate contact pair was used, both contacting bodies were made of Ti6Al4V and had smooth surfaces ($R_a=0.1 \mu\text{m}$) before testing. During the first hundreds of cycles the contact became discontinuous as asperities with a height of $5 \mu\text{m}$ to $10 \mu\text{m}$ appeared. By the asperity interaction the peaks in the corresponding fretting logs could

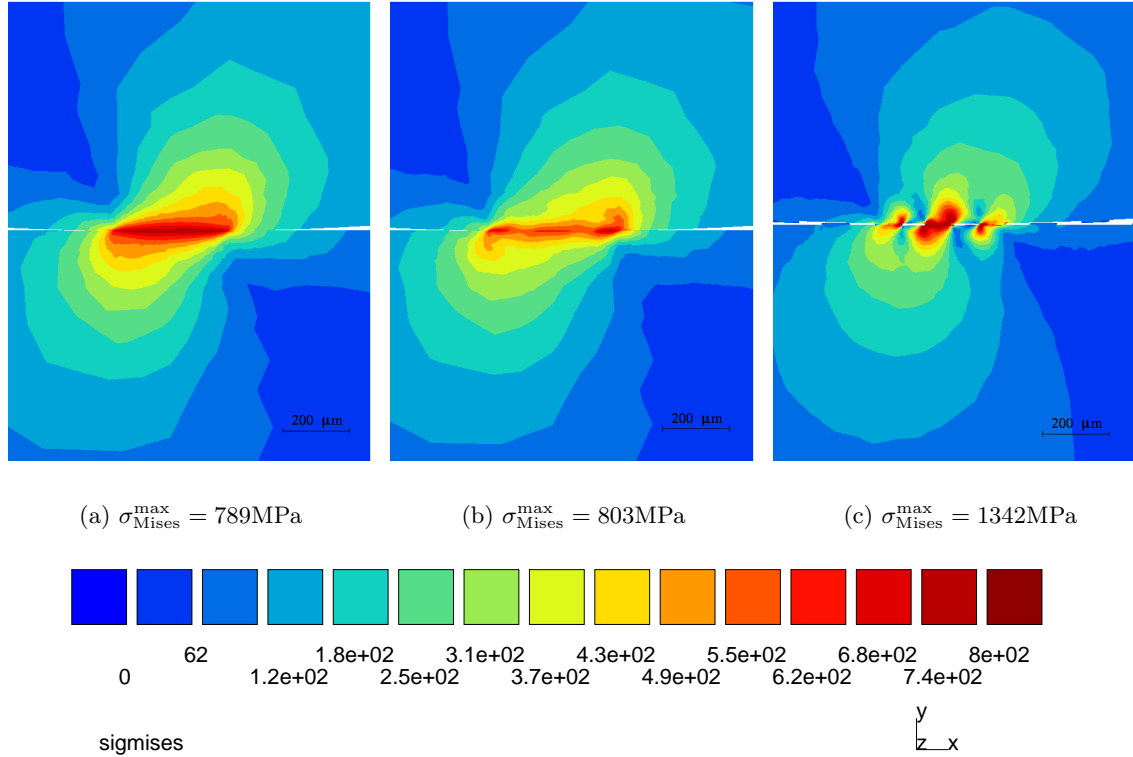


Figure V.7 : von Mises stress (σ_{mises}) in total sliding, at $\delta = 0$, after 100 cycles. (a): smooth contact, $\mu = 0.8$, conventional material model. (b): smooth contact, $\mu = 0.8$, multikinematic material model. (c): FE computation using a mesh of a fretting scar after 100 cycles, $\mu = 0.5$, conventional material model

be explained. When 1000 cycles were performed no asperities but a rather homogeneous field of debris was found in the contact and the peaks in the fretting logs had given place to a linear evolution. The evolution of the contact surface morphology and of the fretting log could not be modelled using refined von Mises material models and FE meshes with initially smooth contact surfaces. Modelling the surface morphology of the 100th cycle in a FE computation a fretting log with the same shape as in the experiment was obtained. The elevated stresses and plastic strains in this computation may explain the soon destruction of this contact morphology and its replacement by a debris field. Then all wear mechanisms including wear particle generation, oxidation, refinement and ejection establish. And the dissipated energy approach (Fouvry et al., 1996) may be used for wear prediction.

V.2 Contact geometry change by wear

V.2.1 Introduction

Many approaches to wear modelling have been developed. Nevertheless one of the oldest methods published by Archard is still widely used (Archard, 1953). This is a global approach where the wear volume is a function of a wear constant ($K_{Archard}$), the normal force (P) and the sliding distance (S).

$$V_{wear} = K_{Archard}PS \quad (\text{V.1})$$

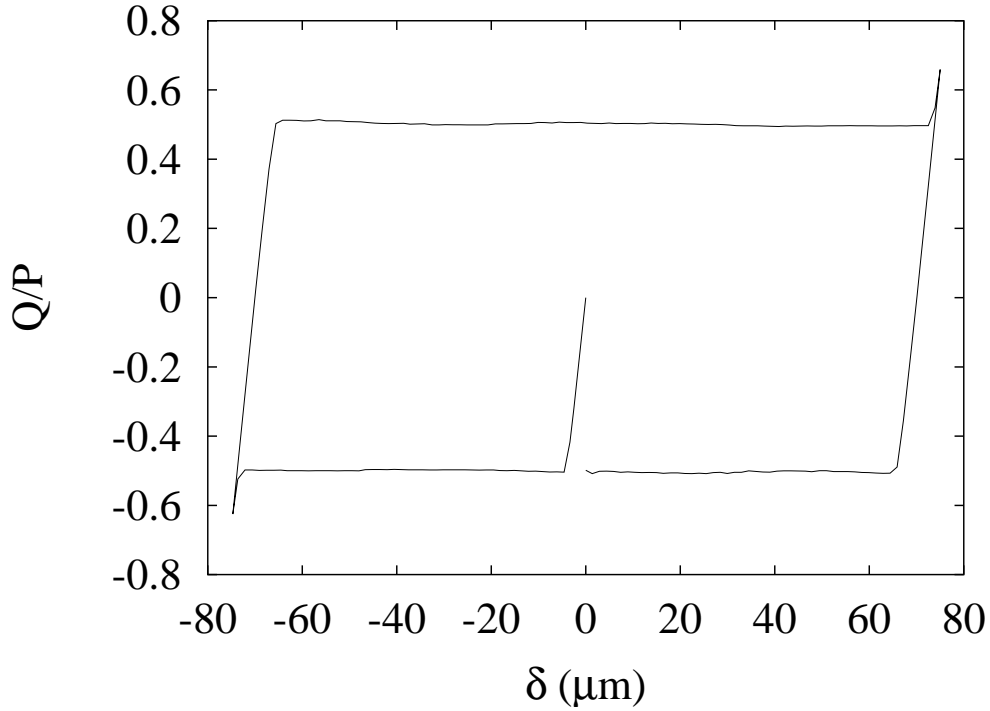


Figure V.8 : Fretting log, computed in finite elements with a schematic mesh of the contact geometry of a specimen after 100 fretting cycles

For wear prediction in fretting we use a similar method called "dissipated energy approach", developed at the LTDS / Ecole Centrale de Lyon by Siegfried Fouvry (Fouvry et al., 1996). The main difference to the Archard equation is the introduction of the friction coefficient μ , see section II.3.3.

$$V_{wear} = K_{Energy} E_{dc} = K_{Energy} P \mu S \quad (V.2)$$

Wear causes a geometry change at the contacting surfaces of two bodies. This in turn causes a change of the stress/strain state at the contact proximity which again changes the fatigue life of the involved parts. So by taking wear into account fatigue life prediction can be improved. (Oqvist, 2001; Ratsimba et al., 2004) have published work where contact geometry change caused by wear was accounted for. These authors use the finite element method with a local version of the Archard equation as a wear criterion. This means that they substitute the normal force (P) with a local contact pressure (p) and the sliding distance (S) with a local sliding distance (s) to obtain a wear height (h_{Wear}) instead of a wear volume (V_{Wear}).

$$h_{wear} = K_{Archard} p s \quad (V.3)$$

As both authors use the FE method, local means that the equation is applied at each contact node of the FE mesh. The authors update the mesh geometry after each computed fretting cycle. By many consecutive computation–mesh updating sequences they model the whole lifetime of fretting contacts, whereby they reduce computation times by the introduction of a multiplier to the wear constant.

V.2.2 Mesh geometry updating strategy

In this work wear computation is performed using the FE code Zebulon. In this program contact is introduced by an impactor/target technique, among other variables contact

pressure, accumulated slide, local coefficient of friction and dissipated energy are computed at the impactor nodes. Consequently wear computation is performed on the impactor side of the contact while the target side remains unchanged. Technically contact geometry updating is performed as shown in figure (V.9).

- At first one fretting cycle is computed.
- Next a post processing is performed which writes the dissipated energy that has accumulated during the last cycle at each node $e_{dc(i)}$ to a separate file. The nodal accumulated dissipated energy is computed by the integration of the following formula

$$de_{dc(i)} = p_{(i)}\mu_{(i)}ds_{(i)} \quad (\text{V.4})$$

where p_i is the nodal contact pressure, μ_i the nodal friction coefficient and s_i the nodal sliding distance.

- Then a meshing routine computes the wear height at each impactor node,

$$h_{wear(i)} = K_{Energy}e_{dc(i)} \quad (\text{V.5})$$

where K_{Energy} is the wear constant. For each impactor node a unitary vector (\vec{n}), which points to the outside of the body and is normal to the surface, is defined. The impactor surface geometry is updated by displacing each impactor node by:

$$\vec{h}_{wear(i)} = -h_{wear(i)}\vec{n} \quad (\text{V.6})$$

Additionally nodes that are not on the surface but just near to it are displaced. By this accumulated wear heights that are bigger than the typical element size can be computed while it is assured that the finite elements retain allowable shapes.

This procedure is repeated until the demanded number of fretting cycles has been computed.

V.2.3 Computation setup

FE mesh: A cylinder/plate fretting wear test is represented in a FE computation (Fig.V.10). The cylinder has a radius of 10 mm. At distance from the contact zone free domains with plane strain 3-noded triangular full integration elements are used, the mesh is gradually refined towards the contact. The proximity of the contact zone is meshed with regular domains consisting of plain strain rectangular 4-noded full integration elements with a size of 20 μm by 18 μm . Additionally a 3D model is constructed by the extension of the 2D model by 4 elements over 100 μm in the z direction.

Boundary conditions: The loading is done in two steps. The locations where the boundary conditions are applied are marked in the mesh (Fig. V.10). At first either a vertical displacement (u2) of 7.4 μm (causing an initial normal load of 142N/mm) or a load (R2) of 147N/mm is imposed at the top of the half cylinder while the plate is fixed by locking its bottom and side nodes. Then the cyclic loading is started. The cylinder is fixed by locking the top nodes in the 1-direction. The plate performs an oscillating horizontal movement (u1) with an amplitude of 75 μm with a triangular time-displacement curve. In the 3D model the nodes at the front face ($z = 0\mu m$) and back face ($z = -100\mu m$) are blocked in direction 3.

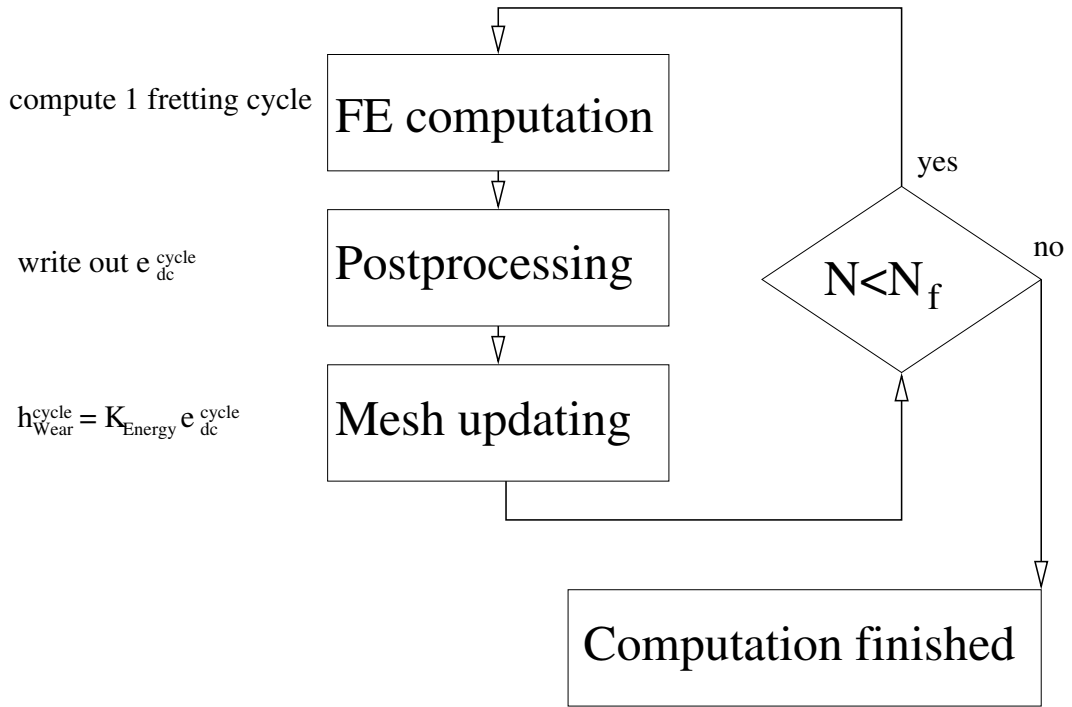


Figure V.9 : Schema of a cyclic fretting computation including wear and related geometry change.

Friction and wear: The coefficient of friction is set to 0.8 which represents the behaviour of a dry fretting Ti6Al4V-Ti6Al4V contact. In the following computations the wear coefficient is set to $K_{Energy} = 40 \cdot 10^{-8} \text{mm}^3/\text{mJ}$. It has been found to be the highest value with which still no perturbations by wear geometry updating are introduced in the strain/stress response in the contact zone of the cylinder/plate model. With the chosen value a maximum wear height of about $0.05 \mu\text{m}$ per updating step is obtained which is close to the results reported by (Ratsimba et al., 2004). In experiments the wear coefficient is not really constant (Fridrici, 2002). It depends on the fretting condition which is determined by contact load and sliding amplitude and on the number of fretting cycles over which the wear coefficient is determined. Wear is more severe during the first ten thousands of cycles and milder at higher cycle numbers. Wear coefficients for dry titanium contacts have been measured by Vincent Fridrici and Christophe Paulin at the Ecole Centrale de Lyon. Wear coefficients measured in the first 20 000 cycles are four times higher than in the remaining 250 000 cycles of a given fretting test. The ratio between numerical and experimental wear coefficient gives the computational acceleration factor.

Material model: The material model for cylinder and plate is linear elastic with the parameters $E = 119 \text{GPa}$ and $\nu = 0.29$ to represent the titanium alloy Ti6Al4V.

V.2.4 Results and discussion

a) Model verification

At first computations with 2D and 3D meshes are made. In both computations the same boundary conditions with imposed displacements are applied. 100 fretting cycles are calculated. Wear and related geometry change are computed on the plate. In Fig. V.11

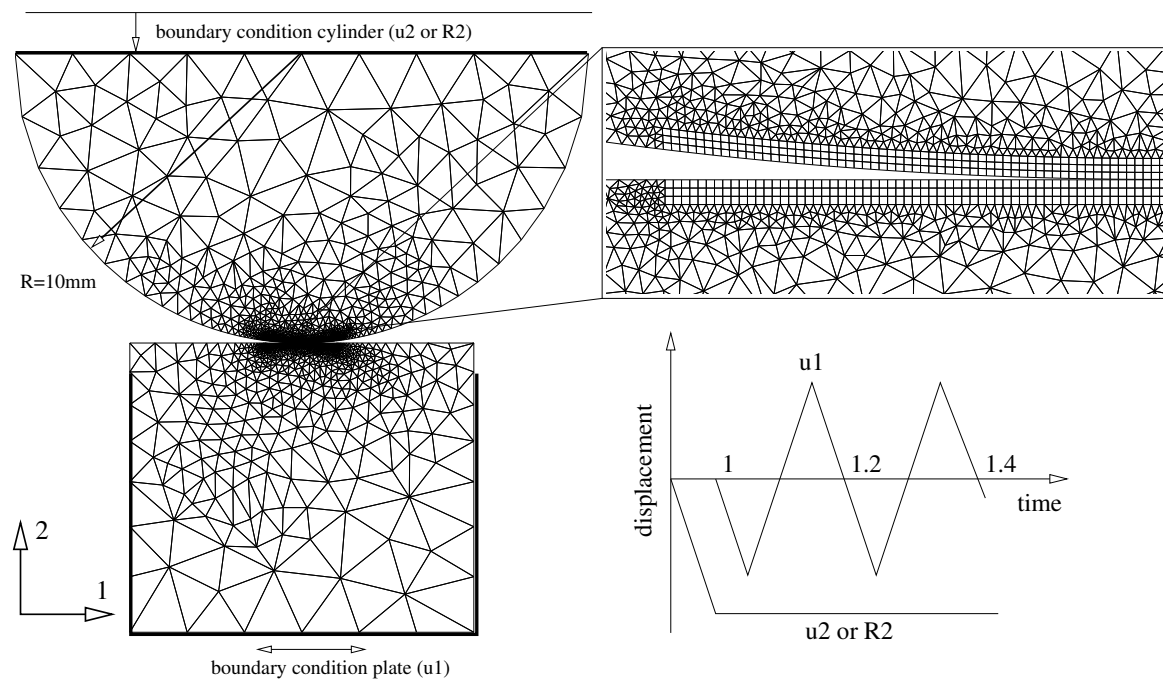


Figure V.10 : FE mesh of a cylinder/plate contact model and boundary conditions

the geometry change by wear on the plate surface is shown. The comparison of 2D and 3D computations shows that both have been implemented and give the same result. The initial contact half length in these computations is $170\mu m$. The width of the wear scar, obtained after the first cycle is equal to twice the sum of contact half length and displacement amplitude which gives $490\mu m$. During 100 fretting cycles the wear scar broadens to approximately $600\mu m$, its maximum depth is $2.74\mu m$. As the contact loading is imposed by displacements the wear causes a decrease of the normal force which is shown in Fig. V.12. The consequence is a decrease of the wear rate in the computations. If many more fretting cycles were calculated the normal force would approach zero and wear would stop.

To make sure that the mesh geometry change is correctly accounted for a check can be performed. Two nodes on cylinder and plate, which share the same horizontal position (coordinate 1) when only a normal load is applied are regarded (see Fig. V.13(a)). During a fretting computation, when the contacting bodies are sliding, the two nodes are close to each others when $u_1 = 0$. It is the elastic deformation of cylinder and plate due to which the two nodes are then not exactly at the same position. But the difference between their vertical displacements should be approximately equal to the gap between them in the unloaded, non-deformed mesh. During the computation wear widens the gap, which necessitates a greater relative displacements of the two regarded nodes. In Fig. V.13(b) it can be seen that the gap before any wear is equal to $1\mu m$. During 100 cycles the gap between the two nodes increases by $2.74\mu m$ (they are located at the centre of contact). The relative displacement of the two nodes follows the gap which assures us of the correctness of the computation. A small difference between the two curves diminishes as the normal force causing elastic deformation decreases.

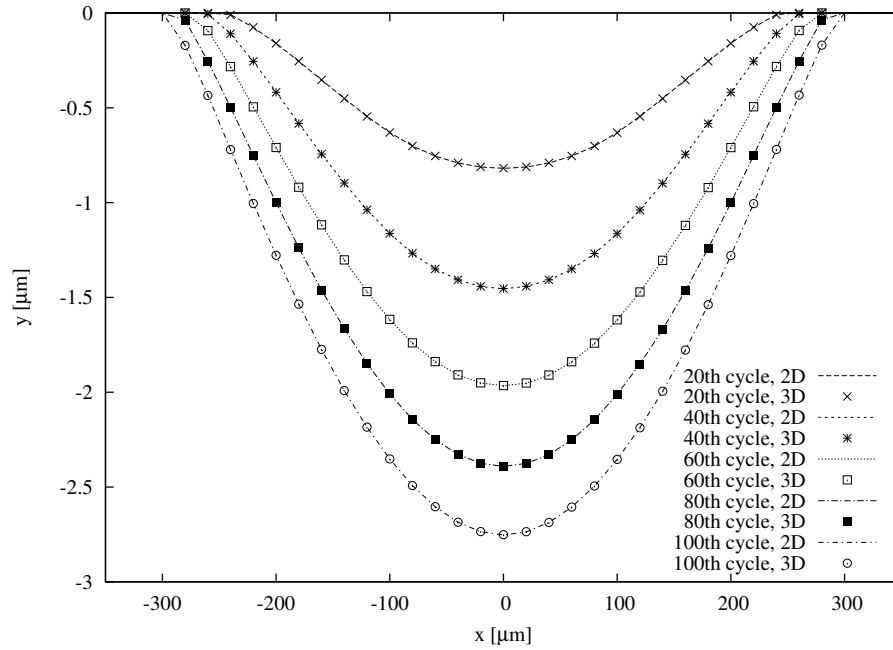


Figure V.11 : Surface geometry change of the plate's contact surface due to wear in a 2D and 3D computation. For the 3D computation a profile at $z = -50\mu\text{m}$ is shown.

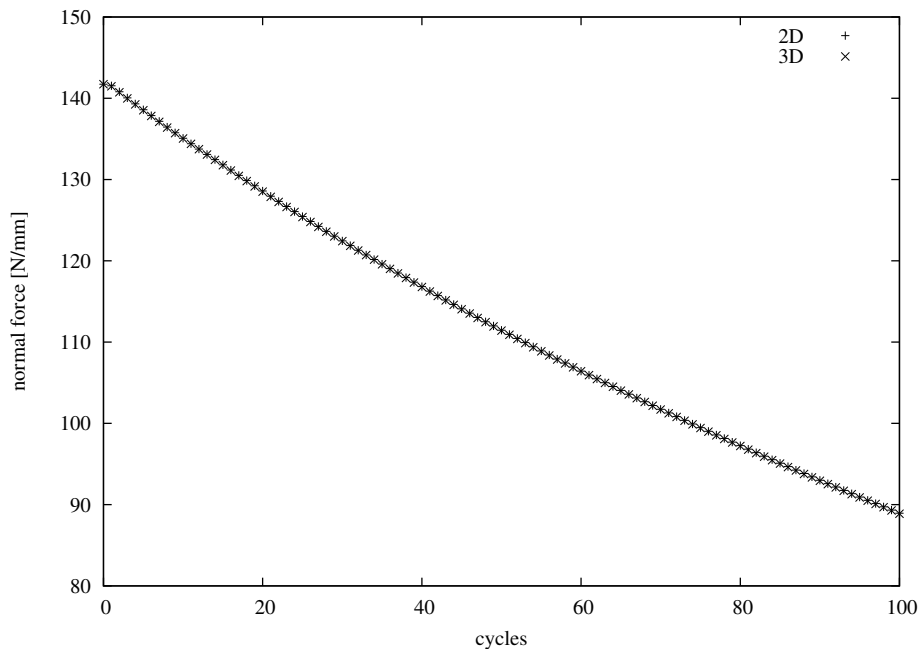


Figure V.12 : Decreasing normal force in a 100 cycle wear computation where the normal loading is imposed by displacements. The shown values have been obtained at the end of each fretting cycle when $u_1 = 0\mu\text{m}$.

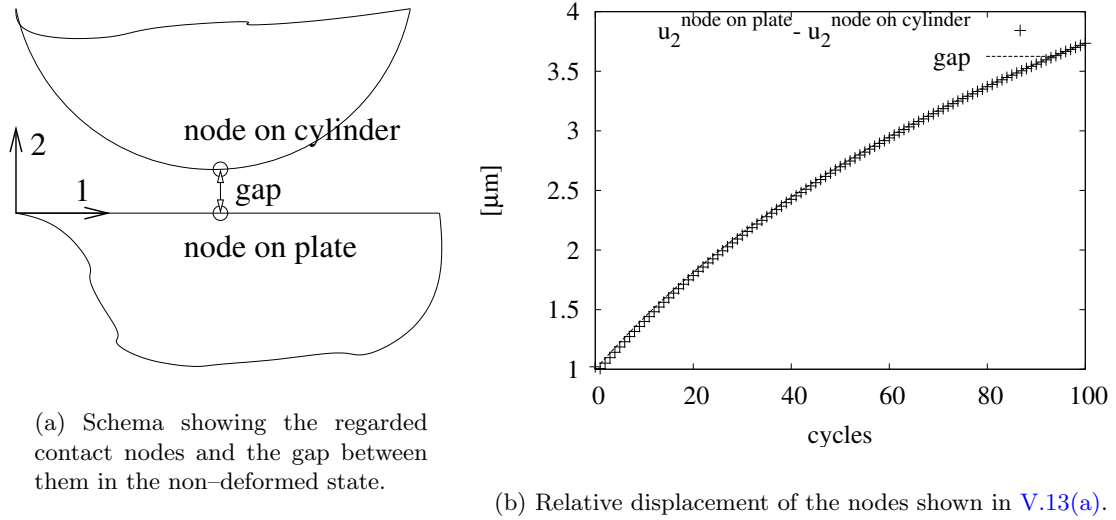


Figure V.13 : Control of the correctness of the wear computation.

b) Unilateral versus bilateral geometry change by wear

In the following part only 2D computations are shown. The normal loading is imposed by a force ($R_2=147 \text{ N/mm}$) at the top nodes of the cylinder, so it is constant and independent of wear. In one computation wear and related geometry change are computed for the plate surface (unilateral wear). In the other computation this is performed for both contacting surface which is implemented by inverting the impactor/target pair after each wear computation (bilateral wear). So in the first cycle wear changes the plate surface geometry, in the second the cylinder geometry, in the third the plate geometry is again changed. This goes on until the required number of fretting cycles has been reached. In both computations 4000 cycles have been computed.

Wear scar: Then the wear scars in the two computations can be compared (see Fig. V.14). For unilateral wear the contact surface of the plate, which changes with the number of computed wear cycles, is plotted. In bilateral wear the surfaces of cylinder and plate change. So in the non-deformed but worn mesh for each contact point (1-direction) the sum of wear on cylinder and plate is computed and shown in Fig. V.14. It can be seen that the resulting wear scar is very similar in both computations. However in the bilateral wear computation more wear is obtained in the centre of contact and less at the ends of the scar. This is so because the dissipated energy on the cylinder is more concentrated than on the plate. A point of the cylinder is (at least in the first cycle) always in contact and experiences a constant contact pressure. On the plate there are points that are in contact (and under pressure) during a part of the fretting cycle and out of contact (experiencing no pressure) during the other. Consequently they suffer less wear.

Fretting log: In a computation with an unworn FE mesh a fretting log, where the ratio of tangential and normal contact load during sliding is constant and equal to the imposed coefficient of friction is obtained. As wear proceeds this initial shape of the fretting log changes. For the 400th and 4000th computed fretting cycle the fretting logs obtained with uni- and bilateral wear are shown in Fig. V.15. In both computations the ratio of tangential

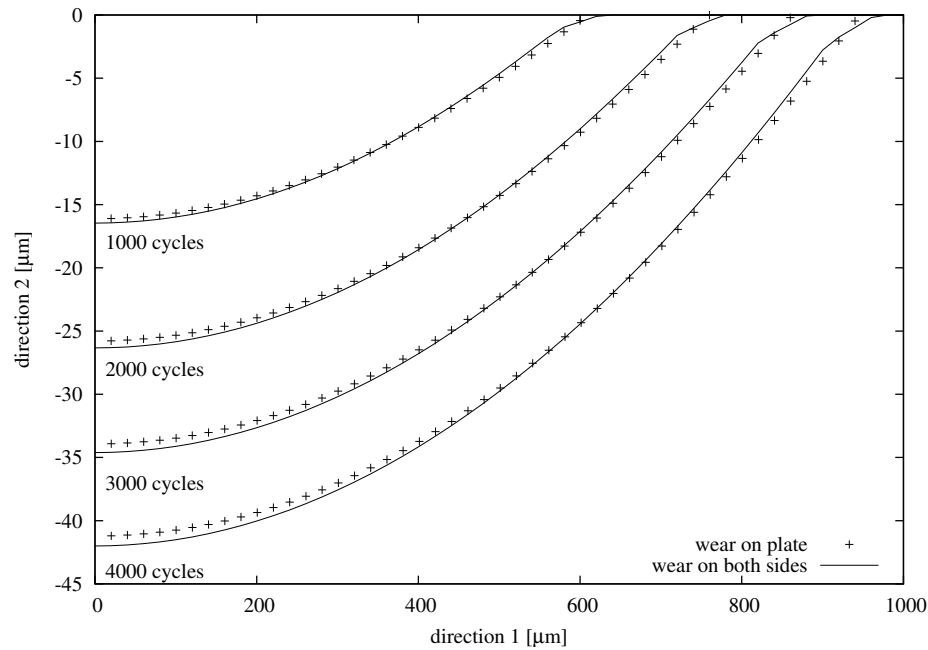


Figure V.14 : Build up of the wear scar during 4000 computed wear cycles. For unilateral wear the geometry of the non-deformed plate is given. For bilateral wear for each point in the 1-direction the sum of geometry change on plate and cylinder is plotted in the non-deformed mesh.

and normal contact load is non-constant during a sliding stroke. After the change of the sliding direction the ratio is smaller than the imposed friction coefficient. Then during sliding the ratio grows monotonically and reaches a peak value that is higher than the imposed friction coefficient when the other sliding amplitude is reached. In computations with unilateral wear this effect is stronger than in corresponding computations with bilateral wear. At higher wear cycle numbers the effect gets more pronounced in both computations. Fretting experiments with the same setup and the same boundary conditions as modelled here have been performed by Christophe Paulin at the Ecole Centrale de Lyon (see section V.1). The fretting log of the 1000th experimental cycle is shown in Fig. V.3(c). We attempt a comparison of this experiment with our model. From available SEM pictures an approximate wear scar width of $920\mu\text{m}$ has been measured, the wear scar depth is unknown. The same wear scar width is obtained in the 400th computational fretting cycle. This is why its fretting log which is shown in Fig. V.15 is compared to the 1000th experimental cycle. In the computation the change of the tangential force is weaker than in the experiment but becomes more distinctive at higher cycle numbers. An explanation can be that some asperity interlocking might still be responsible for the shape of the experimental fretting log (see section V.1.4) and wear may not be fully installed at this early stage of a fretting wear test. Once wear is fully installed the geometry of the wear scar is responsible for the shape of the fretting log.

Contact pressure: A comparison of the contact pressure in both computations is given in Fig. V.16. In the graph on top the contact pressure during sliding when $u_1 = 0$ is shown. In the first cycle before any wear the maximum contact pressure is 560 MPa and the contact width is about $340\mu\text{m}$. After 4000 computational wear cycles maximum contact pressure and contact width are 150 MPa / $1280\mu\text{m}$ and 100 MPa / $1660\mu\text{m}$ in the unilateral and bilateral

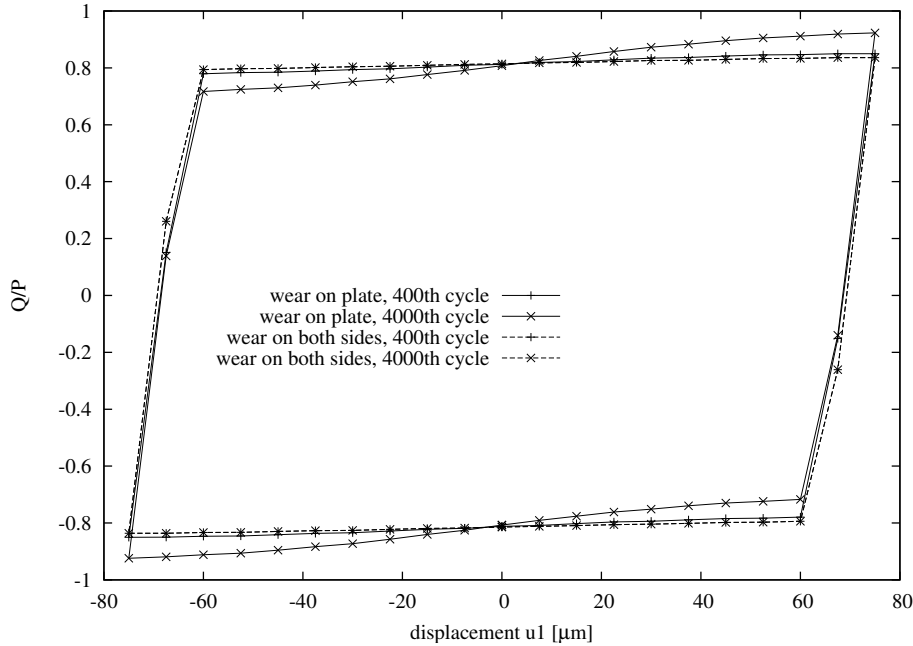


Figure V.15 : Fretting log in the 400th and 4000th cycle. In one computation wear and related geometry change were computed on the plate, in the other wear and geometry change were computed on both surfaces.

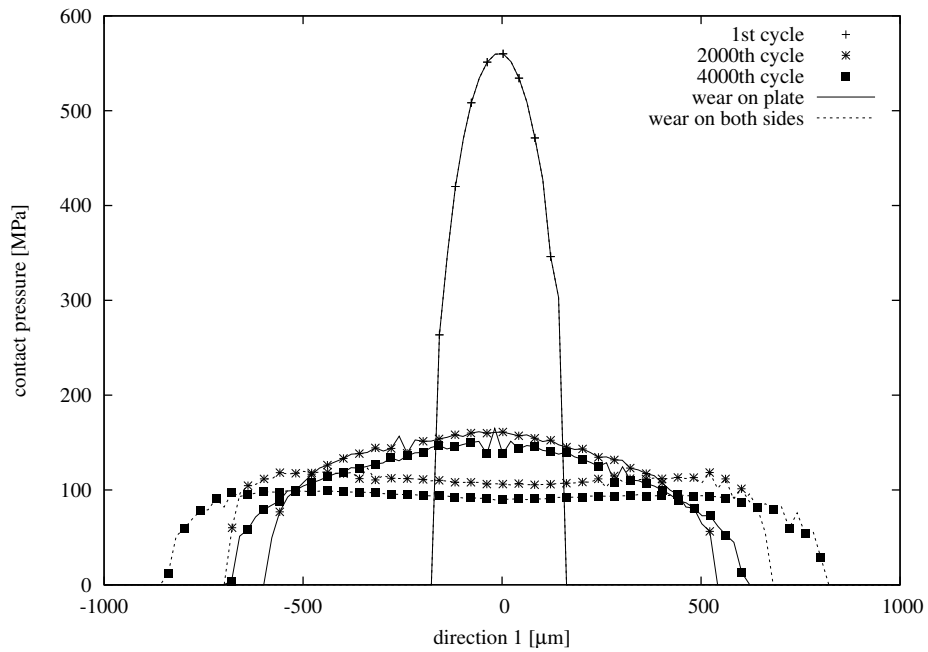
wear computations, respectively. In the unilateral computation the peak pressure is situated at the centre of contact, in the bilateral computation a more flat distribution with peaks at the sides is obtained. The graph at the bottom shows the contact pressure distribution at the sliding amplitude when $u1 = 75$. In the first cycle the contact pressure distribution is symmetric and identical to that when $u1 = 0$. In the 4000th cycle the shape is asymmetric, the peak pressure is located at the border of contact. Maximum contact pressure and the contact width are $700 \text{ MPa} / 720 \mu\text{m}$ and $630 \text{ MPa} / 1040 \mu\text{m}$ in the unilateral and bilateral wear computations, respectively. Generally in bilateral wear computations the contact pressure is lower and the contact width greater than in unilateral wear computations. In the graph it can be seen that the mesh refinement is insufficient to resolve the gradients of the contact pressure distribution.

V.2.5 Conclusion

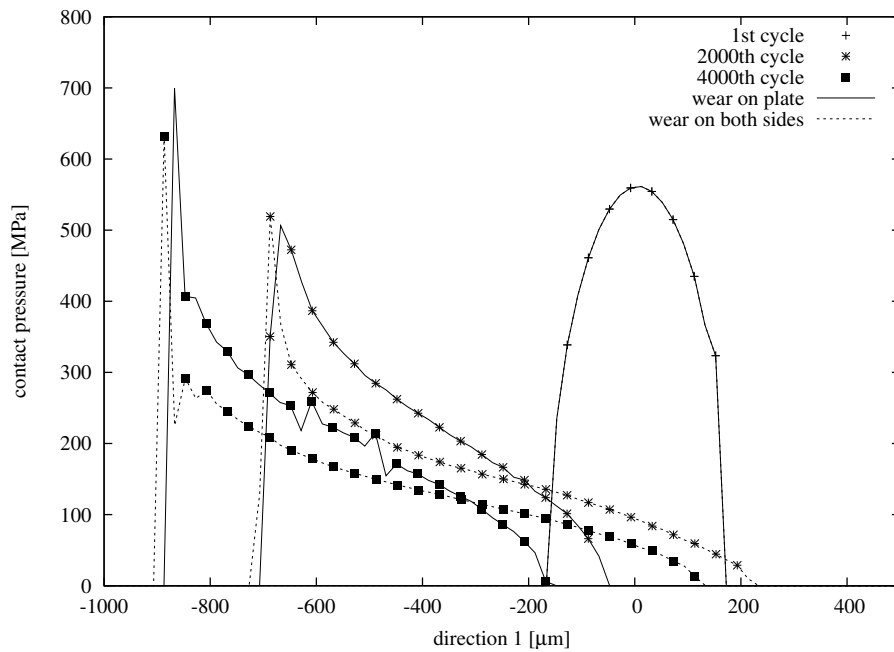
Fretting computations where the contact geometry change by wear is taken into account have been performed. As a wear criterion the dissipated energy approach developed by Siegfried Fouvry at the Ecole Centrale de Lyon has been used. In an exemplary cylinder/plate computation it has been shown that 2D as well as 3D computations can be made and the correctness of both types of computations has been assessed.

Then two 2D wear computations that were identical with one exception were compared. In one computation wear and related geometry change was calculated on the plate (unilateral wear), in the other geometry change was calculated on cylinder and plate in an alternating manner (bilateral wear). The results showed that in bilateral wear computations more wear is obtained in the centre and less at the borders of the wear scar. Also the obtained contact pressures are lower and the contact width is greater than in the unilateral wear computation. In both computations a nonlinear fretting log that is also measured in experiments is obtained.

It is concluded that the particular shape of the fretting log shown in Fig. [V.3\(c\)](#) is caused by contact geometry change by wear.



(a) In sliding contact when $u_1 = 0$



(b) In sliding contact at the displacement amplitude when $u_1 = 75 \mu m$

Figure V.16 : Contact pressure in the first, 2000th and 4000th cycle. Computed once with unilateral and once with bilateral wear and contact geometry change.

Chapter -VI-

Fretting fatigue prediction

VI.1 Introduction

The prediction of fretting fatigue is still inaccurate and more than one peculiarity of fretting contacts contributes to the difficulties. Among the identified problems are the high stress gradients near the fretting surface (Nowell and Dini, 2003), the facilitation of surface crack nucleation by wear mechanisms (Szolwinski and Farris, 1996), the assessment of local friction properties of the contact (Dini and Nowell, 2003; Swalla and Neu, 2001) and the change of the loading path during cycling both by strain ratchetting (Kapoor, 1994; Ambrico and Begley, 2000; Goh et al., 2003b) and severe contact geometry change by wear (Fouvry et al., 1996).

J.M. Ambrico et al. (Ambrico and Begley, 2000; Ambrico and Begley, 2001) showed the influence of plasticity on the stress fields in fretting contacts by a FE model of a cylinder/plate contact. They compared the elastic material solution to computations with three plastic material models (elastic/perfectly plastic, Ramberg-Osgood isotropic hardening and kinematic hardening). They classified the material response into the strain mechanisms shakedown, ratchetting and cyclic plasticity. In these computations under different fretting conditions ratchetting always diminished rapidly while cyclic plasticity was more persistent and did not necessarily shake down. They remarked that different types of materials may promote different strain mechanisms. A comparison of elastic and plastic results showed that material flow by ratchetting reduces the stress amplitudes while residual stresses raise them. Generally taking plasticity into account should improve the fatigue life predictions in fretting contacts.

In fretting contacts small material volumes at the microstructural scale typically experience high stresses and high stress gradients. On this microscopic scale, polycrystalline materials as Ti6Al4V should not be modelled with initially isotropic J_2 material models. Polycrystal plasticity models are more adequate as has been shown by Morrissey et al. (Morrissey et al., 2001) and Schoenfeld et al. (Schoenfeld and Kad, 2002). This model has been applied to a FE fretting model (Morrissey et al., 2003). Comparing crystal plasticity to J_2 computations, more extensive regions of plastic deformation and higher levels of strain ratchetting were found. The crystal plasticity computations compared more favourably to experiments than equivalent J_2 computations.

In this chapter fretting computations using von Mises and polycrystal plasticity material models will be presented. A close look at the plastic material response will be taken.

Fretting fatigue prediction will be treated distinguishing strain ratchetting and cyclic plastic deformation as causes of two different fatigue mechanisms.

VI.2 Fatigue prediction with J_2 material models

VI.2.1 FE mesh and boundary conditions for fretting modelling

In this section the von Mises material models described in section IV.2 are used in a model of a fretting cylinder/plate contact. One material model has been identified from fatigue tests in a classical manner. So the model has an elastic limit as normally used by engineers, additionally nonlinear isotropic softening and nonlinear kinematic hardening are present. The second material model reflects an approach to material modelling which has been shown to be suitable for taking ratchetting – a second order effect – into account. This is done by the use of a lower initial elastic limit compensated with two equations of nonlinear kinematic hardening with a very fast plastic strain response. The coefficients of the material model for ratchetting have not been identified because no ratchetting experiments were available, so it remains qualitative. But by its application to fretting modelling the susceptibility of the material near the contacting surfaces to strain ratchetting can be assessed. This is why computations using the same cylinder/plate contact with both material models are shown and compared here.

The same 2D finite element mesh and boundary conditions as in section V.1.3 are used. Wear and geometry change by wear is not taken into account.

VI.2.2 Results and discussion

a) Plastic deformation

Figure VI.1 shows a contour plot of the accumulated plastic strain ($\dot{p} = \left[\frac{2}{3} \dot{\epsilon}_{ij}^p \dot{\epsilon}_{ij}^p \right]^{1/2}$) after 100 cycles with the multikinematic identification method under the contact into a depth of 20 μm . The left half width of the contact is visible, the symmetry axis of the cylinder is indicated by a vertical line. The material parameter set coming from the multikinematic identification procedure produces an extended zone of plasticity. The plate is more affected than the cylinder and the maximum accumulated plasticity is located under the outer border of the contact. Since the plastic strain during an individual cycle is very small, material hardening and structural stress accommodation are not instantaneous but take place over many cycles. As a consequence it can be assumed that the first cycle of the multikinematic computation is representative for all cycles of the "conventional" computation which gives a purely elastic result. It is also for this reason that an asymmetry of the accumulated plastic strain induced by the initial contact gliding is very small and can be neglected.

b) Contact pressure

The contact pressure (stress component normal to the contact surface) is plotted along the contact line in Figure VI.2. The point $x = 0$ corresponds to the symmetry axis of the cylinder. The analytic solution (Johnson, 1987) is well fitted by the results obtained from the FE computation with the multikinematic identification method after one fretting cycle. The contact half width is $a=170 \mu m$ and the maximum contact pressure is $p_{\max} = 564 \text{ MPa}$. The shape of the curve is stable during the whole fretting cycle. After 100 cycles the stress distribution has changed considerably. The maximum contact pressure has decreased by 90

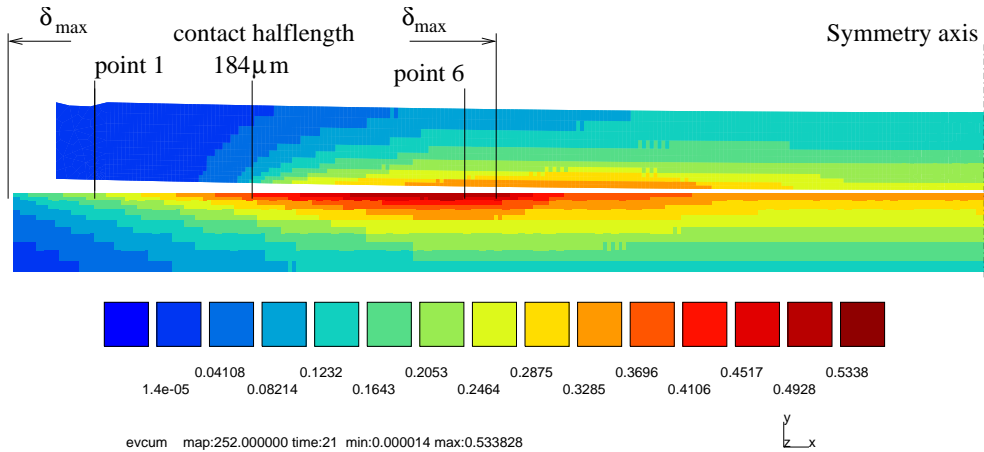


Figure VI.1 : Accumulated plastic strain at the contact after 100 cycles, multikinematic identification method. The left half of the contact is shown. In the vertical direction the first $20 \mu\text{m}$ from the contact surface into the material are shown.

MPa and the contact half width has increased by $14 \mu\text{m}$. The curve is not anymore regular in shape and it changes during the fretting cycle. In the central position $\delta = 0$ it is symmetric in shape and has local peaks at the sides. At the maximum displacement of the cycle ($\delta_{max} = 75 \mu\text{m}$) the curve is nonsymmetric with a sharp peak on one side, depending on the current sliding direction. Different locations under the fretting surface undergo strain ratchetting with varying speed and sign, which leads to geometry change and structural stress redistribution.

c) Fatigue modelling

In fatigue prediction with von Mises material models, different modes of cyclic plastic deformation are connected to different fatigue modes. Elastic response, elastic shakedown (initial plastic, then only elastic deformation) and cyclic plasticity (cyclic plastic deformation whereby the mean plastic deformation is constant) are linked to crack initiation, which is commonly predicted using fatigue parameters as that of Fatemi–Socie, Smith–Watson–Topper, Dang Van and others (Fatemi and Socie, 1988; Smith et al., 1970; Dang Van, 1993). Strain ratchetting (cyclic plastic deformation whereby the mean plastic deformation grows, see section ??) leads to material failure as observed in a tensile test. In this case a critical ratchetting strain may serve as criterion for fatigue (Kapoor, 1994; Morrissey et al., 1999).

The material response at two integration points one micrometer under the surface (see Fig. VI.1) of the plate is plotted in Fig. VI.3. In this figure the stress component in the horizontal direction σ_{11} is drawn over the corresponding viscoplastic strain for the 1st, 10th, 20th, ..., 100th cycle. The surface over point 1 is only in contact with the cylinder when the plate is near $\delta = -75 \mu\text{m}$, point 6 in contrast is in contact during the majority of time except for $\delta = +75 \mu\text{m}$. At integration point 6 ratchetting prevails from the beginning and takes on speed because of material softening. The stress amplitudes stay approximately constant. At integration point 1 structural stress redistribution as well as material softening lead to increasing strain ratchetting. Generally different locations under the fretting surface undergo strain ratchetting with varying speed and sign, which leads to geometry change and structural stress redistribution. After 100 cycles no cyclic steady state response is obtained. At the high ratchetting strains observed here failure by ratchetting can be expected after just a few thousand cycles. The obtained strain ratchetting nevertheless depends on the

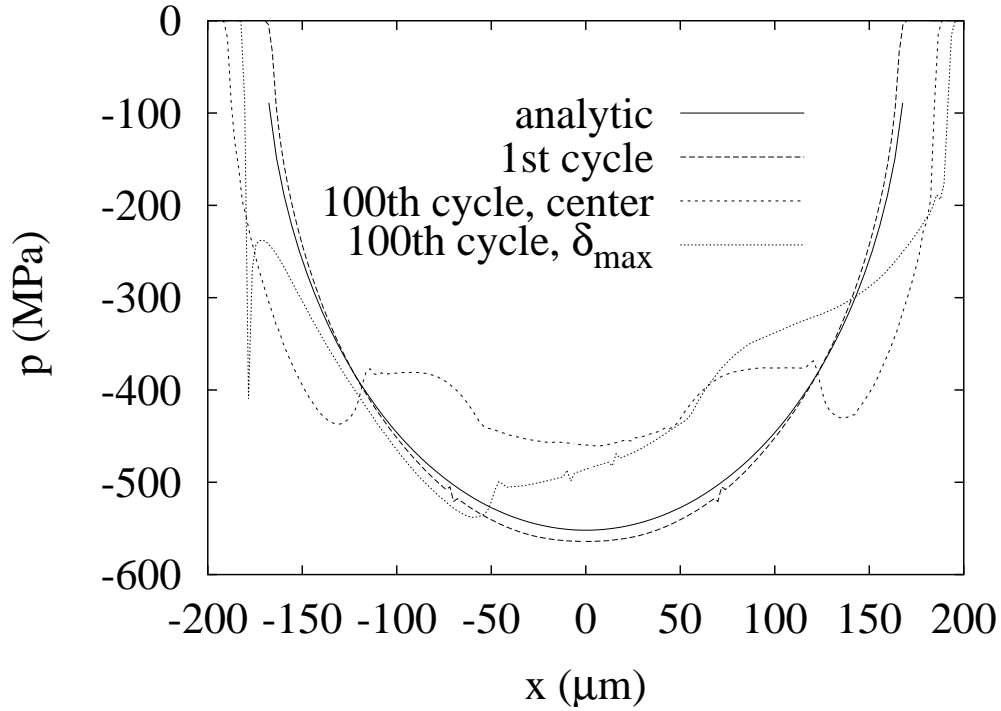


Figure VI.2 : Contact pressure evolution in a fretting computations using the multikinematic von Mises material model

employed material model. The used material model is only of qualitative nature showing the susceptibility of the fretting contact to develop strain ratchetting.

In the following part the multiaxial parameter of Dang Van for crack initiation in HCF is used. By this the effect of strain ratchetting on HCF prediction can be shown. The HCF parameter of Dang Van, conventionally used with von Mises (J_2) material models, is described by the following equation.

$$f(\sigma) = R + a_{DV}T - b_{DV} \quad (\text{VI.1})$$

This is a local criterion that is applied to each integration point in a post processing of the FE computation. High cycle fatigue failure is predicted when $f(\sigma) > 0$ at least once during the loading cycle. In this criterion the stress range R is the von Mises stress of the distance between the actual stress and the mean stress \bar{C} of a loading cycle. The mean stress \bar{C} is found as the centre of the smallest sphere in 6 dimensional stress space which can be circumscribed to the stress trajectory of the loading cycle. The diameter D of the sphere is equal to two times the von Mises stress of the greatest distance between the mean deviatoric stress and the actual deviatoric stress during a loading cycle. T is the hydrostatic tension, a and b are material constants which can be found from pure tension and shear fatigue tests (or just tension with two different load ratios). For Ti6Al4V $a_{DV} = 1.956$ and $b_{DV} = 864$ have been found.

The Dang Van HCF criterion is computed (Fig. VI.4) for the first and the 100th cycle. The zones, in which the high cycle fatigue limit is surpassed are white. The fatigue map, obtained from the first cycle (top, left side) is the definitive result of a computation with the conventional identification method which shows only elastic response. For the 100th cycle the fatigue criterion is computed again (top, right side). It is not the definitive result for the multikinematic identification method since the structure has not reached a stabilised strain

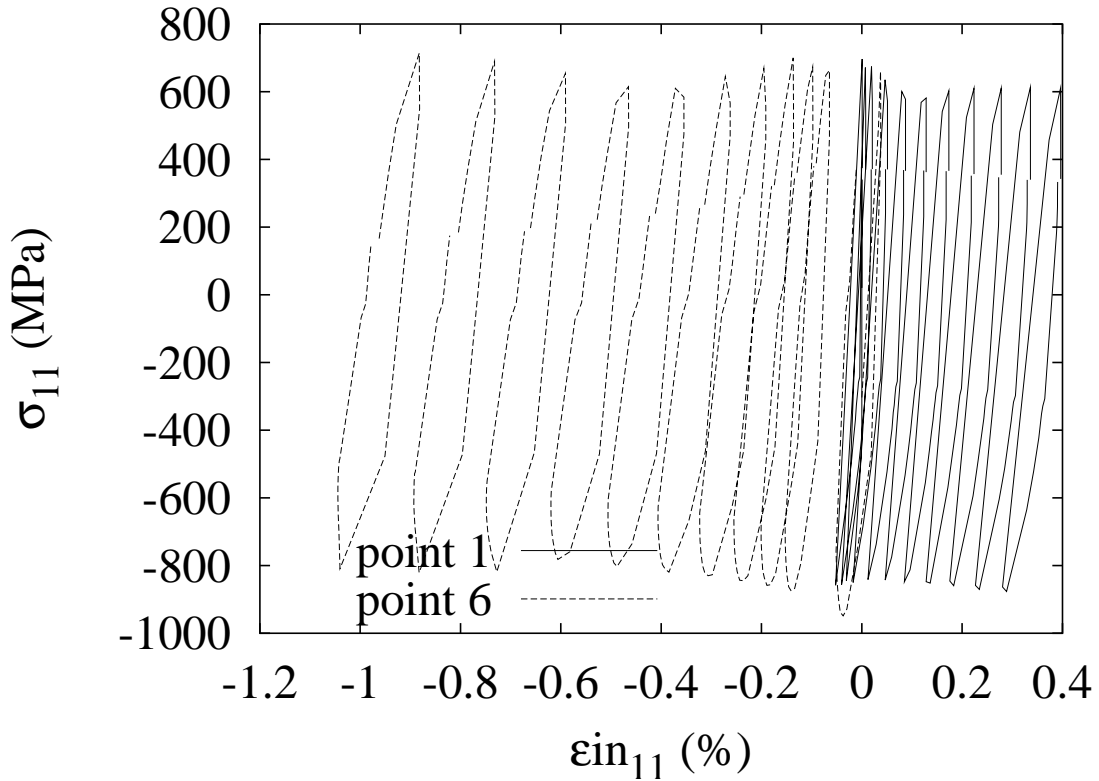


Figure VI.3 : Strain–stress response at integration points marked in Fig. VI.1.

response. The purpose of the computation though is to allow a judgement about the influence of ratchetting on high cycle fatigue. It can be stated that after 100 cycles the fatigue zone is smaller and shifted towards the outer end of the contact.

For one integration point on the cylinder and one at the plate (see Fig.) the Dang Van plot is given. In these graphs the criterion shown in equation VI.1 appears as a straight line. Additionally stress range R and hydrostatic tension T of the first and 100th cycle are given. Whenever their trajectory exceeds the criterion given by the straight line, HCF is predicted. The most critical point in a loading cycle is that which is nearest to the criterion or exceeds it most. The shown integration points exhibit the most critical Dang Van HCF parameter on cylinder and plate during the first fretting cycle. At both points stress redistribution by strain ratchetting during 100 computed cycles has the effect of lowering the Dang Van parameter. The curves on the cylinder have a different shape than those on the plate. This is so because the stresses in the cylinder are constant while it slides on the plate. Points on the plate experience transient stresses as the cylinder is approaching or moving away.

VI.3 Fatigue prediction with polycrystal plasticity

VI.3.1 FE mesh and boundary conditions for fretting modelling

A fretting wear test is now modelled using the FE code ZeBuLon. A $50\ \mu\text{m}$ slice of the cylinder/plate assembly is represented in a 3D mesh using linear full integration elements (see Fig. VI.5). This mesh is gradually refined towards the contact. At the left side of the plate, a regular domain with an element size of $5.36\ \mu\text{m}$ by $5.36\ \mu\text{m}$ by $6.25\ \mu\text{m}$ is

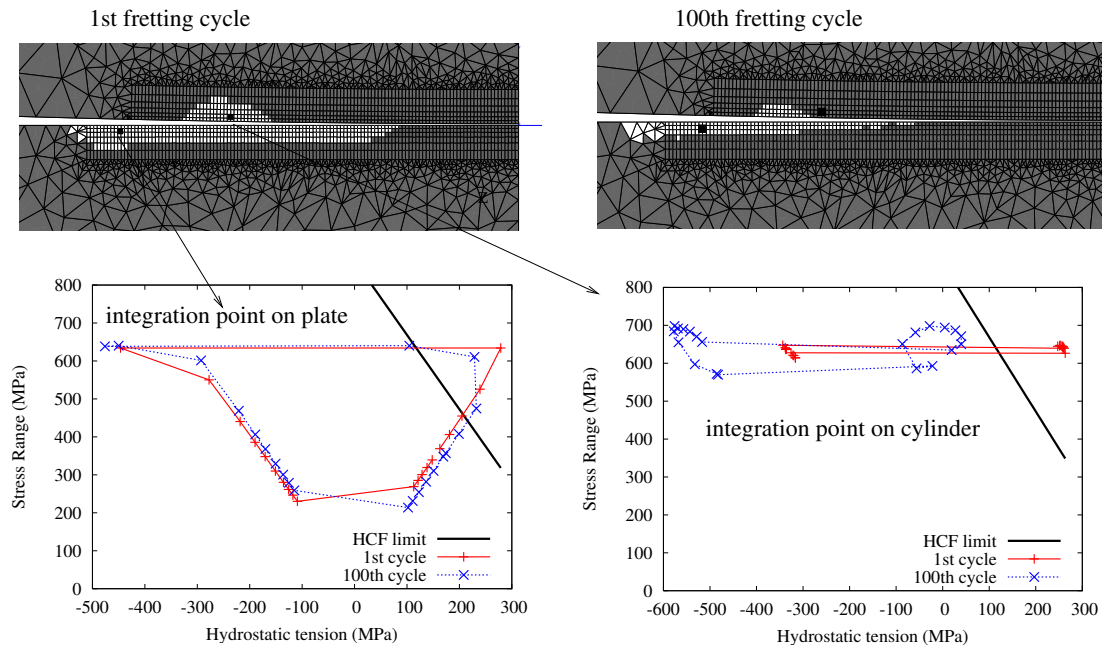


Figure VI.4 : DangVan high cycle fatigue criterion. Top: Contour plots for the 1st and 100th fretting cycle, on the left half of the cylinder/plate contact. Zones where the HCF limit is violated are white. Bottom: Dang Van plots at two integration points on cylinder and plate where the Dang Van criterion of the first fretting cycle is maximum.

present. The box where crystal plasticity is used as a material model has a size of $330 \mu\text{m}$ by $75 \mu\text{m}$ by $50 \mu\text{m}$. Here Voronoi polyhedra shaped groups of integration points constitute grains with a common crystal orientation and the crystal plasticity material model is used. The average grain size is $30 \mu\text{m}$. The same basal texture as described in section IV.3 is used, the normal direction ND coincides with direction "3" in the mesh. The rest of the structure is computed with the elastic material properties of Ti6Al4V. This was decided after a preliminary computation that showed that the applied loading does not induce von Mises stresses that are greater than the apparent yield limit of Ti6Al4V. The contact is modeled with an impactor/target technique, the frictional contact force is introduced by a Coulomb law with a constant isotropic coefficient of friction of 0.8.

The loading is applied under displacement control and imposed in two steps. The locations where the boundary conditions are applied are marked with thick lines. First, a vertical displacement (U_2) is imposed at the top of the half cylinder while the plate is fixed by locking its bottom and side nodes. The displacement (U_2) is calibrated to cause a vertical force (P) of 147 N/mm . Then the cyclic loading is started. The cylinder is fixed by locking the top nodes. The plate performs an oscillating horizontal movement (U_1) with a triangular time-displacement curve (see the loading scheme in Fig. V.2). This movement is imposed on the bottom and side nodes of the plate with an amplitude of $\delta_{\text{max}} = 75 \mu\text{m}$ and a frequency of 5 Hz . All nodes that lie on the front and on the back surfaces of the cylinder and the plate are fixed in direction U_3 .

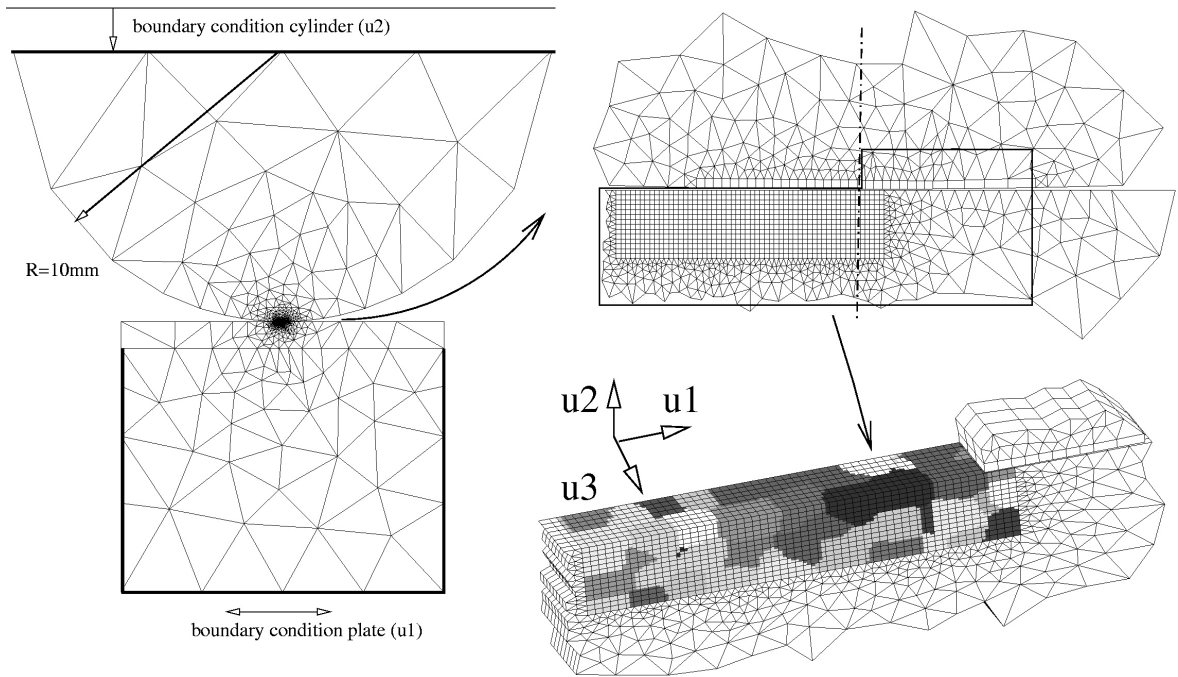


Figure VI.5 : 3D FE mesh for crystal plasticity computations

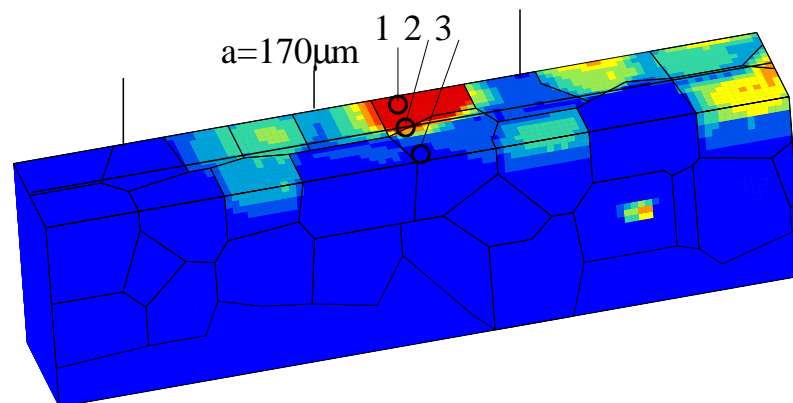
VI.3.2 Fretting modelling results and discussion

a) Plastic deformation

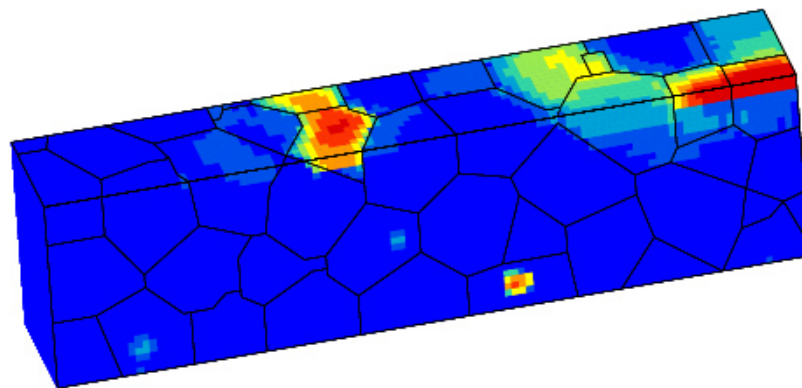
The equivalent inelastic strain, defined as $\varepsilon_{eq}^{in} = ((2/3)\varepsilon_{ij}^{in}\varepsilon_{ij}^{in})^{1/2}$ in the contact area, obtained after 10 fretting cycles, is shown in Fig. VI.6. Three 3D crystal plasticity computations with the same FE mesh but different realisations of the grain shapes and orientations are shown. In these computations the local stress and strain fields are heterogeneous and depend on the grain orientation and shape, so that the three computations are not identical even though the same loading conditions and FE mesh are used. The figures show a part of the regularly meshed domain where the crystal plasticity material model is used whereby the right edge coincides with the center of the cylinder/plate assembly. The regular elements are not highlighted but the grain boundaries are marked with black lines. In realisation 1 the border of contact when the cylinder is at its left and right displacement amplitudes is marked. The initial contact border when the cylinder is at $\delta = 0$ is indicated and labeled with the initial contact halflength ($a = 170\mu\text{m}$). Some isolated red spots in the contour maps are artefacts originating from the FE problem resolution and can be ignored. All equivalent inelastic strain maps use one color scale ranging from 0% to 1%. The range is inferior to the maximum values obtained in the computations but it is suitable for a comparison of the locality and spread of plastic material response. The maximum equivalent inelastic strain in the crystal plasticity computations are $\varepsilon_{eq}^{in,max} = 1.47\%$, $\varepsilon_{eq}^{in,max} = 0.69\%$, $\varepsilon_{eq}^{in,max} = 1.65\%$, for the first, second and third realisation, respectively, located in favourably oriented grains. In these computations plastic material response is found from the surface down to a depth of three times the grain size.

b) Contact pressure

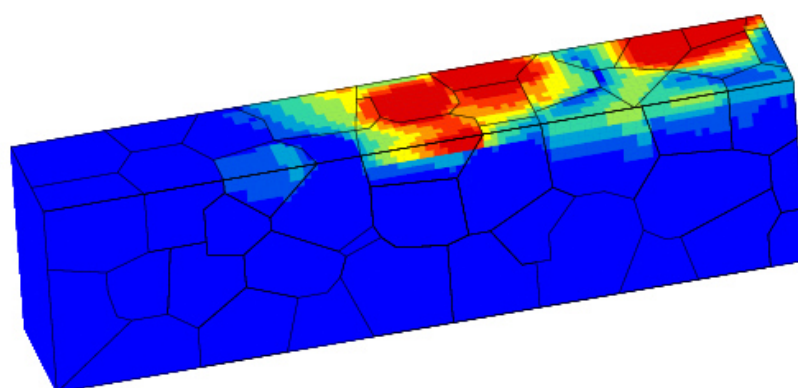
For this cylinder/plate contact, the elastic properties of the titanium alloy and the normal force imposed in the FE computation ($P=147\text{N/mm}$) the contact pressure can be computed



(a) crystal plasticity, realisation 1



(b) crystal plasticity, realisation 2



(c) crystal plasticity, realisation 3

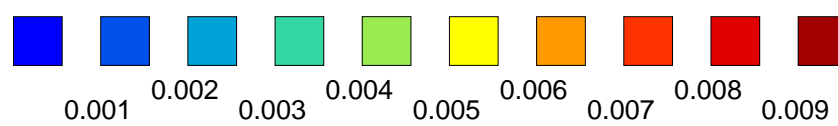


Figure VI.6 : Equivalent inelastic strain maps after the 10th fretting cycle in three realisations of grain shape and orientation using the model including crystal plasticity.

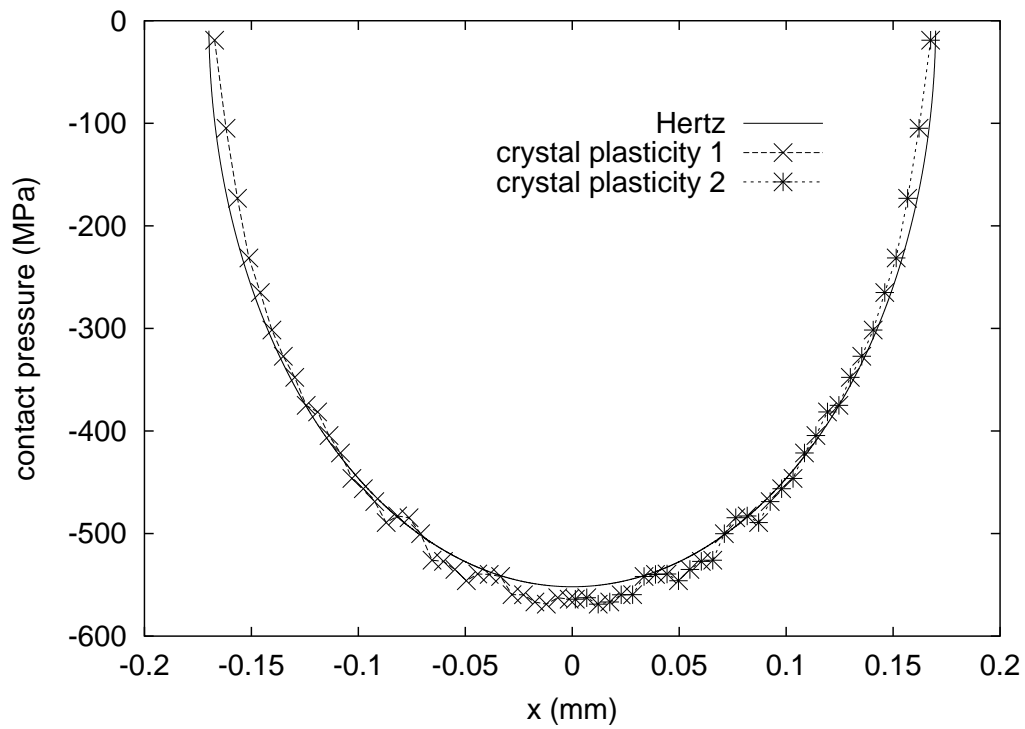
using the analytical Hertz solution and is shown in Fig. VI.7. The resulting contact halfwidth is 170 μm and the maximum contact pressure is 552 MPa. The contact pressure resulting from the finite element computations with only normal loading is shown in Fig. VI.7(a). On the left half the result of the computation with microstructure-realisation 1, on the other side the result of realisation 2, mirrored about the y -axis, is shown. The contact pressure of the crystal plasticity computation was obtained from the contact nodes lying on the straight line designated in Fig VI.6(a). Both FE computations show a small deviation from the Hertz solution even though no plastic deformation happens in both models. In the FE computations the contact halfwidth is about 170 μm , the maximum contact pressure is 564 MPa. The deviation of the contact pressure in FE model and Hertz solution is caused by the limited FE mesh refinement of the contact region. If an even finer mesh was used this difference decreased. Because a higher mesh refinement would increase the FE problem size the shown mesh has been chosen as a good tradeoff between computational cost and accuracy. In Fig. VI.7(b) the contact pressure after the 10th fretting cycle is shown. Realisations 1 and 2 are plotted in the same manner as before. During the fretting computation plastic deformation at the contact surface, depending on the crystallographic orientation of the grains, has taken place. Consequently the contact pressure is very heterogeneous and the 2 realisations give different results. The deviation between the Hertz solution and crystal plasticity results reaches up to 150 MPa while the contact halflength remains unchanged.

c) Fatigue prevision

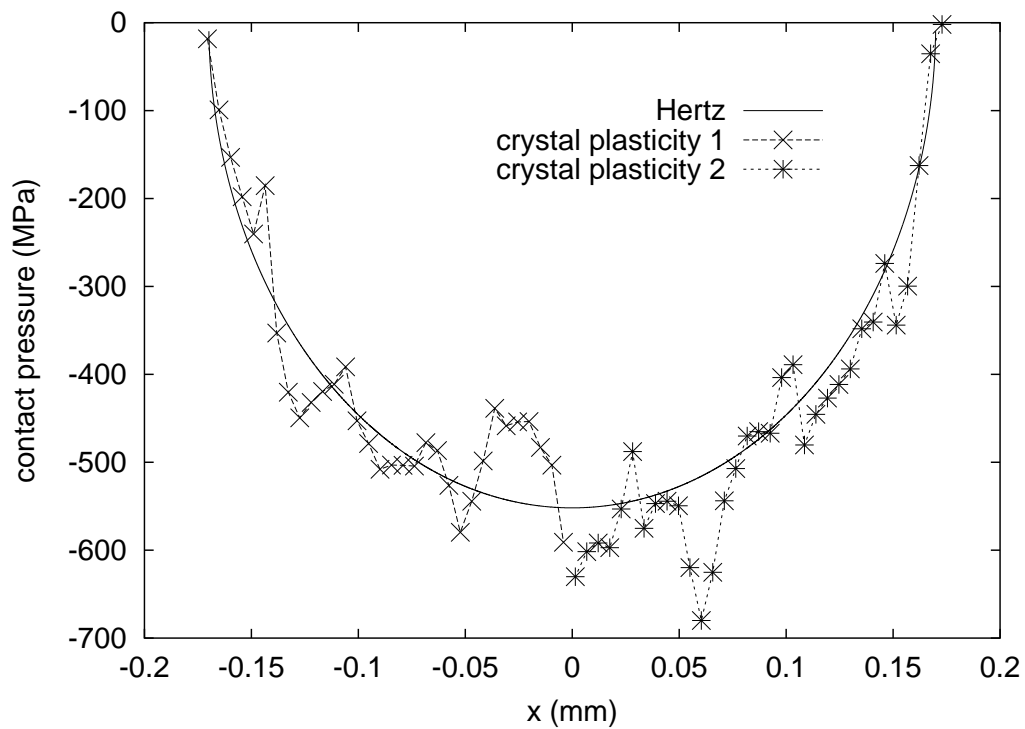
Fretting fatigue modeling with polycrystal plasticity models enhances the resolution of the local stress/strain fields because the heterogeneous nature of the material is taken into account. So when only elastic deformation or elastic shakedown are obtained in polycrystal plasticity computations, no damage accumulation and consequently no cracking may be predicted. Otherwise the before mentioned macro scale approach to fatigue prediction, where ratchetting and cyclic plasticity are distinguished, is still applicable as the underlying physical mechanisms are the same.

By a closer look at the plastic deformation of individual integration points just under the fretting surface, the relevance of these deformation modes to fretting fatigue prediction may be shown. The development of the equivalent inelastic strain at three integration points designated in Fig. VI.6 during 40 fretting cycles is shown in Fig. VI.8. At the hindmost point (point 1) cyclic plasticity is active. During the first 10 cycles strain ratchetting is eminent, then it shakes down. At the central point (point 2) the same deformation mechanisms are present. Strain ratchetting decelerates, but between cycle 20 and 40 the ratchetting strain rate is still $14 \cdot 10^{-5}\%$ per cycle. If this was the stabilized material response the impressive amount of 140% ratchetting deformation would accumulate in 10^6 fretting cycles. This shows the necessity to compute and store a sufficient number of fretting cycles to assure that the stabilized material response has been found. As the power of computer hardware increases this will become more and more feasible. The foremost point (point 3) is near elastic shakedown, small amounts of cyclic plasticity and ratchetting are present.

On the microstructural scale the Dang Van HCF parameter is again applied. This parameter has been developed having microstructural plasticity in polycrystalline metals in mind, so it can be re-evaluated using the polycrystal plasticity material model. As mentioned in section c) the parameter consists of the stress range R and hydrostatic tension P . While it can be assumed that the hydrostatic tension will play the same role on the microstructural scale a closer look should be taken at the stress range. In Fig. VI.9 the projection of the stress trajectory to the deviatoric stress components $\sigma_{11}^{dev} - \sigma_{22}^{dev}$ is given at integration point 1 (marked in Fig. VI.6 in realisation 1) for the second and 40th fretting cycle. The difference



(a) before the 1st cycle



(b) after the 10th cycle

Figure VI.7 : Contact pressure in the fretting model including polycrystal plasticity and the analytic Hertz solution.

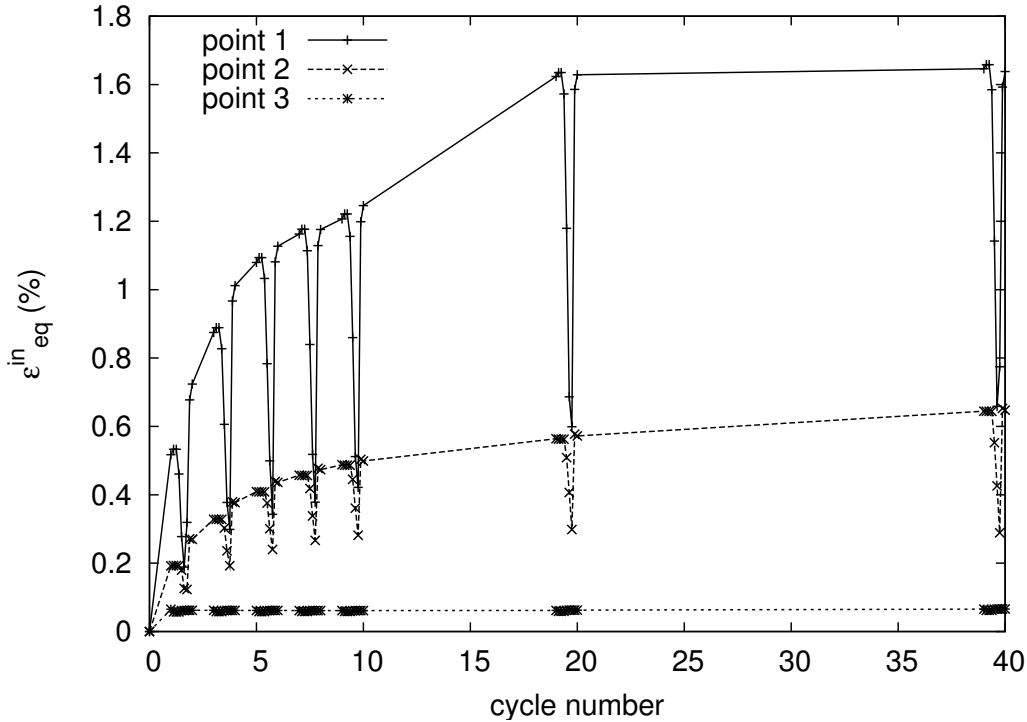


Figure VI.8 : Equivalent inelastic deformation at three integration points marked in Fig. VI.6 in realisation 1.

between the trajectories is small, the projected deviatoric mean stress (marked with points) has not become zero but it has only changed a bit. A cycle represents the smallest sphere in 6 dimensional stress space which can be circumscribed to the stress trajectory of the loading cycle. The mean stress is its center, D its diameter. While strain ratcheting and cyclic plastic deformation act at point 1 (see Fig. VI.8) the stress trajectory has barely changed and the mean stress has not disappeared. On the same part of the FE mesh as in Fig. VI.6 the von Mises norm of the mean stress tensor \bar{C} can be shown for the second and 40th cycle (see Fig. VI.10). The regions with the highest mean stresses are located under the border of contact on the left of the contour plot, but in this region no plastic deformation takes place so no change in the mean stress happens. Near the contact surface, the mean stress is lower. There is some grain dependence, some grain boundaries are marked by zones with high mean stresses. In the 40th fretting cycle, the mean stress is increased in grains with high plastic deformation and unchanged in grains with little or no plastic deformation. The highest increase can be observed near grain boundaries.

As the mean stress in plastically deforming grains near the contact surface does not relax but increase, the Dang Van HCF parameter should be adapted by replacing the stress range (R) by the plain von Mises stress (J_2). The HCF parameter needs to be computed using a loading cycle with the cyclically stabilized stress/strain response. During the 40 fretting cycles computed with this model total stabilisation may not have been reached, but the main part of material adaptation has taken place, so the last cycle may be suitable for a coarse HCF prediction. The Dang Van plot of point 1 marked in Fig. VI.6 in realisation 1 is given in Fig. VI.11. Classically stress range and hydrostatic tension are the variables of the criteria. If the stress range R is replaced by the von Mises stress J_2 the trajectory at low hydrostatic tensions gets wider. The most critical point where the distance between the HCF limit and the

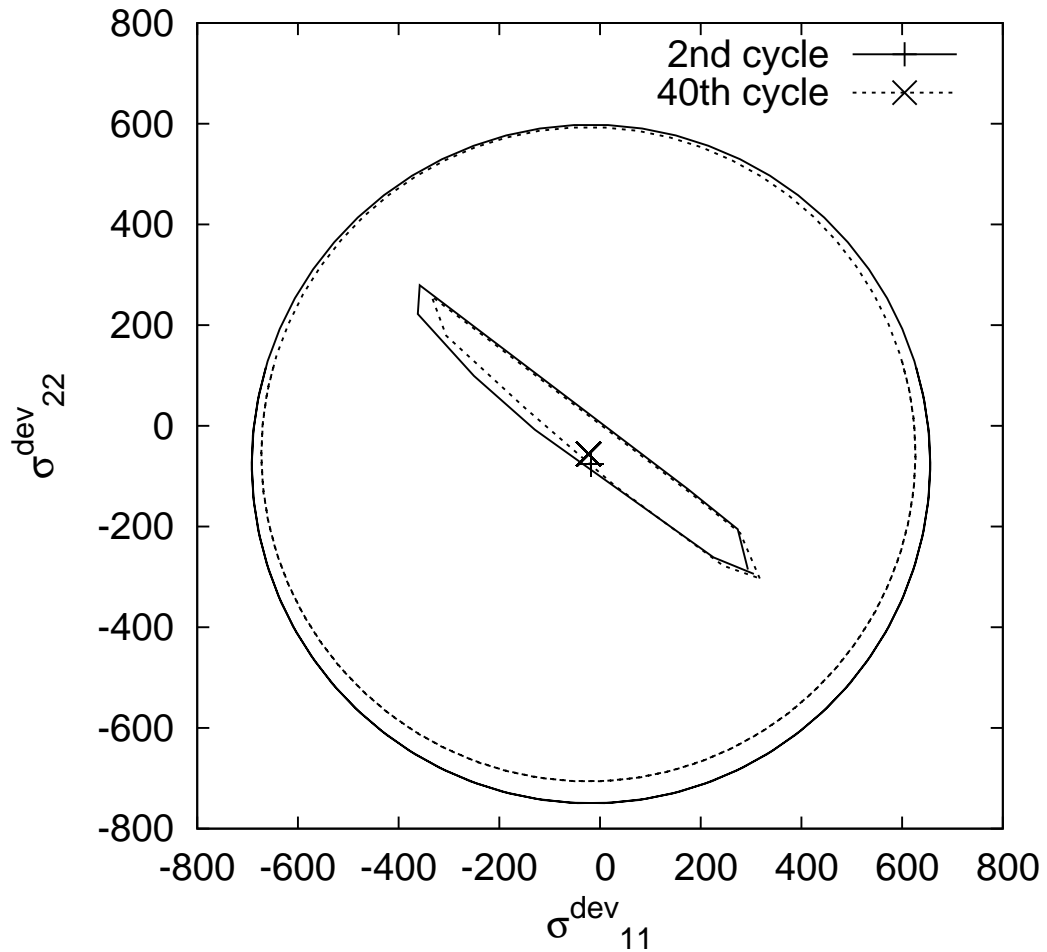


Figure VI.9 : $\sigma_{11}^{dev}-\sigma_{22}^{dev}$ trajectory (designated with lines), mean stress (designated with points) and the radius of the smallest sphere in 6 dimensional stress space which can be circumscribed to the stress trajectory of the loading cycle (designated by a circle). Shown for point 1 marked in Fig. VI.6 in realisation 1 for cycle two and 40.

trajectory is smallest is located at high hydrostatic tension where the difference between stress range R and von Mises stress J_2 is smallest, so the fatigue parameter remains unchanged. In Fig. VI.12 zones where high cycle fatigue is predicted using the 40th fretting cycle, are marked. Once the classical Dang Van criteria is used, once the stress range is replaced by the von Mises stress. Some isolated black spots on the contour maps are artefacts originating from the FE problem resolution and can be ignored. The difference between the two results is small and most pronounced at the left border of the contact surface.

Comparing the contour maps of the Dang Van parameter with that of the equivalent inelastic strain, it appears that zones with high plastic deformation are not necessarily predicted to experience fatigue, independently of the type of Dang Van parameter employed for computation. On the other hand microplasticity is acknowledged to be the driving force of HCF. So fatigue prediction with microstructural material models may better be performed using a plastic deformation measure. For the application with polycrystal material models the fatigue parameters of Smith-Watson-Topper (Socie, 1987) and Fatemi-Socie (Fatemi and Socie, 1988) have been adapted and applied by Goh et. al (Goh et al., 2001). A further evaluation of HCF parameters for the use with polycrystal plasticity material models should

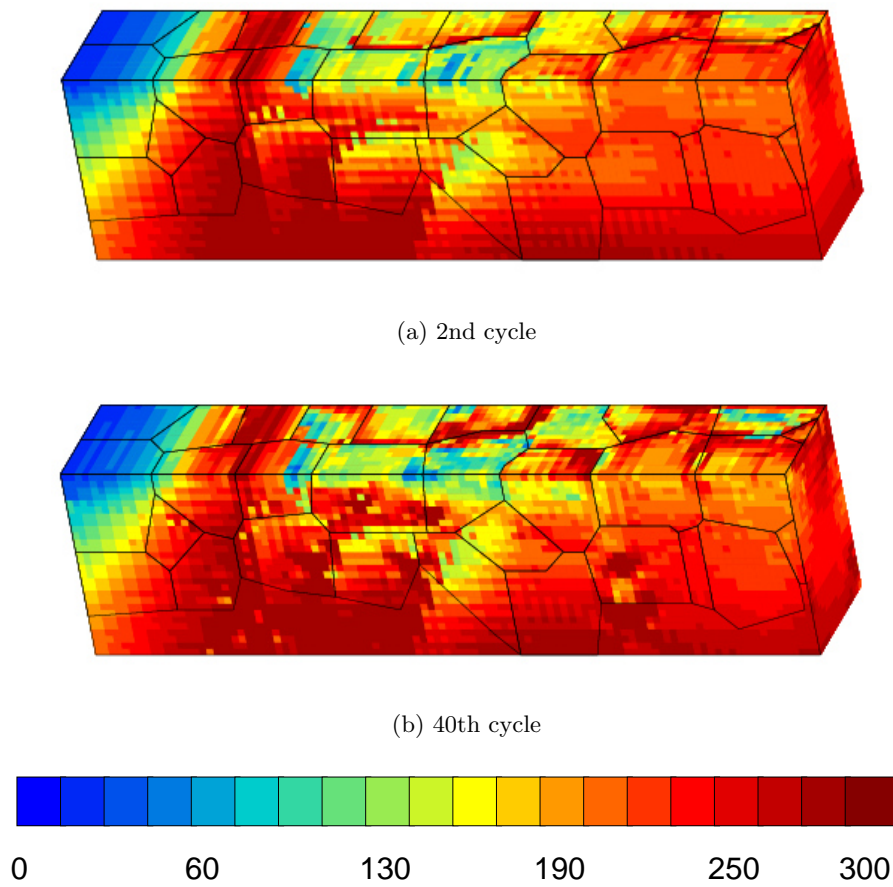


Figure VI.10 : Von Mises norm of the mean stress tensor in the second and 40th cycle on the left half of the plate where the polycrystal plasticity model is used.

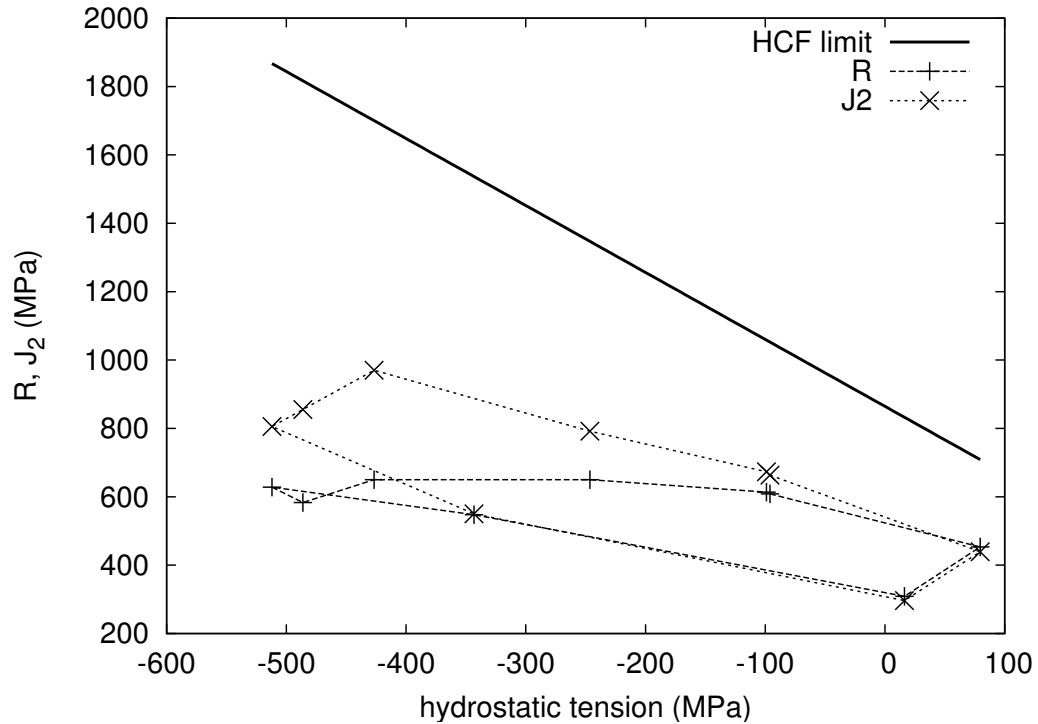


Figure VI.11 : Dang Van curve at point 1 marked in Fig. VI.6 in realisation 1. Stress range R and alternatively the von Mises stress J_2 are plotted over the hydrostatic tension. The straight line represents the HCF limit found with equ. VI.1.

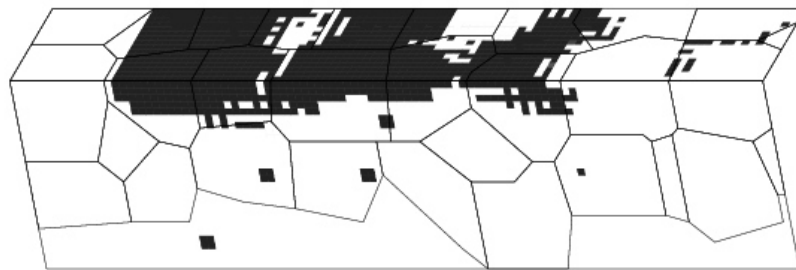
be made using microscale fatigue observations as a reference.

VI.4 Discussion of J_2 and polycrystal plasticity approach

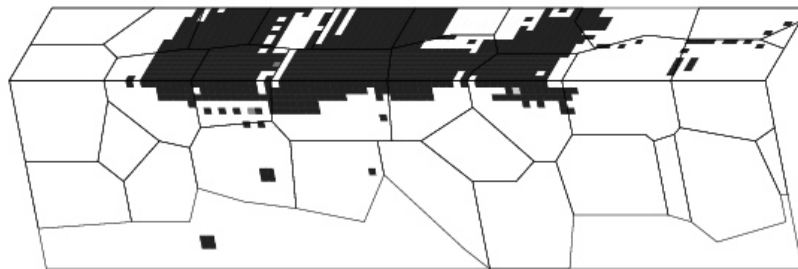
All fretting computations in this section only differ in the employed material model, so the behaviour of all material models in contact and their influence on fatigue prediction can now be compared. The J_2 computations shows the *structural* influence on material plasticity which is determined by the cylinder/plate contact. The polycrystal plasticity computations additionally show the *micro structural* influence on material plasticity which is determined by the geometry and crystallographic orientation of the grains. Since only a few grains fit into this contact's half width, the macro and micro structural influences are of equal importance when stress and strain fields are to be assessed.

The contact situation is special to fatigue prediction because neither strain nor stress are imposed. As a consequence it is not a priori known whether fatigue by strain ratchetting or by cyclic plastic deformation will happen. So material models should be able to cope with all possible types of material reaction, among which are cyclic plasticity with hardening/softening, ratchetting and mean stress relaxation.

(i) With the classical J_2 material model which is commonly used by engineers, the response of the whole system remains elastic, so no geometry change and consequently no change in the contact pressure is obtained. At the same time it is known that in this modelling approach a higher than realistic elastic limit is used. As a consequence strain ratchetting, which is characterised by very small plastic deformation per cycle at relatively low stress levels, cannot



(a) Dang Van HCF limit: $f(\sigma) = R - aP - b$



(b) Dang Van HCF limit: $f(\sigma) = J_2 - aP - b$

Figure VI.12 : Contour maps of the HCF limit using the Dang Van parameter, once using the stress range R and once using the von Mises stress J_2 , 40th fretting cycle, left half of the plate where the polycrystal plasticity model is used.

be described.

(ii) A J_2 material model with a multikinematic identification method has been proved to be able to describe strain ratchetting (Chaboche and Nouailhas, 1989a; Chaboche and Nouailhas, 1989b), so this approach has been adapted here in a qualitative manner next. When it is used, the computations give an extended plastically deformed zone near the contact. It has been shown that strain ratchetting proceeds and does not shake down nor decelerate, but due to cyclic material softening it even accelerates. The consequence is a cycle by cycle change of the contact pressure whereby the pressure at the centre of contact diminishes and peaks at the contact borders form. Stress redistribution by ratchetting has a positive effect on crack initiation as predicted by Dang Van's multiaxial fatigue criterion. The zones on cylinder and plate where crack initiation is predicted diminish with the number of loading cycles. As high strain ratchetting rates are obtained in this computation it may be concluded that ratchetting is the mechanism that leads to failure. Then a critical deformation as proposed by (Kapoor, 1994) may be a suitable fatigue criterion. Such a conclusion is premature as the employed material model could not be identified from ratchetting tests because none were available. What has been shown is the susceptibility of the fretting contact to ratchetting, the ratchetting rate may be grossly exaggerated.

(iii) A crystal plasticity material model has been employed next. This allows the resolution of micro structural stress and strain fields. Also the cyclic material response, including mean stress relaxation, can be described in a quantitative manner. Mean stress relaxation is observed in fatigue tests under deformation control, strain ratchetting is observed under stress control. Both phenomena may be suspected to have the same cause which is a slow, cycle by cycle adaptation of the sample to an external loading by elongation. Consequently it may be assumed that the crystal plasticity material model, even though it is not identified from ratchetting tests, allows a coarse estimation of the material's ratchetting behaviour. In fretting computations with polycrystal plasticity, strain ratchetting generally decelerates in the first 40 fretting cycles. Less strain ratchetting than in computations with the multikinematic material model is obtained. The strain and stress fields at the contact are heterogeneous depending on the geometry and crystallographic orientation of grains. In some grains ε_{eq}^{in} reaches over 1%, which is due to strain ratchetting (which shakes down or decelerates) and cyclic plasticity (which increases due to cyclic material softening). Comparing the contact pressure distribution after some fretting cycles in this computation to that with a multikinematic J_2 material model, a more heterogeneous result depending on the micro structure is found. A general diminution of the contact stresses and the increase in the contact half width as in computations with the multikinematic material model are not obtained because strain ratchetting is comparatively small. Some uncertainty comes from the fact that polycrystal plasticity was only employed on the left half of the plate while the rest of the structure was computed using the classical J_2 material model which in this computation deformed elastically only. As ratchetting in the polycrystal plasticity computation is less intense and reduces during the 40 computed fretting cycles its influence on HCF prediction by the Dang Van parameter is less pronounced.

VI.5 Conclusion

- Using the *multikinematic von Mises material model* it has been shown that fretting contacts are susceptible to strain ratchetting. Strain ratchetting leads to contact geometry change, stress redistribution and residual stress fields.
- Fretting computations with *polycrystal plasticity* showed that the micro structural heterogeneity of Ti6Al4V has a strong influence on the strain and stress fields in the

fretting contact. The results depend on the stochastic orientation of the grains and is consequently different from that obtained with von Mises material models. This may be one cause for the higher scatter among in fretting fatigue tests when compared to conventional fatigue tests where bigger material volumes are critically loaded.

- Strain ratchetting and crack initiation as predicted by multiaxial fatigue parameters are considered as two different fatigue mechanisms. For fatigue prediction on the structural scale the Dang Van parameter is proposed. If ratchetting leads to material failure a critical deformation may serve as fatigue criterion (Kapoor, 1994).
- The Dang Van HCF parameter has been reevaluated using the polycrystal material model. It has been found that the hypothesis of mean stress relaxation in plastically deforming grains, which justifies the disregard of the mean stress and the use of a stress range in the model, is not fulfilled at the contact surface when a polycrystal plasticity model is used. Consequently the Dang Van parameter has been applied in a modified version where the stress range was replaced by the actual von Mises stress.

Chapter -VII-

Interaction of wear and fatigue in fretting contacts

VII.1 Comparing experiments with crystal plasticity computations

VII.1.1 Introduction

The damage mechanisms in fretting tests are wear and fatigue cracking. Using the 10^6 cycle fretting tests of Vincent Fridrici (Fridrici, 2002) a material response fretting map can be drawn (see Fig. VII.1). Depending on the displacement amplitude and the normal load in a test no damage, fatigue cracking, fatigue cracking and wear or only wear was obtained. These four domains are indicated in this material response fretting map. Additionally the running condition is given: By linear elastic computations the field can be split into a partial slip and a total slip domain. In elasto-plastic computations an additional domain can be found where the bodys relative displacements are not accommodated by contact sliding but by surface near material shearing. In this work FE fretting computations with polycrystal plasticity are made. Because of the heterogeneous material properties in crystal plasticity the transition between contact slip and material shearing is continuous in such computations. The border indicated in Fig. VII.1 marks the onset of plastic shearing.

In the partial slip domain no damage is obtained in experiments with low normal forces (133 MPa), at higher normal forces (233 MPa, 333 MPa) cracks have been detected in tests with sufficiently high displacement amplitudes. In the total slip and plastic shearing regimes wear is the only damage mechanism at low normal forces (133 MPa). At higher normal forces (233 MPa, 333 MPa) wear and cracking are both detected at lower, only wear at higher displacement amplitudes. In the total slip regime wear is detected irrespective of the normal loading. In section V.1 it has been concluded that adhesion is a main source of wear at low normal forces and material deformation as computed using von Mises material models is not sufficient to explain the wear process. But in section VI.3 it has been shown that with a microstructural scale material model plastic deformation at the contacting surfaces is obtained, so in addition to adhesion micro scale material plasticity may be a source for wear. And this effect is of increasing importance when the normal force of increased – then wear by material plasticity may be more dominant than wear by adhesion. The deepest cracks in

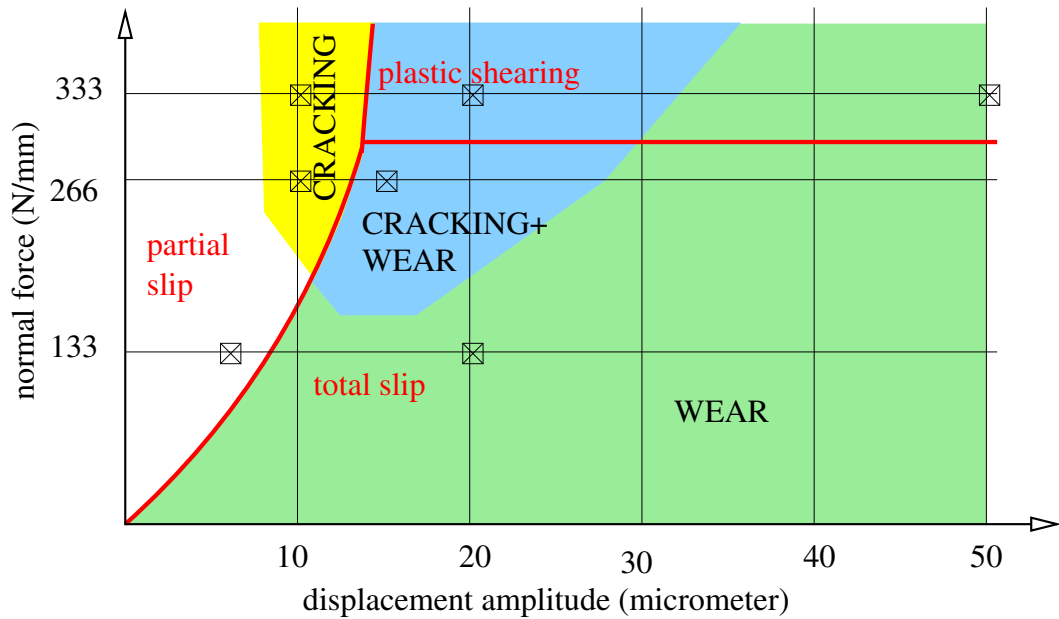


Figure VII.1 : Material response fretting map as found by (Fridrici, 2002). The loading conditions of computations shown in this section are marked.

fretting tests are obtained in the "mixed slip regime" where wear is observed too. (see section II.2, in fretting computations this "mixed slip regime" corresponds to the total slip regime with low displacement amplitudes). It has been reported by (Fouvry et al., 1999a) that wear has the effect of eliminating small cracks before they can grow into the material. Or else wear might be the result of many simultaneous micro cracks that coalesce detaching wear particles instead of propagating into the material (Szolwinski and Farris, 1996). Wear increases with increasing sliding amplitudes, above a critical sliding amplitude no cracking is observed.

In this work an approach focusing on material modelling by crystal plasticity is adapted to simulate wear, fatigue and their interaction. For doing this, a crystal plasticity material model is used with a 3D model of a fretting wear test to make computations in different running conditions. The results are compared to fretting wear tests performed by Vincent Fridrici (Fridrici, 2002).

VII.1.2 Computation setup

Basically the same type of FE mesh as in section VI.3 is used. A 50 μm slice of the cylinder/plate assembly is represented in a 3D mesh using linear full integration elements (see Fig.VI.5). This mesh is gradually refined towards the contact. At the left side of the plate, a regular domain with an element size of 6.0 μm by 5.9 μm by 6.25 μm is present. The box where crystal plasticity is used as a material model has a size of 350 μm by 100 μm by 50 μm . Here Voronoi polyhedra shaped groups of integration points constitute grains with a common crystal orientation and the crystal plasticity material model are used. The same basal texture as described in section IV.3 is used, the normal direction ND coincides with direction "3" in the mesh. The rest of the structure is computed using the conventional von Mises material model given in section IV.2. The contact is modeled with an impactor/target technique, the frictional contact force is introduced by a Coulomb law with a constant isotropic coefficient of friction of 0.8.

As in section VI.3 the loading is applied under displacement control and imposed in two

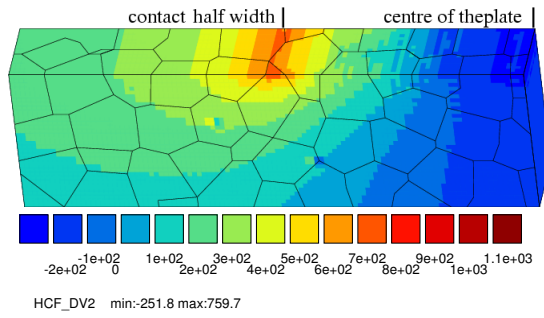
steps. First, a vertical displacement (U2) is imposed at the top of the half cylinder while the plate is fixed by locking its bottom and side nodes. The displacement (U2) is calibrated to cause a vertical forces (P) of 133 N/mm, 267 N/mm or 333 N/mm . Then the cyclic loading is started. The cylinder is fixed by locking the top nodes. The plate performs an oscillating horizontal movement (U1) with a triangular time-displacement curve (see the loading scheme in Fig. V.2). This movement is imposed on the bottom and side nodes of the plate with varying displacement amplitudes and a frequency of 5 Hz, one fretting cycle is computed. All nodes that lie on the front and on the back surfaces of the cylinder and the plate are fixed in direction U3. The imposed boundary conditions in terms of normal forces (P) and displacement amplitudes (δ^*) of all performed computations are indicated with points in the fretting map shown in Fig. VII.1.

VII.1.3 Results and discussion

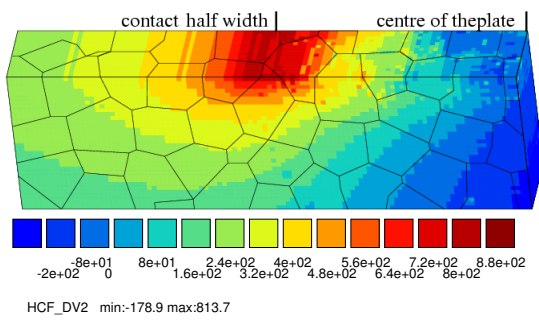
In Fig. VII.2 the Dang Van parameter on the left half of the plate's contacting surface, where crystal plasticity is used as material model, is shown for seven fretting conditions. The indicated values give the stress amplitude of an equivalent fatigue test in the $R_\epsilon = -1$ condition. SNECMA Vernon have provided us with fatigue data of Ti6Al4V. They indicate a stress amplitude of 523 MPa for the high cycle fatigue (HCF) limit in the $R_\epsilon = -1$ condition. So an integration point with a Dang Van parameter higher than 523 MPa is predicted to experience crack initiation. In Fig. VII.3 a measure for the accumulated plastic deformation is given for the same seven fretting conditions. This measure (all_glide) is found at each integration point by the sum of the accumulated basal, prismatic and pyramidal slip.

Looking at the results with a normal force of 133 N/mm it can be stated that a higher displacement amplitude gives rise to higher fatigue parameter values. At the contact border the values are highest and surpass the HCF limit of Ti6Al4V, so crack initiation is predicted (while no crack initiation has been observed in corresponding experiments). A small amount of plastic deformation is obtained in isolated grains in partial slip as well as in total slip. At a normal force of 267 N/mm in the partial slip regime ($\delta^* = 10\mu m$) the qualitative result is the same as in computations with 133 N/mm. Only the maximum fatigue parameter values and accumulated plastic deformation are greater. In total slip ($\delta^* = 15\mu m$) the Dang Van contour plot changes, the highest values are still found at the contact border but some peaks appear nearer to the centre of the plate (right side of the shown contour plot). This is accompanied by heterogeneous but continuous plastic deformation through the whole contacting surface. With a normal force of 333 N/mm in partial slip ($\delta^* = 10\mu m$) the result resembles the before mentioned computations in the partial slip regime. In total slip with $\delta^* = 20\mu m$ the result is similar to that in total slip with $P=267$ N/mm, only the maximum values of fatigue parameter and accumulated deformation are greater. At further increased displacement amplitudes ($\delta^* = 50\mu m$) the fatigue parameter values at the contact border are dwarfed by those at the centre of contact and the amount of accumulated plastic deformation at the contacting surface is further increased.

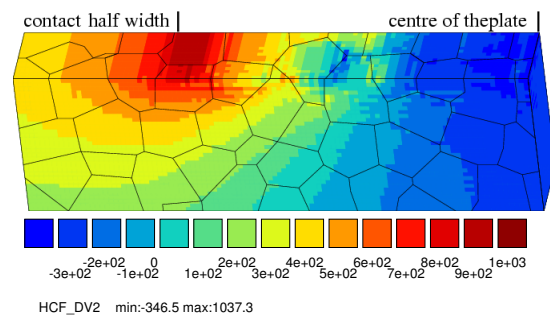
These particular results in fatigue prediction are only obtained with a crystal plasticity material model. In order to proof this the classical von Mises material model given in section IV.2 has been used in a computation with a normal load of 333 N/mm and $\delta^* = 50\mu m$. The results are given in Fig. VII.4 and can be compared to the results of an equivalent computation with crystal plasticity shown in Fig. VII.2(g) and Fig. VII.3(g). The plastic deformation in the von Mises computation is more homogeneous than in the crystal plasticity computation which additionally incorporates the microstructural impact. In the crystal plasticity computations it is the heterogeneous plastic deformation that causes the high fatigue parameter values throughout the contact. In the von Mises computation crack



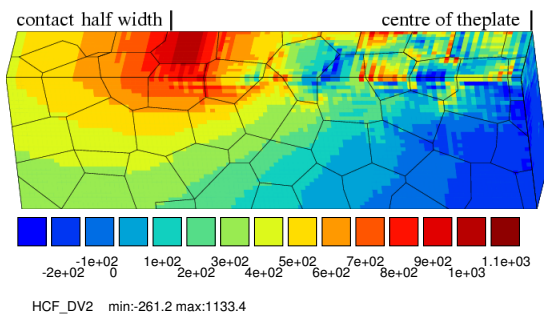
(a) $P=133\text{N/mm}$, $\delta^*=6\mu\text{m}$



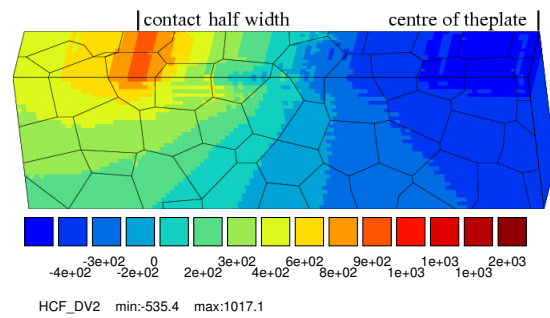
(b) $P=133\text{N/mm}$, $\delta^*=20\mu\text{m}$



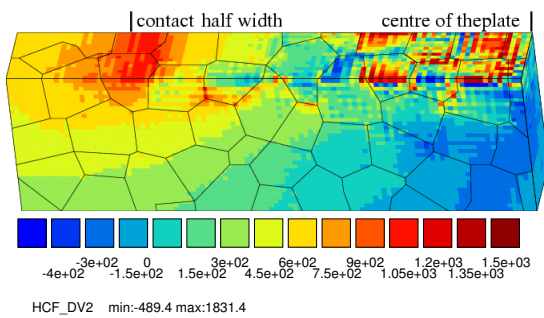
(c) $P=267\text{N/mm}$, $\delta^*=10\mu\text{m}$



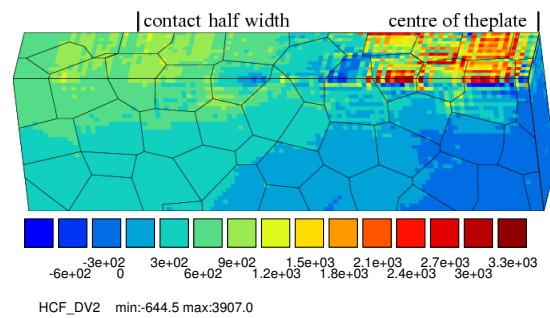
(d) $P=267\text{N/mm}$, $\delta^*=15\mu\text{m}$



(e) $P=333\text{N/mm}$, $\delta^*=10\mu\text{m}$



(f) $P=333\text{N/mm}$, $\delta^*=20\mu\text{m}$



(g) $P=333\text{N/mm}$, $\delta^*=50\mu\text{m}$

Figure VII.2 : Dang Van HCF criterion computed for the first fretting cycle under various loading conditions.

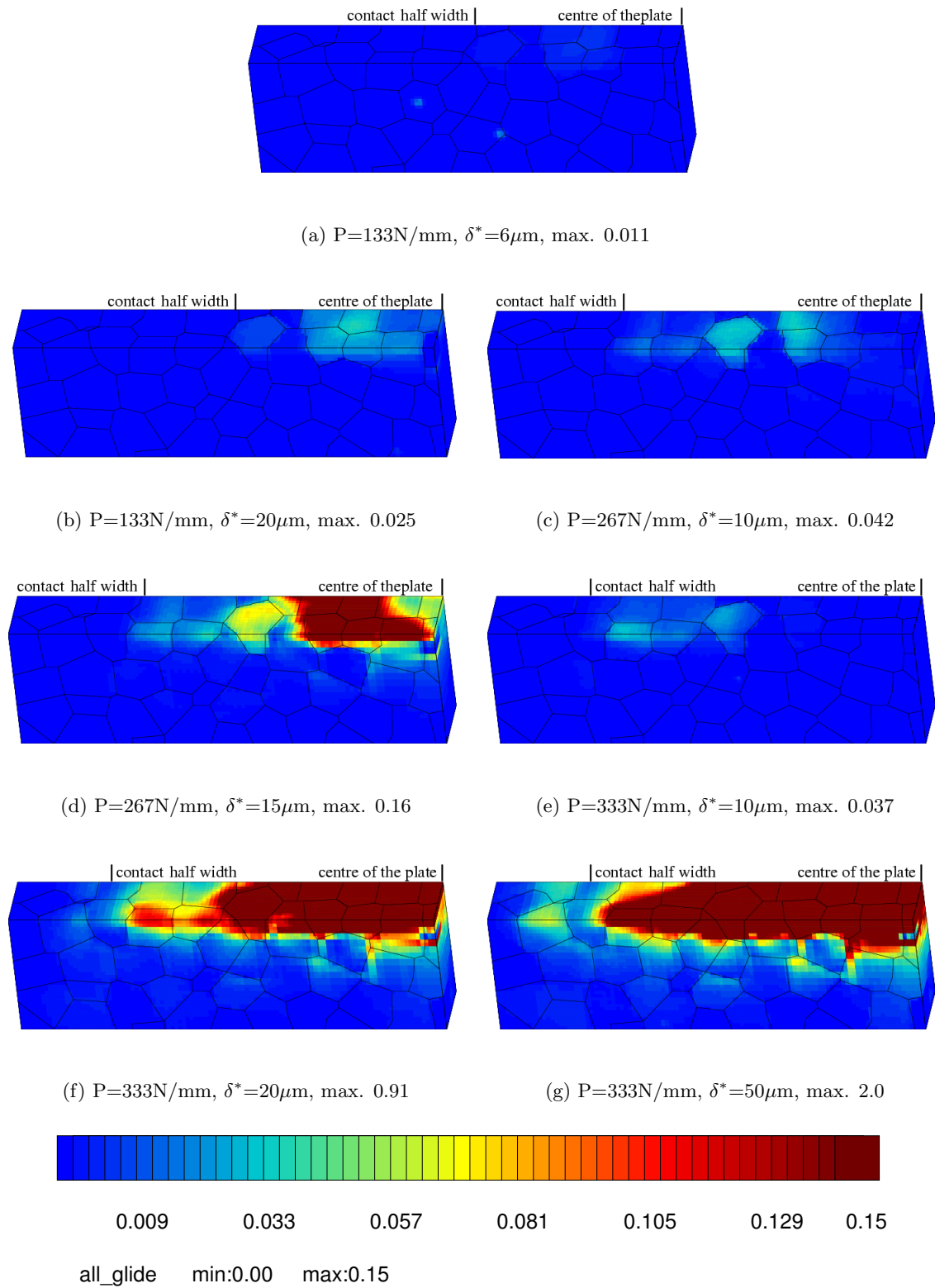


Figure VII.3 : Sum of all accumulated crystallographic slip after the first fretting cycle under various loading conditions.

initiation is only predicted at the contact borders.

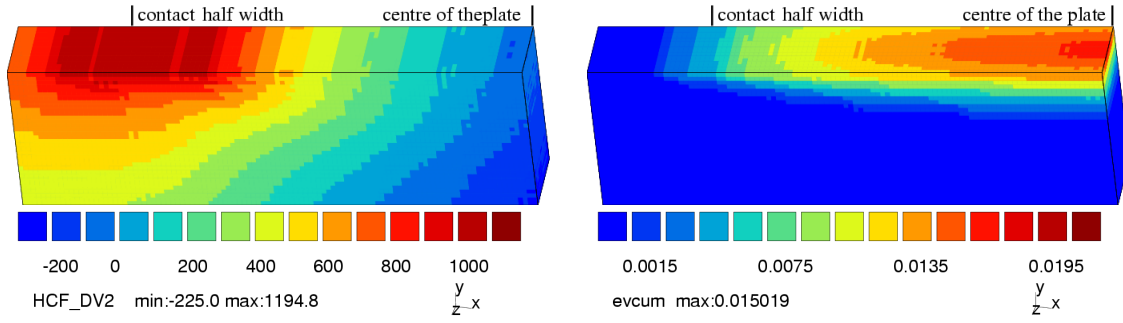
Clearly many effects are neglected in the shown computations. (i) First of all only one fretting cycle was calculated in these computations while fretting damage accumulates over thousands of cycles. (ii) In some computations with high normal forces and displacement amplitudes the small deformations assumption is not applicable and finite strains should be used. (iii) Adhesive wear has not been taken into account. In section V it has been shown that adhesive wear leads to an immediate change of surface roughness. In 10^5 cycles the contact width increases by a factor of 5 and the contact stresses change completely. (iv) Particle generation and ejection is not taken into account. (v) Oxidation is known to play an important role in wear and friction in fretting contacts (Czichos, 1978).

In fretting computations with low normal forces the amount of plastic deformation and the level of the fatigue parameter values is too low to explain the wear obtained in experiments in the total slip regime. Wear is most likely caused by adhesion (see chapter V). At the contact border crack initiation is predicted that is not observed in corresponding experiments. This is a frequently encountered discrepancy that is usually attributed to a size effect and remedied by averaging the stress fields over a determined volume before computing the fatigue parameter (Araujo and Nowell, 2002; Fouvry et al., 1999b). Nevertheless at higher normal loads considerable plastic deformation is obtained in crystal plasticity computations. And plastic deformation and fatigue might then play a more prominent role in the wear process. Here a qualitative attempt to describe wear-fatigue interaction is made:

- (Fridrici, 2002) reported that in partial slip fatigue cracks are always observed at the contact borders. That is also predicted by the fatigue parameter in the computation.
- In the mixed slip regime cracking and wear are observed in fretting experiments. In computations with these fretting conditions high fatigue parameter values are not only found at the contact border but also at multiple sites nearer to the centre of the plate. Multiple cracks in the contact may coalesce and detach wear particles. More isolated cracks at the contact border may grow into the material thus giving raise to the coexistence of fatigue and wear.
- When the sliding amplitude is raised over a limit in experiments, wear is the only damage mechanism and no cracking is observed. At higher displacement amplitudes in computations the fatigue parameter throughout the contact is even more elevated, so more cracks may form. Then all cracks may coalesce forming wear particles and no cracks may escape from the surface, wear would be the only observed damage mechanism.

VII.1.4 Conclusions

Using a 3D crystal plasticity material model fretting computations with different normal forces and displacement amplitudes have been performed and the Dang Van HCF parameter has been used for fatigue prediction. The results were compared to corresponding fretting wear experiments performed by (Fridrici, 2002). In fretting computations with low normal forces the amount of plastic deformation and the level of fatigue parameter values is too low to explain the wear obtained in experiments in the total slip regime. At higher normal forces plastic deformation stretches over the whole subsurface region of the plate and it is assumed that material fatigue is then an important wear mechanism. Possibly the competition of wear and fatigue at increased normal forces may be described by material fatigue. The results indicate crack initiation at the contact border in partial slip. In total slip with low displacement amplitudes cracking at the contact border and multiple site cracking nearer



(a) Dang Van HCF parameter

(b) Accumulated viscoplastic deformation

Figure VII.4 : Fretting computation using the classical von Mises material model (section IV.2). Normal load and displacement amplitude are 333 N/mm and $\delta^*=50\mu\text{m}$ respectively.

to the centre of the plate is predicted. Multiple cracks may coalesce and detach wear particles. This may explain the presence of both wear and fatigue in corresponding fretting experiments. At high displacement amplitudes the fatigue parameter indicates more intensive crack initiation throughout the contact. As the crack density is then high all cracks may coalesce detaching wear particles and no crack escapes from the proximity of the fretting surface.

Many aspects of fretting damage are neglected in the present computations. Among these aspects are cyclic material response, finite strains, adhesive wear and contact geometry change by wear and oxidation. Nevertheless in future work some of them may be integrated. This could be done by taking geometry change by wear into account as shown in section V.2. As a wear criterion the dissipated energy approach or alternatively some material damage parameter could be used. Crack initiation could be modelled using an own damage parameter. Then cracks would form if material volumes managed to accumulate the damage for crack nucleation before they were wiped out by wear.

VII.2 FE models of wear and fatigue in the blade-disc contact

VII.2.1 Introduction

In section V.2 an approach to the computation of wear and related geometry change has been described. The results of computations with a cylinder-plate contact pair have shown that the impact of wear on the stress fields in the contact proximity is large. These cyclic stress fields are used for lifetime prediction. The consequence is that wear has an impact on fatigue prediction which needs to be assessed. SNECMA has provided us with 2D and 3D FE meshes of the blade-disc assembly. In this section these meshes are used for fretting modelling whereby wear and related geometry change are taken into account. In successive cyclic computations the worn meshes are used to assess the influence of wear and cyclic plastic deformation on the predicted fatigue life. For fatigue prediction the Dang Van HCF parameter is used.

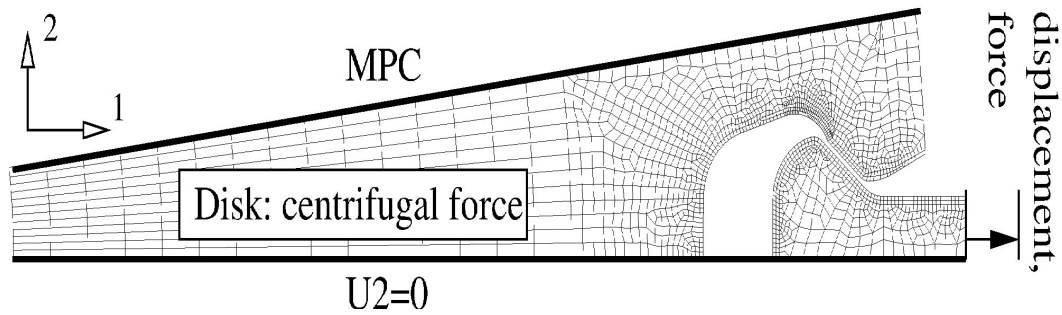


Figure VII.5 : FE mesh and loading schema of the 2D blade/disc contact model.

VII.2.2 Computations with a 2D mesh of blade and disc

a) Computation setup

A 2D representation of the blade/disc assembly in a FE mesh is shown in Fig. VII.5. It is sufficient to take one half of a symmetric section of the assembly into account. So the symmetry within the section is modelled imposing the vertical displacements on the symmetry axis to be zero ($U_2=0$). The radial periodic repetition of the blade/disc sections is taken into account using multiple point constraints. All nodes on this sectional symmetry axis are obliged to share the same displacement vector direction with has a given inclination angle to direction "1". Linear plane strain full integration elements are used. The blade/disc assembly has a cross section which is approximately equal to the cross section of the 3D disc. The assembly is cyclically loaded whereby all loads are applied in phase. One cycle consists of the rise of all loads to the maximum value during one second and the subsequent decrease to zero during one second. A triangular signal shape is used. The disc is subject to a centrifugal loading whereas the angular speed changes between minimum and maximum value, the density of the disc is $4.45 \cdot 10^{-9} \text{ t/mm}^3$. On the half blade a cyclical force is imposed at the vertical right-hand surface indicated in Fig. VII.5. In two computations this force is applied in different ways. Once it is directly applied by force control. And once it is applied by displacement control. That means that a displacement between zero and a maximum value is applied in a way that the maximum force in an elastic computation with the initial unworn mesh is equal to the desired one.

With this FE model wear and related contact geometry change in 100 numerical wear cycles are computed using the same method as applied in section V.2. It is assumed that wear proceeds only on one contacting surface (unilateral wear) which has two reasons. (i) The mesh is too coarse for a detailed description of the contact geometry, the assumption of unilateral wear has a smaller deteriorating influence on the result. (ii) The disc has sharp contact edges and consequently features contact nodes at these locations, the more flat blade does not necessarily have nodes at the contact edges. For the contact description an impactor/target technique is used and wear is computed on the impactor side. The best description of wear and contact pressure at the contact edges is obtained when the disc is set to be impactor. The coefficient of friction is set to 0.9 which represents the behaviour of a dry fretting Ti6Al4V-Ti6Al4V contact. The numerical wear coefficient is set to the highest value with which still no perturbations by wear geometry updating are introduced in the strain/stress response in the contact zone of the FE model. The wear computations are performed using an elastic material model of Ti6Al4V with a Young's modulus of 119 GPa and a Poisson ration of 0.29.

The worn FE meshes are then used for computations with the multikinematic von Mises material model introduced in section IV.2. 100 fretting cycles are calculated using the same

boundary conditions as in the wear computations.

b) Results

In Fig. VII.6(a) the wear per numerical cycle in a computation where the loading of the blade is directly implemented by an imposed force is shown. At the contact borders the greatest wear heights are obtained. It reaches $0.1 \mu\text{m}/\text{cycle}$ in the second wear cycle and decreases to the half during 100 numerical wear cycles. In the contact centre the wear rate stays almost unchanged at about $0.02 \mu\text{m}/\text{cycle}$ and less wear is obtained on the left than on the right contact side. In Fig. VII.6(b) the equivalent result in a computation where the loading of the blade is implemented by displacements is shown. In this computation the amount of wear is greater with $0.16 \mu\text{m}/\text{cycle}$ at the contact borders and about $0.06 \mu\text{m}/\text{cycle}$ in the centre. During 100 numerical wear cycles the wear rate at the contact borders decreases, and the same wear rate of about $0.06 \mu\text{m}/\text{cycle}$ is obtained in the whole contact. A comparison of the accumulated wear of 100 cycles for the two computations is given in Fig. VII.6(c). Evidently a greater wear scar is obtained in a computation with imposed displacements. And on the left side of the contact the difference between the two results is most pronounced. As shown in Fig. VII.6 in both computations the contact pressure at the contact borders diminishes during 100 wear cycles. This effect is more pronounced in the computation with an imposed force on the blade. The difference between the computations can be explained as follows. When the blade is loaded imposing a force, blade and disc are pressed into contact and contact slip accommodates their different elastic deformation. When the load is removed the elastic deformation is reduced and again accommodated by reverse contact slip. But when the external load is zero the two surfaces are still pressed into contact because the frictional force blocks total reverse contact slip. To overcome the frictional force an external force with negative sign would be necessary. So less wear is obtained in the computation with an imposed force (on the blade) where blade and disc are always in contact than in the computation with imposed displacements (on the blade) where the total separation of blade and disc after in each cycle is assured. In the computation where displacements on the blade are imposed the accumulation of wear results in a decrease of the resulting reaction force. After 100 numerical wear cycles this decrease amounts to 4 % of the initial reaction force.

Next it is assessed how the computed wear influences fatigue prediction. This is done performing fretting computations using the initial blade/disc FE mesh and the meshes after 20 and 100 numerical wear cycles. Again computations with imposed force or imposed displacements on the blade are performed. Using the elastic material behaviour of Ti6Al4V the influence of computed wear on HCF prediction can be singled out. By the use of the multikinematic material model (see section IV.2) and the computation of 100 fretting cycles the influence of cyclic plastic deformation and ratchetting is additionally taken into account. The fatigue life is calculated using the Dang Van HCF parameter (see section VI.2), a summary of the results is given in Tab. VII.1. For Ti6Al4V high cycle fatigue is predicted if the fatigue parameter reaches a value greater than 523 MPa. For each computation the maximum value of the von Mises stress and the Dang Van HCF parameter on blade and disc is given. From the given results it can be concluded that:

- In all computations von Mises stress and Dang Van HCF parameter on the disc are greater than on the blade.
- Von Mises stress and Dang Van HCF parameter in computations with imposed displacements on the blade are smaller than in computations with an imposed force on the blade.

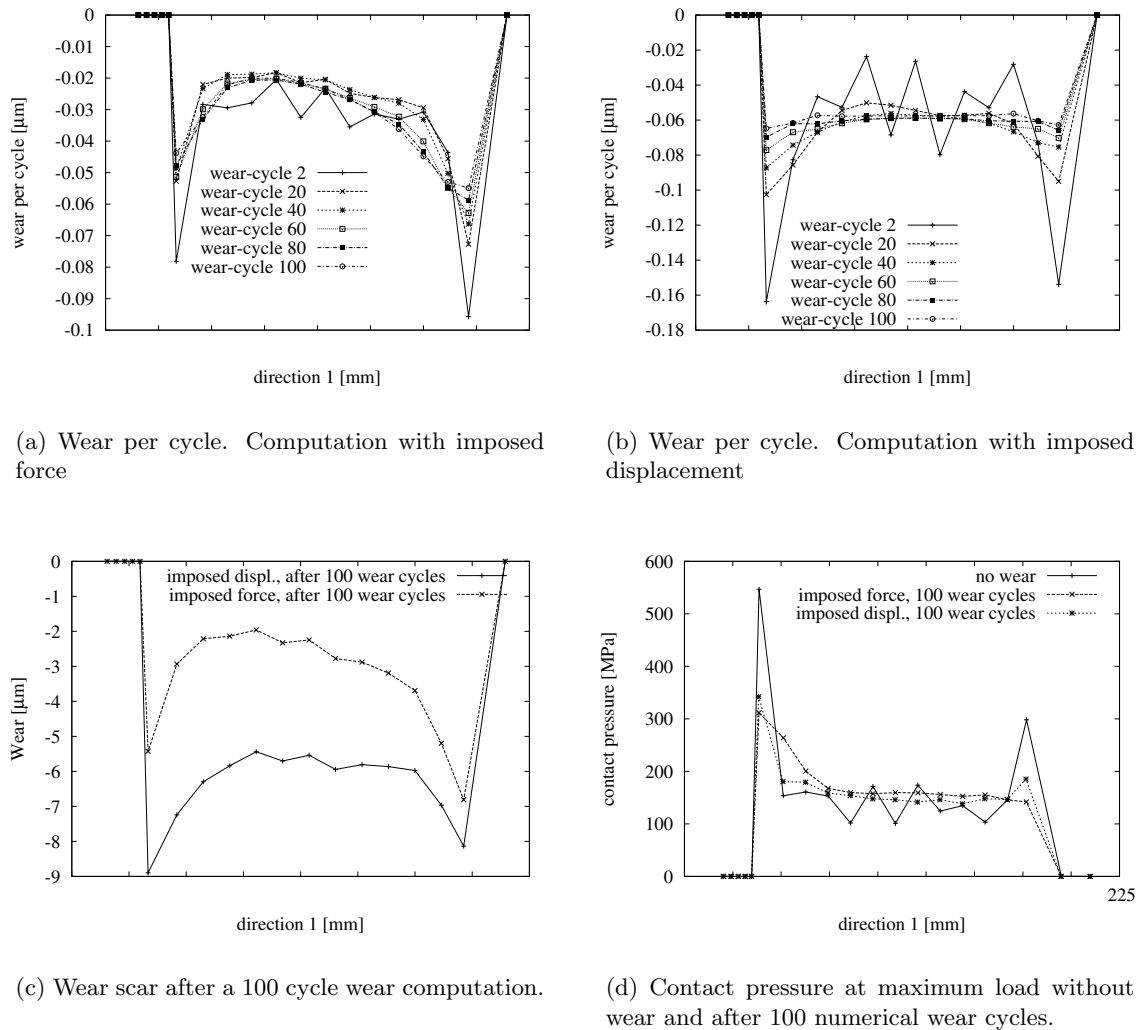


Figure VII.6 : Comparison of wear computations with imposed displacement and imposed force. Elastic material model.

- Wear during 100 numerical cycles is predicted to lead to an improvement of the fatigue life of blade and disc. Assuming that the wear kinetics in cylinder/plate fretting wear experiments performed at the LTDS / Ecole Centrale de Lyon is similar to that in the blade/disc contact it follows that one numerical wear cycle corresponds to 200 experimental wear cycle. Then 100 computed wear cycles correspond to 20000 experimental wear cycles.
- Taking the cyclic plastic material accommodation into account by computing 100 fretting cycles using the multikinematic material model further increases the predicted fatigue life.

The integration points that experience the maximum von Mises stresses are not the same for which the highest Dang Van HCF parameter is calculated. In all computations the maximum von Mises stresses on blade and disc are located at the contact borders and the maximum Dang Van HCF parameters are located away from contact at the surfaces of the bends on disc and blade. In Fig. VII.7 this is shown for the 100th fretting cycle using the multikinematic von Mises material model and the FE mesh after 100 numerical wear cycles.

| Wear | | no wear | | | | 20 wear cyc. | | | | 100 wear cyc. | | | |
|------------|--------------------------------|---------|------|---------------|------|--------------|------|---------------|------|---------------|------|---------------|------|
| Material | | el. | | J_2 -100cyc | | el. | | J_2 -100cyc | | el. | | J_2 -100cyc | |
| Part | | blade | disc | blade | disc | blade | disc | blade | disc | blade | disc | blade | disc |
| imp. force | DV^{\max} | 520 | 531 | 518 | 523 | 515 | 531 | 510 | 526 | 504 | 524 | 500 | 519 |
| | $\sigma_{\text{mises}}^{\max}$ | 572 | 688 | 521 | 597 | 559 | 632 | 522 | 587 | 526 | 559 | 511 | 540 |
| imp. dist. | DV^{\max} | 516 | 520 | 512 | 516 | 502 | 516 | 496 | 509 | 483 | 502 | 481 | 493 |
| | $\sigma_{\text{mises}}^{\max}$ | 564 | 534 | 533 | 617 | 547 | 620 | 527 | 575 | 504 | 534 | 501 | 527 |

Table VII.1 : 2D blade–disc model, maximum values of von Mises stress and Dang Van HCF parameter on blade and disc. Using meshes with no, 20 and 100 cycles of computational wear. With these meshes once an elastic and once a multikinematic J_2 plasticity model was used. In the elastic computation the values were taken from the 2nd, in the J_2 computations from the 100th cycle. All values have the unit MPa.

As has been mentioned in section VI.2, in computations with elasto–plastic material models a fatigue parameter needs to be computed using the stabilised state of the strain–stress response. This is why the strain–stress response of two integration points that experience the maximum von Mises stress and Dang Van parameter is given in Fig. VII.8(a). The location of the two integration points is given in Fig. VII.7, the maximum von Mises stress is located on the disc at the contact border and the maximum Dang Van parameter is located in the bend of the disc. At both integration points strain ratchetting is the main plastic deformation mode. The ratchetting rate decreases and in the 100th cycle it seems not far from shaking down, so the 100th cycle is assumed to serve for a good definitive estimate of the fatigue life.

A Dang Van plot for the same two integration points marked in Fig. VII.7 may give further insight. In a Dang Van plot the stress range is drawn over the hydrostatic tension (see Fig. VII.8(b)). In this plane the HCF limit is given by a straight line and when the trajectory at an integration point crosses the line high cycle fatigue is predicted. Both integration points experience a similar stress range, the big difference between them comes from hydrostatic tension. While the contact edge is protected by hydrostatic compression the bend is not. Hence the fatigue parameter values out of contact are higher. In this computation the fatigue limit is reached by neither of them, so no crack initiation is predicted in this computation.

VII.2.3 Computations with a 3D mesh of blade and disc

a) Computation setup

A blade and a section of a disc are represented in a FE mesh with linear full integration 3D elements. In Fig. VII.9 the whole blade/disc assembly is shown together with the coordinate system and the boundary conditions. Blade and disc have two contact zones. In the z –direction the contact zones are curved, smaller element sizes are used at the front and back ends, in the contact centre the biggest elements span over a 10 times greater length.

The radial sectional periodicity of the disc is modelled using multi point constraints. In the x – y plane all nodes on the surfaces of periodicity are obliged to share the same displacement vector direction which has a given inclination angle to the x –axis, in the z –direction their displacement is unconstrained. This is only an approximation of the sectional periodicity which would be fully valid if the x –axis were a twofold symmetry axis of the blade–disc assembly. The error introduced by this assumption is significant at the surfaces of periodicity but minor in the proximity of the blade–disc contacts. As only the strain–stress fields at the contact proximities are searched for the simplified treatment of the disc’s sectional periodicity is judged to be sufficiently accurate.

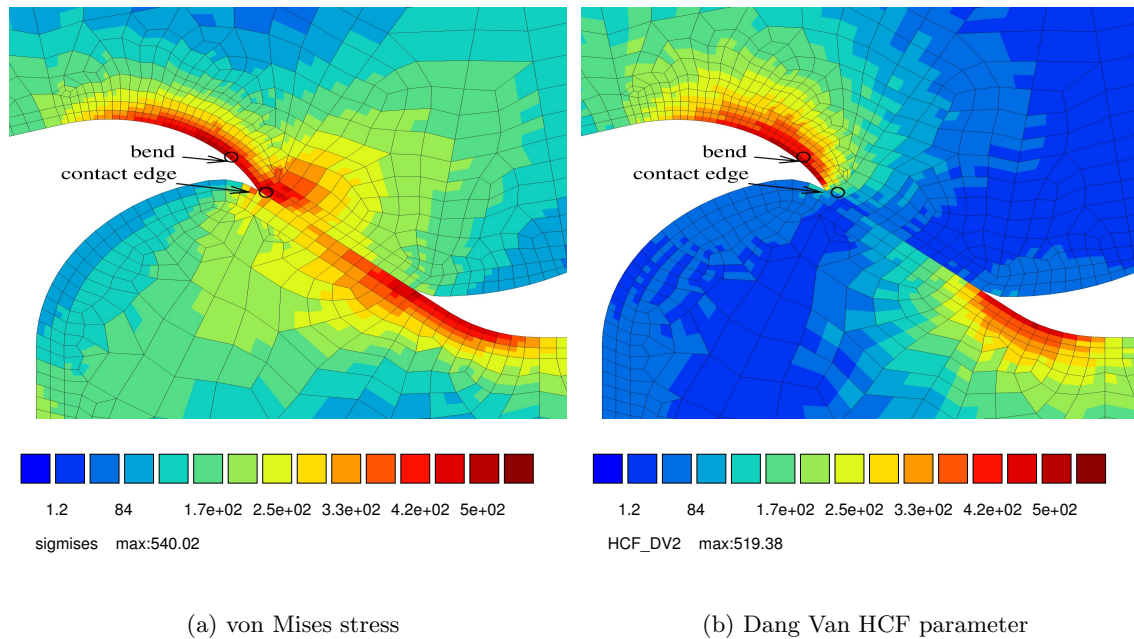


Figure VII.7 : Contour plots of the blade/disc contact after 100 numerical wear cycles and consecutively 100 computational cycles with the multikinematic von Mises material model.

The assembly is cyclically loaded, one cycle consists of the rise of the load to the maximum value during one second and the subsequent decrease to zero during one second, a triangular signal shape is used. The disc and blade are subjected to a centrifugal loading whereas the angular speed changes between a minimum and maximum value. A few nodes marked in Fig. VII.9 are fixed in the z -direction to render the computation statically determinate.

With this FE model wear and related contact geometry change in 100 numerical wear cycles are computed using the same method as applied in section V.2. For the same reasons as in the 2D computation it is assumed that wear proceeds only on one contacting surface (unilateral wear). As in the 2D computation an impactor/target technique is used for contact description and the disc is set to be impactor. The numerical wear coefficient is set to the highest value with which still no perturbations by wear geometry updating are introduced in the strain/stress response in in the contact zone of the FE model. The coefficient of friction is equal to 0.9. The wear computations are performed using an elastic material model of Ti6Al4V with a Young's modulus of 119 GPa and a Poisson ration of 0.29. The worn FE meshes are used for computations using the multikinematic von Mises material model introduced in section IV.2.

FE modelling with the 3D mesh is computationally demanding. The model needs 5 gigabyte of RAM, the computation of one fretting cycle takes one day. This is why a limited number of 29 numerical wear cycles are computed. Using the multikinematic material model 5 fretting cycles are computed.

b) Results

In Fig. VII.10(a) the wear on the disc contact surface in the second numerical cycle is shown. In this graph the blade-disc contact is seen from outside towards the axis of rotation. Between the two contact zones the blade is suspended. Wear is confined to a small fraction of the contact surface. In the contact zone on top the peak value of $9 \mu\text{m}$ is located at the top right

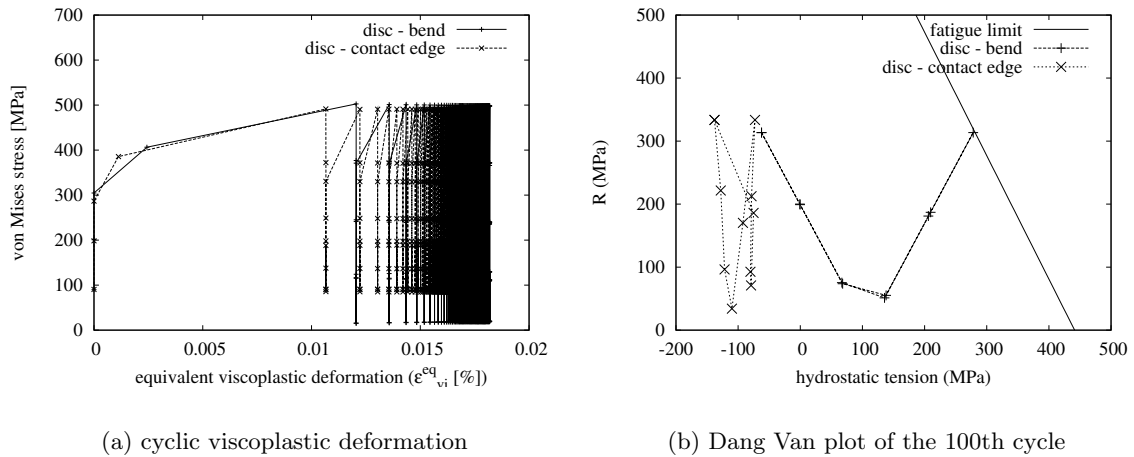


Figure VII.8 : Contour plots of the blade/disc contact after 100 numerical wear cycles and consecutively 100 computational cycles with the multikinematic von Mises material model.

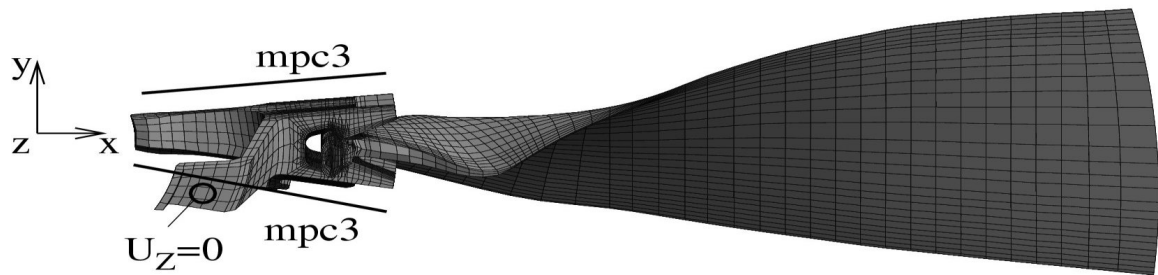
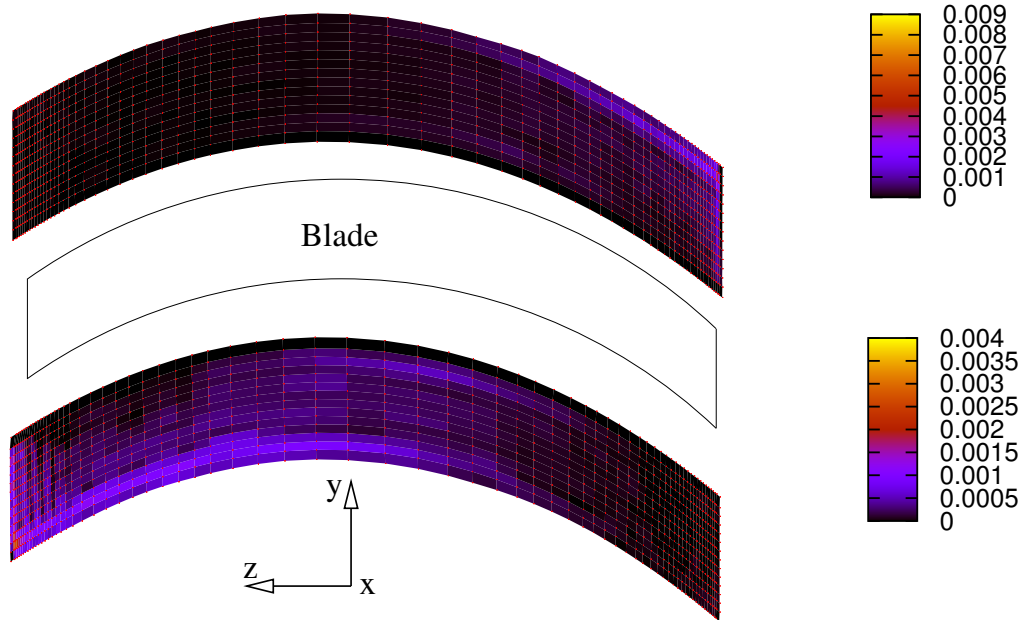


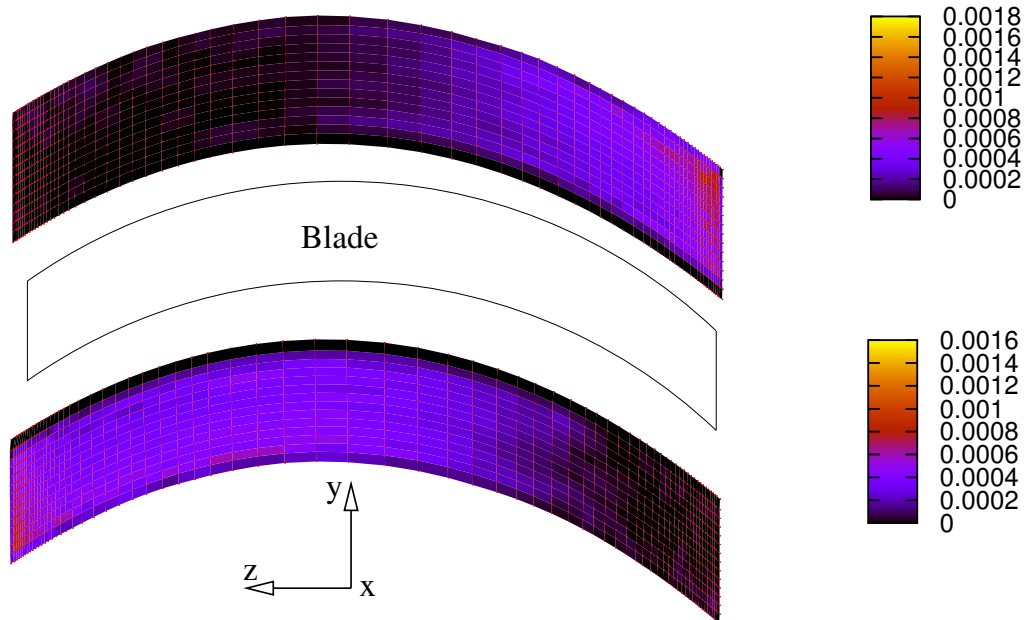
Figure VII.9 : FE mesh, dimensions and boundary conditions

contact edge and severe wear is calculated at the contact borders next to this edge. Small amounts of wear are calculated elsewhere on the right half of this contact zone, on the left half wear is insignificant. In the second (bottom) contact zone wear is computed to be highest with $4 \mu\text{m}$ at the opposite (bottom left) edge. Wear is less concentrated in this contact zone, the left side is more hit than the right. The computed wear as computed in the 29th cycle is shown in Fig. VII.10(b). In comparison to the 2nd cycle wear is spread over a much greater share of the contacting surfaces, the distribution is more even, the maximum wear height is below $2 \mu\text{m}$. But still the left half of the top contact zone and the rightmost part of the bottom contact zone are subject to only comparatively small amounts of wear. The accumulated wear of all 29 wear cycles together is shown in Fig. VII.11. The distribution of wear on the contact surfaces is similar to that in the 29th wear cycle only. In the contact zone on top the peak wear height of approximately $40 \mu\text{m}$ is greater and wear is more concentrated on one (the right) side than in the bottom contact zone with a maximum wear height of about $35 \mu\text{m}$. There wear is more severe on the left side. These results are qualitatively coherent with field experience for this type of blade/disk contact.

As in the 2D computations it is assessed how the computed wear influences fatigue prediction. This is done performing fretting computations using the initial blade/disc FE mesh and meshes after 10 and 20 numerical wear cycles. Using the elastic material behaviour of Ti6Al4V the influence of computed wear on HCF prediction can be singled out. By



(a) wear cycle 2



(b) wear cycle 29

Figure VII.10 : Wear per cycle in the contact on the disc. The units are mm/cycle.

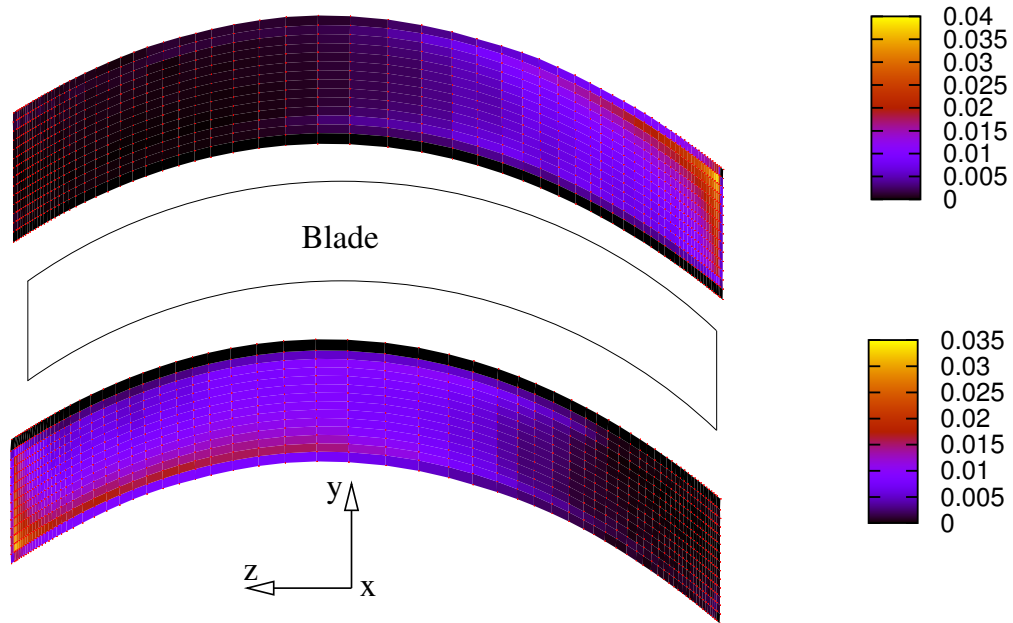


Figure VII.11 : Total wear in the contact on the disc during 29 numerical wear cycles. The wear height is given in the units mm.

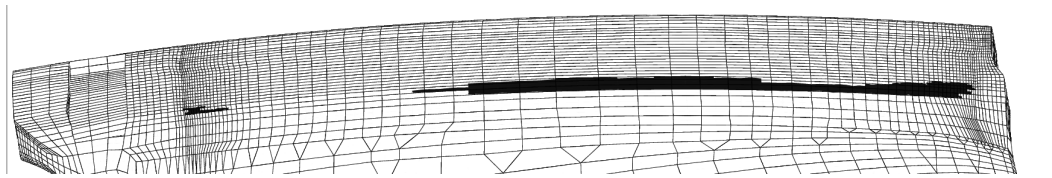
| Wear | no wear | | | | 10 wear cyc. | | | | 20 wear cyc. | | | |
|--------------------------------|---------|------|-------------|------|--------------|------|-------------|------|--------------|------|-------------|------|
| | el. | | J_2 -5cyc | | el. | | J_2 -5cyc | | el. | | J_2 -5cyc | |
| Part | blade | disc | blade | disc | blade | disc | blade | disc | blade | disc | blade | disc |
| DV^{\max} | 902 | 2106 | | | 860 | 1287 | | | 857 | 1192 | 963 | 1414 |
| $\sigma_{\text{mises}}^{\max}$ | 2267 | 2894 | | | 2291 | 2497 | | | 2298 | 2434 | 948 | 1050 |

Table VII.2 : 3D blade-disk computation, maximum values of von Mises stress and Dang Van HCF parameter on blade and disk. Using meshes with no, 10 and 20 cycles of computational wear. With these meshes once an elastic and once a multikinematic J_2 plasticity model was used. In the elastic computation the values were taken from the 2nd, in the J_2 computations from the 5th cycle. All values have the unit MPa.

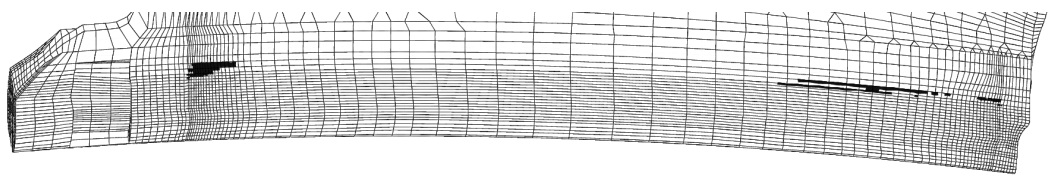
the use of the multikinematic material model (see section IV.2) and the computation of some fretting cycles the influence of reversed cyclic plastic deformation and ratchetting is additionally accounted for. The fatigue life is calculated using the Dang Van HCF parameter (see section VI.2), a summary of the results is given in Tab. VII.2. For Ti6Al4V high cycle fatigue is predicted if the fatigue parameter reaches a value greater than 523 MPa. For each computation the maximum value of the von Mises stress and the Dang Van HCF parameter on blade and disc is given. From the given results it is concluded that:

- In computations with material elasticity (and no representation of plastic deformation) unrealistic von Mises stresses higher than 2000 MPa are obtained while the tensile strength of Ti6Al4V is approximately 1000 MPa.
- Wear leads to a decrease of the maximum von Mises stress and maximum Dang Van parameter on the disc. On the blade the maximum von Mises stress slightly increases, the maximum Dang Van parameter decreases. Wear during 20 numerical cycles is predicted to lead to an improvement of the fatigue life of blade and disc. In all computations maximum Von Mises stress and Dang Van HCF parameter on the disc are greater than on the blade.
- Taking cyclic plasticity into account by computing 5 fretting cycles using the multikinematic material model reduces the predicted fatigue life of blade and disc.

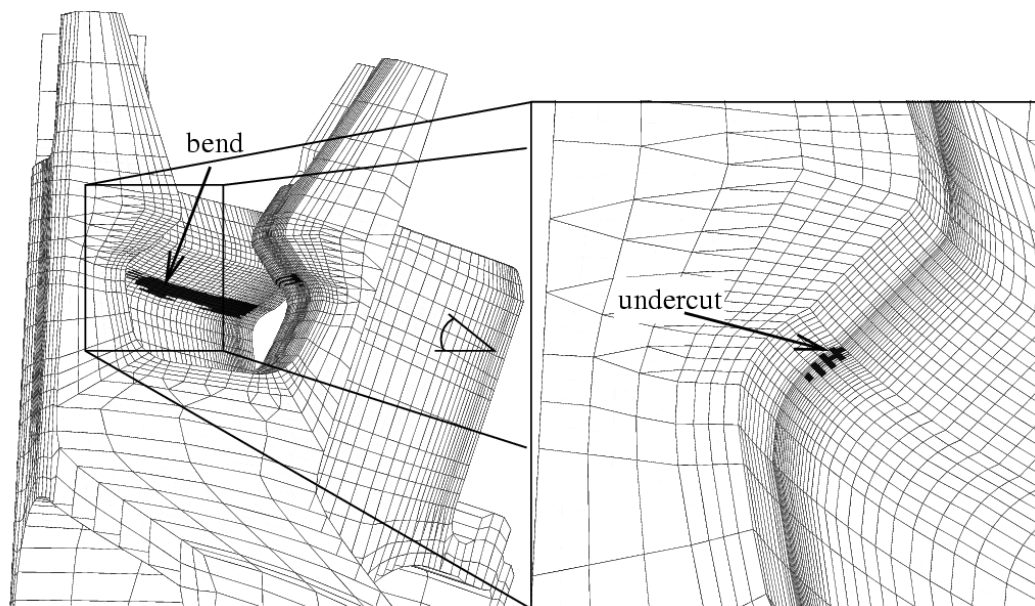
The Dang Van HCF parameter, computed with the 5th fretting cycle using the multikinematic material model and the FE mesh after 20 wear cycles is shown in Fig. VII.12. In these figures integration points that are predicted to experience high cycle fatigue are marked with black colour. The HCF parameter predicts fissuration next to the contacting surfaces in the bend of the blade and the bend of the disc. On blade and disc in the bends shown in Fig. VII.12(a) and Fig. VII.12(c) more extended regions are concerned by fissuration than near the other side (in the y -direction). Near both contact zones the right side (in the z -direction) is more concerned than the left. Peaks of the Dang Van HCF parameter exist in the bends of blade and disc at the contact edges. The highest value of the Dang Van HCF parameter is obtained at an integration point located in the undercut next to the contact edge, its position is indicated in Fig. VII.12(c). A closer look at the change of the Dang Van parameter in the course of wear and cyclic plastic deformation can be made using a Dang Van plot (see Fig. VII.13(b)). In this plot hydrostatic tension (P) and stress range (R) are the x and y coordinates, the fatigue limit appears as a line. In this plane the HCF limit is given by a straight line and when the trajectory at an integration point crosses the line high cycle fatigue is predicted. The trajectory computed using the unworn mesh and elasticity surpasses the HCF limit. The trajectory after 20 wear cycles surpasses it by a lesser amount. The trajectory of the 5th cycle in a computation using the mesh after 20 wear cycles and the multikinematic material model indicates again an increase of the Dang Van parameter. The Dang Van plot shows that wear lowers the Dang Van parameter by decreasing the hydrostatic tension while cyclic plasticity has the opposite effect. The cyclic plastic deformation of the integration point is shown in Fig. VII.13(c). the equivalent viscoplastic deformation, defined as $\varepsilon_{eq}^{in} = ((2/3)\varepsilon_{ij}^{in}\varepsilon_{ij}^{in})^{1/2}$, of the first and fifth fretting cycle indicates reversed plastic deformation and ratchetting. During five cycles none of these deformation mechanisms does shake down. For an integration point in the bend of the disc (indicated in Fig. VII.12(c)) the Dang Van trajectories of the same computations are shown in Fig. VII.13(a). The plot indicates that neither 29 numerical cycles of wear nor cyclic plastic deformation cause a change of the predicted fatigue life at that point. In viscoplastic computations the integration point experiences some strain ratchetting, by the 5th cycle the ratchetting rate is very small (see Fig. VII.13(c)).



(a) Contact proximity of the blade. This side corresponds to the shown part of the disc.

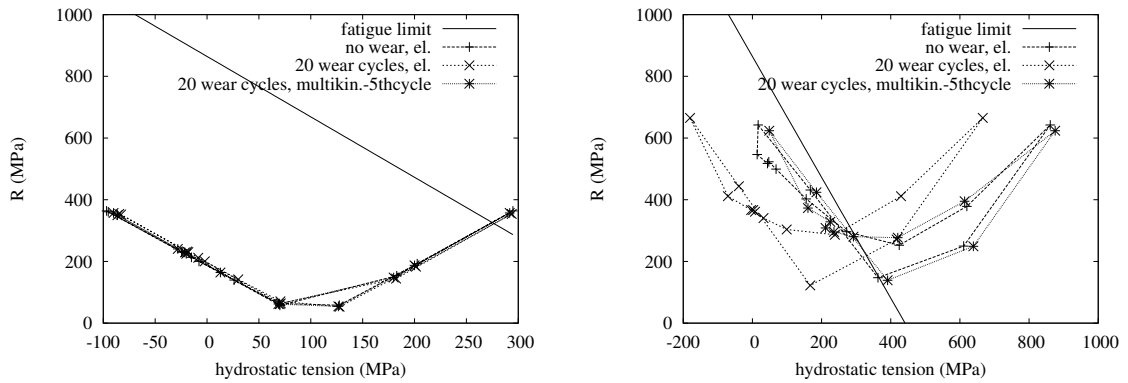


(b) Contact proximity of the blade, side 1



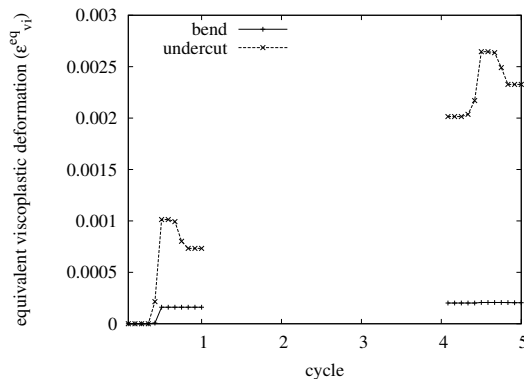
(c) Contact proximity of the disc. On the right side the region with the highest Dang Van HCF parameter is shown.

Figure VII.12 : Contour plot of the Dang Van HCF parameter. The computations have been made with the FE mesh after 20 computational wear cycles. The multikinematic J_2 material model has been used and the Dang Van parameter has been computed on the 5th computational cycle. Regions where high cycle fatigue is predicted are black.



(a) Dang Van plot at an integration point in the bend of the disc (see Fig. VII.12(c)).

(b) Dang Van plot at an integration point at the undercut at the disc's contact proximity (see Fig. VII.12(c)).



(c) Cyclic plastic deformation response at two integration points marked in Fig. VII.12(c).

Figure VII.13 : Cyclic plastic deformation and development of the Dang Van HCF parameter at 2 integration points marked in Fig. VII.12(c). The computations have been made with the FE mesh after 20 computational wear cycles. The multikinematic J_2 material model has been used and the Dang Van parameter has been computed on the 5th computational cycle.

VII.2.4 Discussion

2D and 3D computation are models of the same blade–disc assembly under the same cyclic loading. In the 2D computations more simplifications are made. These include the assumption of (i) symmetry of a blade–disc section (direction 1 is the symmetry axis), (ii) a constant thickness of blade and disc (in direction 3), (iii) the substitution of a centrifugal force on the blade by a force and (iv) the assumption of plane strain. We may start our comparison looking at the computed wear. In the 2D computation the maximum wear height in the second cycle is $0.17\ \mu\text{m}$, the 3D computation gives $9\ \mu\text{m}$. In the 29th wear cycle the maximum wear height is about $0.09\ \mu\text{m}$ and $1.8\ \mu\text{m}$ in the 2D and 3D computations, respectively. The minimum wear height is $0.06\ \mu\text{m}$ and approximately zero in the 2D and 3D computations, in the second as well as in the 29th cycle. Comparing the maximum von Mises stress in the computations with elastic material behaviour it can be stated that plausible results are obtained in 2D as the von Mises stresses do not exceed the apparent elastic limit of Ti6Al4V. In the 3D computation the elastic limit is exceeded by a factor 3 so plastic deformation cannot be neglected. In the 2D and 3D model the application of the Dang Van HCF parameter indicates that wear has a beneficial effect by retarding crack initiation. But in 3D the maximum values are higher than in 2D. In computations with the multikinematic material model the 2D and 3D models give contrary results. The amount of cyclic plastic deformation in 2D computations is by an order of magnitude smaller and has a beneficial effect on fatigue life while it is aggravating in 3D.

On the whole the comparison shows that this 3D problem cannot be reduced to 2D. A contact border that is a line in 3D is represented by a point in 2D. A contact edge in contrary, that is a point in 3D is not represented in a 2D computation. It is the proximity of the contact edges where the shortest fatigue life is predicted in 3D. Also the variation of wear and fatigue on the z-axis in the 3D computation shows that the asymmetry of the curved contact zones and of the loading have a strong influence on the result that is not accounted for in 2D computations. Observations have revealed that crack initiation in the blade–disc contact always happens in the contact proximity of the disc. 2D and 3D computations are consistent with this as the maximum Dang Van parameter is higher on the disc than on the blade. But only the 3D model predicts first cracking in the contact proximity (at the contact edges, the 2D model gives the shortest fatigue lifetime in the disc bend).

Neither the 2D nor the 3D model has a sufficient mesh refinement for an accurate calculation of the stress–strain state and the fatigue parameter. This can be seen in Fig. VII.6(d) where contact pressure peaks are resolved by one node only. In Fig. VII.7(a) the von Mises stress between two integration points changes by hundreds of MPa near contact in the disc bend. Additionally the linear full integration elements are not capable of giving a faithful description of the hydrostatic pressure. This needs to be corrected by averaging this value in each elements. As this would further deteriorate the local resolution of the result no averaging is performed in this work.

VII.2.5 Conclusion

Using 2D and 3D FE models of a blade–disc assembly geometry change by wear during cyclic loading and its influence on fatigue prediction were calculated. Wear was computed using the dissipated energy approach as a local wear criterion. The wear cyclic wear computations were performed using an elastic material model of Ti6Al4V. The change of the contact surface of the disc has been taken into account by updating the position of the disc’s contact nodes by wear after each loading cycle. 100 numerical wear cycles which may correspond to approximately 20000 experimental wear cycles have been computed. Using the worn FE meshes cyclic fretting computations with alternatively elastic material behaviour or a multikinematic von Mises material model were performed. The results can be summarised as follows:

- 2D as well as 3D computations indicate that geometry change by wear has a beneficial effect on the fatigue lifetime of the blade–disc structure.
- In 2D computations cyclic plasticity increased the fatigue lifetime of the structure while it reduced fatigue lifetime in the 3D computations. Cyclic plastic deformation is stronger in 3D than in 2D computations.
- In 2D as well as in 3D computations the highest Dang Van HCF parameter was obtained disc on the disc. In 2D computations the maximum was located in the bend of the disc, in the 3D computation it was located in the proximity of a contact edge. The 3D result matches with the observation that cracks in blade–disc contacts nucleate on the disc at the contact border on the side of the bend.
- Computed wear and fatigue in 2D and 3D computations differ in orders of magnitude. A main reason for this is the non–uniformity of the blade–disc contact in the 3–direction caused by the curvature of the contact zones.
- The mesh refinement of both the 2D and 3D computation is insufficient for the resolution of all stress gradients. Due to this the calculated fatigue lives are probably too optimistic.

In future work 3D FE modelling will be indispensable for obtaining realistic wear and fatigue predictions in the blade–disc contact. The assumption of elastic material behaviour is not realistic and cyclic plastic deformation should be taken into account when wear and related geometry change are computed. Also a better mesh refinement is necessary to resolve the high stress gradients at the contact proximity and in the bends of blade and disc.

Chapter -VIII-

General conclusions and outlook

During the service life of turbo engines fan blades and disc are pressed into contact by centrifugal forces and perform a micrometer size oscillatory relative motion. This promotes fretting damage at the blade and disc contact sites by cracking and wear. In this work aspects of fretting damage modelling in the blade/disc contact are treated by means of finite element computations.

Frictional modelling: A friction model for the description of the friction coefficient during the degradation of the palliative coatings used by SNECMA to shield the blade–disc Ti6Al4V–Ti6Al4V contact (Fridrici, 2002) is developed. In the friction model it is assumed that the solid lubricant coating (Molydag) and the very rough plasma sprayed CuNiIn coating form a composite contact whereby Molydag fills the wholes between CuNiIn asperities. If the surface share, the material properties and the friction coefficients of the composite contact component materials are known, upper and lower bounds of the global friction coefficient (COF) can be computed with the analytical method developed in this thesis. Finite element computations, where a variety of exemplary morphologies of the composite contact is introduced, are then performed. Additionally computations with different characteristic sizes of the composite contact patterns in relation to the contact size are made and the influence of material plasticity on the global friction coefficient is addressed. In all finite element computations the computed global friction coefficient (COF) lies within the bounds given by the analytic model.

In the scope of this thesis the friction model is not applied to blade–disc computations. In future work it can become part of a model for the description of the change of the global friction coefficient in fretting contacts with rough coated contact surfaces as encountered in the fan of SNECMA CFM–56 turbines:

- For this the morphology of the CuNiIn surface roughness needs to be measured and modelled. Then it is assumed that Molydag fills the space between the CuNiIn asperities.
- By wear material is removed slice by slice. This can be computed using the dissipated energy approach, alternatively an asperity scale wear criterion can be developed.
- Due to wear the surface share of the composite contact components and the morphology on the composite contact layer change. As a consequence the global friction coefficient changes which can be calculated using the model shown in chapter V and (Dick and Cailletaud, 2006a).

Wear modelling: In fretting tests with dry Ti6Al4V–Ti6Al4V contacts friction coefficient and fretting log, the wear rate and the contact geometry are all not constant but change. For example during the first view hundred cycles in cylinder–plate fretting tests the contact geometry and the fretting log change while no material loss by wear is obtained in measurements (Sauger et al., 2000). The fretting log develops a particular shape whereby peaks of the tangential force at displacement amplitudes appear. The results of fretting tests performed during a collaboration by Christophe Paulin at the LTDS/ECL show that this change of the fretting log is accompanied by the build up of asperities on both contact surfaces. This cannot be predicted by FE computations using a constant friction coefficient and refined von Mises material models as have been performed by us. But by an FE model including the observed asperities we can show in which way asperity interaction changes the fretting log. From tests and computations we conclude that adhesion, which is not accounted for in the model, is the main cause of damage in the initial phase of this fretting wear test (Dick et al., 2006). This work was conducted in a collaboration between the LTDS (Ecole Centrale de Lyon) performing fretting experiments and us performing computations. It permitted us a better understanding of the friction mechanisms during fretting experiments. It would be fruitful to extend the common work to experiments with greater cycle numbers.

In fretting experiments it is observed that after the destruction of the asperities and the establishment of a debris bed in the contact, material loss by wear starts. In this work wear and related contact geometry change, the change of contact stresses and fretting log are calculated in 2D and 3D FE computations. This is done by iteratively updating the position of the contact nodes during cyclic computations. For node position updating a wear criterion using the dissipated friction energy is applied (Fouvry et al., 1996). The difference between computations, where geometry change by wear is assumed to proceed on one or both surfaces is explored (uni-, bilateral wear). It is shown that in bilateral wear the resulting wear scar is deeper, the contact pressures are lower and the contact size is greater than in unilateral wear computations. In the computations a fretting log with a similar shape as in corresponding fretting wear experiments is obtained. So we conclude that the typical shape of the fretting log during this phase of a fretting experiment is caused by the wear scar geometry. In future work one may combine the computation of geometry change by wear with a remeshing procedure that includes a transfer of the state variables from the old to the new mesh. Then such computations can be performed with nonlinear material models.

Material modelling and fatigue prediction: Other authors have shown that strain ratchetting is a possible deformation mode in fretting contacts (Ambrico and Begley, 2000). In this work a von Mises material model using a multikinematic identification method, which has been proved to be suitable for the modelling of strain ratchetting (Chaboche and Nouailhas, 1989a) is applied to the titanium alloy Ti6Al4V in a qualitative manner. Computations with this multikinematic material model and a model of a cylinder/plate fretting test show the susceptibility of the fretting situation to strain ratchetting. The consequences of ratchetting are a small cycle by cycle change of the contact geometry and a change of contact pressure distribution. This has implications to fatigue prediction. On one hand ratchetting may be beneficial to the contact lifetime since it reduces stress peaks and consequently retards crack initiation. This effect can be computed using the Dang Van HCF parameter (Dang Van, 1993). On the other hand continuing strain ratchetting may lead to another material rupture mode similar to that in a tensile or torsion test. A possible criterion for this would be a critical ratchetting strain (Kapoor, 1994). For a further assessment of these two damage modes a quantitatively sound multikinematic material model of Ti6Al4V needs to be identified from ratchetting tests.

Another peculiarity in fretting damage is that micrometer scale material volumes

experience high cyclical stresses. On the micrometer scale the assumption inherent to von Mises material models, that metals are homogeneous materials, is not valid. This is why a polycrystal plasticity material model of Ti6Al4V is identified in this work (Dick and Cailletaud, 2006b). Only hexagonal α -phase of the alloy is taken into account, material texture is integrated in a qualitative manner, the hardening parameters are identified from macroscopic fatigue tests in the $R_\epsilon = 0$ and $R_\epsilon = -1$ conditions. With this model the mean stress relaxation, which is not complete but stops at a threshold, can be described. The polycrystal plasticity model can be further improved by the integration of the microstructure's lamellar $\alpha - \beta$ zones, of quantitative texture measurements and more extensive (but computationally costly) parameter identification.

The application of this material model to a 3D model of the fretting cylinder/plate contact demonstrates an important influence of the Ti6Al4V micro structure on the stress and strain response (Dick and Cailletaud, 2006c). The use of the micro structural scale material models is an opportunity to reassess HCF prediction. In this thesis a first attempt is made by discussing the Dang Van HCF parameter assumptions, which base on a scale transition between microstructural and structural stress response. Then an adaptation of the parameter is proposed. The adaptation causes only a minor change of predicted fretting fatigue. In future work other fatigue parameters, which use plastic strain measures, can be considered for fatigue prediction with polycrystal plasticity material models. By this the material model's ability to resolve plastic deformation in grains can be confronted with the observation that cracks form in grains that experience continual cyclic plastic deformation when ductile polycrystalline metals are loaded in the HCF regime.

Interaction of wear and fatigue: In fretting experiments at elevated contact loads, fatigue is the observed damage mechanism in partial slip when the displacement amplitudes are small. When the displacement amplitude is increased, in total slip, both wear and cracking are observed. If the displacement amplitude is further increased only wear and no cracking can be found in contact. This interaction between wear and fatigue in fretting contacts is investigated in this thesis.

If two fatigue cracks coalesce they may detach a wear particle instead of propagating into the material (Szolwinski and Farris, 1996). To test this hypothesis 3D cylinder-plate fretting computations with different normal loads and displacement amplitudes using polycrystal plasticity are performed in this work and the Dang Van HCF criterion is used for the prediction of cracking. At small displacement amplitudes the fatigue criterion predicts a crack at the contact borders which is consistent with experimental results. At more elevated displacement amplitudes a crack at the contact border and multiple cracks in the centre of contact (possibly detaching wear particles) are predicted. This is consistent with the observation of cracking and wear in the contact surfaces of specimens after tests with similar fretting conditions. In computations with further increased displacement amplitudes cracking all over the contact is predicted. If the cracks all coalesce detaching particles, wear is the only apparent damage mechanism as in corresponding fretting tests.

Wear may have the effect of eliminating small cracks before they can grow to a critical length (Fouvry et al., 1999a). Or wear may just change the contact geometry, thus abate the cyclic stresses and retard or stop crack nucleation. In this work this effect is studied using 2D and 3D FE models of fretting blade-disc contacts. This is done by computing wear and related geometry change in the same way as done for cylinder-plate contacts in earlier work. The worn meshes are used for fretting computations with elastic material behaviour and subsequently with the multikinematic von Mises material model. Fatigue is calculated using the Dang Van HCF parameter. It can be shown that wear has the effect of increasing the fatigue lifetime of the blade-disc contact. The first fatigue cracks are predicted to initiate

on the disc in the vicinity of the contact edges on the side of the bend, which is also observed in tests with the real blade–disc structure. The results show that the blade–disc problem cannot be reduced to a 2D model. In future work 3D FE modelling will be indispensable for obtaining realistic wear and fatigue predictions. Also a better mesh refinement is necessary to resolve the high stress gradients at the contact proximity and in the bends of blade and disc.

Bibliography

- AMBRICO J. M. AND BEGLEY M. R. (2000). *Plasticity in fretting contact*. Journal of the Mechanics and Physics of Solids, vol. 48 n° 11, pp 2391–2417.
- AMBRICO J. M. AND BEGLEY M. R. (2001). *The role of macroscopic plastic deformation in fretting fatigue life predictions*. International Journal of Fatigue, vol. 23 n° 2, pp 121–128.
- AMONTONS G. (1699). *De la résistance causée dans les machines*. Mémoires de l'Académie Royale, vol. A, pp 275–282.
- ARAUJO J. A. AND NOWELL D. (2002). *The effect of rapidly varying contact stress fields on fretting fatigue*. International Journal of Fatigue, vol. 24 n° 7, pp 763–775.
- ARCHARD J. F. (1953). *Contact and rubbing of flat surfaces*. Journal of Applied Physics, vol. 24, pp 981–988.
- ARI-GUR P. AND SEMIATIN S. L. (1998). *Evolution of microstructure, macrotecture and microtexture during hot rolling of Ti-6Al-4V*. Materials Science and Engineering, vol. A257, pp 118–127.
- BARBE F., DECKER L., JEULIN D., AND CAILLETAUD G. (2001). *Intergranular and intragranular behavior of polycrystalline aggregates. Part 1: F.E. model*. International Journal of Plasticity, vol. 17, pp 513–536.
- BERTHIER Y., VINCENT L., AND GODET M. (1989). *Fretting fatigue and fretting wear*. Tribology International, vol. 22, pp 235–242.
- BESSON J., CAILLETAUD G., CHABOCHE J.-L., AND FOREST S. (2001). *Mécanique non linéaire des matériaux*. Hermès.
- BESSON J. AND FOERCH R. (1998). *Object-oriented programming applied to the finite element method. Part I: General concepts*. Revue Européenne des Éléments Finis, vol. 7 n° 5, pp 535–566.
- BESSON J., RICHE R. LE, FOERCH R., AND CAILLETAUD G. (1998). *Object-oriented programming applied to the finite element method. Part II: Application to material behaviors*. Revue Européenne des Éléments Finis, vol. 7 n° 5, pp 567–588.
- éds. Bornert M., Bretheau T., and Gilormini P. (2001). *Homogénéisation en mécanique des matériaux 1: Matériaux aléatoires élastiques et milieux périodiques*. Hermès science publications, Paris.
- CARMAN G. P., LESKO J. J., REIFSNIDER K. L., AND DILLARD D. A. (1993). *Micromechanical Model of Composite Materials Subjected to Ball Indentation*. Journal of Composite Materials, vol. 27 n° 3, pp 303–329.

- CHABOCHE J. L. (1991). *On some modifications of kinematic hardening to improve the description of ratchetting effects*. International Journal of Plasticity, vol. 7 n° 7, pp 661–678.
- CHABOCHE J. L., CHARLES J. L., FEYEL F., GALLERNEAU F., KANOUTÉ P., KRUCH S., LAURIN F., OUSSET Y., PACOU D., POIRIER D., AZZOUZ F., FOREST S., CAILLETAUD G., DICK T., QUILICI S., RUAU J., GOMEZ P., AND MARIGO J. J. *Programme Pluriannuel de Recherche Concerté en Durée de vie – Rapport d’avancement CRA 2.3 des travaux de l’ONERA de la phase I à t0+18 mois*. Technical Report RT 2/08618 DMSE, ONERA, Châtillon.
- CHABOCHE J. L. AND LEMAITRE J. (2001). *Mécanique des matériaux solides*. Dunod, 2 edition.
- CHABOCHE J. L. AND NOUAILHAS D. (1989a). *Constitutive modeling of ratchetting effects. I: Experimental facts and properties of the classical models*. Journal of Engineering Materials and Technology, vol. 111 n° 4, pp 384–392.
- CHABOCHE J. L. AND NOUAILHAS D. (1989b). *Constitutive modeling of ratchetting effects. II: Possibilities of some additional kinematic rules*. Journal of Engineering Materials and Technology, vol. 111 n° 4, pp 409–416.
- CHAN K. S., LEE Y-D, DAVIDSON D. L., AND HUDAK S. J. (2001). *A fracture mechanics approach to high cycle fretting fatigue based on the worst case fret concept, I. Model development*. International Journal of Fracture, vol. 112, pp 299–330.
- CHEIKH M., QUILICI S., AND CAILLETAUD G. (2004). *Presentation of a phenomenological model of variable friction in fretting contact*. Submitted to wear, vol. .
- COMBRES Y. AND CHAMPIN B. (1991). *Titanium Alloys Processing: State of Art and Perspectives*. Materiaux et Techniques, vol. 79 n° 5–6, pp 31–41.
- COULOMB A. (1821). *Théorie des machines simples*. Paris.
- CZICHOS H. (1978). *Tribology. A Systems Approach to the Science and Technology of Friction, Lubrication and Wear*. Elsevier Scientific Publishing Co.
- DANG VAN K. (1993). *Macro-micro approach in high-cycle multiaxial fatigue*. In : Multiaxial Fatigue, eds. McDowell D. L. and Ellis R., ASTM STP 1191, pp 120–130, Philadelphia. ASTM.
- DANG VAN K., CAILLETAUD G., FLAVENOT J. F., LE DOUARON A., AND LIEURADE H. P. (1984). *Critère d’amorçage en fatigue à grands nombres de cycles sous sollicitations multiaxiales*. Technical Report RE1123, Institut de recherches de la sidérurgie française, Paris.
- DECKER L. AND JEULIN D. (2000). *Simulation 3D de matériaux aléatoires polycristallins*. Revue de Métallurgie–CIT/Science et Génie des Matériaux, vol. 97, pp 271–275.
- DICK T. AND CAILLETAUD G. (2006a). *Analytic and FE based estimations of the coefficient of friction of composite surfaces*. Accepted in Wear, vol. .
- DICK T. AND CAILLETAUD G. (2006b). *Fretting modelling with a crystal plasticity model of Ti6Al4V*. Accepted in Computational Materials Science, vol. .

- DICK T. AND CAILLETAUD G. (2006c). *Numerical modelling in fretting of TA6V including crystal plasticity*. In : 14èmes Journées Francophones de Tribologie, la tribologie dans les transports, in Press, Tarbes.
- DICK T., PAULIN C., CAILLETAUD G., AND FOUVRY S. (2006). *Experimental and numerical analysis of local and global plastic behaviour in fretting wear*. Accepted in Tribology International, vol. .
- DINI D. AND NOWELL D. (2003). *Prediction of the slip zone friction coefficient in flat and rounded contact*. Wear, vol. 254 n° 3-4, pp 364–369.
- DRAGON-LOUISET M. (2001). *On a predictive macroscopic contact–sliding wear model based on micromechanical considerations*. International Journal of Solids and Structures, vol. 38, pp 1625–1639.
- ESHELBY J. D. (1957). *The Determination of the Elastic Field of an Ellipsoidal Inclusion, and Related Problems*. Proceedings of the Royal Society of London A, vol. 241, pp 376–396.
- FATEMI A. AND SOCIE D. F. (1988). *A critical plane approach to multiaxial fatigue damage including out-of-phase loading*. Fatigue & Fracture of Engineering Materials & Structures, vol. 11 n° 3, pp 149–165.
- FLAVENOT J. F. AND SKALLI N. (1989). *A Critical Depth Criterion for the Evaluation of Long-Life Fatigue Strength under Multiaxial Loading and a Stress Gradient*. In : Biaxial and Multiaxial Fatigue, eds. Brown M. W. and Miller K. J., pp 355–365, London. EGF 3, Mechanical Engineering Publications.
- FOUVRY S., KAPSA P., AND VINCENT L. (1999a). *Fretting wear and fretting fatigue: relation through a mapping concept*. In : Fretting fatigue: current technology and practices, eds. Hoepfner D. W., Chandrasekaran V., and Elliot C. B., ASTM STP 1367, pp 49–64.
- FOUVRY S., KAPSA P., AND VINCENT L. (1999b). *A multiaxial fatigue analysis of fretting contact taking into account the size effect*. In : Fretting fatigue: current technology and practices, eds. Hoepfner D. W., Chandrasekaran V., and Elliot C. B., ASTM STP 1367, pp 167–182.
- FOUVRY S., KAPSA P., ZAHOUANI H., AND VINCENT L. (1997). *Wear analysis in fretting of hard coatings through a dissipated energy concept*. Wear, vol. 203–204, pp 393–403.
- FOUVRY S., LISKIEWICZ T., KAPSA P., HANNEL S., AND SAUGER E. (2003). *An energy description of wear mechanisms and its applications to oscillating sliding contacts*. Wear, vol. 255 n° 1, pp 287–298.
- FOUVRY S., VINCENT L., AND KAPSA P. (1996). *Quantification of fretting damage*. Wear, vol. 200 n° 1-2, pp 186–205.
- FRIDRICI V. (2002). *Fretting d'un alliage de titane revêtu et lubrifié application au contact aube/disque*. PhD thesis, École Centrale de Lyon, Ecully.
- FRIDRICI V., FOUVRY S., KAPSA P., AND PERRUCHAUT P. (2003). *Impact of contact size and geometry on the lifetime of a solid lubricant*. Wear, vol. 255 n° 7-12, pp 875–882.
- FUNDENBERGER J. J., PHILIPPE M.J., WAGNER F., AND ESLING C. (1997). *Modelling and prediction of mechanical properties for materials with hexagonal symmetry (zinc, titanium and zirconium alloys)*. Acta materialia, vol. 45 n° 10, pp 4041–4055.

- GIANNAKOPOULOS A. E., LINDLEY T. C., AND SURESH S. (1998). *Aspects of equivalence between contact mechanics and fracture mechanics: theoretical connections and a life-prediction methodology for fretting-fatigue*. *Acta Materialia*, vol. 46 n° 9, pp 2955–2968.
- GIANNAKOPOULOS A. E., LINDLEY T. C., SURESH S., AND CHENUT C. (2000). *Similarities of stress concentrations in contact at round punches and fatigue at notches: implications to fretting fatigue crack initiation*. *Fatigue & Fracture of Engineering Materials & Structures*, vol. 23, pp 561–571.
- GODET M. (1984). *The Third-Body Approach: a Mechanical View of Wear*. *Wear*, vol. 100 n° 1–3, pp 437–452.
- GOH C. H., MCDOWELL D. L., AND NEU R. W. (2003a). *Characteristics of plastic deformation field in polycrystalline fretting contacts*. *International Journal of Fatigue*, vol. 25 n° 9-11, pp 1047–1058.
- GOH C.-H., NEU R. W., AND MCDOWELL D. L. (2003b). *Crystallographic plasticity in fretting of Ti-6Al-4V*. *International Journal of Plasticity*, vol. 19 n° 10, pp 1627–1650.
- GOH C. H., WALLACE J. M., NEU R. W., AND MCDOWELL D. L. (2001). *Polycrystal plasticity simulations of fretting fatigue*. *International Journal of Fatigue*, vol. 23 n° Supplement 1, pp 423–435.
- GORYACHEVA I. G. (1998). *Contact Mechanics in Tribology*. Kluwer Academic Publishers, Dordrecht.
- GUERRIER K. LE BIAVANT (2000). *Etude de l'amorçage de fissures de fatigue dans le Ti-6Al-4V*. PhD thesis, École Centrale de Paris, Paris.
- HILL R. (1965). *Continuum micro-mechanics of elastoplastic polycrystals (Internal stress and strain inhomogeneities in arbitrarily deformed aggregate of elastoplastic crystals)*. *Journal of the Mechanics and Physics of Solids*, vol. 13, pp 89–101.
- HILLS D. A. AND NOWELL D. (1994). *Mechanics of fretting fatigue*. Kluwer, Dordrecht.
- HILLS D. A., NOWELL D., AND O'CONNOR J. J. (1988). *On the mechanics of fretting fatigue*. *Wear*, vol. 125, pp 129–146.
- HOLM R. (1946). *Electric Contacts*. Almquist & Wiksells, Uppsala.
- HSU S. M., SHEN M. C., AND RUFF A. W. (1997). *Wear prediction for metals*. *Tribology International*, vol. 30 n° 5, pp 377–383.
- HUTSON A., NIINOMI M., NICHOLAS T., AND EYLON D. (2002). *Effect of various surface conditions on fretting fatigue behavior of Ti-6Al-4V*. *International Journal of Fatigue*, pp 1223–1234.
- IREMAN P., KLARBRING A., AND STROMBERG N. (2002). *Finite element algorithms for thermoelastic wear problems*. *European Journal of Mechanics - A/Solids*, vol. 21 n° 3, pp 423–440.
- JEAN M. AND TOUZOT G. (1988). *Implementation of unilateral contact and dry friction in computer codes dealing with large deformations problems*. *Journal de Mécanique théorique et appliquée*, vol. 7, pp 145–160. Special issue, supplement Nr. 1.
- JOHNSON K. L. (1987). *Contact mechanics*. Cambridge University Press, Cambridge.

- KAPOOR A. (1994). *A re-evaluation of the life to rupture of ductile metals by cyclic plastic strain*. Fatigue & Fracture of Engineering Materials & Structures, vol. 17 n° 2, pp 201–219.
- KOCKS U. F. AND BROWN T. J. (1966). *Latent hardening in aluminium*. Acta Metallurgica, vol. 14, pp 87–98.
- KROENER E. (1961). *Zur plastischen Verformung des Vielkristalls*. Acta Metallurgica, vol. 9, pp 155–161.
- LIM S. C. AND ASHBY M. F. (1987). *Wear-mechanism maps*. Acta metallurgica, vol. 35 n° 1, pp 1–24.
- LUDEMA K. C. AND MENG H. C. (1995). *Wear models and predictive equations: their form and content*. Wear, vol. 181–183, pp 443–457.
- MAXIAN T. A., BROWN T. D., PEDERSEN D. R., AND CALLAGHAN J. J. (1996). *A sliding-distance-coupled finite element formulation for polyethylene wear in total hip arthroplasty*. Journal of Biomechanics, vol. 29 n° 5, pp 687–692.
- MCDOWELL D. L. (1995). *Stress state dependence of cyclic ratchetting behavior of two rail steels*. International Journal of Plasticity, vol. 11 n° 4, pp 397–421.
- MÉRIC L. AND CAILLETAUD G. (1991). *Single Crystal Modeling for Structural Calculations. Part 2: Finite Element Implementation*. Journal of Engineering Materials and Technology, vol. 113, pp 171–182.
- MORRISSEY R., GOH C.-H., AND MCDOWELL D. L. (2003). *Microstructure-scale modeling of HCF deformation*. Mechanics of Materials, vol. 35 n° 3-6, pp 295–311.
- MORRISSEY R. J., MCDOWELL D. L., AND NICHOLAS T. (1999). *Frequency and stress ratio effects in high cycle fatigue of Ti-6Al-4V*. International Journal of Fatigue, vol. 21 n° 7, pp 679–685.
- MORRISSEY R. J., MCDOWELL D. L., AND NICHOLAS T. (2001). *Microplasticity in HCF of Ti-6Al-4V*. International Journal of Fatigue, vol. 23 n° Supplement 1, pp 55–64.
- NABOULSI S. AND MALL S. (2003). *Fretting fatigue crack initiation behavior using process volume approach and finite element analysis*. Tribology International, vol. 36 n° 2, pp 121–131.
- NABOULSI S. AND NICHOLAS T. (2003). *Limitations of the Coulomb friction assumption in fretting fatigue analysis*. International Journal of Solids and Structures, vol. 40 n° 23, pp 6497–6512.
- NICHOLAS T., HUTSON A., JOHN R., AND OLSON S. (2003). *A fracture mechanics methodology assessment for fretting fatigue*. International Journal of Fatigue, vol. 25 n° 9-11, pp 1069–1077.
- NOWELL D. AND DINI D. (2003). *Stress gradient effects in fretting fatigue*. Tribology International, vol. 36 n° 2, pp 71–78.
- NOWELL D. AND HILLS D. A. (1990). *Crack initiation criteria in fretting fatigue*. Wear, vol. 136, pp 329–343.

- OQVIST M. (2001). *Numerical simulations of mild wear using updated geometry with different step size approaches*. *Wear*, vol. 249 n° 1-2, pp 6–11.
- PERILLA J. A. MEDINA AND SEVILLANO J. GIL (1995). *Two-dimensional sections of the yield locus of a Ti-6%Al-4%V alloy with a strong transverse-type crystallographic alpha-texture*. *Materials Science and Engineering A*, vol. 201 n° 1–2, pp 103–110.
- PHILIPPE M. J., ESLING C., AND HOCHÉID B. (1988). *Role of Twinning in Texture Development and in Plastic Deformation of Hexagonal Materials*. *Textures and Microstructures*, vol. 7, pp 265–301.
- PHILIPPE M. J., SERGHAT M., HOUTTE P. VAN, AND ESLING C. (1995). *Modelling of texture evolution for materials of hexagonal symmetry. II. Application to zirconium and titanium alpha or near alpha alloys*. *Acta Metallurgica et Materialia*, vol. 43 n° 4, pp 1619–1630.
- RATSIMBA C.H.H., MCCOLL I.R., WILLIAMS E.J., LEEN S.B., AND SOH H.P. (2004). *Measurement, analysis and prediction of fretting wear damage in a representative aeroengine spline coupling*. *Wear*, vol. 257 n° 11, pp 1193–1206.
- RUIZ C., BODDINGTON P. H. B., AND CHEN K. C. (1984). *An investigation of fatigue and fretting in a dovetail joint*. *Experimental Mechanics*, vol. 24 n° 3, pp 208–217.
- SAUGER E., FOUVRY S., PONSONNET L., KAPSA PH., MARTIN J. M., AND VINCENT L. (2000). *Tribologically transformed structure in fretting*. *Wear*, vol. 245 n° 1-2, pp 39–52.
- SCHOENFELD S. E. AND KAD B. (2002). *Texture effects on shear response in Ti-6Al-4V plastes*. *International Journal of Plasticity*, vol. 18, pp 461–486.
- SHIMA M., SUETAKE H., MCCOLL I. R., WATERHOUSE R. B., AND TAKEUCHI M. (1997). *On the behaviour of an oil lubricated fretting contact*. *Wear*, vol. 210, pp 304–310.
- SMITH K. N., WATSON P., AND TOPPER T. H. (1970). *A Stress-Strain Function for the Fatigue of Metals*. *Journal of Materials*, vol. 5 n° 4, pp 767–778.
- SOCIE D. (1987). *Multiaxial Fatigue Damage Models*. *Journal of Engineering Materials and Technology*, vol. 109, pp 293–298.
- STUPKIEWICZ S. AND MROZ Z. (1999). *A model of third body abrasive friction and wear in hot metal forming*. *Wear*, vol. 231, pp 124–138.
- SWALLA D. R. AND NEU R. W. (2001). *Influence of coefficient of friction on fretting fatigue crack nucleation prediction*. *Tribology International*, vol. 34 n° 7, pp 493–503.
- SWALLA D. R. AND NEU R. W. (2003). *Characterisation of fretting process volume using finite element analysis*. In : *Fretting fatigue: advances in basic understanding and applications*, éd. Mutoh Y., Kinyon S. E., and Hoepfner D. H., ASTM STP 1425.
- SZOLWINSKI M. P. AND FARRIS T. N. (1996). *Mechanics of fretting fatigue crack formation*. *Wear*, vol. 198 n° 1-2, pp 93–107.
- TAYLOR G. (1938). *Plastic strain in metals*. *Journal of the Institute of Metals*, vol. 62, pp 307–324.
- VALANIS K. C. (1980). *Fundamental consequences of a new intrinsic time measure plasticity as a limit of the endochronic theory*. *Archives of Mechanics*, vol. 32, pp 171.

- VINGSBO O. AND SODERBERG S. (1988). *On fretting maps 1*. Wear, vol. 126 n° 2, pp 131–147.
- WU L., HOLLOWAY B. C., BEESABATHINA D. P., KALIL C., AND MANOS D. M. (2000). *Analysis of diamond-like carbon and Ti MoS₂ coatings on Ti-6Al-4V substrates for applicability to turbine engine applications*. Surface and Coatings Technology, vol. 130, pp 207–217.
- XU G. H., ZHU M., LIU J., ZHOU Z., AND LIANG H. (2003a). *The effect of pre-treatment of substrate on fretting tribological behavior of MoS₂ coatings*1*. Wear, vol. 255 n° 1-6, pp 246–252.
- XU J., ZHU M. H., ZHOU Z. R., KAPSA P., AND VINCENT L. (2003b). *An investigation on fretting wear life of bonded MoS₂ solid lubricant coatings in complex conditions*1*. Wear, vol. 255 n° 1-6, pp 253–258.
- ZAEFFERER S. (1996). *Entwicklung und Anwendungen eines elektronenmikroskopischen on-line Verfahrens zur Bestimmung von Verformungssystemen in hexagonalen Werkstoffen*. PhD thesis, Techn. Univ. Clausthal, Clausthal.
- ZHU M. H. AND ZHOU Z. R. (2001). *An investigation of molybdenum disulfide bonded solid lubricant coatings in fretting conditions*. Surface and Coatings Technology, vol. 141, pp 240–245.